Leibniz-Institut für
Astrophysik Potsdam

Stars under influence: evidence of tidal interactions between stars and substellar companions

Nikoleta Ilić Petković

Universitätsdissertation
zur Erlangung des akademischen Grades

doctor rerum naturalium
(Dr. rer. nat.)

in der Wissenschaftsdisziplin
Astrophysik

eingereicht an der
Mathematisch-Naturwissenschaftlichen Fakultät
der Universität Potsdam

Datum der Disputation: 21. November 2023

Betreuer

Prof. Dr. Katja Poppenhaeger
Leibniz-Institut für Astrophysik Potsdam / Universität Potsdam

Gutachter

Prof. Dr. Katja Poppenhaeger
Leibniz-Institut für Astrophysik Potsdam / Universität Potsdam

Dr. Cristina Chiappini
Leibniz-Institut für Astrophysik Potsdam

Prof. Dr. Christopher Watson
Queen's University Belfast

Published online on the
Publication Server of the University of Potsdam:
https://doi.org/10.25932/publishup-61597
https://nbn-resolving.org/urn:nbn:de:kobv:517-opus4-615972

Abstract

Tidal interactions occur between gravitationally bound astrophysical bodies. If their spatial separation is sufficiently small, the bodies can induce tides on each other, leading to angular momentum transfer and altering of evolutionary path the bodies would have followed if they were single objects. The tidal processes are well established in the Solar planet-moon systems and close stellar binary systems. However, how do stars behave if they are orbited by a substellar companion (e.g. a planet or a brown dwarf) on a tight orbit?

Typically, a substellar companion inside the corotation radius of a star will migrate toward the star as it loses orbital angular momentum. On the other hand, the star will gain angular momentum which has the potential to increase its rotation rate. The effect should be more pronounced if the substellar companion is more massive. As the stellar rotation rate and the magnetic activity level are coupled, the star should appear more magnetically active under the tidal influence of the orbiting substellar companion. However, the difficulty in proving that a star has a higher magnetic activity level due to tidal interactions lies in the fact that (I) substellar companions around active stars are easier to detect if they are more massive, leading to a bias toward massive companions around active stars and mimicking the tidal interaction effect, and that (II) the age of a main-sequence star cannot be easily determined, leaving the possibility that a star is more active due to its young age.

In our work, we overcome these issues by employing wide stellar binary systems where one star hosts a substellar companion, and where the other star provides the magnetic activity baseline for the host star, assuming they have coevolved, and thereby provides the host's activity level if tidal interactions have no effect on it. Firstly, we find that extrasolar planets can noticeably increase the host star's X-ray luminosity and that the effect is more pronounced if the exoplanet is at least Jupiter-like in mass and close to the star. Further, we find that a brown dwarf will have an even stronger effect, as expected, and that the X-ray surface flux difference between the host star and the wide stellar companion is a significant outlier when compared to a large sample of similar wide binary systems without any known substellar companions. This result proves that substellar hosting wide binary systems can be good tools to reveal the tidal effect on host stars, and also show that the typical stellar age indicators as activity or rotation cannot be used for these stars. Finally, knowing that the activity difference is a good tracer of the substellar companion's tidal impact, we develop an analytical method to calculate the modified tidal quality factor Q' of individual host stars, which defines the tidal dissipation efficiency in the convective envelope of a given main-sequence star.

Zusammenfassung

Gezeitenwechselwirkungen treten zwischen gravitativ gebundenen astrophysikalischen Körpern auf. Wenn ihr räumlicher Abstand hinreichend gering ist, können die Körper gegenseitig Gezeiten hervorrufen, die eine Drehimpulsübertragung bewirken und den Entwicklungsweg der Körper verändern, den sie als Einzelobjekte einschlagen würden. Die Gezeitenprozesse sind in den Planet-Mond-Systemen des Sonnensystems und in engen Doppelsternsystemen gut bekannt. Wie verhalten sich jedoch Sterne, die von einem substellaren Begleiter (z. B. einem Planeten oder einem Braunen Zwerg) auf einer engen Bahn umkreist werden?

In der Regel wandert ein substellarer Begleiter innerhalb des Korotationsradius eines Sterns in Richtung des Sterns, da er an Bahndrehimpuls verliert. Auf der anderen Seite gewinnt der Stern an Drehimpuls, was seine Rotationsrate erhöhen kann. Dieser Effekt dürfte umso ausgeprägter sein, je massereicher der substellare Begleiter ist. Da die Rotationsrate des Sterns und das Niveau der magnetischen Aktivität gekoppelt sind, sollte der Stern unter dem Gezeiteneinfluss des ihn umkreisenden substellaren Begleiters magnetisch aktiver erscheinen. Die Schwierigkeit beim Nachweis, dass ein Stern aufgrund von Gezeitenwechselwirkungen eine höhere magnetische Aktivität aufweist, liegt jedoch darin, dass (I) substellare Begleiter um aktive Sterne leichter aufzuspüren sind, wenn sie massereicher sind, wodurch eine Tendenz zu massereichen Begleitern um aktive Sterne entsteht und der Effekt der Gezeitenwechselwirkung nachgeahmt wird, und dass (II) das Alter eines Hauptreihensterns nicht leicht bestimmt werden kann, so dass die Möglichkeit besteht, dass ein Stern aufgrund seines jungen Alters aktiver ist.

In unserer Arbeit überwinden wir diese Hindernisse, indem wir weiträumige Doppelsternsysteme verwenden, in denen ein Stern einen substellaren Begleiter beherbergt und in denen der andere Stern den Referenzwert für die magnetische Aktivität des Wirtssterns liefert im Fall das Gezeitenwechselwirkungen keinen Einfluss auf ihn haben, wobei wir davon ausgehen, dass die Sterne sich gemeinsam entwickelt haben. Erstens stellen wir fest, dass extrasolare Planeten die Röntgenleuchtkraft des Wirtssterns merklich erhöhen können und dass der Effekt ausgeprägter ist, wenn der Exoplanet mindestens eine jupiterähnliche Masse hat und sich nahe am Stern befindet. Darüber hinaus stellen wir fest, dass ein Brauner Zwerg erwartungsgemäß einen noch stärkeren Einfluss hat und dass der Unterschied im Röntgenflächenfluss zwischen dem Wirtsstern und dem weiträumigen stellaren Begleiter ein signifikanter Ausreißer im Vergleich zu einer großen Stichprobe ähnlicher weiträumiger Doppelsternsysteme ohne bekannte substellare Begleiter ist. Dieses Ergebnis beweist, dass weiträumige Doppelsternsysteme mit substellaren Begleitern ein gutes Werkzeug sein können, um den Gezeiteneffekt auf Wirtssterne aufzudecken, und zeigt auch, dass die typischen stellaren Altersindikatoren wie Aktivität oder Rotation für diese Sterne nicht verwendet werden können. Mit dem Wissen, dass der Aktivitätsunterschied ein guter Indikator für den Gezeiteneinfluss des substellaren Begleiters ist, entwickeln wir schließlich eine analytische Methode zur Berechnung des modifizierten Gezeitenqualitätsfaktors Q' für einzelne Wirtssterne, der die Effizienz der Gezeitendissipation in der konvektiven Hülle eines gegebenen Hauptreihensterns definiert.

Statement of contribution

This doctoral dissertation is based on two peer-reviewed articles (Chapters 2 and 3), and one article in preparation for submission to a peer-reviewed journal (Chapter 4). The cross-references between the chapters of the dissertation and the aforementioned articles are provided. The formatting of these articles was adopted to give the doctoral dissertation uniform layout. In the following, I (Ilić, N.) outline my contribution and those of the co-authors.

- Ilić, N., Poppenhaeger, K., Hosseini, S.M.: *Tidal star-planet interaction and its observed impact on stellar activity in planet-hosting wide binary systems*; MNRAS, Volume 513, Issue 3 (2022). DOI: 10.1093/mnras/stac861.
  In this article, we analyse wide stellar binary systems with star-planet systems and show the tidal impact planets have on stars. I defined the stellar wide binary sample, obtained and analysed the archival observations from the Chandra X-ray Telescope and XMM-Newton Space Observatory data archives. I created a pipeline to calculate the stellar X-ray luminosity from detected X-ray photons for both observatories. These steps were done under the supervision of Prof. Dr. Katja Poppenhaeger. S.M. Hosseini did a literature research for rotation periods of stars in the sample. I implemented and calculated the tidal interaction parameters for each star-planet systems. I wrote the manuscript and created all displayed figures with the helpful guidance by Prof. Dr. Katja Poppenhaeger.

- Ilić, N., Poppenhaeger, K., Dsouza, D., Wolk, S.J., Agüeros, M.A., Stelzer, B.: *The first evidence of tidally induced activity in a brown dwarf-M dwarf pair: A Chandra study of the NLTT 41135/41136 system*; MNRAS, Volume 524, Issue 4 (2023). DOI: 10.1093/mnras/stad2277.
  In this article, we analyse more than 30 M dwarf wide binary systems, out of which one system hosts a brown dwarf, and calculate the tidal-impact significance of the brown dwarf. Prof. Dr. Katja Poppenhaeger and Prof. Dr. Marcel A. Agüeros wrote and submitted the observation proposal for the NLTT 41135/41136 system to the Chandra X-ray Center. I defined the sample of systems used in this study, and calculated the X-ray fluxes of stars in systems observed by the XMM-Newton Space Observatory, including the NLTT 41135/41136 system observed with the Chandra X-ray Telescope. Prof. Dr. Katja Poppenhaeger provided the X-ray fluxes of stars in systems observed with eROSITA, Desmond Dsouza calculated the X-ray fluxes of stars in systems observed by the Chandra X-ray Telescope. Dr. Scott J. Wolk provided the X-ray fluxes of stars in the GJ 65 system. I created the pipeline to calculate the radii and X-ray surface fluxes of all stars. I wrote the manuscript and created all displayed figures with the helpful guidance by Prof. Dr. Katja Poppenhaeger, Prof. Dr. Marcel A. Agüeros, Prof. Dr. Beate Stelzer, and Dr. Scott J. Wolk.

- Ilić, N., Poppenhaeger, K., Queiroz, A.B.A, Chiappini, C.: *Constraining stellar tidal quality factors from planet-induced stellar spin-up*; to be submitted to the peer-reviewed journal Astronomische Nachrichten.
  In this article, we provide an analytical method for calculating the modified tidal quality factors of planet-hosting stars. Prof. Dr. Katja Popenhaeger and I formulated the steps of the method. I tested the method on the planet-hosting wide stellar binary system HD 189733. Dr. Anna Barbara A. Queiroz calculated the age of the planet-hosting star HD 189733 A. I wrote the manuscript and created all displayed figures with the helpful guidance by Prof. Dr. Katja Poppenhaeger and Dr. Cristina Chiappini.

Contents

1 Introduction

1.1 A short story of a star's life

Stars are diverse. These glowing balls of hydrogen, helium, and some trace elements, called metals in the field of astrophysics, might be some of the most important (astrophysical) objects in the context of life's existence. Although the topic of life is not of concern in this text, it is still worth acknowledging this fact.

Stars themselves go through various stages of evolution during their life where they behave in different ways: in the current cosmological time and space, they are formed from an interstellar cloud of gas and dust; they contract and ignite the nuclei merging process in their core called nuclear fusion; they live relatively long as *main-sequence* stars; close to the end of their life, they become giants, and, depending on their mass, go quietly or with a blow, yielding a compact remnant [LL17].

Many stars* in our Universe follow this scheme of existence and it may sound dull. One might think that by knowing one star, all other stars are known and understood. Having in mind that stars are too far away for detailed observations, this is a useful assumption, and the star closest to us, the Sun might be a good benchmark for some types of stars. The Sun is a G2V-type dwarf in the middle of its life. It steadily burns hydrogen in its radiative core, creating γ photons, which by interacting with the surrounding particles change their wavelength [Kee14]. They pass through a convective envelope and finally reach the surface. This process can last for several million years [Sti03]. Thereafter, they move freely through space and time, maybe reaching a curious observer several parsecs away.

Some stars that are like our Sun in terms of mass, might have formed with a different abundance of metals, with a different initial rotation rate, or they may not have formed alone but have a very close stellar or substellar companion which influences their evolution. Therefore, knowing one star gives us an idea of how (some) stars (should) work, but all these *small* differences can have a cumulative effect throughout the lifetime of a star, which can make it appear quite different. Hence, stars are diverse.

The following text will mostly focus on the aspect of the stellar rotation rate change under the gravitational influence of a close substellar-mass companion. Beforehand, we will learn why stars rotate, why they gradually decrease their rotation rate, what the stellar magnetic field has to do with it, and how can we observe it. After we (roughly) understood how stars work, we will take a look at empirical indications of star-planet interactions in general, and the physical mechanisms behind tidal interactions in particular.

*A star whose initial mass is less than 0.25 $M_\odot$ will not become a giant star [LBA97].

1.2 Evolution of the stellar rotation rate and magnetic activity level

1.2.1 How stars acquire angular momentum

Most stars are known to be magnetized[†], rotating spheres, composed mostly of ionized hydrogen, helium, and other elements called metals, that have collapsed under their gravitational potential [Hal08; Pay25; Pen65]. Firstly, a cloud of gas and dust in interstellar space experiences an initial disturbance. This can be caused by e.g. a nearby supernova explosion or a similar high-energy event that can produce a shock wave and acts as an initiator of star formation [MK04]. After the initial *kick*, the material starts slowly collapsing to the center of mass. The density and temperature inside the cloud increase gradually, while gravity battles internal gas pressure as heat is radiated away.

The increase in density and temperature leads to the formation of a first hydrostatic core which will further heat up until molecular hydrogen dissociates at $\sim$ 2000 K. This leads to a second collapse, ending in the formation of the second hydrostatic core, the protostar [Lar69; MI00]. In the next phase, the stage is set for the initial angular momentum of the star to be. As the protostar acquires mass from its circumstellar disk through the process of accretion, it is also gaining angular momentum. Here, its luminosity is dominated by the accretion process as well. Also, here, the protostars can experience a phase of "disk-locking", where the rotation rate does not evolve with time due to magnetic interactions with the circumstellar disk [HM05; Koe91]. More precisely, the angular momentum loss due to the magnetic torque between the disk and the protostellar surface is balanced by the angular momentum gain from the accreting matter.

After all the available material has been accreted[‡], the angular momentum $L = I\omega$ of the star is constant. However, due to ongoing gravitational contraction, the moment of inertia I of the star decreases leading to the increase of the rotation rate ω. About 40 Myr after the initial *kick* [Cho+16], a Sun-like star will reach the zero-age main sequence as the process of nuclear fusion is *ignited* in the stellar core at a temperature and pressure of $\sim 10^7$ K and $\sim 100\,\mathrm{g/cm^3}$, respectively, and the gravitational pressure forcing the star to collapse is equalized by the radiation pressure. The initial rotation rate the star has, depends on the time it was locked to the circumstellar disk and potentially on its mass [BFA97; JBG21a]. Now, the star is in the longest and most stable phase of its life, the main-sequence phase. From this point in time onward, until the star stops burning hydrogen in its core and starts evolving away from the main sequence, its rotation rate and angular momentum are governed by magnetic processes.

1.2.2 Angular momentum loss of the Sun and other low-mass main sequence stars

In its main-sequence phase, a single star cannot gain angular momentum, only loss it via its *magnetized* wind. The existence of a wind-like structure expanding from the solar atmosphere out into the interplanetary space was first suggested after observing the

[†]Massive stars seem to rarely have observable magnetic fields [Hub+08].

[‡]The median disk lifetime is estimated to be $\sim$ 3 Myr, but can span from a few 0.1 up to a few 10 Myr [BFA97].

acceleration of ion tails of comets [Bie51; Bie52; Bie57]. This behavior of the comet tails was assigned to its interaction with the fast-moving *solar corpuscular radiation*. Previous to this observation, it was thought that the outer corona was an extension of the Zodiacal light [van47]; however, it was shown that, if the corona has a temperature of a few million kelvins, necessary to accelerate and ionize the cometary tails to the observed values, it must expand [Par58; Par60]. The idea of the solar wind, as a hydrodynamic phenomenon, was born.

A magnetohydrodynamic description of the effects of the solar wind was introduced somewhat later [WD67a], where, aside from the thermal pressure gradient and gravity, also the solar magnetic field was assumed to play a role in the solar-wind flow. It was found that not all matter that expands away from the Sun is actually lost. A boundary surface at an average radial distance r_a from the Sun exists, where some ionized particles will have sufficient kinetic energy to escape the solar magnetic field and therefore contribute to the solar mass and angular momentum loss. This process of solar spin-down is called magnetic braking. The rate of angular momentum loss for the Sun was found to be [WD67a]:

$$\frac{dL_\odot}{dt} = \frac{2}{3}\Omega r_a^2 \frac{dM_\odot}{dt}, \tag{1.1}$$

where Ω is the solar rotation rate at the equator, and $\frac{dM_\odot}{dt}$ is the solar mass loss rate.

The scheme of the solar magnetic braking and the rates of mass and angular momentum loss was later generalized for stars other than the Sun [Kaw88; Mes68]. The last instance needed to facilitate the hypothesis of stellar spin-down was given with the observation of rotation rate decrease in stellar clusters of increasing ages [Sku72].

1.2.3 The stellar magnetic fields

We can now anticipate that the magnetic field is one of the main actors in the story of a star's life. In particular, stars that have convection in their interior are thought to be able to maintain the dynamo action needed to generate some of the observed phenomena associated with the existence of the magnetic field. However, for the dynamo action to start operating, a star needs to have an initial magnetic field. The leading hypotheses about how stars acquire the initial magnetic field starts at the protostellar stage: while a protostar forms from the interstellar cloud, the weak magnetic field immersed in the cloud collapses together with the matter, increasing its density, and creating the initial stellar magnetic field [MIM07].

Once on the main sequence, the star maintains nuclear fusion in its core due to the high pressure and temperature. The energy released in this process is transported outward through the radiative and convective zone interior to the stellar surface of a Sun-like star. In the radiative zone, the energy is transferred in the form of radiation: the low opacity of the environment and its high temperature and density allow for effective radiative diffusion via scattering [KW90b]. Once the density and temperature of the environment decrease sufficiently and its opacity increases, the energy in the form of radiation is absorbed by surrounding matter, and buoyant convective cells are formed. They then transport the energy, now in the form of heat (thermal energy), to cooler, less dense regions, where they expand, release the stored energy, and fall back to higher-density regions due to their lack of buoyancy [KW90a]. This large-scale movement of ionized

matter, i.e. plasma, in the convective zone of the star, is another key ingredient in the generation of stellar magnetic fields. Part of the energy released from the expanding convective cell at the top of the convective layer movies in the form of radiation through the stellar atmosphere layers: the photosphere, chromosphere, and corona.

1.2.3.1 Dynamo theory of the Sun

The closest and therefore best-known star is the Sun. The magnetic phenomena observed on its surface laid the path to the dynamo theory assumed to be valid for most, if not all partly convective stars. In particular, properties like the 11-year activity cycle [Sch49], the migration of spot groups toward the equator (Spörer's Law [Spö79]), their bipolar appearance with the leading spots having the same polarity during one cycle and in one hemisphere (Hale's Law [Hal08]), where the leading spots are closer to the equator (Joy's Law [Hal+19]) were significant in determining the mechanism behind the solar magnetic field generation.

The main idea is that the Sun's magnetic field is maintained by its interaction with plasma motions [Her58; Par55a; Rob70]. Therefore, the large-scale motion in form of convection and rotation, whose interaction drives global flows such as differential rotation [How09; Sch+98] and meridional circulation [Ulr10] are fundamental for the existence of the magnetic field. Similarly important for its existence is the conductivity of the flowing plasma. Considering that the conductive plasma is flowing through a(n initial) magnetic field, the magnetic induction equation can be applied to the whole system [Dav01]:

$$\frac{\partial \vec{B}}{\partial t} = \eta \nabla^2 \vec{B} + \nabla \times (\vec{v} \times \vec{B}). \tag{1.2}$$

Here η is the magnetic diffusivity, $\vec{B}$ is the magnetic field vector, and $\vec{v}$ is the velocity field vector of the plasma flow.

The two terms on the right-hand side represent the diffusion and advection induction mechanisms. Depending on the magnetic diffusivity, the typical velocity scale U, and the typical length scale L, which are combined in the magnetic Reynolds number $R_m = UL/\eta$ for a given system, one of the two mechanisms will dominate. For the Sun, and stars in general, given the large spatial scales and the fast surface plasma flows of ~ 1 km/s [Oba+17], the magnetic Reynolds number is $R_m >> 1$. In these kinds of systems, the magnetic induction is dominated by advection, and the magnetic field lines are frozen in the plasma [PF00].

This conclusion lays the path to the $\alpha\omega$-dynamo action thought to maintain and amplify the solar magnetic field, as well as the magnetic field of stars with convection [CS15; Par55a]. Simply put, the ω-effect of the $\alpha\omega$-dynamo explains the existence of the toroidal magnetic field, responsible for the bipolar nature and east-west orientation of Sunspots. The α-effect, on the other hand, is responsible for the generation of a poloidal field from the toroidal field after an activity cycle is completed.

The ω-effect generates the toroidal field due to the poloidal field being winded up by the differential rotation of the Sun. It is also postulated that the toroidal field is located at the tachocline, the shear layer between the radiative core[§] and the convective envelope

[§]Hereafter, as the radiative core is considered the region in a star which envelopes the core, where nuclear fusion takes place, and the radiative zone.

of the Sun [Mie05; SZ92]. Here, the magnetic field is amplified due to the frozen flux theorem since the stretching of magnetic field lines amplifies the magnetic field amplitude. Finally, due to the convective motion of the cooling plasma, active regions emerge on the solar photosphere [Par09; Web+23].

The ω-effect is well established, whereas the reversal from the toroidal field back to a poloidal one is still a matter of discussion. One hypothesis is the α-effect [Par55b]: a turbulent flow can twist toroidal field lines into poloidal ones. If a toroidal field line experiences turbulent twisting such that many detached loops along it can be produced, they induce a toroidal current causing a large-scale poloidal field.

An alternative mechanism for creating a poloidal field from a toroidal one is the Babcock- Leighton mechanism [Bab61; Lei69]. Here, the toroidal magnetic field lines and the associated magnetic flux tubes located in the tachocline are stretched and experience an updrift due to the buoyancy force of convection. The flux tubes exit the solar surface forming two Sunspots of opposite polarities (Hale's law). Under the influence of the upward motion and the Coriolis force, the following sunspots experience a drift toward the pole causing the spot group to be tilted with respect to the equator (Joy's law). The formation of the poloidal field out of the toroidal field is explained by the meridional circulation which drifts the decaying sun spots, where their magnetic field will reverse the polarity of the preexisting magnetic field.

1.2.3.2 Dynamo action in fully convective stars

Looking at lower-mass stars, particularly those below the fully convective boundary [CB97], where the heat transport from the center to the surface of a star happens purely through convection, one can consider a different scenario of magnetic field generation. The major difference, in terms of the dynamo action, between partly and fully convective stars is the absence of a radiative core and, therefore, the tachocline.

There are several hypotheses about how fully convective stars generate their magnetic fields. For example, it is postulated that helical turbulence [DDR93], where only the turbulent velocity field due to convection rather than differential or global rotation, is responsible for the existence of a magnetic field. Taking the stellar rotation into account, magnetic field generation in fully convective stars is explained via the α^2-dynamo where the helicity is generated by the action of the Coriolis force on the convective motion [CK06]. Also, 3D dynamo models without a tachocline showed that fully convective stars can generate large-scale magnetic fields where the stellar rotation rate impacts the field strength [Bro08; DSB06; Yad+15] .

Recently, it was suggested that fully convective stars actually generate their magnetic fields as partly convective stars do. Empirically, when observing their magnetic appearance and their rotation rate, fully convective stars seem to change both at the same rate as partly convective stars [WD16; Wri+18]. Numerically, models have shown that a tachocline is not mandatory for a toroidal magnetic field to be generated [FF14; Nel+13]. It can be generated throughout the entire convective envelope of a partly convective star, therefore introducing the possibility of a toroidal field in fully convective stars. One issue with this idea is that the magnetic flux tubes are highly buoyant. Having a layer of strong shear where magnetic buoyancy is weak, i.e. a tachocline, is advantageous, as it can provide sufficient time for the magnetic field to be amplified to sufficient strength before it rises to the surface [Par75].

To summarize, the generation of the magnetic field in fully convective stars is still unclear. The biggest issue in understanding their dynamo action is that until recently [Mag+20; Rei+22; Ste+13; Wri+18], only fast rotating fully convective stars with strong magnetic fields were known, providing only a limiting picture of their behavior. It has to be considered that the $\alpha\omega$-dynamo postulated for partly convective stars can be well-tested because we have a stellar prototype at our cosmic front door. This still does not enable us to resolve all the uncertainties and long-standing open questions about the solar-type dynamo [CDB17]. Therefore, not having a clear picture of how fully convective stars generate their magnetic field is comprehensible.

1.2.4 The relation between stellar activity and rotation

There are several ways in which the effects of a stellar magnetic field can be observed. Some *stellar magnetic activity* features are seen as very dark and very bright areas (spots and faculae) on the stellar photosphere[Ber05; FL88]. Others can be observed spectroscopically as *chromospheric emission* in the $H\alpha$ line in the optical part of the spectrum [Sod+93], in Ca II H and K lines in the UV part of the spectrum [MH08], and in the Ca II triplet in the IR part of the spectrum [And+05]. The X-ray[VR78] and radio [Dul85] emission of the corona is the result of the existence of the magnetic field as well. Also, eruption events like flares or coronal mass ejections, happening throughout the stellar atmosphere, are traced back to the magnetic field [Kah92]. Transient activity events, i.e. those that last from a few hours to several days are flares, coronal mass ejections, and spots and faculae. Continuous emissions used as an indicator of stellar magnetic activity are those stemming from chromospheric and coronal emissions. In the following, we will take a look at the chromospheric CaII H and K emission, and the coronal X-ray emission, as their relation with the stellar rotation is well established.

1.2.4.1 Chromospheric emission ratio R'_{HK}

The relationship between stellar rotation- and magnetic activity evolution was studied throughout the last few decades. Initially, it was shown that the average equatorial velocity and the emission in the Ca II H and K lines of G-type stars in different open clusters are decreasing with increasing age [Sku72]. This finding confirmed the assumption that the stellar rotation rate declines with advancing age [Kra67]. Already then, the proposal was made that magnetically coupled winds, similar to the solar wind, are responsible for this observation.

Somewhat later, the rotation period and emission in the Ca II H and K lines in a sample of main-sequence field stars were compared to each other [Noy+84]. Since the variation of the mean chromospheric H-K flux ratio R'_{HK} with observed rotation period P_{rot} showed a considerable scatter, the convective turnover time τ, indirectly accounting for the spectral type of the star and its convective envelope thickness, was introduced. The convective turnover time is the typical timescale for a convective cell to rise due to buoyancy. This parameter was introduced in combination with the stellar rotation period in the form of the Rossby number $R_o = P_{rot}/\tau$. This transformation aimed to convert an observable quantity into a quantity representing a product of the stellar dynamo action. It has to be noted, however, that τ is not a measurable quantity but is determined empirically [Ste94; Wri+11] or derived from theoretical models [KD96].

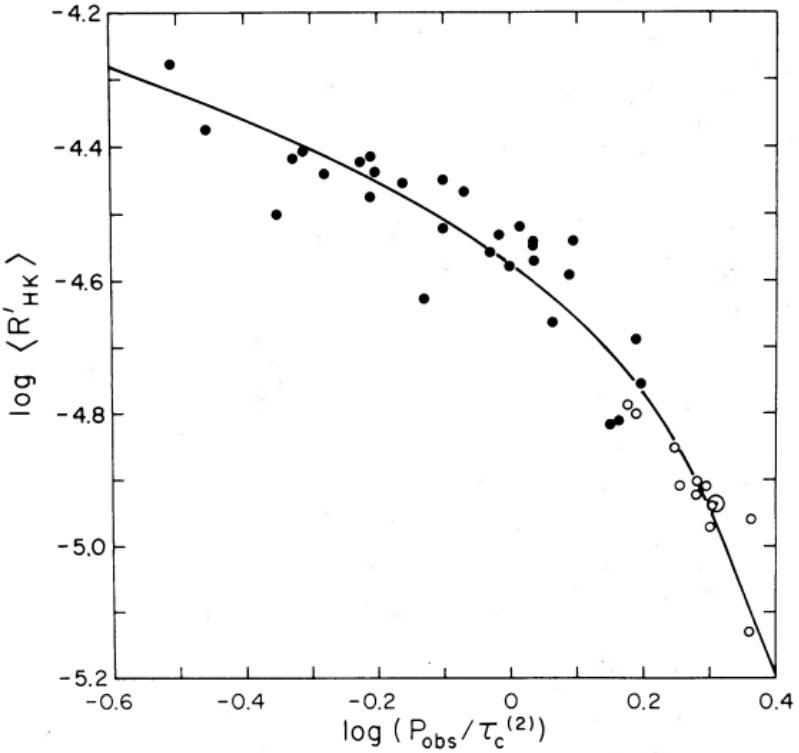

Figure 1.1: The mean chromospheric H-K flux ratio R'_{HK} as a function of the stellar Rossby number. Closed and open circles represent young and old stars, respectively. The solid line represents the best-fitting model for the data, given the modeled value of convective turnover time as a function of α, the ratio of mixing length to scale height in the convective zone. The Figure is adopted from [Noy+84].

From the relation between the chromospheric H-K emission and Rossby number in Figure 1.1, two regimes are anticipated: a strong dependence of the emission on the rotation period to convective turnover time ratio for higher Rossby numbers, and a somewhat less pronounced dependence of the emission on the large scale motion in the stare at smaller Rossby number values. This behavior might be related to saturation in the H-K emission in the region of high magnetic fluxes, or to spot area on active stars and their less efficient chromospheric emission. In any case, this result gave strong support to the idea that the ratio of rotation period to convective turnover time, or the Rossby number, is a major determinant of magnetic field amplification in rotating convective stars, indicating the validity of the $\alpha\omega$ -dynamo theory.

1.2.4.2 Coronal emission ratio R_x

Moving on to the coronal X-ray emission, most stars across the Hertzsprung–Russell diagram are known to emit X-ray photons [Sch97; SL04a]. In main-sequence solar-type and fully convective stars, the X-rays arise from magnetically confined plasma known as the corona that reaches temperatures of several 10^6 K [Sch+85; Vai+81]. One of the first studies linking the stellar X-ray appearance and the rotation rate of these kinds of stars

found the relation [Pal+81]:

$$L_x[erg/s] \sim 10^{27}(v \sin i[km/s])^2, \tag{1.3}$$

where L_x is the stellar X-ray luminosity and $v \sin i$ is the projected stellar rotational velocity. Additionally, a broken power law describing the activity-rotation relation of G dwarf stars indicated a change in the coronal emission regime[Wal82], similar to chromospheric emission. Subsequent studies of the stellar activity-rotation relation in the X-ray regime confirmed the two results [Mag+20; Piz+03; Wri+11; Wri+18].

As with the chromospheric emission ratio, the coronal emission seems to depend on the rotation rate of the observed star. A clearer relation is achieved if taking into account the convective turnover time τ of a star, calculating its Rossby number R_o, and comparing it to the ratio of the stellar X-ray luminosity to the bolometric luminosity $R_x = L_x/L_{bol}$ [DR89]. With the Rossby number, we consider the large-scale motion of the star thought to be responsible for its dynamo action, while choosing the R_x normalization suppresses some of the solely mass-dependent differences in coronal emission attributable to different stellar surface areas or total energy outputs. Therefore, by selecting these parameters, a decrease in the color-dependent scatter across the activity-rotation relation is achieved, as well as the highest correlation between the activity and the rotation of a star.

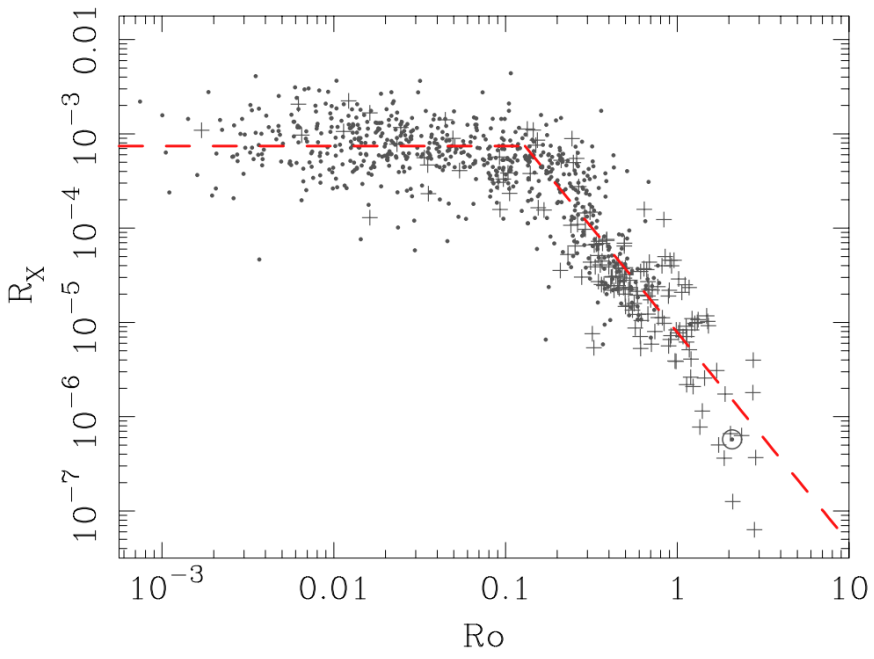

Figure 1.2: The coronal emission ratio R_x as a function of the Rossby number R_o for partly and fully convective stars. Dots are representing single stars, crosses represent resolved binary stars, and the position of the Sun on the diagram is shown with the solar symbol. The red dashed line shows the relation best fitting to the data in terms of Equation 1.4. The Figure is adopted from [Wri+11]

As can be seen in Figure 1.2, the general trend of the stellar X-ray emission above a certain Rossby number is that it decreases with increasing stellar rotation period to convective turnover time ratio, while below that certain Rossby number, the X-ray emission is constant or depends only weakly on the value of the rotation period to

convective turnover time ratio. It follows that the activity-rotation relation for stars that have a convective envelope below their photosphere is of the form:

$$R_x = \begin{cases} C\, R_o^{\beta} & \text{if } R_o > R_{o(sat)} \\ R_{x(sat)} & \text{if } R_o \leq R_{o(sat)} \end{cases} \tag{1.4}$$

Stars with a Rossby number of $R_{o(sat)} = 0.13$ [Wri+11] and smaller seem to have a (quasi)constant X-ray emission. Their X-ray to bolometric luminosity ratio varies around the value of $R_{x(sat)} \approx -3.13$ [Wri+11]. Stars with greater Rossby numbers follow a power law with the power $\beta \approx -2.7$ [Wri+11].

In summary, the activity-rotation relation in the X-ray regime, as in the chromospheric regime, shows that the magnetically induced activity of a star with a Rossby number above $R_{o(sat)}$ increases with increasing rotation rate and decreasing convective turnover time, indicating the importance of large-scale plasma flows for the generation and amplification of the stellar magnetic field via the dynamo action.

1.2.4.3 Chromospheric or coronal activity indicator?

Knowing that both the chromosphere and the corona provide well-established indicators of the stellar magnetic field strength, we can ask which one of the two observables is the better tracer of the activity-rotation behavior of stars. The discussed mean chromospheric H-K flux ratio, as well as the chromospheric H_α emission [Dou+14; New+17] of various stars in the field and open stellar clusters (i.e. of different ages and rotation rates) show the activity-rotation dependence anticipated from the spin-down and magnetic braking scenario. However, what makes the X-ray coronal emission a better tracer of this mechanism is the *sensitivity* of the stellar corona to the changes in magnetic field strength. While R'_{HK} traces changes in emission which span two orders of magnitude, the R_x indicator for the same stellar sample changes almost five orders of magnitude [MH08]. Similarly, the $R_{H\alpha}$ vs. R_o relation follows a power law that is less steep ($\beta = -1.7$) [Dou+14] than what is established between R_x and R_o [Wri+11]. Since our goal is to detect the slightest change in the rotation and therefore activity level of a star that tidally interacts with a substellar companion, looking at the luminosity of stellar coronae is the better choice as it will increase the probability of detecting tidal star-planet(brown dwarf) interactions.

1.2.4.4 Coronal X-ray emission as a magnetic activity indicator

The corona is the uppermost layer of the stellar atmosphere. The solar corona is best observed with the naked eye during solar eclipses when it appears as a veil surrounding the Moon. Its discovery, as a very hot and thin gas surrounding the Sun, was made indirectly from optical coronal lines of highly ionized atoms [ES42; Gro39], and directly by detecting X-ray photons during a rocket flight [Bur49]. In general, coronal emission is a multi-wavelength phenomenon observable from the meter-wave radio range to gamma rays. However, diagnostically most important wavelength regions are decimetric to centimetric radio range, and the X-ray domain. The radio regime is sensitive to accelerated electrons in magnetic fields and provides a direct means of imaging stellar coronal structures, while the soft X-ray domain, where the bulk of the hot plasma radiates,

is instrumental in understanding the mechanisms behind the coronal appearance both on the Sun and other stars.

So, what kind of mechanism can heat the stellar atmosphere from a few 10^3 K to several 10^6 K, and induce such a step temperature gradient within a few stellar radii? There is no conclusive answer to this question. However, observables such as the aforementioned activity-rotation relation in the X-ray regime, or the correlation between the magnetic field strength and the stellar X-ray luminosity [Fis+98; Pev+03] indicate that the stellar magnetic field, generated by an interior magnetic dynamo, plays a key role.

One mechanism suggests that magnetic energy is dissipated in the stellar corona via magneto-hydrodynamic waves [Alf42; Alf47]: if a magnetic field is immersed in an electrically conducting liquid, any motion of the liquid induces magneto-hydrodynamic oscillation of magnetic field lines and gives rise to magneto-hydrodynamic waves which travel parallel to the magnetic field lines. When they travel upwards through the stellar atmosphere, their wave velocity changes significantly because of the change in the surrounding plasma density. If the change is very rapid, as in the transition region between the chromosphere and the corona, a partial reflection of the waves occurs. The reflected waves interact with upward propagating waves causing turbulence. As a result, the wave energy is dissipated along the lines, particularly in the chromosphere and the corona, due to the viscous and resistive effects of the plasma through which the wave propagates [van+11].

An alternative scenario explains the high coronal temperature by assuming the dissipation of *magnetoacoustic* shock waves which propagate upwards from the convective zone where they are generated [Bie48; Sch48]. The basic idea is that stellar surface convective motion, as a turbulent flow field, is able to generate acoustic waves. The mechanical energy carried by the upwardly propagating acoustic waves depends on the density of the medium ρ, its sound speed, and the velocity of the wave v. As the conservation of wave energy flux requires that $v \sim \rho^{-1/2}$, the density decrease in the outer stellar atmosphere results in the rapid growth of the wave amplitude, which leads to shock formation, shock dissipation, and heating of the outer stellar layer. Another mechanism suggests the heating of the corona by microflares: in the strong magnetic field of an active region, the corona is in a state of ceaseless activity and is being heated by many microflares that are continually generated by the photospheric motion [KB98; Lin+84].

The literature on coronal heating mechanisms offers even more suggestions and possible solutions than the three mentioned above [NU90]. There is yet no consensus on which of these mechanisms is responsible for the observed coronal temperature, and the possibility exists that not one but multiple mechanisms contribute to coronal heating. However, it is accepted that the stellar magnetic field is the likely cause of the observed coronal properties, as it reaches into the stellar atmosphere determining its structure by governing plasma flows.

1.2.4.5 The stellar coronal structure

Magnetic structures associated with coronal heating are the coronal loops. Observed on the Sun, they appear as arc-like structures in which hot plasma is confined by magnetic flux tubes (see Figure 1.3). The loop emerges from the photosphere at one end, expands through the chromosphere into the corona, and loops back down into the photosphere at the other end. The two ends of the coronal loop are called photospheric footpoints. The

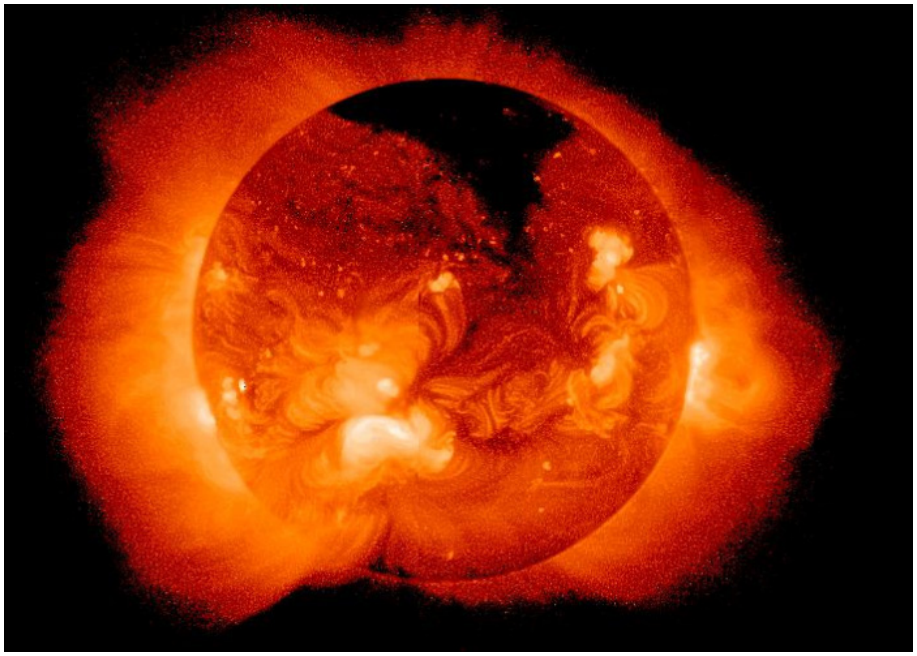

Figure 1.3: The solar corona observed in the soft X-ray domain by the Yohkoh spacecraft [Tsu+91]. The dark area in the northern hemisphere is a coronal hole, while the bright, arc-like structures are coronal loops. Image courtesy: http://solar.physics.montana.edu/.

coronal loops are assumed to be closed magnetic structures, however, the random motion of photospheric footpoints can lead to twisting, braiding, and reconnecting of coronal magnetic field lines [Par72; Par83]. Once a coronal loop breaks, a coronal hole forms. A coronal hole is the part of the solar and stellar corona, where the magnetic field lines open up, allowing the plasma to escape the magnetic flux tube (thereby contributing to a more efficient solar and stellar wind). This results in a cooler and less dense atmosphere than in the surrounding areas [KTR73].

Although coronal loops cannot be observed directly as on the Sun, they likely prevail in the coronae of other stars, and the heating mechanism taking place in the solar corona is likely responsible for the high coronal temperature and X-ray emission observed on other stars [AL80a]. Some studies have however shown, that M dwarfs in particular can have a more complex coronal structure: their coronal spectra are best explained if multiple thermal components are assumed, while the X-ray spectra of Sun-like stars are best explained with single-temperature plasma emission models [Gia+96; RS05; Sch+90]. The basic multi-thermal component model suggests a low- and a high-temperature component: in the first case, compact coronal loops have a temperature of a few $\times 10^6$ K and emit less energetic (softer) X-ray photons, while in the latter, the loop temperature is $\geq 10^7$ K and it appears highly variable while emitting more energetic (harder) X-ray photons. Very active M dwarfs have the bulk of their X-ray emission emitted by the high-temperature component.

Another feature of stellar coronae, not observed on the Sun, but on fast rotating stars, is that their X-ray coronal emission can be saturated. This means that two stars having very high but different rotation rates will have almost the same X-ray emission, i.e. their X-ray emission will not depend on their rotation rate. Considering the activity-rotation diagram shown in Figure 1.2, these stars appear at lower Rossby numbers, where the

coronal emission ratio R_x is independent of R_o. To explain this behavior, it was suggested that the saturated emission is due to a saturation in the dynamo efficiency [CK06; Fed+11; Vis09]. Others suggest that the saturated and the unsaturated emission regimes are due to different dynamo configurations [Wri+11]. Dynamo-independent ideas suggested centrifugal stripping of the corona due to high rotation velocities [JU99], or the saturation of the coronal filling factor [Vil84]. As with coronal heating, the cause of the saturated emission in the X-ray regime of fast-rotating stars is yet to be settled.

1.2.5 Summary

The main driver of the evolution of a single main-sequence star with an outer convective envelope[¶] is the stellar magnetic field and its coupling with the stellar rotation rate. The dynamo action responsible for the generation and amplification of the magnetic field in such stars is the $\alpha\omega$-dynamo mechanism: the ω-effect being responsible for the winding up of the poloidal filed into a toroidal one by differential rotation, while the α-effect of the Babcock-Leighton type explains the formation of the poloidal field from the toroidal one by invoking the meridional flow below the photosphere. The differential rotation, responsible for the existence of the toroidal field lines and thereby active regions on the stellar surface [Par09], depends on the rotation rate of the star [Wri+11]. Therefore, the magnetic activity level is expected to be dependent on the rotation rate of the star assuming the dynamo action is applicable. This assumption has an empirical backup in the activity-rotation relation established for Sun-like and lower-mass stars, where the activity indicator is either emitted by the stellar chromosphere or corona. It has also been shown that coronal X-ray emission is a more useful activity indicator, as it is more sensitive to magnetic strength variability than chromospheric indicators. The existence of a corona was unexpected given the assumption that stars roughly radiate as black bodies. However, the high temperatures established for stellar coronae are explained by the dissipation of magnetic disturbances that propagate up from the stellar convection zone.

1.3 Interaction between stars and their companions

Typically, stars are not alone. It is known for a long time that stars, at least some of them, have stellar companions[Her85]. Depending on the separation and mass ratio between the gravitationally bound components, the system can be sculpted by tidal and/or magnetic interactions. In the first case, only the gravitational force is relevant. On long timescales, the induced tidal bulges on each star can change rotation and orbital rates by angular momentum exchange [Hut81; Zah77], which also results in a continuous increase in the stellar activity level [AL80b]. On short timescales, tidal interaction can be evident as a localized increase in activity, mostly close to the sub-binary point [Cat+96]. Since most stars are also magnetic, if sufficiently close to each other, their magnetic field lines can interact, reconnect, and induce anomalous magnetic activity on short time scales [GWS95; KHH06; Vah95; WW94].

If considering substellar companions, it was only relatively recently discovered that main-sequence stars can be orbited by planets and brown dwarfs [MB00; MQ95a]. In

[¶]Typically a star with mass less than $M = 1.2\mathrm{M}_\odot$ or below the spectral type F7 [Kra67].

these systems, both tidal and magnetic interactions are expected to occur between the interacting bodies, as well as radiation- and particle-driven atmosphere evolution on planets induced by the star. Since the focus of this text lies in the stellar perspective on the mentioned interactions, the atmosphere evolution on planets due to stellar irradiance will be disregarded, as we can expect this interaction to be insignificant for stellar evolution. That leaves magnetic and tidal interactions between stars and their substellar companions. However, why do we expect that these two types of interactions in these kinds of systems have any effect on the star? Star systems have mass ratios closer to unity and have extended magnetic fields, that can locally be very intense, which justifies the expectation of tidal and magnetic effects. Also, if we take a look at our own Solar System, these interactions occur between planets and their moon, not between planets and the Sun. The answer to the question lies in the architecture of discovered exoplanet systems.

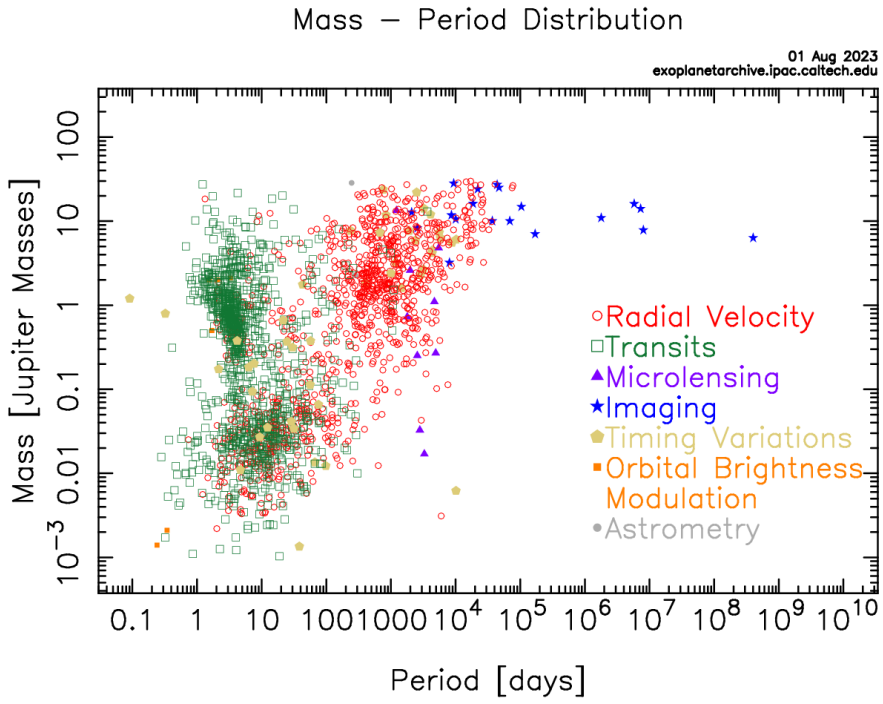

Figure 1.4: The distribution of planetary mass with orbital period for discovered exoplanets. The detection methods are indicated with symbols of different colors and shapes. Image courtesy: https://exoplanetarchive.ipac.caltech.edu/

Figure 1.4 shows the distribution of almost 5500 exoplanets in the mass-orbital period diagram, the color and shape of the symbols indicating different methods with which the planets were discovered. There, we see that many of the discovered planets are at distances from their stars much smaller than what is known for planets in the Solar System. Also, not only Mercury-size planets are close to their parent star, but Jupiter-size and even more massive planets can be found in a very tight orbit. The proximity of some planets to their host star, as well as their significant mass, raises the probability of magnetic and tidal interactions taking place in these distant star-planet systems. Therefore, it is relevant to ask what effects these objects have on their host stars. In the following, I will briefly discuss short-term interaction effects, and in more detail long-term interaction effects, as the latter is expected to affect stellar evolution.

1.3.1 Short-term interaction effects

Consider a system where a Sun-like star is orbited by a Jupiter-like planet (i.e. a Hot Jupiter) or a brown dwarf in a close orbit, and where the orbital rate of the companion and rotation rate of the star are unequal. As the companion orbits around its host, it raises tidal bulges that are in constant expansion and contraction. Since the stellar plasma is a viscous matter, the movement of these bulges can dissipate energy and generate heating, which can give rise to anomalous stellar activity. Because two bulges are raised on the stellar surface, the anomalous activity created by tidal interactions should be modulated by half the orbital period of the companion [SC01].

Consider again the same system configuration with the companion owing a magnetosphere. In certain configurations, magnetic field lines of opposite polarities belonging to the star and to the companion can undergo reconnection, releasing energetic particles that travel toward the star along the stellar magnetic field lines [IKH04]. As these particles impact the stellar atmosphere, particularly the stellar chromosphere at the magnetic footpoints, chromospheric hot spots can be excited. As the companion moves along the orbit, it interacts with different stellar magnetic field lines activating hot spots along the orbit. Therefore, the chromospheric activity should be modulated by the full orbital period of the companion in the case of magnetic interactions [SC01]. However, it has to be noted that the magnetic field topology of the host star can affect the modulation of the chromospheric hot spot as well [Str+19].

An important concept to keep in mind when considering magnetic interactions is the companions orbital distance with respect the *Alfvén surface* of the star. As briefly mentioned in Section 1.2.2, the Alfvén surface separates the regime of the stellar wind that is dominated by magnetic forces (within the surface) or by inertial forces (beyond the surface). Inside the surface, the wind is sub-Alfvénic, and the connection between stellar and companion's magnetic field lines can develop, while in the super-Alfvénic regime, beyond the surface, this is not the case [Str+15]. Therefore, as the stellar magnetism evolves, either within an activity cycle on shorter timescales or generally through the stellar spin-down on long timescales, so will the stellar Alfvén surface and, therefore, magnetic interactions [Kav+19; Nic+16]. Observationally, this behavior can be interpreted as an *on/off* effect of magnetic interactions [Shk+08].

1.3.2 Long-term interaction effects

Above, phenomena were described which can be considered transient, i.e. they happen ones or twice on timescales that are of the order of orbital or stellar rotation periods. However, as there is a transfer of angular momentum and energy between the interacting parties, continuous, long-term effects will take place that play out during the lifetime of system. The consequences of these interactions will be in form of a change in the rotation rate of the star, in addition to the magnetic braking effect, and a change of orbital parameters of the companion: change of orbital alignment, eccentricity, and semi-major axis. Here, we can assume that the companion experienced tidal locking, i.e. the orbital and rotational period of the companion coincide since the timescale for this effect to occur on Hot Jupiters is of the order of a few $\times 10^6$ yr [Gui+96].

1.3.2.1 Magnetic interactions

There are several models interpreting observations of activity and rotation levels of host stars in terms of magnetic interactions. For example, one model proposes that the magnetic helicity[‖] budget of the coronal magnetic field plays a fundamental role in the interaction [Lan08; Lan09]: an orbiting close-in companion with a magnetosphere can trigger reconnection events and thereby increase the helicity dissipation, balancing the helicity transferred into the corona from the photosphere. The dissipation releases magnetic energy in the stellar corona and is transported along the field lines to heat the lower chromospheric layer and induce chromospheric hot spots. Assuming that the motion of the companion reduces magnetic helicity, the occurrence of open magnetic field lines, i.e. coronal holes, is less probable, and the structure of the coronal magnetic field is dominated by closed field lines. This coronal field topology reduces the particle and energy outflow and thereby the angular momentum loss of the star [Lan10].

Another model describing magnetic interactions is concerned with the stellar and companion's Alfvén surfaces and their interaction [Coh+10]: the large-scale structure of the corona is disrupted by the companion, due to the fact that the companion is located close or inside the stellar Alfvén surface, where the stellar corona and stellar wind can interact with its magnetosphere. The companion with its Alfvén surface blocks a significant amount of the stellar wind and prevents it from opening up field lines and escaping [Coh+09]. The companion begins to affect the corona when its Alfvén surface (and not the companion itself) starts to interact with the stellar one. The reduction of angular momentum loss rate depends mostly on the size of companion's magnetosphere, due to the fact that the wind is blocked primarily by the magnetic pressure of the field.

1.3.2.2 Tidal interactions

Considering tidal interactions, to have any continuous change in the system, the stellar spin and the companion's orbital motion have to be asynchronous. Assuming angular momentum conservation for the system, if the companion is orbiting outside the corotation radius, the angular velocity of the orbital motion is smaller than the angular velocity of the stellar spin, and the angular momentum is transferred from the stellar spin to the orbital motion. In the opposite case, where the companion orbits inside the corotation radius, the star will gain angular momentum. If the companion is orbiting at the corotation radius, given as:

$$r_{co} = \left(\frac{GM_*}{\omega_{rot}^2}\right)^{\frac{1}{3}} \tag{1.5}$$

where G is the gravitational constant, M_* is the mass of the star, and ω_{rot} is its angular velocity, the companion and the star will have synchronous motion. The timescale for this particular configuration depends on the mass ratio between the interacting bodies $q = M_p/M_*$ and the scaled distance a/R between them as:

$$\tau_{sync} = Cq^{-2}\left(\frac{a}{R}\right)^6 \tag{1.6}$$

Since the star is expected to loss angular momentum through the stellar wind, its

[‖]Magnetic helicity is a measure of the magnetic field line twist.

corotation radius will change and typically increase in value during the main-sequence phase. Therefore, synchronization is only quasi-stable and will eventually be lost as the star evolves. The synchronization timescale given with Equation 1.6 is derived for stellar binary system [Zah77], where the components have an outer convective layer. The numerical constant C for stellar binary systems and for star-substellar systems is not equal and can be determined through observations.

1.3.3 How do tidal interactions work?

1.3.3.1 Equilibrium tides

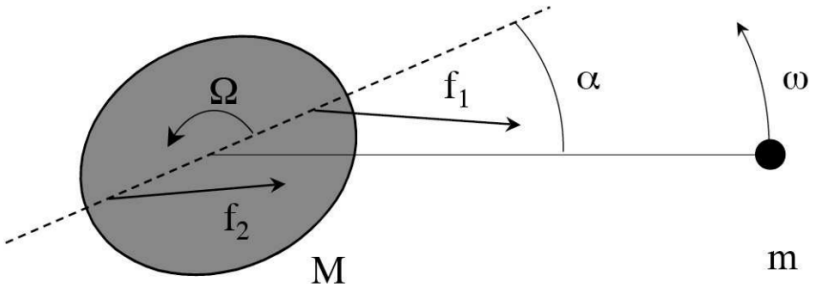

Figure 1.5: A two-body system governed by gravitational forces. The body with mass M has a spin velocity Ω; the body with mass m has an orbital angular velocity ω and is considered to be a point mass. The forces applied on the tidal bulges are f_1 and f_2. The angle between the direction of the point mass and the direction of the tidal bulges is α. The Figure is adopted from [Zah08].

Let us consider an astrophysical, gravitationally bound system where a rotating body is orbited by a point mass (See Figure 1.5). The more massive rotating component is the *primary* and the point mass component is the *secondary*. Consider an ideal case of a circular orbit of the secondary component that is in the equatorial plane of the primary component. The distance of the secondary to the center of the primary is a; the primary has the rotational angular velocity Ω, and the secondary has the orbital angular velocity ω. As the primary is orbited by the secondary, it experiences a periodically varying gravitational potential [Dar79a; Dar79c]. The primary, being a self-gravitating fluid body with a spheroidal shape (under the influence of the centrifugal force induced by its rotation), now has an ellipsoidal shape: two tidal bulges are raised on its surface, one in the direction of the secondary, and the other in the opposite direction. If the primary consists of frictionless fluid, the tidal bulges instantaneously follow the motion of the secondary on its orbit, and move on the surface of the primary regardless of its rotation rate. If the primary consists of viscous fluid (there is friction or drag between the fluid particles), the movement of tidal bulges is now affected by the rotation of the primary and they cannot follow the motion of the secondary as readily as in the frictionless case.

Let us now assume the primary is a star, a stellar object consisting of an electrically conductive fluid called plasma, which has viscous properties. The star will have tidal

bulges that either lag behind or lead in front of the direction of the secondary. In Figure 1.5, we have the case where $\Omega > \omega$ and tidal bulges are leading in front of the line joining the point mass and the center of the star; the mass distribution of the star is shifted by angle α from the equilibrium position, due to the dissipation of kinetic energy. More precisely, the kinetic energy of the large-scale flow that is induced by the tides cascades down to smaller and smaller scales, until it is dissipated into heat by viscous friction [Zah66a; Zah66b; Zah77]. Typically, in the stellar interior, the viscosity due to microscopic processes is very low, and the global viscous timescale exceeds the age of the Universe. However, viscosity still plays a major role in the regions of the star which are turbulent (e.g. convective envelope). There, turbulent viscosity is the main process behind the energy dissipation of tidal flows and the dissipation time scales as the convective turnover time of the star. If the tidal period exceeds the convective timescale, the dissipation will be less efficient because then only a part of the tidal flow will be damped by turbulence.

Since the forces applied by the point mass on the tidal bulges are not equal ($f_1 > f_2$ in Figure 1.5), a torque is exerted on the star, which tends to synchronize its rotation with the orbital motion. The tidal torque has the form:

$$\tau_{tidal} \approx (f1 - f2)R \sin\alpha \approx \frac{Gm^2}{R}\left(\frac{R}{a}\right)^6 \sin\alpha \tag{1.7}$$

Here, R is the radius of the star and m is the mass of the secondary. The sign of the torque, i.e. its direction of impact, depends on the values of the spin and orbital angular velocities. Tides that induce this kind of torque between interacting bodies are called equilibrium tides since it is assumed that they are in a quasi-hydrostatic state given their relatively slow motion (oscillation) across the stellar surface.

The lag angle α between the direction of the point mass and the direction of the bulges depends on the efficiency of the kinetic energy dissipation within the star and thereby its internal structure. It can also be defined as $\alpha = \arctan(1/2Q) \approx 1/2Q$ for $Q >> 1$, where Q is the tidal quality factor [GS66]. Generally, Q is defined as:

$$Q^{-1} = \frac{1}{2\pi E_0} \oint \left(-\frac{dE}{dt}\right) dt, \tag{1.8}$$

where E_0 is the maximum energy associated with the tidal distortion, and the integral over the energy dissipation $-\frac{dE}{dt}$ is the energy lost during one complete cycle. The above definition of the tidal quality factor reflects the fact that the star undergoes a forced oscillation and dissipates a small fraction of the associated energy during each oscillation period.

1.3.3.2 Dynamical tides

Aside from equilibrium tides, stars can also experience dynamical tides. These types of tides are dominant in stars with an outer radiative envelope and fast-rotating stars with an outer convective envelope. Generally, due to its elastic properties, a star can oscillate in various modes: acoustic modes, internal gravity modes, and inertial modes, where the restoring force is the compressibility of the gas, the buoyancy force in stably stratified regions, and the Coriolis force due to rotation, respectively. If their frequency is low

enough, these modes can be excited by the periodic gravitational potential originating from an orbiting body, and the response is called the dynamical tide.

Gravity modes have first been invoked for the tidal evolution of massive main-sequence binaries [Zah75]. The modes that are most excited are those whose frequency is close to the orbital angular velocity ω. These gravity modes are coupled with the periodic tidal potential in the vicinity of the convective core, whereas their damping occurs mainly near the surface, as the damping time is much shorter there than in the deep interior. Due to the radiative dissipation near the surface of the star, the dynamical tidal oscillations do not have the same symmetry properties as the exciting potential. As a consequence, a torque is applied to the star which tends to synchronize its rotation with the orbital motion. The angular momentum drawn from the orbit is deposited near the surface, and therefore the surface layers are synchronized first with the orbital motion. As a direct consequence of radiative dissipation close to the surface, the brightness distribution over the stellar surface is generally shifted with respect to the companion, thereby modifying both the luminosity and the radial velocity that would be observed. The efficiency of the coupling between the tidal potential and gravity modes depends strongly on the size of the convective core, and therefore on the mass of the star.

While gravity modes propagate only in radiative envelopes, the inertial modes are able to propagate also in convection envelopes. As their restoring force is the Coriolis force, their frequency, in the frame of the rotating star, is bound by twice the spin velocity Ω. Therefore, they may be excited by the tidal potential provided $\omega < 2\Omega$. Dynamical tides excited in this manner are damped by viscous dissipation in the convection zone, as equilibrium tides, however, their dissipation efficiency seems to be insensitive to the effective viscosity of the convective envelope [OL07].

1.3.4 Tidal effects in light of the tidal theory

Given the equilibrium tides theory, we now have an understanding of the processes taking place in tidally interacting systems where the star is Sun-like or less massive, and where its rotation period P_{rot} is at least twice the orbital period of the companion P_{orb} ($P_{rot} \geq 2P_{orb}$): due to turbulent viscosity in the stellar convective envelope, tides induced on the stellar surface by an orbiting companion, will lag behind or lead in front of the position of the companion depending on the relative angular velocity between the two objects. Considering the stellar structure, the turbulent viscosity will less or more efficiently dissipate the kinetic energy of the large-scale tidal flow, which will induce a net tidal torque between the star and the orbiting companion. The applied tidal torque is the rate of angular momentum transfer between the orbital motion and the stellar rotation, which changes the configuration of the considered system on long timescales. The system will tend to a spin-orbit synchronization, given that the companion's rotation is quickly synchronized with orbital motion, eventually reaching a double-synchronous state or companion engulfment [Pon09].

The short-term phenomena briefly discussed in Section 1.3.1, are thought to arise due to the tides being able to induce turbulent motion in the sub-surface regions of the star [CSM00; SC01], in addition to the already existing convective motion. The associated turbulent velocity can induce acoustic and magnetic waves, which can lead to increased heating in the stellar atmosphere. Another possibility is that the turbulence leads to locally increased helicity, which can contribute to a locally turbulent dynamo,

and therefore to increased magnetic field production and heating. In both scenarios, the two bulges are expected to yield an activity enhancement with half of the orbital period of the orbiting companion.

Dynamical tides, typically excited in massive or fast-rotating stars, can undergo radiative dampening or turbulent viscosity dissipation, respectively. The gravity and inertial modes damped in this way can lead to angular momentum transfer between the star and the companion. In fast-rotating stars with an outer convective envelope, dynamical tides co-exist with equilibrium tides and are the dominant type if the orbiting companion is outside of the corotation radius, typically during the pre-main-sequence phase [Rao+18]. Therefore, stars that are Sun-like or less massive, and are in the main-sequence phase will predominantly experience equilibrium tides if tidally interacting with an orbiting substellar companion.

1.3.5 Observability of tidal interactions

All the processes and mechanisms described in the previous sections set the stage for the upcoming chapters where I introduce the work done by my collaborators and myself in the past few years. We now have an idea about how stars with convective envelopes work, more precisely how their rotation and activity are coupled, and how orbiting substellar companions (planets and brown dwarfs) can affect them. Empirical indications of tidal interactions in the scientific literature are plentiful. Very often the impact on the companion and its orbital parameters is examined, while the effect on the host star was thought to be less significant. Nevertheless, the tendency that stars hosting close-in companions have an altered rotation rate [Pon09], and an altered X-ray activity [KDS08] was found.

So, how is the work my collaborators and I did different from all the previous studies that looked at tidal effects on stars and how it reflects on their rotation and activity? It mostly has to do with the way substellar companions, particularly exoplanets are detected in the first place.

Not going into much detail about planet detection methods, I will briefly mention the transit and radial velocity methods. The transit method looks for periodic decreases in stellar brightness, where the decrease has a particular shape: the nominal stellar brightness in a given photon wavelength range is disrupted by a gradual decrease as a planet enters the projected area of the stellar disk (ingress), then it transits in front of the projected disk for a certain amount of time, and it exits the disk as gradually as it has entered it (egress). In the ideal case, where the stellar disk has uniform brightness, the transit of almost any kind of planet would be easily detected as the transit depth in a stellar light curve depends on the quadratic ratio between the planet's radius and the stellar radius. However, stars are known to have brightness variability across the stellar surface (spots, faculae, granulation, etc.) due to the existence of the magnetic field, and as the magnetic field is stronger, these features tend to vary more strongly. This activity effect on the stellar surface can mask the transit of particularly small planets (or even induce a transit signal where there is no planet) [Chi+17].

Turning to the radial velocity method, here it is searched for the periodic movement of stellar spectral lines due to the gravitational pull of an orbiting planet on the stars. The effect behind this detection method is the Doppler effect: in a star-planet system both components orbit around the system's barycenter, and as the planet orbits, the star

slightly *wobbles* towards and away from the observer, thereby inducing the Doppler shift of the spectral lines towards the bluer part of the spectrum and then towards the redder part of the spectrum. The shift of the lines between these two positions is indicative of the velocity of the planet on its orbit, and therefore indirectly of its mass. Therefore, the lower the planetary mass, the lower the induced signal in the stellar spectrum. Again, as with the transit method, the magnetic field of the star induces star spots that move across the stellar surface or inhomogeneous convection patterns, which can mask or mimic the radial velocity signal of a low-mass planet [SD97]. The stellar magnetic activity is, therefore, able to impact the detection probability of small and low-mass planets, causing activity bias in planet detection [Har10; PS11c].

As it was discussed on several occasions, long-term tidal interactions are expected to affect the stellar rotation and magnetic activity level. Stars orbited by close-in massive planets can have an increased rotation rate and, given the activity rotation relation for main-sequence stars, also an increased activity level. However, if a planet-hosting stellar sample that suffers from the activity bias in planet detection is analysed, i.e. it has fewer low-mass planets around active stars compared to massive planets, without needing tidal interactions, we will find more close-in massive planets around active stars. Therefore, the effect we expect from tidal interactions is induced in the sample by activity bias in planet detection.

This is the moment where the work my collaborators and I have done, comes into place: instead of comparing the magnetic activity appearance of host stars to one another, we have compared each planet host to another planet-free star that has the same age and stellar properties. This planet-free star is used as an activity proxy for the case if tidal interactions have no impact on the host star. If the activity levels of the two stars are similar, there is no tidal impact by the planet, if the host is more active, the planet has tidally influenced the host. Astrophysical objects which closely fulfill the criterion of co-evolution of (at least) two stars are wide stellar binary systems.

I will tell nothing further since Chapter 2 describes in more detail how these wide binary systems were employed and what conclusion was made based on their analysis. In Chapter 3, we turn from planets to brown dwarfs. In particular, we will take a look at an M dwarf binary system where one star is orbited by a brown dwarf in a tight orbit. We will then see how the activity level increase of the brown dwarf-hosting star compares to the intrinsic activity variability of M dwarfs in general, and how significantly it is impacted by the orbiting brown dwarf. Chapter 4 is of a somewhat different flavor: here we will use a wide binary system to introduce an analytical method to calculate the stellar modified tidal quality factor Q', a relative of the previously introduced tidal quality factor. Finally, in Chapter 5, I will look back at some open questions and give ideas on how to address them in the future.

Now lean back and enjoy the science!

2 Tidal star-planet interaction and its observed impact on stellar activity in planet-hosting wide binary systems

N. Ilić, K. Poppenhaeger, S. Marzieh Hosseini

Monthly Notices of the Royal Astronomical Society, Volume 513, Issue 3 (2022)
DOI: 10.1093/mnras/stac861

Abstract

Tidal interaction between an exoplanet and its host star is a possible pathway to transfer angular momentum between the planetary orbit and the stellar spin. In cases where the planetary orbital period is shorter than the stellar rotation period, this may lead to angular momentum being transferred into the star's rotation, possibly counteracting the intrinsic stellar spin-down induced by magnetic braking. Observationally, detecting altered rotational states of single, cool field stars is challenging, as precise ages for such stars are rarely available. Here we present an empirical investigation of the rotation and magnetic activity of a sample of planet-hosting stars that are accompanied by wide stellar companions. Without needing knowledge about the absolute ages of the stars, we test for relative differences in activity and rotation of the planet hosts and their co-eval companions, using X-ray observations to measure the stellar activity levels. Employing three different tidal interaction models, we find that host stars with planets that are expected to tidally interact display elevated activity levels compared to their companion stars. We also find that those activity levels agree with the observed rotational periods for the host stars along the usual rotation-activity relationships, implying that the effect is indeed caused by a tidal interaction and not a purely magnetic interaction which would be expected to affect the stellar activity, but not necessarily the rotation. We conclude that massive, close-in planets have an impact on the stellar rotational evolution, while the smaller, more distant planets do not have a significant influence.

2.1 Introduction

Since the discovery of the first extra-solar planet [MQ95b], the interaction between a star and its planetary-mass companion, and their common evolution, have been a topic of interest [BLM01; CSM00; DLM04; OL04a; RF96; Shk+05]. The idea of a star-planet interaction comes from the interaction between stellar components in close binary systems, i.e. one regards the star-planet system as a binary system with a very uneven mass ratio [Hut81; Zah77]. The main pathways for star-planet interaction (SPI) are magnetic and tidal interactions. Which of the two types of interaction dominates depends mostly on the initial configuration of the system and the evolutionary phase considered [Ahu+21].

One of the first explorations of the tidal and magnetic interaction was the work by [CSM00], who considered tidal interaction in the form of tidal bulges raised by the planet

on the stellar photosphere, and magnetic interaction in the form of interaction between the planetary magnetosphere and the magnetic field of active regions. In the following works, magnetic and tidal interaction types have been explored in more detail.

In most cases, the effects of magnetic star-planet interaction are thought to happen on short time scales. This type of interaction can produce flaring and other types of high-energy events in the process of magnetic field line reconnection [IKH04]. One of the first observational investigations of possible increased activity level due to SPI was by [Shk+05], where the chromospheric activity of 13 planet-hosting stars was monitored. It was found that two of the stars exhibit activity enhancements in phase with the planetary orbital rate, suggesting magnetic instead of tidal interaction. A follow-up study [Shk+08] found variability with the planetary orbit only for one of the two targets, which was interpreted as on/off behavior of SPI. Further investigations targeted single-epoch coronal observations and investigated stellar activity as a function of planetary mass and orbital period [KDS08; PRS10]. The picture is complicated by selection biases that exist for exoplanet detection and are a function of stellar activity themselves [PS11a]. A large sample of chromospheric measurements showed potential star-planet interaction effects on the stellar activity only for the closest and heaviest exoplanet companions [Mil+15].

The main aspect of tidal star-planet interaction is thought to be the long-term planetary orbital and stellar spin evolution, where the angular momentum transfer between the two components plays a significant role. The orbital evolution is manifested as the change of orbital inclination [Alb+12; Win+10], and the simultaneous change of the semi-major axis and orbital eccentricity [JGB08; Str+17]. One other possibility involves a continuous orbital decay, which may result in the destruction of the planet within the lifetime of the star [Ben+19; Bol+12; PR02].

In general, the spin evolution of a star is determined by its initial spin, contraction rate, and the efficiency of the stellar wind. In particular, the stellar wind is important since it carries away angular momentum from the star. This process, called magnetic braking, slows down the rotation rate of the star over timescales of gigayears [BM76; Kra67; Mes68; WD67b] and can weaken magnetic phenomena such as starspots, stellar winds, and coronal emission. For a star with a close-in massive planet, this scenario can be modified: it is expected that planets with an orbital angular velocity higher than the stellar rotational angular velocity will decrease the spin-down rate of the host star, while their orbit decays, altering the expected stellar rotational evolution (e.g. [Bro+11; Fer+15; Gal+18; Pen+16]). One of the consequences will be the altered activity level of the star.

To trace tidal star-planet interaction, different indicators have been explored. The distribution of stellar rotation rates with planetary mass and distance were examined, where the indication for tidal evolution in transiting planetary systems was found [Pon09]. By calculating the gyrochronological ages of stars using their rotational periods and comparing them to estimated isochrone ages, it was found that the gyro-ages of some transiting exoplanet host stars are significantly lower than the isochrone age estimates, indicating SPI [MSS15]. Another study investigated the galactic velocity dispersion of main-sequence planet-host stars [HS19]. It was shown that the hosts are preferentially younger than a matched sample of field stars which indicated that close-in giant planets are destroyed by tides while their host stars are on the main sequence.

One other commonly used tidal star-planet interaction indicator is the level of stellar activity, in particular, the X-ray luminosity of the stellar corona. Since the X-ray luminosity is a function of stellar rotational rate [Pal+81; Piz+03; Wri+11], if tidal SPI can alter

the rotation rate of the host star and possibly induce a spin-up, a higher X-ray luminosity will be observed.

As discussed by [PRS10] and [PS11a], using stellar activity as an indicator for tidal star-planet interaction can introduce selection effects. Since stellar activity masks the planet-induced radial-velocity signal, small far-out planets are more easily detected around very inactive stars. Therefore, using the RV method, more massive, close-in planets are the only planet type that is easy to detect around active stars. Similarly, smaller planets are easier to detect around magnetically quiet stars and may be missed in the case of magnetically active stars. This is somewhat ameliorated by transit observations, which are less vulnerable to high stellar activity, and small planets have been found around young and active stars [New+19; Pla+20]. However, confirming those planet candidates through mass determinations which mainly involve RV measurements stays observationally costly. Therefore, a given sample of successfully detected exoplanets can be expected to have a detection bias causing an excess of Hot Jupiters known around high-activity stars, which needs to be disentangled from genuine star-planet interaction signatures.

In this study, we utilize the X-ray luminosity of planet-hosting stars as an indicator of stellar activity and avoid the selection effect described above by a particular sample definition. Here, we investigate planet hosts that reside in wide binary systems. Our work, however, differs from that by [PW14] since we do not compare the estimated age of the binary companions but their measured activity level. Our analysis makes use of the assumption that both components formed at similar times and therefore have similar ages, which will leave the activity level of the companions to depend only on their spectral type and possibly on the tidal star-planet interaction strength. After correcting for the spectral class difference, the activity level of the companion star will be used to estimate the expected activity level of the host itself. The secondary does not have a detected planet or has a distant less massive planet. With this approach, we have eliminated the selection effect due to the radial velocity detection method since we do not compare the activity level of the host stars to one another, but an independent activity proxy.

In Section 2.2, we described the observational data obtained for our study and the methods used to analyse the data and calculate the X-ray flux and luminosity of our sources. In Section 2.3 the normalized difference in the X-ray luminosity of the binary system components is estimated, and the parameters accounting for the star-planet tidal interaction strength are calculated. Section 2.4 discusses the relation between the X-ray luminosity difference and the tidal interaction strength, accounting for the possible activity biases in our stellar sample and the influence of magnetic star-planet interaction. Section 2.5 summarizes the finding of our study.

2.2 Observations and data analysis

We constructed a sample of nearby exoplanet host stars in wide common proper motion systems with one or more other stars. Such systems were presented by [Rag+10], who found that ≈ 45% of main-sequence stars of spectral type F6 to K3 have one or more stellar companions and that these statistics also apply to planet-hosting stars. In a recent work by [Mug19], the multiplicity of known planet-hosting stars, in particular, was examined. Using the second data release of the ESA-Gaia mission, the authors found equidistant

stellar companions that share a common proper motion with the planet-hosting stars, thereby establishing gravitationally bound systems. In addition to systems from this survey, we have also included the binary system HAT-P-20 [Knu+14] into our analysis, where the primary component hosts a close-in giant planet.

We acquired our sample by requiring that the two stellar companions have a separation larger than 100 AU* in order to avoid significant star-star interactions during the formation of the system [DB07]. One system which was in our initial sample but was later on excluded is the triple-star system HD 26965 [Ma+18] since the reality of the planet is debated due to the similarity of the stellar rotation period and the potential planet-induced radial velocity signature [Día+18a].

We then collected X-ray data of the systems to measure the stellar activity levels by inspecting data of the XMM-Newton and Chandra X-ray observatories from several observing programs†, as well as archival observations of other systems. This yielded a sample of 34 systems with existing X-ray coverage in XMM-Newton or Chandra.

2.2.1 Analysis of XMM-Newton data

2.2.1.1 XMM-Newton instrumentation

All sources found in the XMM-Newton archive were observed with the telescope's European Photon Imaging Camera (EPIC). EPIC is composed of three cameras, two are Metal Oxide Semiconductor (MOS) CCD arrays and one is a positive-negative junction (pn) CCD array. These two types of cameras differ in their instrument design, the geometry of the CCD arrays, and their readout time. Also, the pn CCDs are back-illuminated, while MOS CCDs are front-illuminated, which affects the chip's quantum efficiency, making the pn camera more sensitive to X-ray photons.

The EPIC cameras perform high-sensitivity imaging observations over the telescope's circular field of view (FoV) of ≈ 30" in radius. They are sensitive to the energy range of 0.15-15 keV with a maximum sensitivity at 1.5 keV. The in-flight on-axis point spread function (PSF) of the cameras, at a photon energy of 1.5 keV, yields a full-width-half-maximum (FWHM) of ≈ 6" for all three cameras [Str+01; Tur+01].

For our sample observations, all EPIC CCDs operated in photon counting mode with a fixed frame read-out frequency, producing event lists. Each detected event is associated with the position on the chip at which they were registered, their arrival time, and energies.

Onboard XMM-Newton is also the EPIC Radiation Monitor (ERM), which is employed for monitoring the space radiative and particle environment, which mostly depends on Earth's radiative belts and solar flares, and an Optical Monitor (OM) and Reflection Grating Spectrometers (RGS), but they were not used for our analysis.

In Table 2.1 are listed all systems acquired in the XMM-Newton archive.

*This value is the lower limit of the range given in the cited research paper. By adopting the upper limit of 300 AU, our final results do not change significantly.

†I.e., XMM-Newton programs 0722030 and 0728970 as well as Chandra program 15200512, PI Poppenhaeger

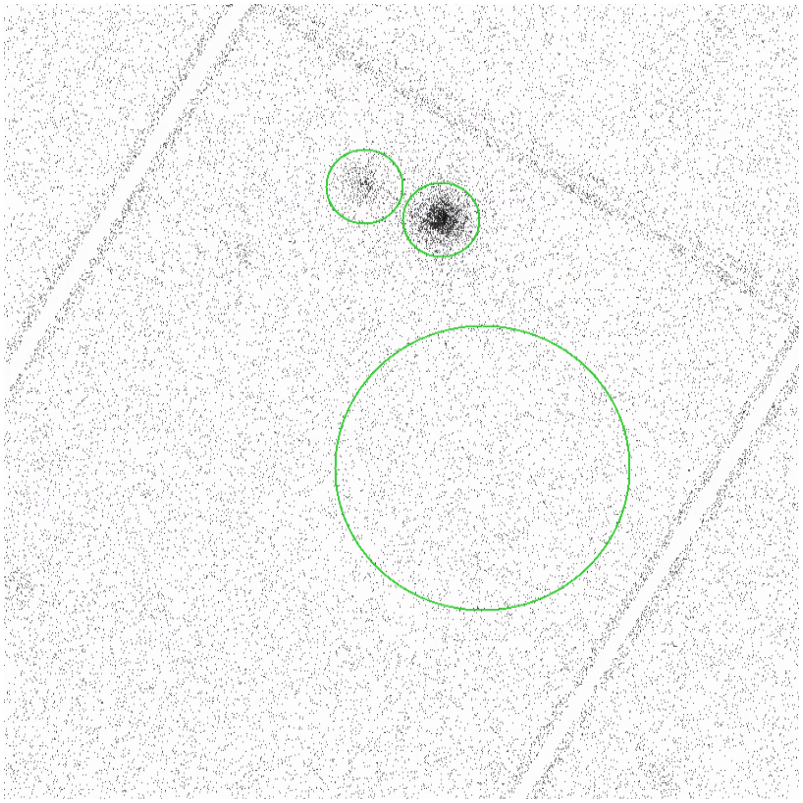

Figure 2.1: Shown is an example of the source and background extraction regions for the binary system Gliese 15 (GJ 15) on the observation taken with the EPIC pn camera. At the top are two source extraction regions: the region on the right encompasses the planet host, while the region on the left encircles the planet-host companion. The large circle at the center represents the background extraction region. The radius of the two source regions and the background region is $\approx$ 15.8" and 60", respectively.

2.2.1.2 Photon event extraction

To analyze the data collected with EPIC, we first processed the observations with the XMM-Newton Science Analysis System (SAS), version 18.0.0. For each observation, we used the appropriate Current Calibration Files (CCF) and run the EPIC reduction meta-task *emproc* and *epproc* to reduce the data collected by the MOS and pn camera, respectively. Then, for every reduced observation, we defined a circular source extraction region for the planet host and its companion(s), and a circular, source-free, background extraction region[‡] (see Figure 2.1). To include most of the camera's PSF, we chose the on-sky source extraction region radius to be between 10" and 20", depending on the angular separation between the stellar components. The background extraction region has a radius of 60", providing a good estimate of the background signal. We extracted X-ray photon events from the source and background regions, restricting ourselves to events with the highest probability of being single-photon events as recommended in the XMM-Newton data analysis handbook.

The stellar coronae of cool stars are best observed in the 0.2-2.0 keV energy band since

[‡]The source-free background extraction region was determined by visual inspection. Each observation was inspected and a region where no obvious source was seen has been chosen for estimation of the X-ray background signal.

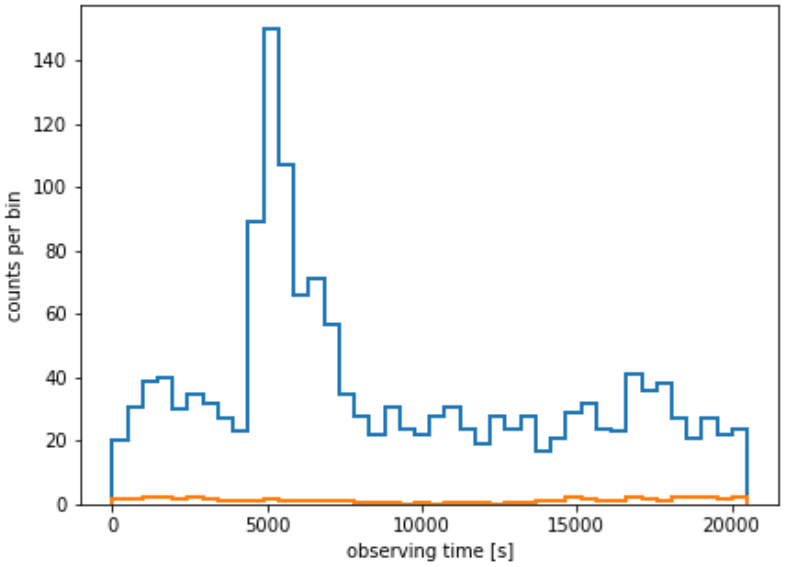

Figure 2.2: The light curve of the planet host GJ 15 A. The blue step function represents the photon counts in a 500s time interval, while the orange line at the bottom represents the scaled background level with the steps ranging the same time interval. The background extraction region is ≈ 14 times larger than the source extraction region of the planet host. Therefore, the background counts are scaled down by a factor of 14.

the bulk of magnetically induced coronal high energy radiation is emitted in this energy range (see for example [GGS97a]). Therefore, we constrained our analysis to the source and background photon events within these energy values. For photon energies higher than 2 keV, usually, the background radiation dominates, lowering the signal-to-noise ratio for the source.

We defined Good Time Intervals (GTI) for each observation, i.e. we excluded times of high background signal (see Appendix 2.6.1 for more details). Furthermore, cool stars are known to flare stochastically [Aud+00; Ili+19; Wal+11]. Since we wanted to avoid a flare dominating the X-ray brightness measurement of our stars and therefore skewing our activity level comparison, we inspected X-ray light curves for possible flaring events. We found only one flaring event in the binary system GJ 15, occurring on the planet host (Figure 2.2). In the first half of the observation, a sharp increase in the source photon counts is observed, while the background level stays constant, followed by a gradual photon count decrease. Therefore, we excluded this time interval from further analysis of this system and only used the quiescent time periods.

2.2.1.3 Determining the excess source photons

After acquiring the appropriate photon event lists, we had to estimate the number of photon events coming from the source itself. This we did by removing the background contribution from photon events gathered in the source extraction region. Hence, we estimated the *net source photon count (n)* and its confidence interval. Since both the

source and background counts have statistical uncertainties following a Poisson process, suitable methods need to be used (see for example [Ayr04; KBN91a]).

In short, whenever we had a strong X-ray source that is visible by eye with more than 100 excess source counts over the background, we approximated the Poissonian uncertainties as Gaussian uncertainties and calculated the uncertainty on the net source counts n as the square root of the observed source counts N, thereby having a 68% confidence interval of $CI = (n - \sqrt{N}, n + \sqrt{N})$. In any case, for those bright sources, the intrinsic astrophysical variability of the star is expected to dominate over the statistical uncertainty of the net source counts.

For fainter sources, both the Poissonian uncertainties on the source and the background need to be taken into account. First, we estimated the probability that the background fluctuation was responsible for the number of counts in the source region by employing the Poisson cumulative distribution function. If the probability was higher than 0.3%, we report an upper limit for the source, and otherwise, we report a detection with a 3σ level of detection significance.

To estimate the net source photon count and its confidence interval for a detected faint source, we applied the Kraft-Burrows-Nousek estimator [KBN91a]. For faint sources over some background, it can in principle occur that the source region has fewer counts than the scaled background region, but this does not indicate negative source fluxes but is a result of small number statistics. The KBN estimator tackles this in a Bayesian manner by explicitly assuming the background signal to stem from a Poisson process as well, and marginalizing over all possible background count numbers in the source detect cell. It assumes the source flux to be non-negative, and yields confidence intervals for the net source count rate. We used the KBN implementation of the `stats.poisson_conf_interval` function in the `astropy` package in our analysis [Ast+13; Ast+18].

For the detected faint sources, we determine the 68% confidence interval and report its center as the net source photon count for this detection. For undetected faint sources, we calculated the maximum X-ray luminosity by setting the upper end of the 95% confidence interval to be the upper limit to the net source photon count.

2.2.1.4 From X-ray counts to X-ray fluxes

To convert the estimated net source photon count into X-ray flux, we need to know the underlying X-ray spectrum of the observed stellar corona and the telescope's instrumentation setup during the observation. For bright sources, this could be done by spectral fitting, but for weaker sources, other inferences on the main variable, namely the coronal temperature, need to be made. Regarding observations acquired with EPIC, we have an instrumentation setup that includes filters of different thicknesses (thin, medium, and thick) and two camera types (pn and MOS). For each setup, there is a *photon count conversion factor (C)* as an estimate for the number of photons to be detected for a given source flux, mean coronal temperature, and energy range.

To estimate the mean coronal temperature of our sources, we calculated the hardness ratio of the detected radiation by utilizing the observations made with the pn camera. The hardness ratio represents the normalized difference of photon counts in two wavelength bands: *HR = (H-S)/(H+S)*. The wavelength bands we have used are S = 0.2-0.7 keV and

Table 2.1: Systems observed by the XMM-Newton telescope. The components with the asterisk symbol are the planet-hosting stars. Most of the stellar components were properly positioned on a CCD chip in all three cameras (marked as *all* in the *camera* column), while in some observations a component was on the edge of the CCD array, or fell on a gap between chips. In these cases, the observation with the given camera was discarded.

system	obs ID	component	camera
16 Cyg	0823050101	AC	all
		B*	all
30 Ari	0075940101	A	all
		B*C	all
55 Cnc	0551020801	A*	all
		B	all
83 Leo	0551021201	A	all
		B*	all
AS 205	0602730101	A*B	all
GJ 15	0801400301	A*	all
		B	all
HAT-P-16	0800733101	A*B	all
		C	all
	0800730701	A*B	all
		C	all
HD 27442	0780510501	A*	all
		B	all
	0551021401	A*	all
		B	all
HD 46375	0304202501	A*B	all
HD 75289	0304200501	A*	all
		B	all
	0722030301	A*	all
		B	all
HD 101930	0555690301	A*	all
		B	pn
HD 107148	0693010401	A*	all
		B	all
HD 190360	0304201101	A*	all
	0304202601	A*	all
		B	pn
Kepler-1008	0550451901	A*	MOS2 & pn
		B	MOS2 & pn
υ And	0722030101	A*	all
		B	all
WASP-18	0673740101	A*	all
		B	all
WASP-33	0785120201	A*B	MOS1 & pn
		C	pn
XO-2	0728970101	S*	all
		N*	all
	0728970201	S*	all
		N*	all

Table 2.2: The parameters for evaluating the X-ray luminosity of binary companions observed with the XMM-Newton telescope are given. The asterisk symbol marks the planet-hosting component. If excess counts do not have a confidence interval given, only the upper limit of the X-ray flux has been estimated. Otherwise, if the confidence interval is symmetric/asymmetric, indicates that we have applied 'bright'/'faint'-source statistics (see Section 2.2.1.3).

system	component	net photon counts	HR	$\log_{10} T$	$F_x \times 10^{-16} \left[\frac{\text{erg}}{\text{cm}^{-2}\text{s}}\right]$	r[pc]	L_x[erg/s]
16 Cyg	B*	276.5 ± 22.091	-0.46	6.464	59.336 ± 4.741	21.139 ± 0.015	$(3.234 \pm 0.258) \times 10^{26}$
	AC	955.658 ± 34.22	-0.466	6.461	204.468 ± 7.321		$(1.115 \pm 0.040) \times 10^{27}$
30 Ari	B*C	21499.292 ± 146.727	0.111	6.665	12978.979 ± 88.578	45.137 ± 0.149	$(3.225 \pm 0.031) \times 10^{29}$
	A	12657.131 ± 112.606	-0.068	6.605	8104.375 ± 72.101		$(2.014 \pm 0.022) \times 10^{29}$
55 Cnc	A*	228.903 ± 16.031	-0.307	6.477	360.448 ± 25.244	12.586 ± 0.012	$(6.964 \pm 0.488) \times 10^{26}$
	B	$51.903^{+9.297}_{-8.628}$	/	6.477	$81.729^{+14.639}_{-13.586}$		$(1.579 \pm 0.273) \times 10^{26}$
83 Leo	A (G III)	2155.188 ± 46.723	-0.056	6.564	1706.574 ± 36.997	18.204 ± 0.058	$(6.898 \pm 0.156) \times 10^{27}$
	B*	160.2 ± 13.342	-0.497	6.402	167.99 ± 13.99		$(6.791 \pm 0.567) \times 10^{26}$
AS 205	A*B	$78.445^{+11.068}_{-10.414}$	/	6.477	$102.988^{+14.530}_{-13.673}$	127.492 ± 1.6	$(2.042 \pm 0.284) \times 10^{28}$
GJ 15	A*	1465.231 ± 39.090	-0.468	6.460	1052.417 ± 28.076	3.5623 ± 0.0005	$(1.629 \pm 0.043) \times 10^{26}$
	B	398.089 ± 21.679	-0.608	6.396	250.571 ± 13.646		$(3.879 \pm 0.211) \times 10^{25}$
HAT-P-16	A*B	$16.518^{+5.926}_{-5.256}$	/	6.477	$17.190^{+6.168}_{-5.470}$	226.637 ± 4.388	$(1.077 \pm 0.367) \times 10^{28}$
	C	$9.611^{+4.485}_{-3.813}$		6.477	$12.395^{+5.784}_{-4.917}$		$(7.766 \pm 3.366) \times 10^{27}$
HD 27442	A*(K III)	152.68 ± 15.906	-0.676	6.331	81.838 ± 8.526	18.27 ± 0.054	$(3.359 \pm 0.350) \times 10^{26}$
	B(WD)	$62.354^{+12.991}_{-12.341}$	/	6.477	$31.171^{+6.494}_{-6.169}$		$(1.280 \pm 0.260) \times 10^{26}$
HD 46375	A*B	$66.051^{+9.407}_{-8.74}$	-0.561	6.418	$110.982^{+15.808}_{-14.684}$	29.553 ± 0.038	$(1.182 \pm 0.162) \times 10^{27}$
HD 75289	A*	$16.741^{+5.836}_{-5.165}$	/	6.477	$11.923^{+4.157}_{-3.679}$	29.116 ± 0.024	$(1.233 \pm 0.405) \times 10^{26}$
	B	235.682 ± 16.062	-0.3	6.527	142.426 ± 9.707		$(1.473 \pm 0.100) \times 10^{27}$
HD 101930	A*	≤ 30.94	/	6.477	≤ 83.215	30.027 ± 0.041	$\leq 9.152 \times 10^{26}$
	B	≤ 18.73	/	6.477	≤ 61.519		$\leq 6.766 \times 10^{26}$
HD 107148	A*	$32.125^{+13.914}_{-6.121}$	/	6.477	$20.281^{+5.883}_{-5.503}$	49.416 ± 0.116	$(6.041 \pm 0.17) \times 10^{26}$
	B(WD)	≤ 13.982	/	6.477	≤ 7.946		$\leq 2.367 \times 10^{26}$
HD 190360	A*	$16.75^{+6.829}_{-6.16}$	/	6.477	$28.143^{+11.474}_{-10.351}$	16.007 ± 0.016	$(8.796 \pm 3.410) \times 10^{25}$
	B	$15.875^{+4.49}_{-3.816}$	-0.449	6.469	$116.032^{+32.815}_{-27.892}$		$(3.626 \pm 0.949) \times 10^{26}$
Kepler-1008	A*	≤ 7.593	/	6.477	≤ 7.473	282.565 ± 1.278	$\leq 7.278 \times 10^{27}$
	B	≤ 10.541	/	6.477	≤ 10.374		$\leq 1.01 \times 10^{28}$
υ And	A*	2286.302 ± 48.61	-0.359	6.457	2740.445 ± 58.266	13.405 ± 0.063	$(6.007 \pm 0.140) \times 10^{27}$
	B	$58.314^{+11.304}_{-10.639}$	/	6.477	$71.500^{+13.861}_{-13.045}$		$(1.567 \pm 0.295) \times 10^{26}$
WASP-18	A*	≤ 13.857	/	6.477	≤ 31.465	123.483 ± 0.37	$\leq 5.852 \times 10^{27}$
	B	≤ 11.578	/	6.477	≤ 26.290		$\leq 4.89 \times 10^{27}$
WASP-33	A*B	≤ 26.869	/	6.477	≤ 53.839	121.944 ± 0.99	$\leq 9.766 \times 10^{27}$
	C	$40.0^{+8.779}_{-8.11}$	0.116	6.692	$110.815^{+24.322}_{-22.468}$		$(2.010 \pm 0.425) \times 10^{28}$
XO-2	S*	$78.137^{+17.746}_{-17.103}$	/	6.477	$21.922^{+4.979}_{-4.798}$	151.398 ± 0.95	$(6.129 \pm 1.369) \times 10^{27}$
	N*	$85.13^{+17.953}_{-17.296}$	/	6.477	$23.884^{+5.037}_{-4.852}$		$(6.678 \pm 1.385) \times 10^{27}$

H = 0.7-2.0 keV [§]. If $HR > 0$, we have a harder X-ray spectrum and a hotter stellar corona, while if $HR < 0$, the spectrum is softer and the stellar corona is cooler.

To calculate the conversion factors, we have used the NASA HEASARC online tool WebPimms [Muk93], version 4.11. With this tool, we estimated the hardness ratio of a hypothetical stellar corona (spectral model of hot plasma – APEC) for a given mean coronal temperature in the energy range of 0.2-2.0 keV, with the source flux of 10^{-12} erg/cm^2/s and the metallicity of 1 solar abundance. No absorption due to interstellar matter was assumed since most of our X-ray-detected sources are within 200 pc from the Sun. Comparing a set of estimated hardness ratios for a given instrumental setup to the observed HR value, we determined the mean coronal temperature of our source of interest. If a source is marked as not detected in the soft or hard energy band, we assume a mean coronal temperature of 3 MK ($\log_{10} T[\mathrm{K}] = 6.477$) since this is the expected coronal temperature for a moderately active star [Fos+21; Sch+90; WN77]. The conversion factors that were used for the conversion of photon counts into X-ray flux of XMM-Newton sources are given in Table 2.9.

Since the observed stellar components are detected as point sources, we also have to take into account the influence of the point spread function (PSF), which describes the dispersion of incoming photons onto the CCD due to their interaction with the telescope's optics. For this task, we used appropriate Encircled Energy Fractions (EEFs) for our photon extraction radii according to calibration documentation for the in-flight calibration of the PSF for the pn camera. The EEF value typically lies between 0.4 and 0.7 and has a weak dependence on the optical off-axis angle.

Having all necessary parameters, including the observation exposure time, that can be extracted from the observation file header, the source X-ray flux can be calculated as the sum of the fluxes detected by all three cameras:

$$F = \sum_{i=MOS1,MOS2,pn} n_i \left(\sum_i t_i C_i EEF_i \right)^{-1} \times 10^{-12} \frac{erg}{cm^2 s}, \tag{2.1}$$

where t represents the exposure time.

Also, some systems were observed multiple times. In these cases, we combined the observations to achieve better X-ray flux accuracy. For them, the flux was calculated as follows:

$$F = \sum_{i,j} n_{ij} \left(\sum_j \left(\sum_i t_i C_i EEF_i \right)_j \right)^{-1} \times 10^{-12} \frac{erg}{cm^2 s}, \tag{2.2}$$

where j is the summation over the multiple observations. Here, we calculated the exposure time-weighted average of the flux from several observations.

[§]The division into the two passbands follows the example of the solar spectrum ([GGS97a], Figure. 5): the photon count rate increases gradually with photon energy, reaching the maximum emissivity at around 0.7 keV and then decreasing steeply. Therefore, the division point was set to be at the peak of the solar X-ray emissivity.

2.2.2 Analysis of Chandra data

2.2.2.1 Chandra instrumentaion

The Chandra X-ray Observatory has two focal plane science instruments, ACIS and HRC (High-Resolution Camera), which provide information about the number, position, energy, and arrival time of incoming X-ray photons. The Chandra Advanced CCD Imaging Spectrometer (ACIS) is the only instrument employed for observing our sources of interest since it provides images as well as energy information about the detected photons. It is sensitive to the energy range of 0.2-10.0 keV and the on-axis angular resolution (FWHM of the PSF) is ≈ 0.5" at 0.277 keV.

The ACIS instrument is composed of ten CCD chips in 2 arrays that provide imaging and spectroscopy: four CCDs (I0 to I3) are employed in the imaging array (ACIS-I), while the other six (S0-S5) compose the spectroscopic array (ACIS-S). The S1 and S3 CCDs are back-illuminated chips, meaning they have a higher sensitivity to X-ray photons. The FoV of ACIS-I is square-shaped measuring 16' × 16', while the spectroscopic array of ACIS-S is elongated measuring an FoV of 8' × 48'.

The shape and size of the telescope PSF vary significantly with the source location on the detector and its spectral energy distribution. It provides the best resolution in an area centered about the optical axis, and it deteriorates strongly with increasing off-axis angle, letting the source appear as extended. Therefore, we took into account the source position on the detector when defining the size of the source extraction region.

Table 2.3 lists all systems obtained in the data archive of the Chandra X-ray observatory.

2.2.2.2 Photon event extraction

The Chandra telescope archival data is calibrated, so no preprocessing, as was the case with XMM-Newton observation, was needed. We used the Chandra Interactive Analysis of Observations (CIAO) X-ray data analysis software, version 4.12, to extract the photon events of interest. First, we defined the source and background extraction regions around the objects of interest and source-free area, respectively. The radius of the source extraction region was between 1" and 2", depending on the angular separation between the stellar components, while the background region had a radius of 15". For sources with an off-axis angle > 2', the source and background extraction regions were chosen to be proportionally larger with the distance to the detector's center. Also, some systems had a large off-axis angle (> 9') and small angular separation between the components, making them appear unresolved. For these cases, we estimated the net source photon count and calculated the flux for the system as a whole.

Having an angular resolution of 0.5", the components of our systems were in most cases resolved. The downside of this resolving power is the lower effective area in comparison with XMM-Newton and therefore the smaller number of event counts we collected within an extraction region. As a result, the event counts were low in most cases. Having the photon event lists for the sources and the background, we applied the same analysis method to determine the net source photon count and confidence interval as for the sources observed with the XMM-Newton telescope.

The same methodology for deriving flux conversion factors was applied here as well. Since Chandra's effective area has changed significantly over the years due to the accu-

Table 2.3: Given are the binary systems observed with the Chandra X-ray observatory. The asterisk symbol marks the planet-hosting companion. The chip column gives the CCD where the system was observed.

system	obs ID	star	chip	off-axis angle ["]
16 Cyg	16647	A	I3	28.9
		B*		25.0
		C		30.7
	18756	A		28.9
		B*		25.0
		C		30.7
55 Cnc	14401	A*	S3	0.7
	14402			1.0
AS 205	16327	A*B	S3	1.2
CoRoT-2	10989	A*	S3	7.5
		B		10.5
HAT-P-20	15711	A*	S3	1.5
		B		5.8
HAT-P-22	15105	A*	I3	258.8
		B		267.1
HATS-65	3282	A*B	I2	592.8
	9382			592.9
HIP 116454	19517	A*B	S2	1070.0
HD 46375	15719	A*	S3	0.6
		B		9.9
HD 96167	5817	A*B	I3	505.5
HD 107148	13665	A*	S3	1.3
		B		35.7
HD 109749	15720	A*	S3	3.1
		B		9.5
HD 178911	13659	B*	S3	2.1
		AC		20.7
HD 185269	15721	A	S3	1.3
		Bab		3.7
HD 188015	13667	A*	S3	2.2
		B		16.1
HD 189733	12340/5	A*	S3	0.5
		B		12.2
HD 197037	7444	A*B	I3	542.2
	8598		I2	542.2
	9770		I2	542.3
	9771		I2	542.4
Kepler-444	17733	A*BC	S3	402.0
	20066			9.9
υ And	10976/9	A*	S3	4.2
WASP-8	15712	A*	S3	1.6
		B		5.0
WASP-18	14566	A*	I3	1.1
WASP-77	15709	A*	S3	1.9
		B		4.4

Table 2.4: The parameters for evaluating the X-ray luminosity of binary companions observed with the Chandra space telescope are given. The asterisk symbol marks the planet-hosting component. The differentiation between non-detections and 'faint'/'bright'-source statistics is the same as in Table 2.2. Here we note that the given coronal effective temperature and the X-ray flux for CoRoT-2 A are adopted from [Sch+11], while the X-ray luminosity was calculated using the geometric distance given by [Bai+18a]. Additionally, the CoRoT-2 A X-ray flux uncertainty corresponds to the limits of a 90% confidence interval (as given in [Sch+11]), while the flux uncertainty given for other sources of our sample corresponds to the 68% confidence interval.

system	component	net photon counts	HR	$\log_{10} T$	$Fx \times 10^{-16} \left[\frac{\text{erg}}{\text{cm}^2\text{s}}\right]$	r[pc]	L_x[erg/s]
16 Cyg	B*	≤ 8.786	/	6.477	≤ 37.352	21.14 ± 0.011	$\leq 2.036 \times 10^{26}$
	A	$42.543^{+6.914}_{-6.243}$	0.863	6.717	$40.930^{+6.651}_{-6.007}$		$(2.231 \pm 0.345) \times 10^{26}$
	C	$4.718^{+2.632}_{-1.944}$	/	6.477	$20.055^{+11.190}_{-8.263}$		$(1.093 \pm 0.53) \times 10^{26}$
55 Cnc	A*	$42.235^{+6.913}_{-6.244}$	-0.865	6.226	$55.020^{+9.007}_{-8.134}$	12.586 ± 0.012	$(1.063 \pm 0.166) \times 10^{26}$
AS 205	A*B	$48.935^{+7.355}_{-6.686}$	0.918	7.18	$657.214^{+98.784}_{-89.790}$	127.492 ± 1.6	$(1.303 \pm 0.19) \times 10^{29}$
CoRoT-2	A*	$62.000^{+8.72}_{-8.051}$	/	6.934	$210.000^{+80.000}_{-130.000}$	213.283 ± 2.457	$(1.165 \pm 0.583) \times 10^{29}$
	B	≤ 3.309	/	6.477	≤ 25.471		$\leq 1.413 \times 10^{28}$
HAT-P-20	A*	$25.920^{+5.460}_{-4.788}$	0.618	6.711	$140.492^{+29.594}_{-25.954}$	71.037 ± 0.199	$(8.648 \pm 1.71) \times 10^{27}$
	B	$1.928^{+1.856}_{-1.136}$	/	6.477	$14.242^{+13.708}_{-8.393}$		$(8.767 \pm 6.802) \times 10^{26}$
HAT-P-22	A*	≤ 4.238	/	6.477	≤ 63.945	81.765 ± 0.25	$\leq 5.215 \times 10^{27}$
	B	≤ 8.684	/	6.477	≤ 131.033		$\leq 1.069 \times 10^{28}$
HATS-65	A*B	≤ 22.508	/	6.477	≤ 32.045	493.32 ± 12.317	$\leq 9.513 \times 10^{28}$
HIP 116454	A*B	≤ 6.25	/	6.477	≤ 291.912	62.449 ± 0.183	$\leq 1.389 \times 10^{28}$
HD 46375	A*	$16.989^{+4.489}_{-3.816}$	-0.177	6.426	$137.573^{+36.357}_{-30.902}$	29.553 ± 0.038	$(1.466 \pm 0.358) \times 10^{27}$
	B	$5.989^{+2.839}_{-2.155}$	-0.336	6.382	$52.064^{+24.685}_{-18.731}$		$(5.547 \pm 2.313) \times 10^{26}$
HD 96167	A*B	$5.032^{+2.839}_{-2.154}$	/	6.477	$76.234^{+43.011}_{-32.637}$	85.301 ± 0.414	$(6.766 \pm 3.358) \times 10^{27}$
HD 107148	A*	$4.93^{+2.632}_{-1.944}$	-0.213	6.438	$30.203^{+16.125}_{-11.908}$	49.416 ± 0.116	$(8.996 \pm 4.175) \times 10^{26}$
	B (WD)	≤ 2.996	/	6.477	≤ 17.414		$\leq 5.187 \times 10^{26}$
HD 109749	A*	$14.907^{+4.242}_{-3.567}$	-0.333	6.383	$46.552^{+13.245}_{-11.139}$	63.082 ± 0.295	$(2.260 \pm 0.592) \times 10^{27}$
	B	$31.907^{+6.016}_{-5.345}$	0.252	6.563	$75.514^{+14.237}_{-12.649}$		$(3.665 \pm 0.653) \times 10^{27}$
HD 178911	B*	$18.910^{+4.724}_{-4.051}$	-0.155	6.455	$109.073^{+27.246}_{-23.365}$	49.394 ± 0.946	$(3.246 \pm 0.763) \times 10^{27}$
	AC	$64.910^{+8.416}_{-7.746}$	0.171	6.566	$331.603^{+42.993}_{-39.575}$		$(9.869 \pm 1.285) \times 10^{27}$
HD 185269	A* (G IV)	$10.127^{+3.691}_{-3.014}$	-0.277	6.398	$16.552^{+6.033}_{-4.926}$	51.992 ± 0.084	$(5.458 \pm 1.807) \times 10^{26}$
	Bab	$8.603^{+3.379}_{-2.7}$	0.126	6.513	$11.577^{+4.547}_{-3.633}$		$(3.817 \pm 1.349) \times 10^{26}$
HD 188015	A*	$16.968^{+4.489}_{-3.816}$	-0.175	6.449	$75.860^{+20.073}_{-17.061}$	50.671 ± 0.109	$(2.376 \pm 0.582) \times 10^{27}$
	B	$7.986^{+3.21}_{-2.53}$	/	6.477	$34.383^{+13.822}_{-10.891}$		$(1.077 \pm 0.387) \times 10^{27}$
HD 189733	A*	6525.709 ± 80.796	0.258	6.6	2720.596 ± 33.684	19.764 ± 0.013	$(1.296 \pm 0.016) \times 10^{28}$
	B	364.813 ± 19.131	0.187	6.573	155.993 ± 8.180		$(7.433 \pm 0.390) \times 10^{26}$
HD 197037	A*B	$27.39^{+6.913}_{-6.244}$	0.378	6.491	$9.840^{+2.484}_{-2.243}$	33.194 ± 0.029	$(1.322 \pm 0.318) \times 10^{26}$
Kepler-444	A*BC	$4.362^{+2.632}_{-1.944}$	/	6.477	$13.164^{+7.943}_{-5.866}$	36.44 ± 0.039	$(2.132 \pm 1.118) \times 10^{26}$
υ And	A*	2836.45 ± 53.272	-0.171	6.481	2266.694 ± 42.572	13.405 ± 0.063	$(4.969 \pm 0.104) \times 10^{27}$
WASP-8	A*	$42.955^{+6.914}_{-6.244}$	0.21	6.579	$218.160^{+35.113}_{-31.710}$	89.961 ± 0.363	$(2.154 \pm 0.33) \times 10^{28}$
	B	≤ 2.996	/	6.477	≤ 16.907		$\leq 1.669 \times 10^{27}$
WASP-18	A*	≤ 4.228	/	6.477	≤ 10.384	123.483 ± 0.37	$\leq 1.931 \times 10^{27}$
WASP-77	A*	$24.899^{+5.361}_{-4.69}$	0.363	6.608	$154.996^{+33.375}_{-29.194}$	105.166 ± 1.196	$(2.091 \pm 0.425) \times 10^{28}$
	B	≤ 4.648	/	6.477	≤ 34.336		$\leq 4.632 \times 10^{27}$

mulation of a contaminant of the optical blocking filters of ACIS[¶], we also calculated different conversion factors for the different observatory cycles. The results are listed in Table 2.10.

2.2.3 X-ray Luminosity

As the last step in the data analysis process, we calculated the X-ray luminosity of our sources. For this, we used the distances calculated by [Bai+18a]. They used a Bayesian method to infer geometric distances from parallax measurements done by the ESO Gaia mission provided in the second data release (DR2). For all stellar components of a system, we used the distance given for the primary component. We calculated the luminosity uncertainty by using the 1σ flux uncertainty and the distance uncertainty and propagating the uncertainties. The net source photon counts, X-ray flux, and luminosity for the system components observed with the XMM-Newton and Chandra telescopes are given in Tables 2.2 and 2.4, respectively. Additionally, parameters calculated as intermediate steps are given. Here, we want to point out that the coronal temperature and the X-ray flux of CoRoT-2 A were adopted from [Sch+11]. The given flux uncertainties represent the 90% confidence interval. Its X-ray luminosity was calculated with the distance given in Table 2.4. For more details on the analysis of the CoRoT-2 system see Section 2.3.2.1.

2.3 Results

2.3.1 Mass estimates of the sample stars

Stars of different masses have different spin-down time scales and therefore different activity levels at a given stellar age. To make the activity levels of the binary companions comparable to one another, we need the knowledge of their stellar spectral type and we chose the stellar mass as the spectral type indicator. For this task, we used the *G-Rp* color and apparent *G* magnitude of individual sources published in the second Gaia data release DR2 [Gai+16a; Gai+18a]. As described in [Lin+18] and [Are+18], we corrected the parallax for the zero point parallax value, checked if the quality indicators are within recommended ranges, and corrected the value of the apparent magnitude[‖]. Additionally, we calculated the re-normalized unit weight error (RUWE) parameter as described in [L L18] for all sources.

We calculated the absolute magnitude assuming no absorption due to interstellar matter and, having the parallax and magnitude uncertainty, we calculated the absolute magnitude uncertainty using the error propagation function. The color and magnitudes for each star of our final sample, for which we estimated a mass, are given in Table 2.11. Some of our sources did not pass the Gaia quality assessment or were below the detection threshold or at the saturation level of the instruments. For these sources, we acquired the stellar mass parameter from the literature, where spectra were used for the spectral type determinations.

We employed an additional check on the stellar sample by testing whether the sample stars are sufficiently close to the main sequence. Stars younger than the main sequence

[¶]More details can be found in the Chandra X-ray Observatory Handbook.
[‖]For the magnitude correction we also used the prescription given in the work of [MW18].

have likely not experienced a significant accumulated tidal interaction with their planets, and stars older than the main sequence have marked changes in their rotation due to their growing radii, making direct activity comparisons inconclusive.

We, therefore, defined the main sequence (MS) in the Gaia CMD by using the stellar properties published by [PM13] in their updated version available as an online table. We fitted a 7^{th} order polynomial to the $G - R_p$ color and the absolute G magnitude of MS stars, and defined a corridor of 0.1 mag at Sun-like temperatures, widening linearly to 0.3 mag at M dwarf temperatures to capture the observed spread in absolute M dwarf brightness [Kim+19].

Therefore, we were able to estimate by interpolation if a given source with observed Gaia color and magnitude falls, within the calculated uncertainties, on the canonical MS as defined by [PM13]. If the stellar source is too faint in magnitude for observed color and too blue for observed magnitude, we mark it as being below the main sequence. Vice versa is true for sources marked as being above the main sequence. For MS stars, again by interpolation, the stellar mass was determined. The X-ray luminosity and mass values, together with the stellar spectral type, are given in Table 2.5.

2.3.2 Activity level difference

As previously discussed, the X-ray luminosity of the stellar companion of a planet-hosting star is used to assess whether the activity of the host star is typical or not, given that the components have co-evolved[**]. When the stellar components of a system have the same spectral type, the difference in the activity level can be determined by directly comparing the activity indicators. However, to make X-ray luminosities of stellar components with different spectral types comparable to each other, we need to normalize their L_x values, and for this task, we used the NEXXUS database of stellar X-ray emission [SL04b].

In the NEXXUS database, ROSAT observations were employed to estimate X-ray luminosities of a volume-limited sample of F/G-, K-, and M-type field stars in the solar neighborhood. The detection completeness of the data set for F/G-type stars within 14 pc of the Sun is 94%, for K-type stars within 12 pc is 96%, and for M- and later type stars within 6 pc of the Sun is 91%, where two of the non-detections are brown dwarf substellar objects. Therefore, it is assumed that the database sufficiently reproduces the X-ray luminosity distribution of stars in the solar neighborhood. With the advent of the eROSITA mission [Pre+21a], there will be X-ray data of larger volume complete stellar samples available in the future, but as of now, the ROSAT data still represents the best volume-complete view of stellar coronae available.

Two main conclusions from the analysis of the solar neighborhood sample were, that all main-sequence stars with outer convection zone are surrounded by hot coronae (I) and that the X-ray luminosities of cool dwarf stars extend over three orders of magnitude with the mean values decreasing with decreasing spectral type (II) (see Figure 2.3). Our further analysis of the activity level difference was based on the second conclusion.

Since ROSAT observed in the energy range between 0.1 - 2.4 keV, X-ray luminosities of solar neighborhood stars given in the NEXXUS database have a somewhat higher value than they have in the 0.2 - 2.0 keV energy range. [Fos+21] calculated the conversion

[**]See the work by [WG01] and [Kou+10] for the discussion on the probability of co-evolution in multiple star systems.

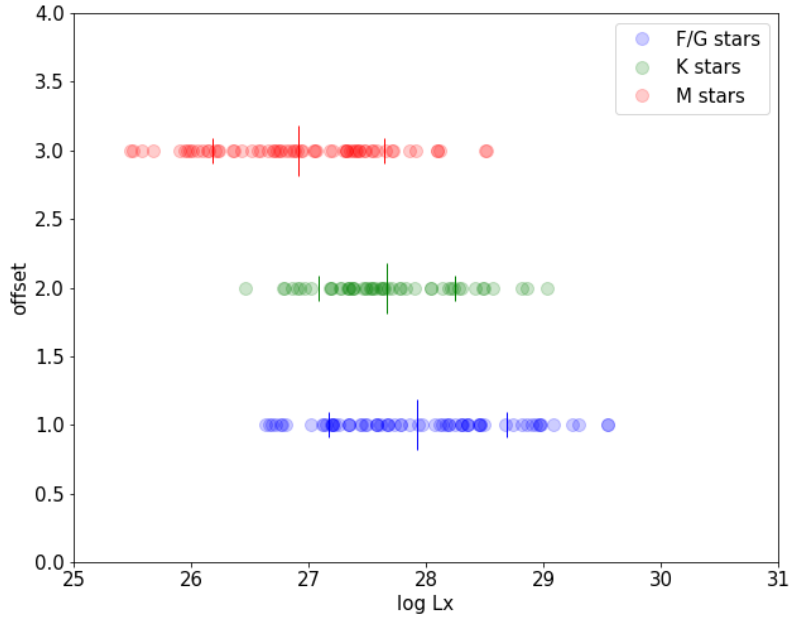

Figure 2.3: Shown is the X-ray luminosity distribution of stellar objects found in the NEXXUS database if they were to be observed in the 0.2-2.0 keV energy range. The distribution of M, K, and F/G type stars are represented by red, green, and blue dots, respectively. The mean of the distribution (50^{th} percentile) is set by the long vertical line, while the standard deviation is set by the short vertical lines (the 15.87^{th} percentile on the left side of the mean or the 84.13^{th} percentile on the right side).

factor that has to be applied when converting from one energy range to the other:

$$F_{X,0.2-2.0\,keV} = 0.87 \times F_{X,0.1-2.4\,keV}. \tag{2.3}$$

In Figure 2.3, we show the X-ray luminosity distributions of objects of different stellar spectral types analyzed in the solar neighborhood sample. The given X-ray luminosity values are corrected and represent the distribution if the stars have been observed in the 0.2-2.0 keV energy range. Although the distributions overlap in their luminosity values, we can estimate the mean value and the standard deviation of each one. If we have a system with stellar components of different spectral types with measured X-ray luminosities, we can use the mean value and standard deviation of the appropriate luminosity distributions and estimate at which percentile in the distribution the components are found. If both stars have a similar state of their rotation and activity evolution, they should be found at similar percentiles of their respective distribution. Then, having the percentile value for each component, we can subtract them from each other and use the difference as an indicator for the discrepancy in the activity level of the stellar components.

Note that the ROSAT volume-complete sample consists of nearby field stars, which have a moderately wide range of ages around the age of our Sun. We will see in the following analysis that none of the stars of our wide binary sample fall outside the range of X-ray luminosities of the ROSAT sample, indicating that the age and activity ranges of our studied sample are reasonably well represented by the ROSAT sample.

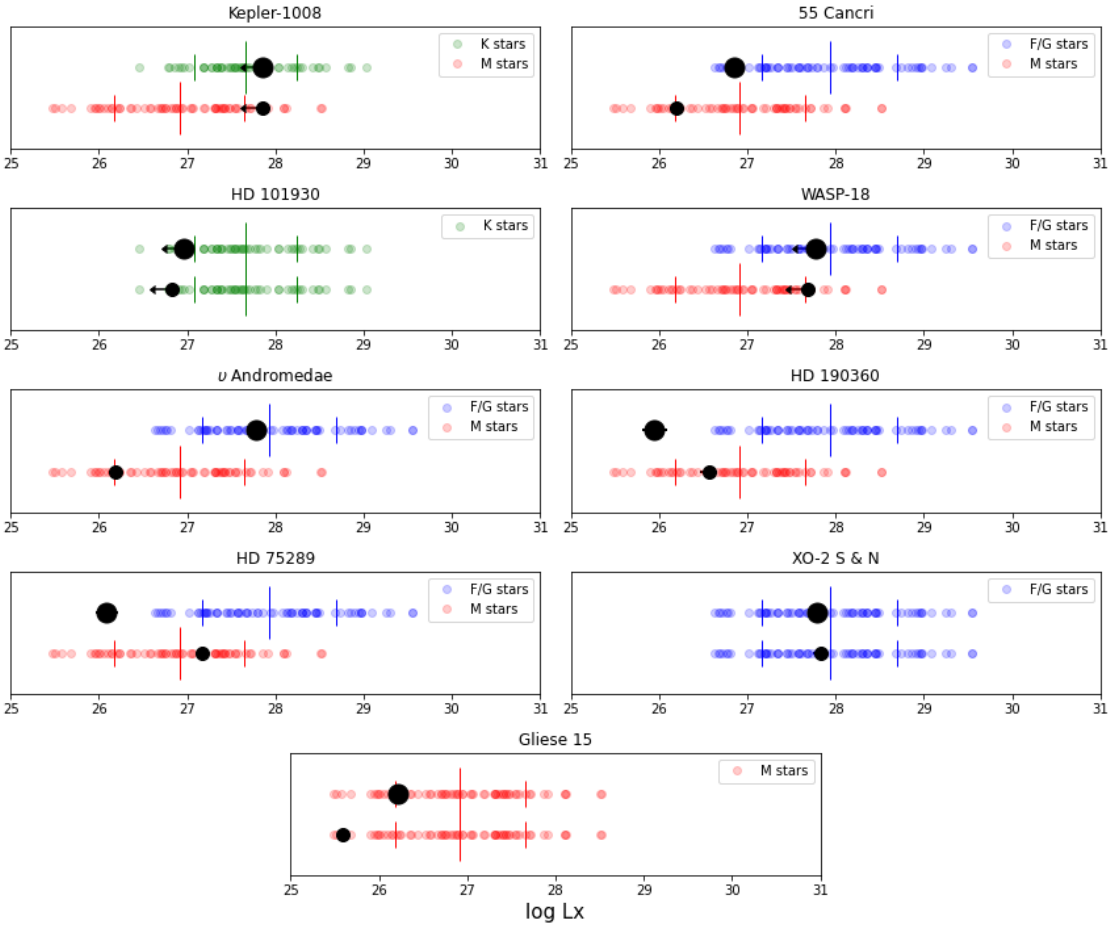

Figure 2.4: Shown are binary systems observed with the XMM-Newton space telescope. The systems shown here have stellar components that are on the Main Sequence. The colored dots represent the X-ray luminosity distribution of stars of the respective spectral type, as shown in Figure 2.3, while the large and the small black dots represent the primary and the secondary stellar component, respectively.

In Figure 2.4, we show some of the binary stellar systems that were observed with the XMM-Newton space telescope. Here, we did not consider systems that have evolved stellar components (HD 27442 and HD 107148) and where two components appear unresolved (HAT-P-16, 30 Ari, HD 46375, AS 205, 16 Cyg, and WASP-33). We also show systems where both stellar components are undetected. However, these systems were not used in the final sample.

In Figure 2.5 are shown some of the systems observed with the Chandra space observatory. From the initial data set, the evolved (HD 107148), unresolved (Kepler-444, HD 197037, HATS-65, AS 205), and evolved & unresolved (HIP 116454, HD 185269, and HD 96167) systems are disregarded. Further, there were three systems (WASP-18, υ And, and 55 Cnc) that had only their primary component in the FoV of the camera, which also resulted in their exclusion. Also, the undetected system HAT-P-22 was discarded from further analysis. Additionally, two of the three components of the system HD 178911 appeared unresolved which resulted in its initial exclusion; however, an analysis method

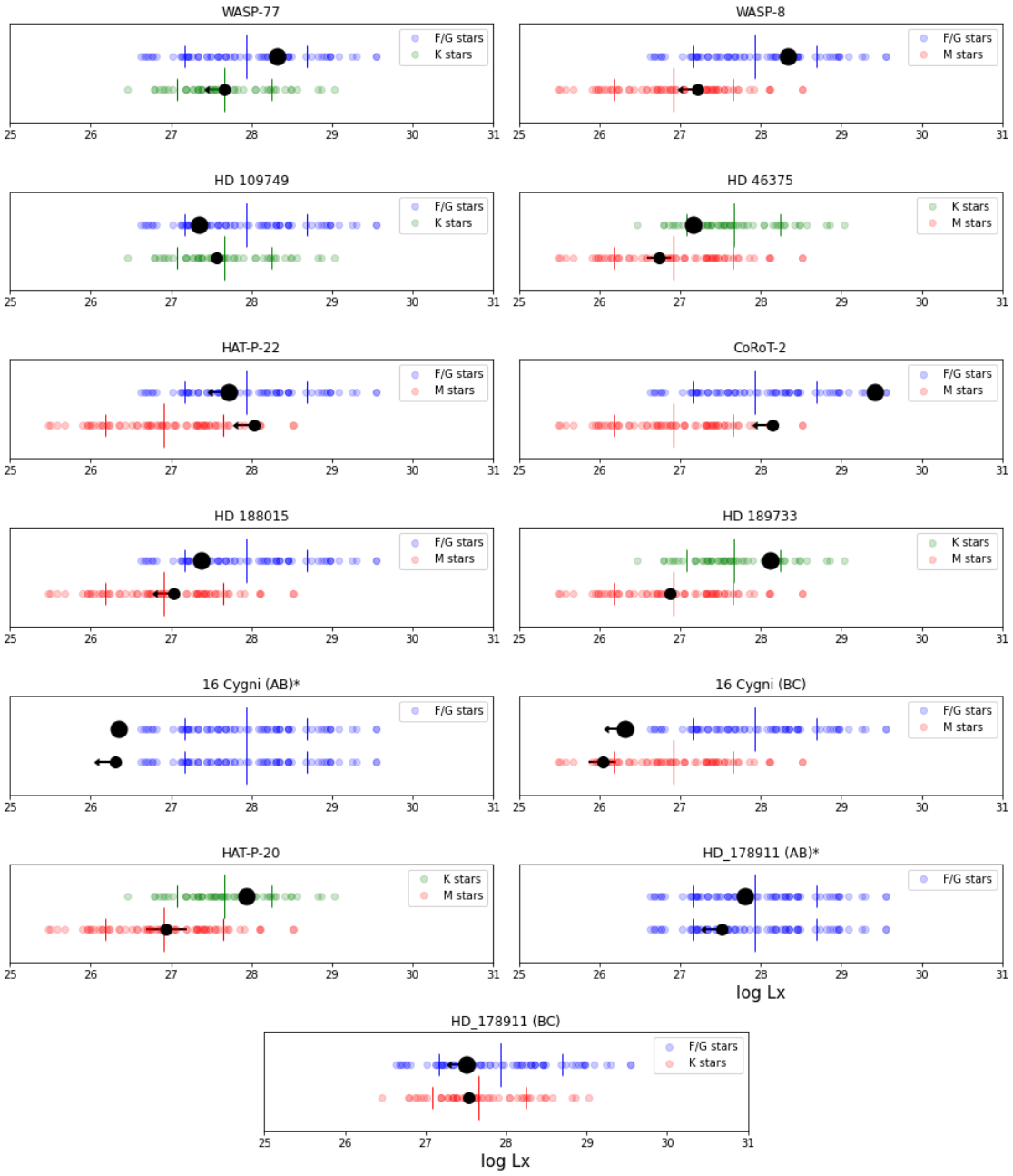

Figure 2.5: Shown are systems observed with the Chandra space observatory. The markings are the same as in Figure 2.4. Only resolved systems with stellar components on the main sequence are represented. Since the Chandra space observatory has a better resolving power than the XMM-Newton space telescope, two systems that appeared unresolved with XMM-Newton (HD 46375 and 16 Cyg) are now resolved.

was later found that enabled the inclusion of this system in the final sample. For more details, see Appendix 2.6.1.

Our final sample of stellar systems that were analyzed consists of 55 Cnc, GJ 15, HD 75289, HD 190360, υ And, and X0-2, which were observed by the XMM-Newton telescope and 16 Cyg, CoRoT-2, HAT-P-20, HD 46375, HD 109749, HD 178911, HD 188015, HD 189733, WASP-8, and WASP-77, that were observed with the Chandra space observatory.

2.3.2.1 The CoRoT-2 system

The CoRoT-2 system takes a special place in the sample. It has a relatively large distance, making it possible that interstellar absorption influences the Chandra X-ray measurements. It has been investigated previously by [Sch+11], who also performed a more detailed spectral analysis. From their spectral analysis of the source photons of the primary, an interstellar absorption with a depth of the absorption column of $\approx 10^{21}$ cm^{-2} and a distance of 270 ± 120 pc was determined. By using an APEC thermal model and fitting it to the X-ray spectrum of CoRoT-2 A, an X-ray luminosity of $L_x = 1.9 \times 10^{29}$ erg/s in the 0.3-4.0 keV energy band was estimated. The secondary component, CoRoT-2 B, was not detected and an upper limit on the X-ray luminosity was determined: $L_x < 9 \times 10^{26}$ erg/s. [Sch+11] also show that there is very little detectable stellar emission below 0.7 keV due to the ISM absorption.

While the updated stellar distances from [Bai+18a] place the system at a distance of ≈ 213 pc instead of 270 pc, the general analysis of [Sch+11] still applies and we use their coronal properties instead of the ones derived from a simple hardness ratio analysis.

However, when we analyse the secondary in the energy range of 0.7-2 keV, we find that the KBN methodology gives a higher upper limit to the secondary's source flux than the one estimated by [Sch+11]. Specifically, we find that the 95% upper limit to the secondary's count number is 3 photons, which translates into an upper limit of $L_x < 1.413 \times 10^{28}$ erg/s. Adopting our estimate of the X-ray luminosity upper limit of the secondary places a more conservative estimate on the activity excess of the planet-hosting primary. Therefore, we used the spectral analysis from [Sch+11] for the primary and our luminosity estimate for the secondary in further analysis.

Furthermore, the available data from Gaia shows that the secondary is more likely to be an M dwarf instead of a late K dwarf, as was estimated by [Sch+11] and [Eva+16]. Therefore, we continue our analysis of the CoRoT-2 system under the assumption that it is a G- and M-dwarf pair.

2.3.3 Star-Planet Interaction Models

The determined difference in activity levels of stars in a system can be related to expected star-planet interaction strength. Different models exist that explore potential tidal star-planet interactions with respect to different observable parameters. [Mil+15], for example, use the ratio of planet mass and the square of its semi-major axis to find systems for which star-planet interaction can be expected[††]. Although the authors were concerned with

[††]The authors use the limit of $\log_{10} M_P/a^2 = 10\,\mathrm{M_{Jup}AU^{-2}}$ as the preferred limit for interaction strength between weakly and strongly interacting systems. According to the given limit, weakly interacting systems from our final sample are HD 190360 A, GJ 15 A, HD 188015 A, and 16 Cyg B.

Table 2.5: Here, we show the calculated luminosities, masses, spectral types, and percentile values for each stellar component of systems that have been used in SPI modeling. The Obs column presents the observatory with which the data was acquired: **X** denotes the XMM-Newton telescope, while **C** stands for the Chandra observatory. The stellar companions 16 Cyg C and WASP-77 B had only their spectral type determined in the corresponding publications. [a] : By employing the method described in Section 2.3.1, the estimated mass of CoRoT-2 A was 0.85 $M_\odot$, which would label it as a K-dwarf. Since this star is a known G-dwarf [Sch+11; Sta+19], we discarded our calculated stellar mass. Here, we note that this was the only star for which the calculated mass and stellar mass from the TESS Input Catalog led to different spectral type estimates.

system	component	L_x[erg/s]	Obs	Mass[$M_\odot$]	SpT	percentile	Mass ref.
16 Cyg	B*	$\leq 2.036 \times 10^{26}$	C	1.060	G	$\leq$ 0.0164	this work
	A	$(2.231 \pm 0.345) \times 10^{26}$		$1.04^{+0.13}_{-0.12}$	G	0.0187	[Sta+19]
	C	$(1.093 \pm 0.53) \times 10^{26}$		/	M	0.1148	[Pat+02]
55 Cnc	A*	$(6.964 \pm 0.488) \times 10^{26}$	X	0.909	G	0.0763	this work
	B	$(1.579 \pm 0.273) \times 10^{26}$		0.237	M	0.163	
CoRoT-2	A*	$(1.165 \pm 0.583) \times 10^{29}$	C	0.97 ± 0.14^a	G	0.933	[Sta+19]
	B	$\leq 1.413 \times 10^{28}$		0.490	M	$\leq$ 0.9547	this work
GJ 15	A*	$(1.629 \pm 0.043) \times 10^{26}$	X	0.432	M	0.1674	this work
	B	$(3.879 \pm 0.211) \times 10^{25}$		0.180	M	0.0345	
HAT-P-20	A*	$(8.648 \pm 1.71) \times 10^{27}$	C	0.702	K	0.681	this work
	B	$(8.767 \pm 6.802) \times 10^{26}$		0.57	M	0.515	[Fon+19]
HD 46375	A*	$(1.466 \pm 0.358) \times 10^{27}$	C	0.892	K	0.1939	this work
	B	$(5.547 \pm 2.313) \times 10^{26}$		0.498	M	0.4072	
HD 75289	A*	$(1.233 \pm 0.405) \times 10^{26}$	X	1.183	F	0.0077	this work
	B	$(1.473 \pm 0.100) \times 10^{27}$		0.14 ± 0.02	M	0.6355	[Sta+19]
HD 109749	A*	$(2.260 \pm 0.592) \times 10^{27}$	C	1.151	F	0.2244	this work
	B	$(3.665 \pm 0.653) \times 10^{27}$		0.780	K	0.4307	[DB07]
HD 178911	B*	$(3.246 \pm 0.763) \times 10^{27}$	C	0.987	G	0.2911	this work
	A	$\leq 6.389 \times 10^{27}$		1.1	G	$\leq$ 0.4354	[Tok+00]
	C	$\leq 3.479 \times 10^{27}$		0.79	K	$\leq$ 0.4154	
HD 188015	A*	$(2.376 \pm 0.582) \times 10^{27}$	C	1.038	G	0.2331	this work
	B	$(1.077 \pm 0.387) \times 10^{27}$		0.180	M	0.5636	
HD 189733	A*	$(1.296 \pm 0.016) \times 10^{28}$	C	0.801	K	0.7808	this work
	B	$(7.433 \pm 0.390) \times 10^{26}$		0.193	M	0.4759	
HD 190360	A*	$(8.796 \pm 3.410) \times 10^{25}$	X	1.039	G	0.0045	this work
	B	$(3.626 \pm 0.949) \times 10^{26}$		0.189	M	0.3129	
υ And	A*	$(6.007 \pm 0.140) \times 10^{27}$	X	1.322	F	0.4216	this work
	B	$(1.567 \pm 0.295) \times 10^{26}$		0.184	M	0.1619	
WASP-8	A*	$(2.154 \pm 0.33) \times 10^{28}$	C	0.981	G	0.7028	this work
	B	$\leq 1.669 \times 10^{27}$		0.492	M	$\leq$ 0.6631	
WASP-77	A*	$(2.091 \pm 0.425) \times 10^{28}$	C	0.954	G	0.6969	this work
	B	$\leq 4.632 \times 10^{27}$		/	K	$\leq$ 0.5006	[Max+13]
XO-2	S*	$(6.129 \pm 1.369) \times 10^{27}$	X	0.948	G	0.4261	this work
	N*	$(6.678 \pm 1.385) \times 10^{27}$		0.947	G	0.4454	

magnetic interaction, these two parameters are also applicable for the tidal interaction strength estimate. Other models additionally use stellar parameters like mass or radius to better define the level of tidal interaction between a planet and its host star. We have chosen three such models, where we used the derived tidal interaction parameter to compare to the measured activity level differences: The first model estimates the timescales for tidal dissipation due to SPI [Alb+12], the second model uses the gravitational perturbation the planet exhibits onto the stellar atmosphere [CSM00], and the third model calculates the angular momentum transfer rate in the star-planet system [Pen+12].

2.3.3.1 Tidal dissipation timescales for Spin-Orbit alignment

In this model, the fundamental approach is to consider time scales for spin-orbit alignment in stellar binaries. It is observed that cool stars with close-in giant planets often have a low obliquity of the planetary orbital plane and the stellar spin, i.e. those planets tend to orbit in the stellar equatorial plane [Alb+12], which is interpreted as a consequence of tidal star-planet interaction. In contrast, hot host stars with a radiative outer layer display a wide range of obliquities. It is hypothesized that cool stars ultimately come into alignment with the orbits because they have higher rates of tidal dissipation due to the deeper convective zone [Win+10]. Hot stars, on the other hand, lack thick convective envelopes and have much longer tidal time scales.

Other studies, however, have shown that alignment between the orbital and stellar equatorial plane, which occurs predominantly in cool-star systems, is not necessarily linked to the tidal interaction between the star and its planet. [Maz+15] have shown, in addition to the hot-cool dichotomy, that the distribution of the amplitude of photometric rotational modulation of Kepler Objects of Interest (KOIs), which is used as a proxy for the obliquity in star-planet systems, is similar for both short period and long period planets, demonstrating the possibility that tidal interaction may not be responsible for the alignment process. Further, [DW17] investigated WASP-107b and found that both spin-orbit alignment and anti-alignment can be ruled out, although the planet is in a relatively tight orbit with a mass of $0.12 M_{Jup}$. Additionally, the authors found that, for a sample of stars with measured obliquities, hot stars are more likely to be misaligned and that cool stars have low obliquity when their planets are close-in, but seem independent of the mass ratio in the system. Following these findings, the authors conclude that scenarios involving tidal realignment are questionable, but, additionally state that there is not any proposed mechanism that can explain the observed obliquities.

Going back to the work of [Alb+12], the dependence of the obliquity of cool stars on the mass ratio was not evident. However, by invoking the tidal timescale formalism and comparing it to the stellar obliquity, a correlation supporting star-planet tidal interaction was found. Therefore, despite the concern regarding the origin of the alignment being in tidal interaction, we find that by comparing the tidal dissipation timescale to the planet host activity excess, we present a methodology that tries to validate or discard the idea of tidal SPI independently of the stellar obliquity.

The formulae for tidal dissipation timescales are adopted from the spin-orbit synchronization timescales in binary star systems [Zah77]. The following relationships

between the star-planet system parameters and the convective (CE) and radiative[‡‡] (RA) timescales for alignment are obtained:

$$\frac{1}{\tau_{CE}} = \frac{1}{10 \times 10^9 yr} q^2 \left(\frac{a/R_*}{40}\right)^{-6} \tag{2.4}$$

and,

$$\frac{1}{\tau_{RA}} = \frac{1}{0.25 \times 5 \times 10^9 yr} q^2 (1+q)^{5/6} \left(\frac{a/R_*}{6}\right)^{-17/2}, \tag{2.5}$$

where q is the planet-to-star mass ratio, R_* is the stellar radius, and a is the semi-major axis of the planetary orbit.

2.3.3.2 Gravitational perturbation model

The idea behind this model is that Hot Jupiters gravitationally influence the outermost atmospheric layers of their stars by raising tidal bulges at the subplanetary point [CSM00]. This may affect both the motion in the stellar convective layer and the flow fields in the outer atmosphere via the tidal bulges if the orbital and rotational periods are not equal. It is expected that this could lead to increased stellar activity because, in the case of different periods of the planet's orbit and the stellar spin, the stellar tidal bulges rise and subside quickly in the stellar rest frame, potentially increasing turbulent motions in the outer convection layer.

The parameter used to describe the SPI in this tidal interaction model by [CSM00] is the gravitational perturbation parameter $\Delta g_*/g_*$, which is defined as

$$\frac{\Delta g_*}{g_*} = \frac{M_p}{M_*} \frac{2R_*^3}{(a - R_*)^3}. \tag{2.6}$$

Here, M_* and R_* are the stellar mass and radius, respectively, M_p is the planetary mass, and a is the semi-major axis of the planetary orbit. The gravitational perturbation parameter has the strongest dependence on the distance between the stellar surface and the planet $a - R_*$.

2.3.3.3 Angular momentum transfer rate in Star-Planet System

The work of [Pen+12] examines the efficiency of tidal dissipation by exoplanets in close-in circular orbits around stars with a surface convective zone. It does so by modeling the rotational evolution of a star that tidally interacts with a close-in planet. It also takes into account the coupling of the stellar convective envelope to the core and angular momentum loss due to the stellar wind. The Equations 2.7 and 2.8 describe the angular momentum transfer rate and the evolution of the semi-major axis given the current value of planetary orbital period and stellar rotation period:

$$\left(\frac{dL_{conv}}{dt}\right)_{tide} = -\frac{1}{2} m_p M_* \sqrt{\frac{G}{a(M_* + m_p)}} \frac{da}{dt} \tag{2.7}$$

[‡‡]Radiative in the sense that stars with a surface temperature hotter than $T_{eff} = 6250$ K have an outer radiative envelope.

$$\frac{da}{dt} = \text{sign}(\omega_{conv} - \omega_{orb}) \frac{9}{2} \sqrt{\frac{G}{aM_*}} \left(\frac{R_*}{a}\right)^5 \frac{m_p}{Q_*}, \tag{2.8}$$

Here, m_p and M_* are the planet and stellar masses, respectively, G is the gravitational constant, a is the semi-major axis of the planet orbit, $\omega_{\rm conv}$ and $\omega_{\rm orb}$ are the angular frequency of the stellar convective zone and orbital angular frequency, respectively. Here, $\omega_{\rm conv}$ is approximated by the observed stellar surface rotation. [Pen+12] estimated that the tidal quality factor Q_* has a value between 10^5 and 10^7. The lower limit implies a higher tidal dissipation efficiency, while the upper limit implies weaker efficiency. By choosing the efficiency to be $Q_* = 10^7$, we adopt a more conservative scenario that assumes that the weakest possible tides are acting.

The factor $\text{sign}(\omega_{\rm conv} - \omega_{\rm orb})$ takes the value 1 when the stellar convective zone is spinning faster than the planet goes about its orbit and the value -1 in the opposite case. Therefore, this factor sets the direction of the angular momentum transfer.

To calculate $\omega_{\rm conv}$, we used the stellar rotation periods from the literature (see Table 2.6), assuming rigid body rotation: $\omega_{\rm conv} = 2\pi/P_{\rm rot}$. We took care to only consider stars for which the rotation period was measured directly from rotational modulation of the broad-band or chromospheric line emission, or from the rotational broadening of spectral lines. We did not use rotation periods that were derived from single-epoch activity measurements assuming a gyrochronology relationship, as such relationships may not be valid in the presence of star-planet interactions.

One constraint of the model is that it is only valid for low stellar masses. For masses larger than approximately $1.2\,M_\odot$ the surface convective zone becomes negligible in mass. However, none of our sample stars has an estimated mass larger than $1.2\,M_\odot$.

2.3.3.4 Model results

We calculated the strength of the tidal star-planet interaction according to the three models for the planet-hosting stars in our sample and then compared them to the observed activity level difference to their same-age stellar companions. Systems that have both stellar components undetected were discarded from this analysis. For these systems, we were not able to estimate an upper or lower limit to the activity level difference. For systems where we have at least one detection, we were able to give either a lower or an upper limit to the activity level difference, depending on which star was detected.

Our activity level difference parameter is calculated as follows: we compare the X-ray luminosity of each individual star to the X-ray luminosity function for the respective spectral type and calculate into which percentile of the distribution the star falls. Then we calculate the difference in percentiles of two stars in a system with respect to their applicable X-ray luminosity functions. If a planet-hosting star is much more active than its companion star with respect to their spectral types, then this will yield a positive percentile difference, if it is much less active, a negative one. If the percentile difference is close to zero, both stars have similar activity levels for their respective spectral types.

Figures 2.6, 2.7, and 2.8 show the activity level difference as a function of the star-planet tidal interaction parameters of the three models described above. In the result figures, we have color-coded the information on the spectral type of the planet host, whereas the symbol shape accounts for the spectral type of the companion. The percentile difference uncertainty is estimated by applying the error propagation function on the

Table 2.6: Given are the stellar and planetary parameters used for the star-planet tidal interaction models. The stellar parameters (M_*, R_*, and T_{eff}) given here are taken from the TESS Input Catalog [Sta+19], while rotation periods were researched individualy: [a]: [Dav+15]; [b]: [Bou+18]; [c]: [Lan+09]; [d]: [How+14]; [e]: [Esp+17]; [f]: [Día+18b]; [f]:[Udr+00]; [g]: [HW07]; [h]: [But+97]; [i]:[Sal+15]; [j]: [Max+13]; [k],[l]: [Dam+15]. For the planetary parametars, we used the publications referred in the NASA Exoplanet Archive [Ake+13]: **16 Cyg b**: [SCG17], **55 Cnc e**: [Bou+18], **CoRoT-2 b**: [Gil+10], **GJ 15 b**: [Pin+18], **HAT-P-20 b**: [Bak+11], **HD 46375 b**: [But+06], **HD 75289 b**: [SCG17], **HD 109749 b**: [Men+18], **HD 178911 b**: [SCG17], **HD 188015 b**: [But+06], **HD 189733 b**: [Bon+17; SCG17], **HD 190360 c**: [Wri+09], ***υ* And b**: [Cur+11], **WASP-8 b**: [Bon+17; SCG17], **WASP-77 b**: [Bon+17; SCG17], **XO-2 Sb**: [SCG17], **XO-2 Nb**: [Bon+17]. If the uncertainty of a stellar or planetary parameter was given as an asymmetrical interval in the corresponding publication, we used the greater value for further analysis.

SP pair	P_{rot} [days]	R_* [$R_\odot$]	M_* [$M_\odot$]	P_{orb} [days]	M_{pl} [M_{jup}]	a [AU]	T_{eff} [K]
16 Cyg Bb	23.2 ± 11.5^a	1.13 ± 0.08	1.03 ± 0.15	798 ± 1	1.78 ± 0.08	1.66 ± 0.03	5747 ± 143
55 Cnc Ae	38.8 ± 0.05^b	0.96 ± 0.08	0.9 ± 0.1	0.736547 ± 10^{-6}	0.025 ± 0.001	0.0154 ± 10^{-4}	5250 ± 171
CoRoT-2 Ab	4.52 ± 0.02^c	0.94 ± 0.12	0.97 ± 0.14	1.742994 ± 10^{-6}	3.47 ± 0.22	0.02798 ± 0.0008	5529 ± 121
GJ 15 Ab	44.8^d	0.41 ± 0.01	0.4 ± 0.02	11.441 ± 0.002	0.0095 ± 0.0014	0.072 ± 0.004	3607 ± 68
HAT-P-20 Ab	14.48 ± 0.02^e	0.68 ± 0.07	0.73 ± 0.1	2.875317 ± 10^{-6}	7.2 ± 0.2	0.0361 ± 0.0005	4604 ± 129
HD 46375 Ab	/	0.92 ± 0.05	0.9 ± 0.13	3.0236 ± 10^{-4}	0.23 ± 0.02	0.0398 ± 0.0023	5092 ± 149
HD 75289 Ab	16.0^f	1.3 ± 0.07	1.3 ± 0.1	3.5093 ± 10^{-4}	0.49 ± 0.03	0.05	6044 ± 156
HD 109749 Ab	/	1.3 ± 0.07	1.06 ± 0.17	5.2399 ± 0.0001	0.27 ± 0.05	0.062 ± 0.004	5868 ± 162
HD 178911 Bb	/	1.02 ± 0.06	0.98 ± 0.18	71.48 ± 0.02	8.03 ± 2.51	0.34 ± 0.01	5564 ± 163
HD 188015 Ab	/	1.084 ± 0.075	1.02 ± 0.15	461.2 ± 1.7	1.5 ± 0.13	1.203 ± 0.07	5727 ± 139
HD 189733 Ab	11.95 ± 0.01^g	0.78 ± 0.06	0.84 ± 0.11	2.2185757 ± 10^{-7}	1.13 ± 0.08	0.0311 ± 0.0005	5023 ± 120
HD 190360 Ac	/	1.17 ± 0.07	0.98 ± 0.07	17.111 ± 0.005	0.06 ± 0.01	0.130 ± 0.008	5549 ± 123
υ And Ab	12.0^h	1.64 ± 0.11	1.15 ± 0.16	$4.61703 \pm 10{-}5$	0.688 ± 0.004	0.0592217 ± 10^{-7}	6183 ± 35
WASP-8 Ab	16.4 ± 1.0^i	0.997 ± 0.06	0.99 ± 0.16	8.15872 ± 10^{-5}	2.54 ± 0.33	0.0801 ± 0.0015	5589 ± 174
WASP-77 Ab	15.4 ± 0.4^j	0.93 ± 0.05	0.99 ± 0.16	1.36003 ± 10^{-5}	2.29 ± 0.33	0.0241 ± 0.0004	5605 ± 115
XO-2 Sb	30.0 ± 4.0^k	0.96 ± 0.05	0.98 ± 0.12	18.16 ± 0.03	0.26 ± 0.04	0.13	5547 ± 118
XO-2 Nb	41.6 ± 1.1^l	1.09 ± 0.09	0.9 ± 0.13	2.6158592 ± 10^{-7}	0.595 ± 0.022	0.0367 ± 0.0006	5267 ± 190

Table 2.7: Given are the tidal interaction strength values and their uncertainties for all three star-planet interaction models used. Regarding the uncertainty given for the angular momentum transfer rate, the rotational period uncertainty was not taken into account since it was never high enough to change the sign of the torque. For the triple systems 16 Cyg and HD 178911, we were able to estimate the X-ray luminosity of all components and, therefore, calculated the activity level difference for each pair.

system	percentile difference	$\Delta g/g$	tidal timescale $\left[\frac{yr}{5\times10^9}\right]$	$dL_{conv}/dt\left[M_\odot\left(\frac{km}{s}\right)^2\right]$
16 Cyg AB 16 Cyg BC	≤ -0.0023 ≤ -0.0984	$(1.057 \pm 0.283) \times 10^{-10}$	$(1.783 \pm 0.952) \times 10^{11}$	$-(1.101 \pm 0.420) \times 10^{-22}$
55 Cnc	-0.0867 ± 0.0239	$(3.647 \pm 1.379) \times 10^{-6}$	1149.778 ± 669.645	$(1.529 \pm 0.631) \times 10^{-14}$
CoRoT-2	≥ -0.0217	$(4.294 \pm 2.038) \times 10^{-5}$	2.928 ± 2.398	$(7.187 \pm 4.665) \times 10^{-12}$
GJ 15	0.1331 ± 0.0042	$(8.928 \pm 2.245) \times 10^{-10}$	$(2.874 \pm 1.423) \times 10^{9}$	$(2.841 \pm 1.349) \times 10^{-21}$
HAT-P-20	0.166 ± 0.0558	$(1.661 \pm 0.585) \times 10^{-5}$	12.251 ± 7.994	$(1.336 \pm 0.663) \times 10^{-12}$
HD 46375	-0.2133 ± 0.1069	$(8.316 \pm 2.618) \times 10^{-7}$	5579.114 ± 3247.165	/
HD 75289	-0.6278 ± 0.0159	$(2.173 \pm 0.560) \times 10^{-6}$	895.898 ± 433.828	$(2.254 \pm 0.667) \times 10^{-14}$
HD 109749	-0.2063 ± 0.0664	$(6.301 \pm 2.293) \times 10^{-7}$	9152.284 ± 6278.918	/
HD 178911 AB HD 178911 BC	-0.1443 ± 0.0563 -0.1243 ± 0.0563	$(4.484 \pm 1.855) \times 10^{-8}$	$(1.057 \pm 0.872) \times 10^{6}$	/
HD 188015	-0.3305 ± 0.0967	$(2.092 \pm 0.677) \times 10^{-10}$	$(4.575 \pm 2.951) \times 10^{10}$	/
HD 189733	0.3049 ± 0.0126	$(5.977 \pm 1.841) \times 10^{-6}$	115.361 ± 64.808	$(1.640 \pm 0.699) \times 10^{-13}$
HD 190360	-0.3084 ± 0.0530	$(9.598 \pm 2.860) \times 10^{-9}$	$(2.737 \pm 1.579) \times 10^{7}$	/
υ And	0.2597 ± 0.0258	$(3.656 \pm 0.961) \times 10^{-6}$	333.397 ± 159.447	$(5.073 \pm 1.648) \times 10^{-14}$
WASP-8	≥ 0.0397	$(1.136 \pm 0.328) \times 10^{-6}$	2164.122 ± 1214.617	$(9.496 \pm 3.922) \times 10^{-15}$
WASP-77	≥ 0.1964	$(4.729 \pm 1.430) \times 10^{-5}$	2.886 ± 1.599	$(7.602 \pm 3.121) \times 10^{-12}$
XO-2 S	-0.0193 ± 0.0677	$(2.307 \pm 0.585) \times 10^{-8}$	$(4.527 \pm 2.264) \times 10^{6}$	$(4.582 \pm 1.846) \times 10^{-18}$
XO-2 N	0.0193 ± 0.0677	$(5.125 \pm 0.165) \times 10^{-6}$	180.842 ± 104.043	$(8.676 \pm 3.652) \times 10^{-14}$

X-ray luminosity uncertainty of both stellar components. This is done for systems where both components are detected.

To assess the relationship between the activity level and the interaction strength, we employ the statistical Spearman's rank analysis. In statistics, Spearman's rank correlation coefficient ρ is a nonparametric measure of rank correlation. It assesses how well the relationship between two variables can be described using a monotonic function of arbitrary form. For this analysis, we used systems where both components are detected, and those where the host star is detected and the stellar companion is undetected, i.e. where we have a lower limit to the activity level difference. We discarded the *16 Cyg* system, where the planet host was undetected, as we were only able to estimate the upper limit of the percentile difference for this system.

The correlation coefficients for the three SPI models are given in Table 2.8. The corresponding p-value gives the probability that the observed value of ρ can be obtained by statistical fluctuations. We find that the first model, where short time scales mean strong tidal interactions, shows strong anticorrelation as expected, the second model shows a highly significant correlation, and the third model shows a mild correlation. We

Table 2.8: Given are the Spearman's rank correlation coefficients for all three star-planet interaction models we used, together with the p-value for each given set of data points.

	SPI models		
	tidal timescale	$\Delta g/g$	dL_{conv}/dt
Spearman's ρ	-0.5382	0.5559	0.3091
p-value	0.0315	0.0254	0.3550

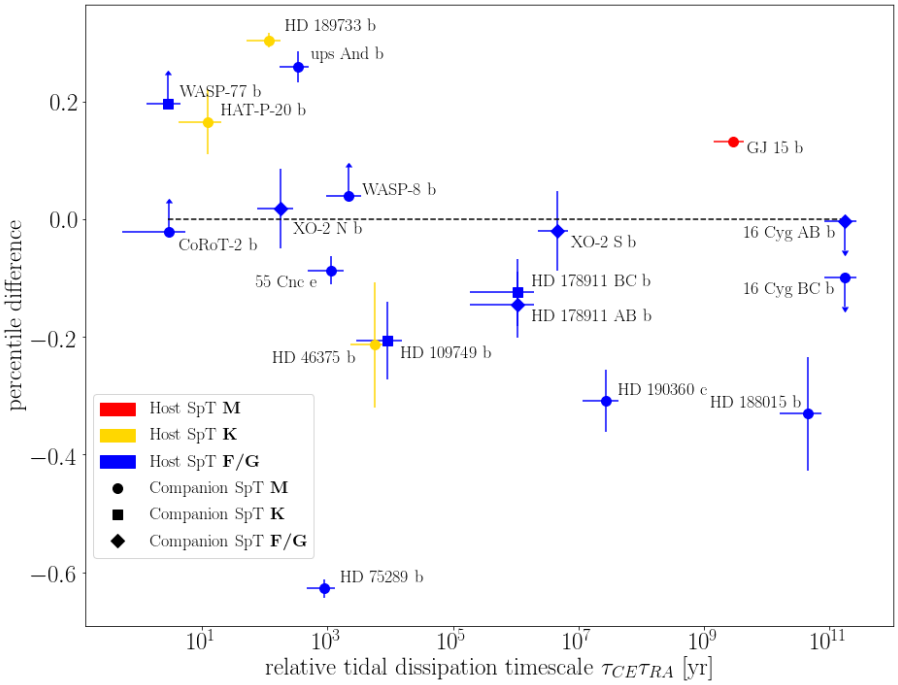

Figure 2.6: Shown is the percentile difference as a function of the tidal dissipation timescale for each star-planet system from our final sample. Here, the star-planet interaction model described in Section 2.3.3.1 was used. Color-coded is the planet host spectral type, while the shape of the marker indicates the spectral type of the stellar companion. The tidal timescales are given relative to the solar age.

point out that the sample that could be used for model three was smaller since it required the rotation period of the host star to be known.

In our sample were five known multiplanet systems: WASP-8 A, 55 Cnc A, HD 190360 A, υ And A, and XO-2 S. We calculated the SPI strength for each star-planet pair; for the WASP-8 A, υ And A, and XO-2 S planet systems, the b planet was the one yielding a stronger influence on the planet host in all three models, while in the system HD 190360 A this was true for the c component. For the 55 Cnc A system, the planet e yielded the strongest influence on the host star.

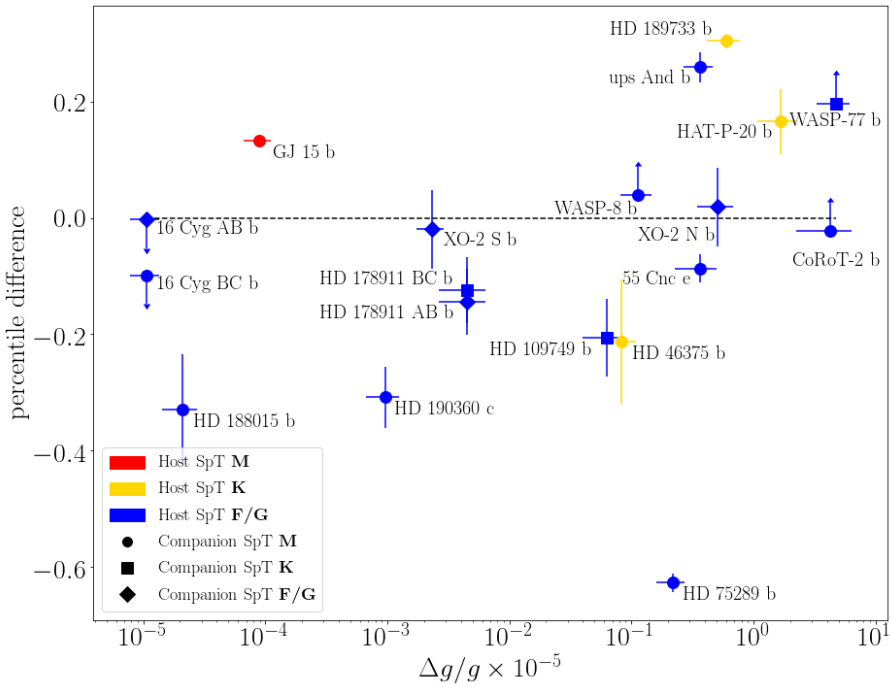

Figure 2.7: This figure shows the percentile difference as a function of the gravitational perturbation parameter described in Section 2.3.3.2. As in Figure 2.6, color-coded is the planet host spectral type, while the shape of the marker indicates the spectral type of the stellar companion.

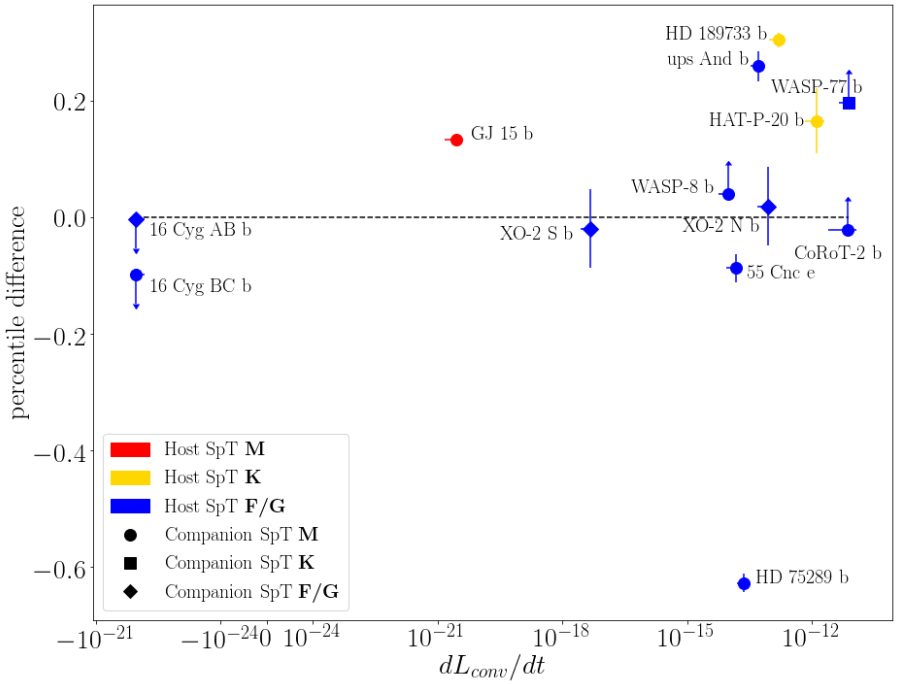

Figure 2.8: Here, the percentile difference as a function of the torque that is transferred between the planet's orbit and stellar spin is given for each system from our final sample. The tidal interaction model described in Section 2.3.3.3 was used to calculate the tidal interaction parameter used. As in previous result figures, color-coded is the planet host spectral type, while the shape of the marker indicates the spectral type of the stellar companion.

2.4 Discussion

2.4.1 Activity bias in planet detections

In general, there exists a detection bias toward close-in giant planets (Hot Jupiters) around more active stars. The radial velocity signal of smaller and/or distant planets is more difficult to detect around active stars because of the low signal-to-noise ratio [Des+07; Hat02; LDM10; SD97]. Therefore, if we compare all activity measurements of the full planet-hosting star sample to one another, we would not be properly accounting for the detection bias. However, if each host star is compared to some age or activity expectation independent of the parameters of the host itself, the detection bias can be overcome. Here, our wide binary stellar systems fulfill that purpose. If a Hot-Jupiter-hosting star has a high activity level, using the stellar companion, we can determine if the activity is due to the young age – the companion then also has a high activity level for the given spectral type (see e.g. [JBG21b] and references therein) – or due to star-planet interaction – the companion then has a significantly lower activity level. With this approach, each planet host has its own activity proxy and the detection bias is properly accounted for.

Also, regarding the age of a system, detecting planets around older stars is somewhat easier, especially with the radial velocity method since older stars tend to be slower rotators with lower magnetic activity. However, since we analyse stellar X-ray activity of the host star *relative* to the other star in the wide binary system, it is not of importance what the true intrinsic age of those systems is since we only compare one star to one other star with the same age.

2.4.2 Interpretation of the observed activity difference

To avoid the activity bias, we have chosen wide binary systems, as discussed previously. Our results show a positive correlation between the magnetic activity level of the planet-hosting star relative to its stellar companion and the star-planet tidal interaction strength in the second and third model. For the first model, we expect an anticorrelation between the tidal timescale and the activity difference, as short timescales indicate strong tidal interaction, and this is indeed what we find.

For illustrative purposes, we can now compare our findings to what we would expect to see if the result was purely driven by any remaining effect of the planet detection bias with respect to the activity. Under a planet detection bias, we expect that Hot Jupiters (i.e. tidally strongly interacting planets) are found around both active and inactive host stars, and small planets in wide orbits (i.e. tidally weakly interacting planets) are found mainly around inactive stars. In our Figure 2.6 this would manifest itself as a population of systems that fill the plot in a triangular shape to the lower left, i.e. the upper right of the plot would be devoid of systems. Conversely, for Figures 2.7 and 2.8 the sample should fill the lower right part of the plot in a triangular shape, meaning that only small, far-out planets around active stars are underrepresented.

However, we see that the strongly interacting planets, i.e. the Hot Jupiters, are actually not found around stars that have any arbitrary activity level in relation to their stellar companion but are primarily found around host stars that tend to be as active or more active than their companion stars. In a more quantitative manner, out of the eight Hot-Jupiter SP systems in our final sample, we find that 75% of them orbit host stars that have

an excess in coronal activity, while the remaining 25% are found around host stars with no significant activity excess.[§§] Therefore, we argue that the observed relation is indeed a signpost of star-planet interaction, and not due to activity biases in exoplanet detections.

One surprising feature of our sample is the fact that host stars of small, far-out planets seem to be on average *less* active than their companion stars, even after we have corrected for spectral type differences (i.e. the lower right corner in Figure 2.6). This trend can be explained by the different main-sequence lifetimes of F to M stars. Several of those low-tidal interaction host stars are of spectral type F/G, while the companion star is of spectral type M (codified by symbol colors and shapes in Figures 2.6, 2.7, and 2.8). For old and inactive F/G stars, where those low-tidal interaction planets are more easily detected, the system age may already be close to the main-sequence lifetime of the primary. However, the secondary M dwarf will not yet be at the end of its main-sequence lifetime. In terms of those two stars' position in the X-ray luminosity functions for their spectral type, the F/G star will be at the faintest end of the luminosity function, while the M dwarf will not have moved fully to the faint end of the M dwarf luminosity function yet. This will cause a net negative activity level difference.

Two of the most inactive systems are HD 190360 and HD 188015 (HD 75289 is discussed separately). The primary components of the two systems are G-dwarfs, while the secondaries are M-dwarfs. Also, both systems seem to be older than the solar age. [Tak+07] estimated the age of HD 190360 and HD 188015 to be 13.4 and 6.2 Gyr, respectively.

We point out that there are also a number of F/G planet host stars with M dwarf secondaries in the high-tidal interaction part of the sample (i.e. at the upper left corner in Figure 2.6). Yet there, the primaries are found to be more active than the secondaries. Therefore we are confident that it is not spectral type differences that are driving the trends in our sample. We also point out that our sample does not allow us to test for different behaviors among stars with a convective versus a radiative envelope, as was done by [Alb+12] and [Win+10]. Our sample does not contain host stars with masses above $1.2 M_{\odot}$, therefore the different tidal efficiencies of model 1 cannot be tested observationally here.

2.4.2.1 The low-activity outlier HD 75289

One strong outlier from the trend established by the other systems is the system HD 75289, which is an F9 star hosting a Hot Jupiter and having an M dwarf companion. The host star is very inactive compared to the lower-mass stellar companion, and we did not find evidence of a flare happening on the M dwarf during the X-ray observations. In fact, the X-ray luminosity of the primary is within the lowest 1% for F/G-dwarfs, while the M-dwarf companion has an average field star luminosity value.

[Tak+07] estimated the age of the system to be 3.28 Gyrs, making this system younger than the Sun. The rotational period of the primary has been measured from the chromospheric activity level and radial velocity to be ca. 16 days [Udr+00], see Table 2.6. When comparing the rotation and X-ray luminosity of the primary to the sample of field stars studied for the rotation-activity relationship by [Piz+03], we find that this star's activity

[§§]Here, we define Hot Jupiters to be planets with an orbital period less than 10 days and a mass higher than $0.25 M_{Jup}$ [DJ18]. The Hot Jupiters in our sample are then: CoRoT-2 A, HAT-P-20 A, HD 75289 A, HD 189733 A, υ Andromedae A, WASP-8 A, WASP-77 A, and XO-2 N; the planet orbiting HD 109749 A may have a mass lower than the given hot-Jupiter limit, considering its mass uncertainty.

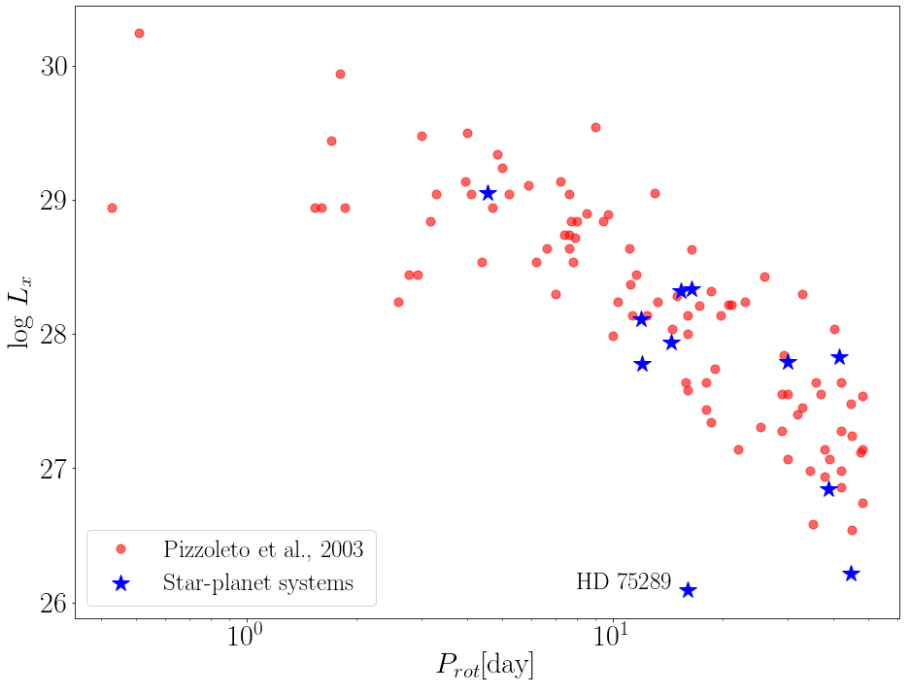

Figure 2.9: Shown is the field-star sample from [Piz+03] together with planet-hosting stars from our analysis that had their rotational period estimated in the literature. Since the field-star sample was observed with the ROSAT space telescope, the conversion between the two relevant energy bands given by the Equation 2.3 was also applied here.

is extremely low for its rotational state (see Figure 2.9). We speculate that this star may be undergoing a low-activity phase in a magnetic cycle, or possibly be in a Maunder minimum state [Edd76].

2.4.3 Tidal or magnetic star-planet interaction?

Assuming that massive planets, as the jovian planets in the Solar system, have magnetic fields, being close to their host stars may induce magnetic interaction in addition to tidal interaction. It is therefore imaginable that the activity discrepancy we observe in our binary sample is, to some part, induced by this interaction. The rotation-activity relationship of field stars has been explored in X-rays by many studies [Pal+81; Piz+03; Wri+11]. We have chosen to show the field stars sample from [Piz+03] in Figure 2.9.

We show the planet-hosting stars from our sample, for which rotation periods are known and the X-ray luminosity has been measured here, in addition to the Pizzolato sample. With the exception of HD 75289 which was discussed above, the host stars do not deviate significantly from the relationship seen in regular field stars. This means that the rotation and activity are in lockstep for our planet-hosting stars. If short-term magnetic star-planet interaction was a strong effect in our sample, we would expect the stars to have elevated activity while their rotation remains unchanged. As this is not the case, we argue that short-term magnetic star-planet interaction does not play a major role in our sample.

However, also the existence of long-term magnetic star-planet interaction has been proposed [Coh+10; Str+14]. In such a scenario, the magnetic interaction between the

star and the planet can modify the stellar wind properties. In particular, the angular momentum loss due to the stellar wind might be decreased and the star retains a higher rotation rate and therefore a higher activity level. This scenario is not excluded by our considerations here, since then both activity and rotation could be changed over the stellar lifetime. One argument against this scenario is however that the systems in which the strongest magnetic interaction is expected, namely the Hot Jupiter systems, may have weak magnetic fields of the exoplanets. This was posited by [Gri+04b] due to the tidal locking of exoplanet spin to their orbital period. In the case of a weak or non-existent planet magnetosphere, the long-term magnetic star-planet interaction is less effective than the tidal star-planet interaction we assume here.

2.4.4 Possible Caveats

One phenomenon that we were not able to take explicitly into account is potential stellar magnetic activity cycles. It is observed that stars, when going through activity cycles, can also exhibit variation in their X-ray luminosity [RSF12]. At first glance, this may be viewed as an issue, but it is statistically unlikely that all the stars showing a higher activity level are in their maximum of the activity cycle while their companions experience an activity minimum. The same can be assumed in the opposite case, where the host stars of small and/or further out planets would have a low activity level due to an activity minimum.

One other magnetic phenomenon that may increase the X-ray luminosity of a star is flares. For systems observed with the Chandra space observatory, we were not able to properly investigate the X-ray light curves for flaring events due to the low number of counts over time[¶¶]. Here, the possibility exists that these planet-hosting stars appear more active because a flare occurred during the observation time. However, it is again unlikely that in the higher activity level regime, all planet hosts experienced a flaring event, while in systems in the lower-activity level regime the planet host companions experienced flares that made them appear more active.

Therefore, we assume that the activity cycles and possible undetected flaring events add to the scatter we see in our activity-tidal interaction strength figures; however, they do not produce the correlation we see.

2.5 Conclusion

As can be seen from the result figures and the Spearman's rank correlation factors, for all three star-planet interaction models there is a strong correlation between the SPI strength parameter and the activity level difference for a given star-planet system residing in a binary system. If we examine more closely emerging correlation, we see that in systems where a massive planet has a tight orbit, the planet-hosting star tends to be more active, i.e. have a hotter corona. If we assume that the activity level difference between the stellar components of a system is not correlated with the tidal interaction strength, we would have star-planet systems where an inactive host is orbited by a close-in massive planet. That would indicate that for a similar tidal interaction strength, we would have

[¶¶]Systems HD 189733 and CoRoT-2 were analysed in more detail by [PSW13] and [Sch+11], respectively, and no flaring events were detected

planet-hosting stars that range from very active (positive percentile difference) to very inactive (negative percentile difference) when compared to its stellar companion's activity level. This would indicate, that the planet does not influence the behavior of its host in any way. Since in our case the low activity-high interaction regime is scarcely populated, tidal star-planet interaction can be efficient in altering the stellar spin evolution and therefore altering its activity level.

Acknowledgements

The authors thank Judy Chebly for discussions on optical data of some of the sample stars. Parts of this work were supported by the German *Leibniz-Gemeinschaft* under project number P67/2018. The scientific results reported in this article are based in part on observations made by the Chandra X-ray Observatory and the X-ray Multi-Mirror Observatory XMM-Newton. This research made use of Astropy, a community-developed core Python package for Astronomy [Ast+13; Ast+18]. This work has made use of data from the European Space Agency (ESA) mission *Gaia* (https://www.cosmos.esa.int/gaia), processed by the *Gaia* Data Processing and Analysis Consortium (DPAC, https://www.cosmos.esa.int/web/gaia/dpac/consortium). Funding for the DPAC has been provided by national institutions, in particular the institutions participating in the *Gaia* Multilateral Agreement.

Data availability

The data in this article are available from the XMM-Newton Science Archive (https://www.cosmos.esa.int/web/xmm-newton/xsa) with the observation IDs as given in Table 2.1 and from the Chandra X-ray Center (https://cxc.cfa.harvard.edu/) with the observation IDs as given in the Table 2.3. The data products generated from the raw data are available upon request from the author.

2.6 Appendix

2.6.1 Notes on individual systems

16 Cyg: This is a hierarchical triple star system, where the AC components form a close binary and the B component is the planet host. There are two observations of this system with XMM-Newton (obsID: 0551021701 and 0823050101). The former observation has a short exposure time and yields only weak or no detection of the components. The latter observation yields two detections where the radiation hardness ratio of the planet host and the unresolved binary system was estimated, therefore we used only this observation for the primary estimate of the X-ray luminosity of the components given in Table 2.2. This system was also observed with Chandra's ACIS-I instrument. Here, the three components are resolved, but the planet host is undetected. We used the Chandra observation for the estimate of the percentile difference between the stellar components since the XMM observations yielded the AC pair as unresolved. The angular separation

between the planet host and the binary system is $\rho = 40.0$", while the separation between the components of the binary is $\rho \approx 3.5$".

30 Ari (HD 16246): The system is a hierarchical triple system (possible quadruple [Rob+15]). The planet host is the B component, which has the C component in close orbit. The angular separation between the components B and C is $\rho = 0.536$", which makes them unresolved in the XMM-Newton observation. The C component is an M1-3 spectral type star with an orbital period of $P \leq 95$ yr [Kan+15]. The angular separation between the components A and B is $\rho = 37.9$" [Mug19]. The system was detected in all three EPIC detectors as two bright X-ray sources.

55 Cnc (HD 75732): Both components of the system were detected in all three EPIC detectors, but the hardness ratio of the radiation detected from the second component could not be estimated. A coronal temperature of $\log_{10} T = 6.477$ was employed to estimate the X-ray luminosity of the secondary. The system was also observed with Chandra, but only the primary component was in the FoV. The angular separation between the two components is $\rho = 85.0$".

83 Leo (HD 99491 and HD 99492): Here, the secondary component is the planet host. Both components are detected in all three EPIC detectors: the primary is a bright and the secondary a faint X-ray source. The angular separation between the components is $\rho = 28.0$".

AS 205: The two components are unresolved in both XMM-Newton and Chandra observations, at an angular separation of $\rho = 1.3$". In XMM-Newton observation, the system was detected in all three EPIC detectors, but the radiation hardness ratio could not be estimated. In Chandra's observation, the system was detected with an HR estimate.

CoRoT-2: This system was observed with Chandra's ACIS-S instrument. The primary component was detected, while the secondary was not. Therefore, we estimated the 2σ upper limit of the X-ray luminosity of the secondary. The angular separation between the components is ≈ 4". Since this system was the topic of research in [Sch+11] where the observed X-ray spectrum was used to characterise the primary component, we used their published X-ray flux value of CoRoT-2 A for further analysis.

GJ 15 (HD 1326): This system was observed with XMM-Newton and has two bright X-ray sources. The primary component has a flaring event with a duration of $\approx$ 3ks. We excluded this time interval from our calculation of the primary component's X-ray luminosity. The angular separation between the components is $\rho = 34.4$".

HAT-P-16: This system is a hierarchical triplet, where the planet host has a close unresolved companion and the C component is at an angular separation of $\rho = 23.3$". There are two observations of this system with XMM-Newton (obsID: 0800733701 and 0800733101). The latter observation had a high background signal rendering the components undetected when combining the observations. Using only the former observation, we had a detection although without the hardness ratio of the radiation. Nevertheless, we were able to calculate the source flux, by assuming a coronal temperature of $\log_{10} T = 6.477$.

HAT-P-20: This system was observed with Chandra's ACIS-S instrument. Both components were detected, but the secondary had no HR estimate. The angular separation between the components is $\rho \approx 7$".

HAT-P-22 (HD 233731): This system was observed by the Chandra Space Observatory. It was not the main target and it was positioned at an off-axis angle of $\approx 4'$. Therefore, we used a somewhat larger source extraction region of $\approx$ 4.5". Both companions are

undetected, therefore the system was not used for further analysis. The angular separation between the components is ≈ 9".

HATS-65: This system was observed with Chandra's ACIS-I instrument. Its position was projected at an off-axis angle of ≈ 10′, which employed us to use a source extraction region with a radius of 10" to collect most of the photon events coming from this system. The angular separation between the components is ≈ 5", which renders this system unresolved. It was also undetected, therefore, we only give the 2σ upper limit for the X-ray luminosity of this system as one source.

HD 27442: This system has two observations with XMM-Newton (obsID: 0780510501 and 0551021401). The primary was detected in both observations, but only the obs no. 0780510501 yields a radiation hardness ratio. The secondary component was detected in the former observation with no HR estimate and in the latter observation, no detection was made. We combined the observations of both the primary and the secondary for a better estimate of the SNR. For the primary, we were able to calculate the HR, but we were not able to calculate a radiation hardness ratio for the secondary. We, therefore, assumed a coronal temperature of $\log_{10} T = 6.477$ for this component. The latter observation also yields a large background signal. The angular separation between the components is $\rho = 13$" and the source extraction region of both components is ≈ 10". We, therefore, could not avoid an overlap between the extraction regions of the two components. This system, however, consists of two evolved stars [But+01; MNM07] and is, therefore, excluded from further analysis.

HD 46375: The system was observed with XMM-Newton, in all three EPIC detectors, as unresolved as the components are at an angular separation of $\rho = 10.4$". It was also observed and detected by Chandra's ACIS-S instrument, where the system appeared as resolved.

HD 75289: This system has two observations with XMM-Newton. The primary component was not detected in both observation runs therefore, we combined them to achieve a better SNR. With the combined observation, we detected the primary component, but no hardness ratio estimate was possible and a coronal temperature of $\log_{10} T = 6.477$ was assumed. The secondary component was detected in both observation runs, but we were able to calculate the radiation hardness ratio for the detection in observation no. 0722030301. For the second component in observation no. 0304200501, we assumed the same HR as in the previous observation and calculated the X-ray luminosity. The angular separation between the components is $\rho = 34.3$".

HD 96167: This system was observed with Chandra's ACIS-I instrument but was not the main target of the observation. It is positioned ≈ 8.5′ from the optical axis. Since the angular separation between the components is ≈ 5.8", we set the source extraction region to encompasses both components and collect most of the photon events that come from the system. The primary component is the planet host and also an evolved stellar object [FV05; Pee+09]. Therefore, we disregard this system from further analysis and give only the X-ray luminosity estimate for the unresolved system.

HD 101930: The primary component was inside the FoV of all three EPIC detectors, whereas the secondary was only in the FoV of pn (in MOS1 and MOS2, the secondary was on the chip edge). Neither component was detected, therefore we estimated an upper limit to their X-ray luminosity assuming a coronal temperature of $\log_{10} T = 6.477$ for both stars. The angular separation between the components is $\rho = 73.0$".

HD 107148: The system was observed with XMM-Newton (all three EPIC detectors) and

Chandra X-ray observatory. The observation with XMM-Newton has a high background noise after approx. 26 ks of exposure time (the exposure time was 41 ks). We, therefore, used the shorter good time interval, where the detector experienced a low background signal. The primary component was detected, but with no hardness ratio estimate. The secondary component was not detected. We assumed for both components a coronal temperature of $\log_{10} T = 6.477$ to estimate their X-ray luminosity. In the Chandra observation, the primary was detected, while the secondary was not. The secondary component is a white dwarf [MD16]. The angular separation between the components is $\rho = 35.0$".

HD 109749: This system was detected by the Chandra ACIS-S instrument. The angular separation of the components is $\rho \approx 8.4$".

HD 178911: This system was observed by Chandras ACIS-I instrument. It is a hierarchical triple star system. The resolved component is the planet host. Since both the unresolved binary system and the planet host were detected, we estimated the X-ray luminosity of the two components in the unresolved system. The binary is a G1-K1 pair [Tok+00], therefore, we used the ratio of the expected X-ray luminosity of stellar corona for these spectral types and applied it to the luminosity we measured for the binary system. With this approach, we were able to use this system for further analysis. The angular separation between the planet host and the unresolved binary is $\rho \approx 16$". For Spearman's rank correlation calculation, we only used the percentile difference and tidal interaction strength parameters calculated for the AB pair.

HD 185269: This system was observed with Chandra's ACIS-S instrument. The primary component, and the planet host of this system, is an evolved stellar object [Joh+06], while the secondary component is an unresolved binary system Bab [Gin+16]. Although both components are marked as detected, this system was not used for further analysis. The angular separation between the projections of the components is $\rho \approx 4.5'$.

HD 188015: This system was observed with the ACIS-S instrument onboard the Chandra space observatory. Both components were detected. The angular separation between the components of this system is $\rho \approx 13$".

HD 189733: This system was observed with Chandra's ACIS-S instrument. Both components were detected. The angular separation between the components is $\rho \approx 11.5$".

HD 190360: The system was observed in two XMM-Newton observations. The primary is a weak X-ray source with no detection in the soft and hard bands. Therefore, we combined the two observations of the primary for a better SNR and set the coronal temperature to $\log_{10} T = 6.477$ to estimate its X-ray luminosity. The secondary displayed a prominent stellar flare in observation no. 0304201101(obsID), and we, therefore, calculated its X-ray luminosity from the signal collected in the quiescent observation 0304202601(obsID).

HD 197037: This system was observed by Chandra, with the ACIS-I instrument. The system projection on the instrument was at an off-axis angle of $\approx 9'$. The angular separation between the components is ≈ 3.5". Therefore, we chose a larger source extraction region that encompasses both components ($r_{extraction} \approx 10$"), which gave us an estimate of the X-ray luminosity of the unresolved system.

HIP 116454: This system was observed by Chandra but was not the main target of the observation. The projected position of this system on the sky had an off-axis angle of $\approx 18'$ putting it on the edge of Chandra's FoV. Since the spatial resolution deteriorates significantly with increasing off-axis angle, the image of the system appears extended

and unresolved. Therefore, we chose an extraction region that encompasses both sources. The extraction region radius is ≈ 22", while the projected angular separation between the components is $\rho = 8.4$". Still, the system was marked as undetected by the ACIS-S camera. Apart from being unresolved, the stellar companion of the planet-hosting star has evolved from the main sequence [Mug19; Van+15], therefore, we disregarded this system from further analysis.

Kepler-444: This system was observed with the Chandra space observatory. It is a hierarchical triple star system [Cam+15], where the secondary component is a spatially unresolved pair of M dwarfs. The projected separation of the A and the BC components is $\rho = 1.8$" ($\approx 70AU$), making this system the most tightly bound in our sample. Neither of the components was detected, therefore we calculated the upper limits to their X-ray luminosities.

Kepler-1008: The two components of this system were observed with the MOS2 and pn detectors (their coordinates on MOS1 were outside the FoV) but were not detected. We estimated an upper limit to their X-ray luminosity. They are at an angular separation of $\rho = 13.4$" from each other.

υ And (HD 9826): This system was observed with XMM-Newton (all three EPIC detectors) and Chandra X-ray observatory. The XMM-Newton observation shows the primary as a bright X-ray source. For the second component, we assumed a coronal temperature of $\log_{10} T = 6.477$ as the estimation of the radiation hardness ratio was not possible. In the Chandra observations, only the primary was in the FoV and was detected. The angular separation between the components is $\rho = 55.6$".

WASP-8: This system was observed by Chandra with ACIS-S. The primary was detected, while the secondary component was not. The projected angular separation between the components is $\rho = 4.5$".

WASP-18: Both components were in the FoV of all three EPIC detectors but were not detected. Therefore, we estimated an upper limit to their X-ray luminosity. This system was also observed with Chandra: the primary component was again not detected, while the secondary component was projected between the ACIS-I chip array and was discarded from our analysis. The angular separation between the components is $\rho = 26.7$".

WASP-33: This system was observed with the XMM-Newton telescope. It is a possible hierarchical triple star system [Mug19]. The primary component is the planet host and has a close unresolved companion at $\rho = 2$". The wider companion is at an angular separation of $\rho = 49.0$". The wide companion was in the FoV of the pn detector, while the unresolved binary was in the FoV of MOS1 and pn. The secondary component was detected and we calculated its X-ray luminosity, while the unresolved binary was undetected and only an upper limit to its X-ray luminosity was estimated.

WASP-77: This system was observed with the Chandra space observatory and the ACIS-S instrument. The two components of this system are at the angular separation of $\rho = 3.3$". The primary component was detected, while for the secondary component we estimated an upper limit for the X-ray flux and luminosity, assuming a coronal temperature of $\log_{10} T = 6.477$.

XO-2: The system has two observations with XMM-Newton. Both components were detected in both observations (obsID: 0728970101 and 0728970201), but a radiation hardness ratio could not be estimated in each separate case. We, therefore, combined the appropriate observations to achieve a better SNR, but we were not able the calculate a hardness ratio. The coronal temperature of $\log_{10} T = 6.477$ was assumed for both

components to calculate their X-ray luminosity. The angular separation between the components is $\rho = 31.0$". Here, both stars are of the same spectral type and have planets: XO-2 N hosts a planet with $M_{pl} \approx 0.6 M_{Jup}$ at $a \approx 0.04 AU$, whereas XO-2 S has a $0.26 M_{Jup}$ planet at a distance of a = 0.13 AU. The XO-2 S star hosts a less massive, wider-orbiting planet and it can be expected that it does not exhibit a strong tidal pull onto its host star when compared to the XO-2 N system.

2.6.2 Photon count conversion factors and Gaia parameters

In Table 2.9 are given the photon count conversion factors for each observation and camera taken with the XMM-Newton space observatory. In Table 2.10 are given the conversion factors for the given observation cycle and CCD chip of the Chandra observatory. The photon count conversion factor was estimated with the WebPimms online tool and by calculating the radiation hardness ratio HR. If the source was not detected in the soft or hard passband, a coronal temperature of $\log_{10} T = 6.477$ was assumed (see Section 2.2.1.4 for more details). Table 2.11 shows the Gaia parameters used for stellar mass estimation of stars in our final sample.

Table 2.9: The photon count conversion factors given in this table are calculated using the online tool WebPimms for observations made with the XMM-Newton space telescope. The conversion factor translating the photon counts detected with the MOS cameras into the X-ray flux has the same value for both MOS1 and MOS2.

system	obs ID	component	detection	HR	*c*(MOS)	*c*(pn)
16 Cyg	0823050101	AC	BRIGHT	-0.466	9.326602e-12	1.045563e-12
		B*	BRIGHT	-0.460	9.284336e-12	1.044785e-12
30 Ari	0075940101	A	BRIGHT	-0.068	6.159409e-12	1.073431e-12
		B*C	BRIGHT	0.111	6.047903e-12	1.096918e-12
55 Cnc	0551020801	A*	FAINT	-0.307	9.084168e-12	1.634601e-12
		B	FAINT/NO HR	/	9.084076e-12	1.634588e-12
83 Leo	0551021201	A	FAINT	-0.497	1.035328e-11	1.803968e-12
		B*	BRIGHT	-0.056	8.384539e-12	1.585091e-12
AS 205	0602730101	A*B	FAINT/NO HR	/	6.510630e-12	1.041020e-12
GJ 15	0801400301	A*	BRIGHT	-0.468	6.622050e-12	1.045839e-12
		B	DETECTED	-0.608	7.080730e-12	1.064492e-12
HAT-P-16	0800733101	A*B	NOT DETECTED	/	5.942612e-12	9.378096e-13
		C	NOT DETECTED	/	5.942612e-12	9.378096e-13
	0800730701	A*B	FAINT/NO HR	/	5.942612e-12	9.378096e-13
		C	FAINT/NO HR	/	5.942612e-12	9.378096e-13
HD 27442	0780510501	A*	FAINT	-0.676	7.328724e-12	1.073849e-12
		B	FAINT/NO HR	/	6.510630e-12	1.041020e-12
	0551021401	A*	FAINT/NO HR	-0.676	1.193506e-11	2.000616e-12
		B	NOT DETECTED	/	9.084076e-12	1.634588e-12
HD 46375	0304202501	A*B	FAINT	-0.561	6.920167e-12	1.058170e-12
HD 75289	0304200501	A*	FAINT/NO HR	/	6.510630e-12	1.041020e-12
		B	FAINT	-0.300	6.310412e-12	1.044406e-12
	0722030301	A*	NOT DETECTED	/	6.510630e-12	1.041020e-12
		B	FAINT	-0.300	6.310441e-12	1.044401e-12
HD 101930	0555690301	A*	NOT DETECTED	/	5.942612e-12	9.378096e-13
		B	NOT DETECTED	/	/	9.378096e-13
HD 107148	0693010401	A*	FAINT/NO HR	/	5.942612e-12	9.378096e-13
		B	FAINT/NO HR	/	5.942612e-12	9.378096e-13
HD 190360	0304201101	A*	NOT DETECTED	/	6.510630e-12	1.041020e-12
	0304202601	A*	FAINT/NO HR	/	6.510630e-12	1.041020e-12
		B	FAINT	-0.449	/	1.043299e-12
Kepler-1008	0550451901	A*	NOT DETECTED	/	6.510630e-12	1.041020e-12
		B	NOT DETECTED	/	6.510630e-12	1.041020e-12
υ And	0722030101	A*	BRIGHT	-0.359	9.400024e-12	1.677780e-12
		B	FAINT/NO HR	/	9.084076e-12	1.634588e-12
WASP-18	0673740101	A*	NOT DETECTED	/	6.510630e-12	1.041020e-12
		B	NOT DETECTED	/	6.510630e-12	1.041020e-12
WASP-33	0785120201	A*B	NOT DETECTED	/	5.942612e-12	9.378096e-13
		C	FAINT	0.116	/	1.042992e-12
XO-2	0728970101	S*	FAINT/NO HR	/	6.510630e-12	1.041020e-12
		N*	FAINT/NO HR	/	6.510630e-12	1.041020e-12
	0728970201	S*	FAINT/NO HR	/	6.510630e-12	1.041020e-12
		N*	FAINT/NO HR	/	6.510630e-12	1.041020e-12

Table 2.10: Given are the photon count conversion factors that are used to calculate the X-ray flux of stars observed with the Chandra space observatory.

system	obsID	component	detection	HR	c
16 Cyg	16647	B*	NOT DETECTED	/	3.141789e-11
		A	FAINT	0.863	1.422014e-11
		C	FAINT/NO HR	/	3.141789e-11
	18756	B*	NOT DETECTED	/	3.141789e-11
		A	FAINT	0.863	1.422014e-11
		C	FAINT/NO HR	/	3.141789e-11
55 Cnc	14401	A*	FAINT	-0.865	7.527662e-12
	14402	A*	FAINT	-0.865	7.527662e-12
AS 205	16327	A*B	FAINT	0.918	4.080275e-12
CoRoT-2	10989	B	NOT DETECTED	/	1.141643e-11
HAT-P-20	15711	A*	FAINT	0.618	5.385769e-12
		B	FAINT/NO HR	/	7.340064e-12
HAT-P-22	15105	A*	NOT DETECTED	/	2.096742e-11
		B	NOT DETECTED	/	2.096742e-11
HATS-65	3282	A*B	NOT DETECTED	/	9.127872e-12
	9382	A*B	NOT DETECTED	/	1.787365e-11
HIP116454	19517	A*B	NOT DETECTED	/	5.099088e-11
HD 46375	15719	A*	FAINT	-0.177	8.042113e-12
		B	FAINT	-0.336	8.633701e-12
HD 96167	5817	A*B	FAINT/NO HR	/	1.563648e-11
HD 107148	13665	A*	FAINT	-0.213	5.851814e-12
		B	NOT DETECTED	/	5.552321e-12
HD 109749	15720	A*	FAINT	-0.333	8.621279e-12
		B	FAINT	0.252	6.533847e-12
HD 178911	13659	B*	FAINT	-0.155	5.720604e-12
		AC	FAINT	0.171	5.066729e-12
HD 185269	15721	A*	FAINT	-0.277	8.414531e-12
		Bab	FAINT	0.126	6.927864e-12
HD 188015	13667	A*	FAINT	-0.175	5.765516e-12
		B	FAINT/NO HR	/	5.552321e-12
HD 189733	12340	A	BRIGHT	0.258	4.854420e-12
		B	BRIGHT	0.187	4.978932e-12
	12341	A	BRIGHT	0.258	4.854420e-12
		B	BRIGHT	0.187	4.978932e-12
	12342	A	BRIGHT	0.258	4.854420e-12
		B	BRIGHT	0.187	4.978932e-12
	12343	A	BRIGHT	0.258	4.854420-12
		B	BRIGHT	0.187	4.978932e-12
	12344	A	BRIGHT	0.258	4.854420e-12
		B	BRIGHT	0.187	4.978932e-12
	12345	A	BRIGHT	0.258	4.854420e-12
		B	BRIGHT	0.187	4.978932e-12
HD 197037	7444	A*B	FAINT	0.378	1.401012e-11
	8598	A*B	FAINT	0.378	1.401012e-11
	9770	A*B	FAINT	0.378	1.401012e-11
	9771	A*B	FAINT	0.378	1.401012e-11
Kepler-444	17733	A*BC	FAINT/NO HR	/	1.203499e-11
	20066	A*BC	FAINT/NO HR	/	1.203499e-11
υ And	10976	A*	BRIGHT	-0.171	4.704921e-12
	10977	A*	BRIGHT	-0.171	4.704921e-12
	10978	A*	BRIGHT	-0.171	4.704921e-12
	10979	A*	BRIGHT	-0.171	4.704921e-12
WASP-8	15712	A*	FAINT	0.210	5.046927e-12
		B	NOT DETECTED	/	5.608443e-12
WASP-18	14566	A*	NOT DETECTED	/	2.096742e-11
WASP-77	15709	A*	FAINT	0.363	6.185815e-12
		B	NOT DETECTED	/	7.340064e-12

Table 2.11: Given are the (corrected) Gaia apparent magnitude, the $G - R_p$ color, the calculated Gaia absolute magnitude, and the renormalised unit weight error (RUWE) for each star of our final sample. The uncertainties given for the color and absolute magnitude were calculated via the error propagation function and are relevant for the estimation of the stellar evolutionary status: on the MS or evolved. The stars which do not have their magnitudes, color, and RUWE given here did not pass some of the quality assessment and their spectral type/mass was acquired from the literature as given in Table 2.5.

system	comp	G	G corr	$G - R_p$	r[pc]	M_G	RUWE
16 Cyg	B*	6.0568	6.0566	0.4709 ± 0.0019	21.139 ± 0.015	4.4311 ± 0.0012	0.9414
	A	/	/	/	/	/	/
	C	/	/	/	/	/	/
55 Cnc	A*	5.7144	5.7297	0.6331 ± 0.0028	12.586 ± 0.012	5.5841 ± 0.0250	0.9865
	B	11.6798	11.6617	1.2495 ± 0.0016	12.477 ± 0.017	11.1817 ± 0.0032	1.3065
CoRoT-2	A*	12.2489	12.2289	0.55659 ± 0.0009	213.283 ± 2.457	5.2304 ± 0.0022	0.8829
	B	15.4750	15.4447	1.1001 ± 0.0056	202.929 ± 2.623	8.9080 ± 0.0281	1.2250
GJ 15	A*	7.2162	7.2123	1.0340 ± 0.0013	3.562 ± 0.001	9.4537 ± 0.0006	0.9172
	B	9.6774	9.6656	1.2051 ± 0.0011	3.561 ± 0.001	11.9077 ± 0.0008	1.0262
HAT-P-20	A*	10.9903	10.9743	0.7556 ± 0.0018	71.037 ± 0.199	6.7169 ± 0.0061	1.0556
	B	/	/	/	/	/	/
HD 46375	A*	7.6953	7.6899	0.5607 ± 0.0020	29.553 ± 0.038	5.3369 ± 0.0028	0.8831
	B	11.2088	11.1921	1.0539 ± 0.0029	29.680 ± 0.059	8.8298 ± 0.0045	1.1117
HD 75289	A*	6.2052	6.2046	0.4120 ± 0.0024	29.116 ± 0.024	3.8839 ± 0.0018	0.8880
	B	/	/	/	/	/	/
HD 109749	A*	8.0245	8.0181	0.4655 ± 0.0017	63.082 ± 0.295	4.0185 ± 0.0102	1.0052
	B	/	/	/	/	/	/
HD 178911	B*	7.8670	7.8611	0.5072 ± 0.0012	40.973 ± 0.046	4.7986 ± 0.0025	0.9443
	A	/	/	/	/	/	/
	C	/	/	/	/	/	/
HD 188015	A*	8.0659	8.0593	0.4897 ± 0.0013	50.671 ± 0.109	4.5355 ± 0.0047	1.0189
	B	15.4531	15.4229	1.2922 ± 0.0040	50.268 ± 0.167	11.9164 ± 0.0074	1.0643
HD 189733	A*	7.4143	7.4098	0.6063 ± 0.0020	19.764 ± 0.013	5.9304 ± 0.0014	0.9279
	B	13.2055	13.1825	1.2572 ± 0.0024	19.711 ± 0.019	11.7089 ± 0.0022	1.1842
HD 190360	A*	5.5336	5.5543	0.5000 ± 0.0029	16.007 ± 0.016	4.5328 ± 0.0024	0.8292
	B	12.7967	12.7750	1.3046 ± 0.0028	15.97 ± 0.015	11.7584 ± 0.0021	1.1162
υ And	A*	3.8985	3.9869	0.3503 ± 0.0081	13.405 ± 0.063	3.3505 ± 0.0121	0.8432
	B	12.5126	12.4918	1.2710 ± 0.0021	13.471 ± 0.016	11.8449 ± 0.0027	1.1438
WASP-8	A*	9.6125	9.6009	0.5074 ± 0.0020	89.961 ± 0.363	4.8307 ± 0.0088	1.0193
	B	13.6980	13.6733	1.1191 ± 0.0081	90.468 ± 0.364	8.8909 ± 0.0088	1.2506
WASP-77	A*	10.0966	10.0835	0.5110 ± 0.0029	105.166 ± 1.196	4.9741 ± 0.0247	1.1304
	B	/	/	/	/	/	/
XO-2	S*	10.9278	10.9121	0.5567 ± 0.0009	151.398 ± 0.95	5.0115 ± 0.0136	0.9168
	N*	10.9718	10.9559	0.5688 ± 0.0013	154.273 ± 1.446	5.0145 ± 0.0203	0.9437

3 The first evidence of tidally induced activity in a brown dwarf-M dwarf pair: A Chandra study of the NLTT 41135/41136 system

Nikoleta Ilić, Katja Poppenhaeger, Desmond Dsouza, Scott J. Wolk, Marcel A. Agüeros, Beate Stelzer

Monthly Notices of the Royal Astronomical Society, Volume 524, Issue 4 (2023)
DOI: 10.1093/mnras/stad2277

Abstract

The magnetic activity of low-mass stars changes as they age. The primary process decreasing the stellar activity level is the angular momentum loss via magnetized stellar wind. However, processes like tidal interactions between stars and their close companions may slow down the braking effect and the subsequent decrease of the activity level. Until now, the tidal impact of substellar objects like brown dwarfs on the evolution of their central stars has not been quantified. Here, we analyse the X-ray properties of NLTT 41135, an M dwarf tightly orbited by a brown dwarf, to determine the impact of tidal interactions between them. We find that NLTT 41135 is more than an order of magnitude brighter in the X-ray regime than its stellar companion NLTT 41136, also an M dwarf star, with whom it forms a wide binary system. To characterize the typical intrinsic activity scatter between coeval M dwarf stars, we analyse a control sample of 25 M dwarf wide binary systems, observed with XMM-Newton and Chandra telescopes and the eROSITA instrument onboard the Spectrum Röntgen Gamma satellite. The activity difference in the NLTT 41135/41136 system is a 3.44σ outlier compared to the intrinsic activity scatter of the control systems. Therefore, the most convincing explanation for the observed activity discrepancy is tidal interactions between the M dwarf and its brown dwarf. This shows that tidal interactions between a star and a substellar companion can moderately alter the expected angular-momentum evolution of the star, making standard observational proxies for its age, such as X-ray emission, unreliable.

3.1 Introduction

Stellar magnetic activity - the collective name for magnetic phenomena of low-mass, main sequence stars* such as coronal X-ray emission, star spots, flares, etc., - is ultimately driven by stellar rotation through the dynamo process. In general, the rotational evolution of a star is determined by its initial spin, its pre-main-sequence contraction rate, and the efficiency of magnetic wind.

The magnetized stellar wind is particularly important, as it carries away angular momentum from the star. This process, called magnetic braking, slows down the rotation

*Mainly stars with an outer convective layer and masses below 1.2 $M_\odot$.

rate of cool stars over timescales of Gyr and weakens the aforementioned magnetic phenomena [BM76; Kra67; Mes68; Sku72; WD67b].

However, if a star has a close-in companion, tidal interactions may alter the stellar rotation and activity evolution described by the spin-down paradigm. This is well-studied for close stellar binaries where the stellar spins are tidally synchronized with the orbital period of the binary. There, the angular momentum loss through stellar winds is replenished from the large angular momentum reservoir of the orbital motion of the two stars [Hut81; Ter+98; Zah77]. Consequently, close binaries are commonly observed to be highly active even when their ages reach Gyr [Yak+09].

Whether substellar close-in companions are able to alter the rotational evolution of a star has been a long-standing question. The so-called Hot Jupiters - close-in massive exoplanets - are the usual suspects in this regard, and many studies have employed different methods to find indications that stars hosting these planets are more active and have a higher spin rate than similar planet-free stars [CSM00; KDS08; Mil+15; MSS15; Pon09; Sch10].

However, obtaining observational confirmation of the increased spin and activity of Hot Jupiter hosts is hard. The main obstacles are the intrinsic variability of stellar magnetic activity [Bal+95; JSA03; RCG17; RSF12], the detection biases against finding exoplanets around magnetically active stars [PRS10; PS11b], as well as a fundamental difficulty in determining ages of single field stars [Lac+99; PE04; Val+15; WS98].

One approach to overcome the problem of the stellar ages has been introduced by [PW14], who used wide binary star systems as a coeval laboratory in which one can test if the activity of the star hosting a potentially tidally interacting body is elevated compared to the coeval companion star. We would expect two stars of very similar masses and with the same age to display similar levels of activity. A clear over-activity of the planet-hosting star would provide an indication that tidal prevention of stellar spin-down is at work. By applying a similar method to a large sample, [IPH22] found that Hot Jupiter-hosting stars can have their activity level elevated by a factor of ≈ 3 in the X-ray regime when compared to their coeval companion.

Although this difference is significant and follows a clear trend between stellar activity and expected tidal interaction strength, it is also known that the usual stellar variability throughout an activity cycle can be of a similar order of magnitude[†] [Ayr14; DDG10; Fav+08; Orl+17]. Applying the method established by [PW14] on a system where one late-type star is orbited by a high-mass sub-stellar companion should yield a more significant result in favor of the tidal-interaction hypothesis. We, therefore, explore a mass regime above Hot Jupiters, but below stellar binaries: brown dwarfs orbiting low-mass stars. Brown dwarfs are typically heavier by a factor of ≈ 30 compared to Jupiters and should have stronger and therefore more definitively measurable tidal effects on their host stars.

For this purpose, we analyse a binary system consisting of two M dwarf stars, the primary NLTT 41136 and secondary NLTT 41135, where the secondary is orbited by a brown dwarf in close orbit. To determine the significance of tidal interactions, we compare the measured activity difference in this system to the activity differences in a control sample of wide binary systems that have stars of similar spectral types. The stellar activity indicator we choose is the X-ray surface flux since it is the best tracer of

[†]For the system HD 189733, which according to [IPH22] shows the highest activity discrepancy between the coeval stars, [Pil+22] have found no indication for the existence of an activity cycle or significant variability of the planet host on the timescales considered in their work.

the average coronal temperature among the usual activity indicators in the X-ray regime and is, therefore, a good representation of the overall coronal activity of a star [JG15].

In Section 3.2, the *Chandra* X-ray observation of the NLTT 41135/41136 system is analysed: we estimate the average coronal temperature, the stellar radius, and calculate the X-ray surface flux. The control sample is introduced in Section 3.3, along with the results of the analysis of the activity difference in these systems and NLTT 41135/41136. Section 3.4 opens the discussion on the activity difference distribution of the control sample and how the activity difference in NLTT 41135/41136 compares to these findings. In Section 3.5, we conclude with a discussion of the significance of the tidal interactions between the M dwarf and the orbiting brown dwarf in NLTT 41135.

3.2 Observations and Analysis of NLTT 41135/41136

3.2.1 The system

NLTT 41135/41136 is a low-mass stellar binary system. It contains two M dwarf stars - NLTT 41136 with spectral type M4V and mass 0.21 M⊙, and NLTT 41135 with spectral type M5V and mass 0.16 M⊙ [Irw+10]. The proper motions of the two stars imply that they form a gravitationally bound and therefore coeval system [Mug19], with an angular separation of 2.3" (≈ 80 AU). The secondary, NLTT 41135, is orbited by a transiting brown dwarf with a mass of 31-34 M_{Jup} and an orbital period of 2.9 days [Irw+10]. By deriving the galactic velocity of the system, [Irw+10] found that it belongs to the old Galactic disk population, suggesting that this system is older than a few Gyr. The spectral type of the brown dwarf is undetermined; however, its mass and the age of the system indicate a spectral type between T6 and T8 [Fil+15; PM13][‡].

The spectroscopic observation of the system yielded the Hα line in emission in the spectrum of NLTT 41135, while in the spectrum of NLTT 41136, there is a hint of absorption at this wavelength [Irw+10]. The authors found this to be consistent with the rapid increase of activity strength in field-age M dwarfs with spectral type around M5 [Wes+04], however, also note that the difference in activity indicated by the Hα line might be due to tidal interactions and subsequent spin-up of the primary by the orbiting brown dwarf.

3.2.2 Chandra observations

We observed the system on two occasions with the imaging detector of the High Resolution Camera (HRC-I) on board the *Chandra* X-ray Observatory. The HRC-I is sensitive to X-ray photons in the energy range from 0.08 to 10 keV but has not the capability of photon energy resolution. The FWHM for this detector is ≈ 0.4", therefore, an extraction region which has a radius larger than ≈ 1" will collect > 90% of the source photons for soft sources[§]. The two observations of NLTT 41135/41136 were taken on September 29th (Obs. ID 23388; PI Poppenhaeger) and October 1st (Obs. ID 26143; PI Poppenhaeger) 2021, both with ≈ 25 ks exposure time.

[‡]We used the mass and age estimate to find the most probable temperature of the brown dwarf using the sample analysed by [Fil+15]; with the temperature estimate, we used the main-sequence parameter table defined by [PM13], which includes parameters of brown dwarfs, to estimate the spectral type.

[§]See Figure 7.5 in Chapter 7 of the 'The *Chandra* Proposers' Observatory Guide', Version 24.0

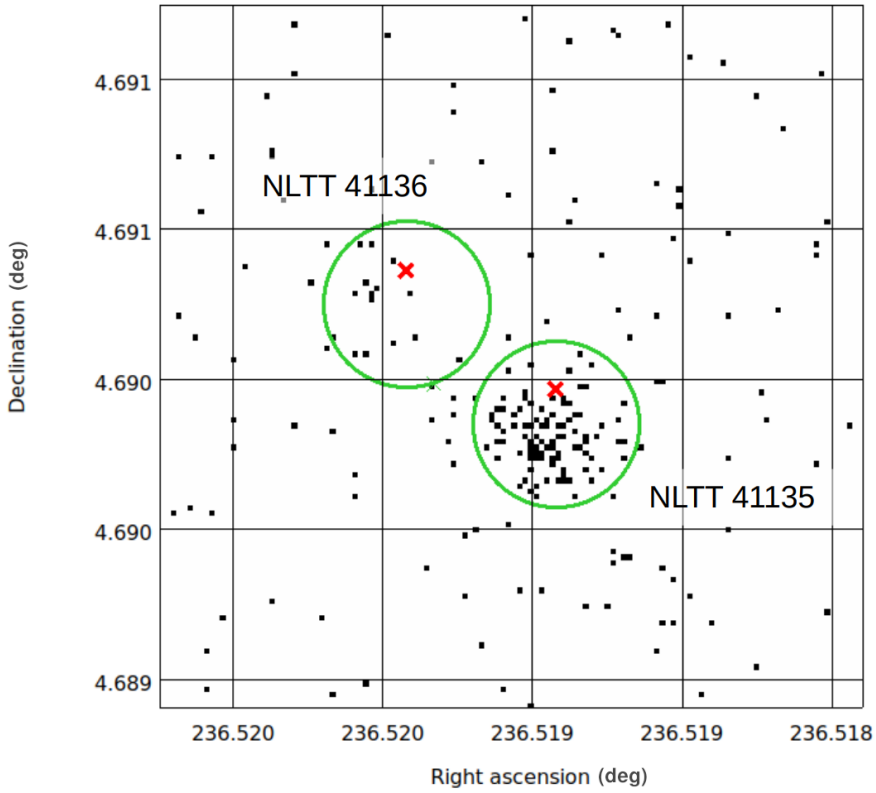

Figure 3.1: Combined *Chandra*/HRC-I observations of the system NLTT 41135/41136 with source extraction regions as green circles and the *Gaia* eDR3 coordinates, propagated to the epoch of observation, as red x-symbols.

Since the stars have a projected angular separation of 2.3", we chose the extraction region radius for both sources to be 1", ensuring that the majority of the detected photons are collected and no overlap between the regions occurs. To estimate the background contribution to the photons in the source region, we also defined a background extraction region with a radius of 15" in a part of the field-of-view (FoV) where the noise appears to have a uniform distribution and no astrophysical X-ray source is visible. After extracting the X-ray photons from the source regions and removing the background contribution, scaled down to the surface area of the source extraction region, we estimated the net source photon counts of the two sources. We combined the two observations to achieve a higher signal-to-noise ratio for both M dwarfs in the system (see Figure 3.1).

The light curve obtained from the observation conducted in October shows a flare occurring on NLTT 41135 at $\approx$ 20 ks after the start of the observation (see Figure 3.2). We estimated the quiescent X-ray flux by excluding the photon counts occurring in the time interval of the flare, but we also calculated the emission parameters from the whole observation time. In general, when further commenting on the activity difference between the NLTT 41135/41136 stellar components, we will be referring to the comparison of the quiescent components of the coronae. When referring to the emission with the flaring event, we will explicitly state it.

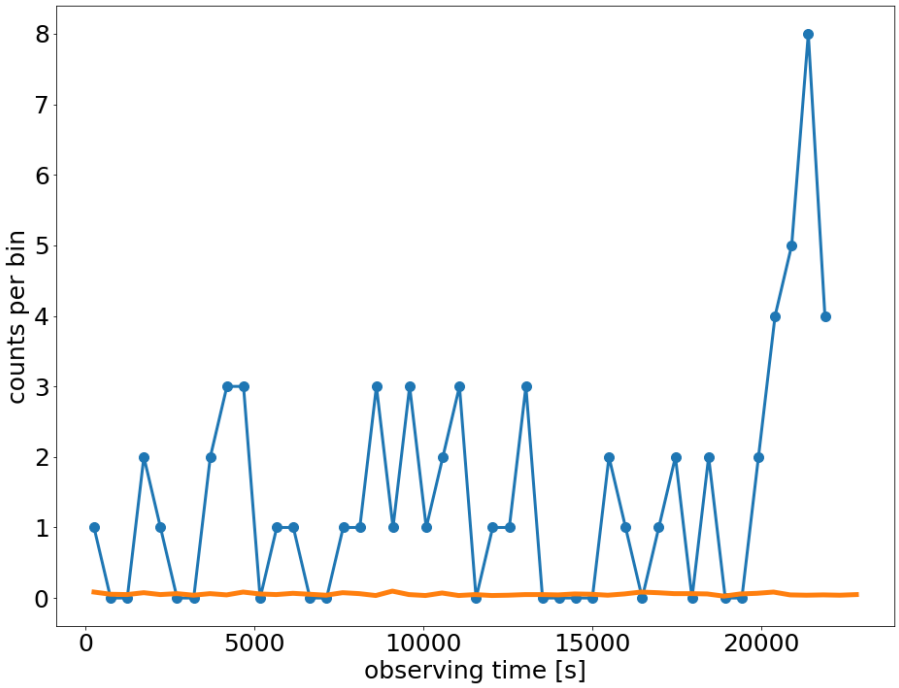

Figure 3.2: X-ray light curve of NLTT 41135 obtained from observation 26143. The blue dots show the count number with 500 s binsize, while the orange line shows the level of scaled background counts. At 20 ks after the observation start, a flare occurred.

3.2.3 Net source photon count

In general, to determine the net source photon count of a faint source, both the Poissonian uncertainties of the source and the background need to be taken into account. For the analysis of the two stars from the NLTT 41135/41136 system, we employed the analysis for faint sources described by [IPH22]. In short, firstly, we estimated the probability that the background fluctuation was responsible for the number of counts in the source region by employing the Poisson cumulative distribution function. For both sources, we found that this probability was lower than 0.3%, securing a 3σ level of detection significance. Furthermore, to estimate the net source photon count and its confidence interval, we applied the Kraft-Burrows-Nousek (KBN) estimator [KBN91a]. The KBN estimator[¶] tackles the small number statistics of faint sources in a Bayesian manner by explicitly assuming the background signal stems from a Poisson process and marginalizing over all possible background count numbers in the source detect cell. It assumes the source flux to be non-negative, and yields confidence intervals for the net source photon count. For the two detected sources, we determined the 68.3% confidence interval and reported the number of counts at its center as the net source photon count in Table 3.1.

3.2.4 Coronal temperature and X-ray surface flux

By choosing an activity indicator from the X-ray regime, we make use of the fact that unsaturated X-ray emission is a function of stellar rotational rate: as single stars age,

[¶]In our analysis, we used the KBN implementation of the `stats.poisson_conf_interval` function in the `astropy` package [Ast+13; Ast+18].

Table 3.1: Observed X-ray emission parameters for the stellar components NLTT 41135 and NLTT 41136 (*src* = source counts; *bg* = scaled background counts). NLTT 41135 flared, and we estimated the parameters with (F) and without (Q) the flare.

component	src	bg	net counts	time [s]	count rate [cts/s]	$\log_{10} T$ [K]	F_x [erg/s/cm^2]
NLTT 41136	15	5.556	$9.444^{+4.240}_{-3.566}$	48138	$0.00020^{+0.00009}_{-0.00007}$	6.3 ± 0.1	$\left(2.220^{+0.964}_{-0.812}\right) \times 10^{-15}$
NLTT 41135 (Q)	85	5.244	$79.762^{+9.565}_{-8.910}$	45078	$0.00177^{+0.00021}_{-0.00020}$	6.6 ± 0.1	$\left(1.596^{+0.192}_{-0.178}\right) \times 10^{-14}$
NLTT 41135 (F)	106	5.556	$100.449^{+10.643}_{-9.983}$	48138	$0.00209^{+0.00022}_{-0.00021}$		$\left(1.883^{+0.199}_{-0.187}\right) \times 10^{-14}$

their rotation rate decreases, and as a consequence, their coronal temperature and X-ray emission reduce. However, if a star experiences spin-up, the average coronal temperature of the star increases, and, therefore, a higher X-ray luminosity and surface flux will be observed.

Since the HRC-I has no intrinsic energy resolution, determining the coronal temperature directly from the observed radiation is not possible. A solution to this issue is the employment of a scaling relation between the average coronal temperature and X-ray surface flux for low-mass main-sequence stars. Observations with various X-ray telescopes have shown that the X-ray surface flux and the coronal temperature of stellar coronae are closely correlated [JG15; Mag+22; Sch97].

We use here the sample presented by [JG15] to test where in the distribution of X-ray surface fluxes and coronal temperatures our sources would fall when assuming different coronal temperatures on a test grid. A caveat with this approach is that the coronae of M dwarfs can have multiple thermal components [Gia+96; RS05; Sch+90], but having no spectral information of the observed coronae only allowed us to estimate the mean coronal temperature.

Inspired by the methodology presented by [AB22], we used the online tool WEBPIMMS (v4.12a) to calculate expected fluxes, for given count rate, for a test grid of coronal temperatures ranging from $\log_{10} T\,[\mathrm{K}] = 6.0 - 7.0$ with 0.1 dex stepsize. The elemental abundances were set to 0.4 of the solar abundance, as suggested by [Irw+10][‖], since NLTT 41135/41136 belongs to the old galactic disk population where the usual abundance is subsolar [Leg92]. The temperature uncertainty is set to be equal to the stepsize of the temperature grid and influences the flux uncertainty much less than the photon count uncertainty provided in Table 3.1.

Using the resulting X-ray flux and the known distance to the system [Bai+18b], we calculated the stellar X-ray luminosity. By normalizing the luminosity with the optical surface area of the star, we arrive at the stellar X-ray surface flux value. We then compared the coronal temperature – X-ray surface flux pairs to the sample from [JG15], which is shown in Figure 3.3. We chose the pair that matches the Johnstone sample best and proceeded with those values as our best estimates for the coronal temperature and X-ray surface flux, as given in Table 3.1.

The flux confidence interval was estimated by using the limits of the 1σ confidence interval of the net source photon count for our sources and applying these values in the `webpimms` tool with the coronal temperature estimated in the previous step. The

[‖][Irw+10] used the subsolar metallicity of *[Fe/H]* = -0.5 to model stellar parameters of the system's components. This value is between 0.2 and 0.4 solar abundances, which are the values that can be selected in `webpimms`; selecting the value of 0.2 changes the resulting X-ray flux by ≈ 5%, which is well within the uncertainties given by the photon count confidence interval for both components.

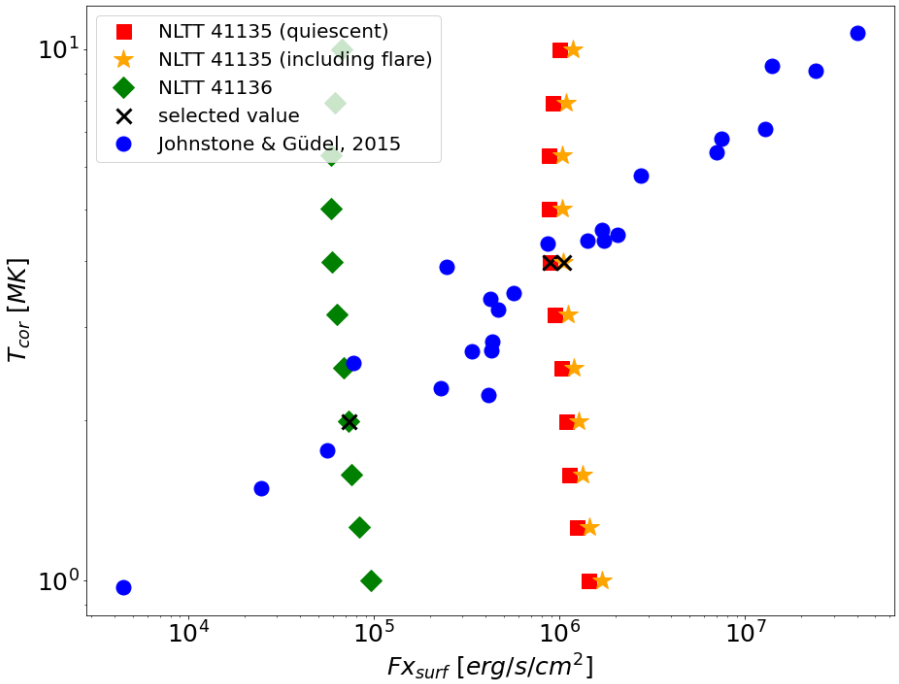

Figure 3.3: Coronal temperature vs. X-ray surface flux from [JG15] with blue dots, and the grid calculated for our targets: for NLTT 41136 with green diamond, and for NLTT 41135 with red squares and orange stars for quiescent and overall emission, respectively.

resulting flux values were used as the upper and lower limits of the 1σ uncertainty of the X-ray flux. With error propagation, we used the estimated X-ray flux uncertainty to estimate the X-ray luminosity and -surface flux uncertainty. The distance uncertainty was not taken into account for error propagation since it is less than 1%.

3.2.5 Stellar radii

Before we are able to calculate the X-ray surface flux, we needed an estimate of the stellar radius. Usually, the radii of M dwarf stars are estimated by applying the empirical relation between the Ks-band magnitude of a star and its radius, published by [Man+15]. However, the NLTT 41135/41136 system, together with several systems from the control sample, does not have a published detection in the Ks band for both components. Therefore, to have uniformly estimated stellar radii for all stars, we estimate the absolute magnitude of a star and use the main-sequence parameters published by [PM13]. We employ the photometric measurement made by the ESA *Gaia* mission [Gai+16b; Gai+18b] and geometric distances to the stars [Bai+18b] to calculate the absolute G magnitude. We then estimate the stellar radius for each star by interpolating the stellar radius vs. absolute G magnitude function for main-sequence stars** for the observed magnitude. In Table 3.2, we give the distance, *Gaia* photometry, and calculated radii of all stars in our sample: the NLTT 41135/41136 system, and the control binary systems (see Section 3.3.2).

For GJ 65, one of the control systems, the radii estimated from interferometric measurements of the stars' angular diameters [Ker+16] were available as well. We also

**The work by [PM13] is extended with the *Gaia* photometry for main-sequence stars in the online version: https://www.pas.rochester.edu/~emamajek/EEM_dwarf_UBVIJHK_colors_Teff.txt

estimate the stellar radii for this system and find a discrepancy of ≈ 10% between the interferometric and our values. This is not that surprising since it was found that stellar evolutionary models, by using photometric measurements, underestimate the stellar radius of M dwarfs [Rib06; Tor13]. Since we are interested in the flux ratio of binary stars, we expect that, to the first order, the effect of radius discrepancy between real and model values will cancel out and will not significantly impact the final result.

3.3 Results

3.3.1 The X-ray properties of NLTT 41135/41136

Although the two M dwarfs in this system have similar stellar parameters, their coronal activity levels differ greatly. Firstly, from the inspection of the X-ray light curve obtained from the observation with ID 26143, a flaring event on NLTT 41135 took place towards the end. On the other hand, the primary NLTT 41136 does not show any evidence of flaring for the entire 50 ks of the observation. The quiescent count rate and the estimated average coronal temperature of the two components indicate a similar conclusion: the secondary has a count rate of 1.8×10^{-3} count/s and a coronal temperature of $\log_{10} T[\mathrm{K}] = 6.6$, while the primary has an order of magnitude lower count rate of 2×10^{-4} count/s and a lower temperature of $\log_{10} T[\mathrm{K}] = 6.3$ (see Table 3.1 for more details). Finally, by comparing the X-ray surface fluxes of the two stars, we establish the significant difference in activity between the two stars: the brown dwarf-hosting star, NLTT 41135 with $F\mathrm{x}_{\mathrm{surf}} = 8.9 \times 10^5$ erg/s/cm^2, shows more than an order of magnitude greater X-ray surface flux than the primary NLTT 41136, which has a flux of $F\mathrm{x}_{\mathrm{surf}} = 7.2{\times}10^4$ erg/s/cm^2 (see Table 3.3 for more details).

3.3.2 M dwarf wide binary systems for activity difference comparison

To determine the significance of the measured coronal activity difference between NLTT 41135 and NLLT 41136, and, therefore, the tidal influence of the brown dwarf, we constructed a comparison sample of wide M dwarf binaries without known close-in substellar companions. We searched the [ER18] wide stellar binaries catalog for M dwarf pairs that harbor stars with similar *Gaia* $G - G_{\mathrm{RP}}$ color. We selected pairs where the absolute value of the color difference is $|d(G - G_{\mathrm{RP}})| \leq 0.2$, i.e. where the stellar components can differ by up to three spectral subtypes. We expect that coeval M dwarfs with colors differing by more than the equivalent of three spectral subtypes will follow somewhat different stellar evolutionary paths, leading the stars to display noticeably different activity levels in the X-ray regime. This scenario might be true for some coeval stars differing by $|d(G - G_{\mathrm{RP}})| \leq 0.2$; however, the selected color-difference limit is a compromise between having a significant number of systems for comparison and them having intrinsically different stars. Aside from the color-difference constraint, we also imposed a constraint on the distance to the systems since most moderately active M dwarfs will not be detected in routine X-ray observations at larger distances. Below, we describe the query for M dwarf pairs in the source catalogs and data archives of three X-ray space

observatories: the *XMM-Newton* space telescope, the *Chandra* X-ray Observatory, and the eROSITA instrument onboard the Spectrum Röntgen Gamma satellite.

3.3.2.1 XMM-Newton

To find M dwarf pairs observed with *XMM-Newton*'s European Photon Imaging Camera (EPIC), we used input pairs from the [ER18] sample as described above and considered pairs within a distance of 100 pc and where the two stars have a separation of at least 15" since stars at closer separation are typically spatially blended in EPIC observations. We used the 4XMM-DR10 catalog, version 1.0 [Web+20] for cross-matching. Since *XMM-Newton* observations have been conducted since 1999 and several of our nearby input pairs display significant proper motions, we first searched for potential matches between the [ER18] sample with coordinates evolved to the J2010.0 epoch and the *XMM-Newton* catalog with a large matching radius of 30". We then extracted the actual observational epoch(s) from the *XMM-Newton* catalog, evolved the stellar coordinates to that specific epoch, or in case of multiple *XMM-Newton* observations to the average epoch, and refined the cross-match by using a matching radius of 5" with the updated coordinates. A visual inspection of the resulting matches in ESASky[††] showed that for some pairs there was source confusion present, especially when the targets were located at the edge of the EPIC field of view. We, therefore, proceeded by downloading the individual observational data sets from the *XMM-Newton* archive and performed a customized analysis by hand.

The query of the 4XMM-DR10 catalog resulted in 10 M dwarf systems. One of these systems, BX Tri, is a hierarchical system hosting a tight pair that was not flagged as such in the [ER18] catalog, and which is not spatially resolved by *XMM-Newton*. We analysed the observations of the remaining nine systems, obtained from the XMM-Newton data archive, as described by [IPH22], and find six systems where both components are detected, and three systems where one component is not detected. We report the fluxes of the detected M dwarfs, and the upper limits[‡‡] of the undetected ones in Table 3.3. There, the flux values are given for the energy range of 0.2-2.0 keV, where stellar coronae typically emit the bulk of their radiation [GGS97b]. The values of the X-ray fluxes are computed assuming an underlying thermal spectrum with a coronal temperature estimated from the observed hardness ratio, as described in more detail by [IPH22, see Appendix 3.6.2 for the details on individual systems].

3.3.2.2 Chandra

The *Chandra* X-ray observatory has a higher spatial resolution, but generally lower sensitivity than *XMM-Newton*. We, therefore, selected M dwarf pairs with a spatial separation of at least 2" and within a distance of 50 pc from the [ER18] sample and cross-matched them with the *Chandra* Source Catalog 2.0 (CSC2.0, [EC18]) in a similar manner as we did for the *XMM-Newton*. Again, since *Chandra* has been in operation since 1999, we used stellar coordinates evolved to an epoch of J2010.0 for initial cross-matching with a matching radius of 30". We then directly proceeded by downloading the individual

[††] https://sky.esa.int/esasky/, [Gio+18]

[‡‡] We estimated the upper limit of the flux values for all undetected M dwarfs in the control sample by calculating the 99.7% (3σ) one-sided confidence interval of the underlying Poissonian distribution of photons found in a suitable background-region, scaled down to the size of the source extraction region.

observation files from the *Chandra* archive[§§] and performed source detection analysis as described by [IPH22]. We found two systems where both components are detected, three systems where no component was detected, and three systems where one component is not detected; for all undetected stars, we again report the one-sided 3σ confidence interval as the upper limit on the X-ray flux. Out of those eight systems, all but one were observed with the ACIS instrument, and we estimated energy conversion factors as described by [IPH22] from hardness ratios and reported X-ray fluxes in the 0.2-2.0 keV energy band. For the one system that was observed with the HRC instrument, we perform the same analysis as described in section 3.2.4 for the NLTT41135/41136 system to find its X-ray flux in the full HRC energy band of 0.08-10 keV. In Appendix 3.6.2 we provide more details on individual systems together with the observed radiation hardness ratio and estimated coronal temperature used for the X-ray flux calculation.

We also added the known binary system GJ 65 to the control sample, which was not included in the wide stellar binary catalog by [ER18]. A detailed analysis of the two recent observations (obs ID: 22344 and 22876) is performed by Wolk et al. (in prep) and the resulting fluxes are included here. The X-ray photometry of M dwarfs observed with *Chandra* is reported in Table 3.3.

3.3.2.3 eROSITA

We compared the selected M dwarf wide binaries from the catalog described above to the catalog of X-ray sources detected with the Röntgen Survey with an Imaging Telescope Array (eROSITA) [Bru+22; Den+20; Fre+20; Mer+12; Pre+21b], an X-ray instrument onboard the Russian Spectrum-Röntgen-Gamma spacecraft [Pav+21; Sun+21]. It was launched in mid-2019 into an orbit around the L_2 Lagrange point of the Sun-Earth system. eROSITA consists of seven Wolter telescopes with one camera assembly each and is sensitive to photon energies between 0.2-10 keV [Mei+20]. eROSITA started an all-sky survey in 2019, where it scans the whole sky every six months in great circles roughly perpendicular to the ecliptic. Any point on the sky is scanned every four hours for several eROSITA slews, with the number of slews when a given target is in the field of view depending on the ecliptic latitude of the target.

eROSITA has completed four all-sky surveys to date (named eRASS1 to eRASS4), as well as a partially-completed fifth all-sky survey (eRASS5). In addition to source catalogs from each of those surveys, the eROSITA_DE consortium has also produced a catalog from the stacked data of the four completed eRASS surveys in the German part of the eROSITA sky, called eRASS:4, accessible within the eROSITA consortium in the data reduction version from October 31, 2022. eROSITA has wide wings of its PSF; to avoid issues with source blending and upper limit calculations, we selected known M dwarf binary pairs within a volume of 50 pc that have a separation of at least 50" between the two stars. We then matched those individual stars to the catalog with a matching radius of 10" and checked that all matched X-ray sources are likely to be of stellar nature, as described by [Fos+22].

The stacked eRASS:4 survey (as well as the individual eRASS surveys) is shallow, with total exposure times of the order of 500 s. M dwarfs frequently produce X-ray flares, which increases the probability that some of the M dwarf detections in eRASS:4 were only achieved because the M dwarf flared during the exposure time. Indeed, there is evidence

[§§] https://cda.harvard.edu/chaser/

of this reported in [Ste+22]. Since we want to compare the quiescent X-ray emission levels of stars, we, therefore, clean the initially matched sample as follows: we require that a given star, in addition to being detected in the stacked eRASS:4 survey, is detected in at least three of the five individual eRASS1 to eRASS5 surveys, meaning we have likely seen the quiescent emission from the star. We then estimate the quiescent flux of the star by taking the median of the individually detected flux values, and its uncertainty by the standard deviation of those detected individual fluxes. We note that three detections is the minimum number required to identify one outlier and determine the typical flux via the median.

Systems in which fewer than three flux detections were achieved were considered to be dominated by flaring emission and, since we do not have a way to characterize the quiescent flux from the available data, they were discarded. Systems in which one star had a detected quiescent flux as described above, but the other star had no detection, were kept in the sample and an upper limit to the flux of the undetected star was computed using the prescription of Tubín-Arenas et al. 2023 (submitted), i.e. by performing X-ray photometry on the eROSITA standard calibration data products (counts image, background image, and exposure time), following the Bayesian approach described by [KBN91b]. The upper limits are given as one-sided 3σ confidence intervals in the eROSITA soft band, which has an energy range of 0.2-2.3 keV, and using appropriate energy conversion factors for a stellar corona with a temperature of $kT = 0.3$ keV, typical for moderately active stars [Fos+22; Sch+90]. This procedure yielded ten pairs where both stars have a detected quiescent flux and five pairs where one star has a detected quiescent flux and the other star has an upper limit.

3.3.3 Intrabinary X-ray surface flux difference

Having estimated the X-ray surface flux of NLTT 41135 and NLTT 41136, and of the binaries in the control sample, as a next step, we estimated the coronal activity level difference between the two stars of each binary. The activity difference is calculated as the absolute logarithmic value of the ratio of the stellar X-ray surface fluxes of the two stars. In Table 3.3, the values of the stellar X-ray surface flux together with the activity difference ratio for each binary are given. The mean coronal activity difference in the X-ray regime between coeval M dwarfs in the control sample is $|\log(F\mathrm{x}_{\mathrm{surfA}}/F\mathrm{x}_{\mathrm{surfB}})| = 0.34 \pm 0.22$, with A and B denoting the surface flux of the primary and the secondary component, respectively. This means that, on average, the X-ray surface flux between two coeval M dwarfs can differ by a factor of 2.2 ± 1.7, which is similar to the intrinsic variability seen in single M dwarf stars in time-averaged X-ray data [Mag+22; MMP00; Ste+13]. The mean activity difference was calculated including systems where one star is undetected, and for these systems, we consider the activity difference given in Table 3.3. Since the sample has three systems with components separated by less than 100 AU, which is the lower limit for binary systems to be considered as wide [DB07], we tested if a correlation between the activity difference indicator and the spatial separation between coeval stars exists, and found none.

We did not include the following systems in the analysis: TIC 293303829 / TIC 293303832, Gaia DR2 4899032116649119616 / Gaia DR2 4899029951985608576, LP 320-163 / LP 320-162, and TIC 20446899 / Gaia DR2 3532611086293698560. All systems have one undetected stellar component that has an upper limit value higher than the flux of

Table 3.2: Spectral type (SpT) and projected physical separation (ρ) of the components together with their *Gaia* DR2 photometry and distances [Bai+18b] used to calculate the absolute G magnitudes and the radii. Additionally, the absolute value of the color difference between the binary components and their *Gaia* DR2 stellar proper motion are given.

component	SpT	ρ [AU]	dist [pc]	G	$G - G_{RP}$	M_G	R_{Gaia} [$R_\odot$]	$\lvert d(G - G_{RP})\rvert$	$\mu_\alpha \cdot \cos\delta$ [mas/yr]	μ_δ [mas/yr]
NLTT 41136	M4	79	34.319	13.966	1.284	11.289	0.269	0.075	153.670 ± 0.243	−281.981 ± 0.241
NLTT 41135	M5		34.136	14.936	1.359	12.270	0.205		162.509 ± 0.182	−282.725 ± 0.182
GJ 15 B	M3	122	3.561	9.677	1.205	11.919	0.225	0.171	2863.284 ± 0.069	336.529 ± 0.039
GJ 15 A	M1		3.562	7.216	1.034	9.458	0.435		2891.525 ± 0.061	411.903 ± 0.034
Gaia DR2 1608710752684301312	M4	4908	74.594	15.646	1.294	11.283	0.269	0.004	−27.898 ± 0.095	30.127 ± 0.084
Gaia DR2 1608710791338814208	M4		75.330	16.155	1.290	11.770	0.236		−29.958 ± 0.103	29.634 ± 0.085
Ross 868	M3	181	10.751	10.137	1.170	9.980	0.372	0.106	−214.777 ± 0.077	351.001 ± 0.084
Ross 867	M4		10.753	11.456	1.276	11.298	0.268		−226.132 ± 0.098	355.284 ± 0.105
TIC 293303829	M1	4576	55.871	12.230	1.019	8.494	0.538	0.023	−24.591 ± 0.117	−167.143 ± 0.057
TIC 293303832	M0		55.853	12.063	0.996	8.328	0.562		−24.573 ± 0.095	−166.795 ± 0.046
Gaia DR2 3074577322667614976	M3	17201	53.705	13.730	1.199	10.080	0.359	0.047	−43.033 ± 0.092	−86.589 ± 0.065
Gaia DR2 3074630580262065536	M4		53.625	14.777	1.246	11.130	0.280		−42.529 ± 0.106	−86.487 ± 0.066
TIC 436632332	M4	2176	83.799	14.970	1.282	10.353	0.338	0.039	19.706 ± 0.148	−43.233 ± 0.086
TIC 436632331	M4		83.769	14.970	1.322	10.355	0.338		20.083 ± 0.141	−43.467 ± 0.083
Gaia DR2 4768120070358120064	M4	3219	91.156	16.887	1.272	12.088	0.215	0.16	37.732 ± 0.156	11.151 ± 0.182
Gaia DR2 4768120104717857792	M2		91.011	14.854	1.112	10.058	0.360		37.515 ± 0.078	10.981 ± 0.099
G 202-66	M3	1526	60.676	13.395	1.179	9.480	0.433	0.039	−239.59 ± 0.058	174.561 ± 0.064
G 202-67	M3		60.676	15.046	1.218	11.131	0.280		−241.61 ± 0.072	175.549 ± 0.089
LTT 6326	M0	1640	61.690	12.796	0.990	8.845	0.498	0.042	−55.483 ± 0.037	−334.752 ± 0.042
LTT 6325	M0		61.774	12.397	0.948	8.443	0.544		−55.444 ± 0.038	−333.655 ± 0.042
LP320-163	M6	102	45.653	16.098	1.447	12.801	0.180	0.032	−212.555 ± 0.155	27.959 ± 0.12
LP320-162	M5		46.370	16.152	1.416	12.821	0.180		−218.427 ± 0.153	28.591 ± 0.118
LP920-61 B	M3	87	18.234	12.506	1.197	11.202	0.275	0.024	−121.425 ± 0.105	−122.807 ± 0.075
LP920-61 A	M3		18.268	12.450	1.173	11.141	0.279		−113.453 ± 0.106	−123.013 ± 0.075
SCR J0602-3952-B	M3	126	45.719	14.274	1.232	10.973	0.292	0.054	75.063 ± 0.073	178.107 ± 0.07
SCR J0602-3952-A	M3		45.885	13.436	1.178	10.127	0.355		72.687 ± 0.051	175.841 ± 0.049
TIC 20446899	M0	1778	40.659	11.402	0.969	8.356	0.557	0.184	−170.787 ± 0.093	4.69 ± 0.068
Gaia DR2 3532611086293698560	M3		40.566	13.127	1.152	10.086	0.358		−172.895 ± 0.096	7.383 ± 0.066
G236-1	M2	1054	11.850	9.563	1.097	9.195	0.457	0.043	−671.954 ± 0.045	−271.231 ± 0.058
G236-2	M3		11.873	10.067	1.141	9.695	0.417		−671.125 ± 0.055	−265.525 ± 0.062
Gaia DR2 7159285151835511040	M4	387	36.055	14.404	1.275	11.619	0.246	0.118	4.986 ± 0.101	53.474 ± 0.096
TIC 16151129	M3		35.905	12.839	1.157	10.063	0.360		3.271 ± 0.08	58.59 ± 0.07
Ross 110 B	M4	68	21.557	13.196	1.262	11.529	0.252	0.014	544.582 ± 0.062	−549.415 ± 0.062
Ross 110 A	M4		21.479	12.904	1.248	11.244	0.272		547.56 ± 0.125	−535.855 ± 0.119
GJ 65 A	M6	6	2.703	10.507	1.440	13.348	0.156	0.092	3385.827 ± 0.492	532.040 ± 0.374
GJ 65 B	M7		2.687	10.869	1.532	13.723	0.148		3182.734 ± 0.552	592.104 ± 0.427

Table 3.2: Continued

component	SpT	ρ [AU]	dist [pc]	G	$G - G_{RP}$	M_G	$R_{Gaia}[R_\odot]$	$\lvert d(G - G_{RP})\rvert$	$\mu_\alpha \cdot \cos\delta$[mas/yr]	μ_δ[mas/yr]
TIC 206617096	M4	18438	34.690	14.375	1.274	11.674	0.242	0.018	1.598 ± 0.077	84.663 ± 0.075
TIC 206617113	M4		34.703	14.168	1.257	11.467	0.256		1.177 ± 0.063	85.017 ± 0.056
GJ 3148	M3	1415	13.408	10.777	1.174	10.140	0.354	0.059	684.129 ± 0.127	248.772 ± 0.103
GJ 3149	M3		13.433	11.749	1.232	11.108	0.282		683.716 ± 0.161	246.394 ± 0.134
UCAC4 235-004550	M1	2601	39.520	11.739	1.031	8.755	0.508	0.085	35.9 ± 0.043	−33.357 ± 0.061
UCAC4 235-004546	M2		39.551	12.384	1.116	9.398	0.439		37.114 ± 0.048	−32.231 ± 0.078
Gaia DR2 4899032116649119616	M4	13801	38.939	14.766	1.269	11.814	0.233	0.121	−28.019 ± 0.073	−45.644 ± 0.077
Gaia DR2 4899029951985608576	M5		39.098	16.142	1.391	13.181	0.164		−28.182 ± 0.109	−46.464 ± 0.113
TIC 167422188	M1	13368	40.774	11.890	1.007	8.839	0.499	0.081	79.093 ± 0.048	234.317 ± 0.046
TIC 167417695	M2		41.058	12.628	1.089	9.561	0.428		78.676 ± 0.053	233.277 ± 0.054
TIC 106344480	M1	45353	24.390	10.606	1.041	8.670	0.518	0.172	37.481 ± 0.038	−34.252 ± 0.039
TIC 106493402	M3		24.466	12.216	1.213	10.274	0.344		36.45 ± 0.051	−31.75 ± 0.067
TIC 416857959	M2	5204	39.125	12.356	1.103	9.393	0.439	0.047	−36.339 ± 0.051	47.232 ± 0.054
TIC 450297524	M1		39.122	12.097	1.056	9.135	0.464		−36.251 ± 0.051	48.66 ± 0.048
TIC 36765037	M3	2631	30.149	13.589	1.231	11.192	0.275	0.02	−183.1 ± 0.462	−26.428 ± 0.697
TIC 36765044	M3		31.660	13.626	1.211	11.124	0.281		−182.39 ± 0.152	−25.195 ± 0.129
TIC 151639642	M2	3799	36.792	12.031	1.087	9.202	0.456	0.081	31.746 ± 0.043	−79.325 ± 0.045
UCAC4 270-056947	M3		36.838	12.738	1.168	9.906	0.384		31.723 ± 0.049	−78.358 ± 0.05
UCAC4 150-081944	M4	6132	30.374	14.268	1.296	11.855	0.230	0.14	−145.97 ± 0.097	−64.886 ± 0.08
TIC 317385747	M3		30.317	12.357	1.156	9.949	0.377		−147.448 ± 0.054	−66.219 ± 0.047
TIC 392786054	M3	9659	26.342	12.641	1.223	10.538	0.325	0.07	159.768 ± 0.113	−83.222 ± 0.098
TIC 392785968	M4		26.445	13.618	1.293	11.506	0.254		160.361 ± 0.124	−82.213 ± 0.098
WT 2090	M4	5413	21.426	13.371	1.279	11.716	0.239	0.107	−171.652 ± 0.125	−247.082 ± 0.11
Wolf 1501	M3		21.408	12.113	1.172	10.461	0.330		−170.941 ± 0.093	−247.728 ± 0.081
TIC 410458113	M2	4370	27.554	11.787	1.119	9.586	0.427	0.045	88.314 ± 0.119	−98.339 ± 0.082
UCAC4 385-070621	M3		27.579	12.656	1.164	10.453	0.331		89.838 ± 0.121	−95.569 ± 0.082
TIC 229807000	M2	35099	45.987	11.983	1.129	8.670	0.518	0.144	73.503 ± 0.041	−68.137 ± 0.042
TIC 229807051	M4		45.885	13.875	1.273	10.566	0.323		73.624 ± 0.071	−68.011 ± 0.071

Table 3.3: X-ray parameters for all the stars in our sample, together with the activity difference in each binary. Provided is the instrument with which *Chandra (C)* systems were observed; *XMM-Newton (XMM)* systems were observed with the EPIC instrument.

mission	component	$F_x \times 10^{-14}$ [erg/s/cm^2]	$L_x \times 10^{27}$ [erg/s]	$Fx_{surf} \times 10^5$ $[erg/s/cm^2]$	$L_{bol} \times 10^{31}$ [erg/s]	$\log R_x$	$\log \frac{Fx_{surfA}}{Fx_{surfB}}$
	NLTT 41136	0.22 ± 0.09	0.32 ± 0.13	0.72 ± 0.29	2.61	-4.91	
C/HRC	NLTT 41135 (quiescent)	1.6 ± 0.2	2.3 ± 0.3	8.9 ± 1.0		-3.76	1.09 ± 0.18
	NLTT 41135 (average)	1.9 ± 0.2	2.7 ± 0.3	10.0 ± 1.0	1.31×10^{31}	-3.69	1.16 ± 0.18
	GJ 15 B	2.506 ± 0.136	0.04 ± 0.0	0.13 ± 0.01	1.67	-5.63	
XMM	GJ 15 A	12.992 ± 0.285	0.2 ± 0.0	0.17 ± 0.0	10.02	-5.70	0.14 ± 0.03
	Gaia DR2 1608710752684301312	1.88 ± 0.144	12.76 ± 0.98	29.0 ± 2.23	2.64	-3.32	
XMM	Gaia DR2 1608710791338814208	0.341 ± 0.068	2.36 ± 0.47	7.0 ± 1.39	1.86	-3.90	0.62 ± 0.09
	Ross 868	67.726 ± 0.802	9.55 ± 0.11	11.34 ± 0.13	6.65	-3.84	
XMM	Ross 867	69.566 ± 0.815	9.81 ± 0.11	22.47 ± 0.26	2.62	-3.43	0.3 ± 0.01
	TIC 293303829	0.178 ± 0.055	0.68 ± 0.21	0.38 ± 0.12	19.86	-5.47	
XMM	TIC 293303832	≤ 0.451	≤ 1.72	≤ 0.89	22.85	≤ −5.12	/
	Gaia DR2 3074577322667614976	13.115 ± 0.219	46.14 ± 0.77	58.93 ± 0.98	6.11	-3.12	
XMM	Gaia DR2 3074630580262065536	4.934 ± 0.152	17.31 ± 0.53	36.26 ± 1.12	2.96	-3.23	0.21 ± 0.02
	TIC 436632332	4.698 ± 0.272	40.25 ± 2.33	57.77 ± 3.34	5.08	-3.10	
XMM	TIC 436632331	2.582 ± 0.197	22.1 ± 1.69	31.75 ± 2.42	5.08	-3.36	0.26 ± 0.04
	Gaia DR2 4768120070358120064	0.08 ± 0.021	0.82 ± 0.21	2.91 ± 0.76	1.48	-4.26	
XMM	Gaia DR2 4768120104717857792	≤ 0.05	≤ 0.51	≤ 0.64	6.2	≤ −5.09	≥ 0.66
	G 202-66	7.999 ± 0.3	35.92 ± 1.35	31.43 ± 1.18	9.88	-3.44	
XMM	G 202-67	0.514 ± 0.093	2.31 ± 0.42	4.84 ± 0.88	2.96	-4.11	0.81 ± 0.08
	LTT 6326	0.084 ± 0.027	0.39 ± 0.12	0.26 ± 0.08	15.39	-5.60	
XMM	LTT 6325	≤ 0.08	≤ 0.37	≤ 0.21	20.61	≤ −5.74	≥ 0.1
	LP 320-163	0.098 ± 0.109	0.25 ± 0.28	1.25 ± 1.4	0.91	-4.57	
C/ACIS	LP 320-162	≤ 0.564	≤ 1.48	≤ 7.55	0.9	≤ −3.78	/
	LP 920-61 B	6.634 ± 2.549	2.69 ± 1.03	5.87 ± 2.25	2.8	-4.02	
C/ACIS	LP 920-61 A	≤ 5.474	≤ 2.23	≤ 4.7	2.93	≤ −4.12	≥ 0.1
	SCR J0602-3952-B	≤ 0.255	≤ 0.65	≤ 1.25	3.32	≤ −4.71	
C/ACIS	SCR J0602-3952-A	≤ 0.342	≤ 0.88	≤ 1.15	5.92	≤ −4.83	/
	Ross 868	142.48 ± 6.377	20.09 ± 0.9	23.86 ± 1.07	6.65	-3.52	
C/ACIS	Ross 867	105.183 ± 6.508	14.84 ± 0.92	33.97 ± 2.1	2.62	-3.25	0.15 ± 0.03
	TIC 20446899	0.018 ± 0.007	0.04 ± 0.01	0.02 ± 0.01	22.28	-6.79	
C/ACIS	Gaia DR2 3532611086293698560	≤ 0.076	≤ 0.15	≤ 0.2	6.09	≤ −5.60	/
	G236-1	56.11 ± 2.026	9.61 ± 0.35	7.56 ± 0.27	11.91	-4.09	
C/HRC	G236-2	71.16 ± 2.281	12.24 ± 0.39	11.56 ± 0.37	8.62	-3.85	0.18 ± 0.02
	Gaia DR2 7159285151835511040	≤ 1.464	≤ 2.32	≤ 6.31	2.07	≤ −3.95	
C/ACIS	TIC 16151129	≤ 1.076	≤ 1.69	≤ 2.15	6.18	≤ −4.56	/
	Ross 110 B	≤ 0.235	≤ 0.13	≤ 0.34	2.21	≤ −5.22	
C/ACIS	Ross 110 A	≤ 0.189	≤ 0.11	≤ 0.24	2.72	≤ −5.41	/

Table 3.3: continued

mission	component	$F_x \times 10^{-14}$ $[erg/s/cm^2]$	$L_x \times 10^{27}$ [erg/s]	$Fx_{surf} \times 10^5$ $[erg/s/cm^2]$	$L_{bol} \times 10^{31}$ [erg/s]	$\log R_x$	$\log \frac{Fx_{surfA}}{Fx_{surfB}}$
C/HRC	GJ 65 A	268.0 ± 5.6	2.39 ± 0.05	14.4 ± 0.3	0.62	-3.41	0.14 ± 0.02
	GJ 65 B	351.5 ± 7.9	3.10 ± 0.07	20.1 ± 0.4	0.52	-3.22	
eROSITA	TIC 206617096	5.721 ± 0.339	8.4 ± 0.5	23.55 ± 1.4	1.99	-3.38	0.22 ± 0.03
	TIC 206617113	10.637 ± 0.574	15.63 ± 0.84	39.09 ± 2.11	2.32	-3.17	
eROSITA	GJ 3148	145.246 ± 1.889	31.85 ± 0.41	41.72 ± 0.54	5.87	-3.27	0.25 ± 0.01
	GJ 3149	51.654 ± 1.088	11.37 ± 0.24	23.54 ± 0.5	3.01	-3.42	
eROSITA	UCAC4 235-004550	87.329 ± 0.798	166.37 ± 1.52	105.83 ± 0.97	16.43	-2.99	0.27 ± 0.01
	UCAC4 235-004546	35.253 ± 0.602	67.27 ± 1.15	57.42 ± 0.98	10.39	-3.19	
eROSITA	Gaia DR2 4899032116649119616	5.881 ± 0.22	10.88 ± 0.41	33.08 ± 1.24	1.8	-3.22	/
	Gaia DR2 4899029951985608576	≤ 27.522	≤ 51.32	≤ 315.58	0.7	≤ −2.14	
eROSITA	TIC 167422188	1.354 ± 0.02	2.75 ± 0.04	1.81 ± 0.03	15.46	-4.75	0.09 ± 0.03
	TIC 167417695	0.794 ± 0.048	1.63 ± 0.1	1.46 ± 0.09	9.41	-4.76	
eROSITA	TIC 106344480	225.667 ± 1.148	163.76 ± 0.83	100.37 ± 0.51	17.47	-3.03	0.07 ± 0.06
	TIC 106493402	84.167 ± 10.925	61.45 ± 7.98	85.2 ± 11.06	5.37	-2.94	
eROSITA	TIC 416857959	21.059 ± 0.45	39.32 ± 0.84	33.52 ± 0.72	10.42	-3.42	≥ 0.63
	TIC 450297524	≤ 5.536	≤ 10.34	≤ 7.89	12.44	≤ −4.08	
eROSITA	TIC 36765037	15.775 ± 1.173	17.49 ± 1.3	37.93 ± 2.82	2.82	-3.21	≥ 0.4
	TIC 36765044	≤ 5.905	≤ 7.22	≤ 15.08	2.97	≤ −3.61	
eROSITA	TIC 151639642	4.742 ± 0.24	7.83 ± 0.4	6.19 ± 0.31	11.84	-4.18	0.69 ± 0.04
	UCAC4 270-056947	16.486 ± 1.323	27.29 ± 2.19	30.48 ± 2.45	7.11	-3.42	
eROSITA	UCAC4 150-081944	7.455 ± 0.727	8.39 ± 0.82	26.14 ± 2.55	1.75	-3.32	0.49 ± 0.04
	TIC 317385747	62.761 ± 0.868	70.36 ± 0.97	81.42 ± 1.13	6.84	-2.99	
eROSITA	TIC 392786054	10.25 ± 0.548	8.68 ± 0.46	13.53 ± 0.72	4.49	-3.71	0.41 ± 0.03
	TIC 392785968	16.011 ± 0.35	13.66 ± 0.3	34.9 ± 0.76	2.25	-3.22	
eROSITA	WT 2090	24.581 ± 0.953	13.76 ± 0.53	39.54 ± 1.53	1.93	-3.15	≥ 0.53
	Wolf 1501	≤ 13.757	≤ 7.69	≤ 11.58	4.73	≤ −3.79	
eROSITA	TIC 410458113	17.912 ± 0.407	16.59 ± 0.38	14.99 ± 0.34	9.27	-3.75	≥ 0.46
	UCAC4 385-070621	≤ 3.753	≤ 3.48	≤ 5.22	4.75	≤ −4.14	
eROSITA	TIC 229807000	130.399 ± 1.647	336.38 ± 4.25	206.17 ± 2.6	17.47	-2.72	0.28 ± 0.01
	TIC 229807051	26.966 ± 0.832	69.26 ± 2.14	109.43 ± 3.38	4.4	-2.80	

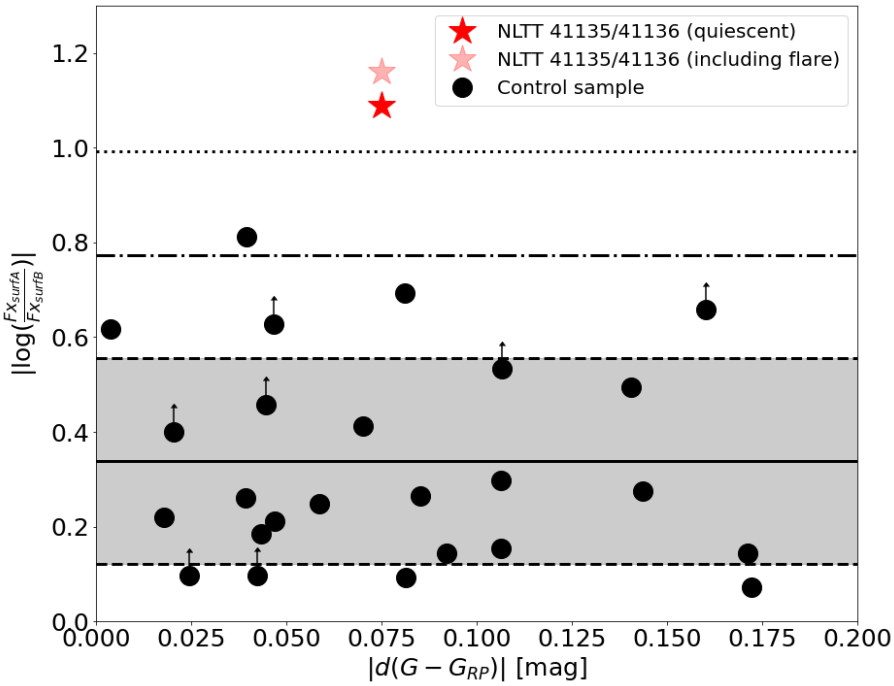

Figure 3.4: The activity difference as a function of the absolute value of color difference, which corresponds to the mass difference between the components of the wide binary. The binary systems from the control sample are shown as black dots and the NLTT 41135/41136 system as the red asterisk symbol, with the fainter red asterisk including the flaring episode. The solid black line is the mean of the activity difference of the control sample, the shaded area indicates the 1σ confidence interval around the mean, while the dashed and dotted lines represent the $+2\sigma$ and $+3\sigma$ confidence interval limits, respectively.

the detected component, due to differences in the exposure times and in the detectors used. This means that the activity difference of each pair is unconstrained. Additionally, we did not include the undetected systems SCR J0602-3952 A/B, Ross 110 A/B, and Gaia DR2 7159285151835110 40/TIC 16151129, where the activity difference between the components is unconstrained as well.

In Figure 3.4, the coronal activity difference is shown as a function of the absolute value of the $G - G_{\rm RP}$ color difference between the stars in each binary. The 68.3% confidence interval of the control sample distribution is marked with the shaded region, and the mean of the distribution is presented as the black solid line. The coronal activity level difference between NLTT 41135 and NLTT 41136 is $|\log(F\mathrm{x}_{\rm surfA}/F\mathrm{x}_{\rm surfB})| = 1.09 \pm 0.18$ and is given as red asterisk symbol. Here, the brown dwarf-hosting M dwarf has an X-ray surface flux more than an order of magnitude higher than that of its stellar companion. Considering the X-ray surface flux of NLTT 41135 calculated including the flare emission, the activity difference rises to $|\log(F\mathrm{x}_{\rm surfA}/F\mathrm{x}_{\rm surfB})| = 1.16 \pm 0.18$.

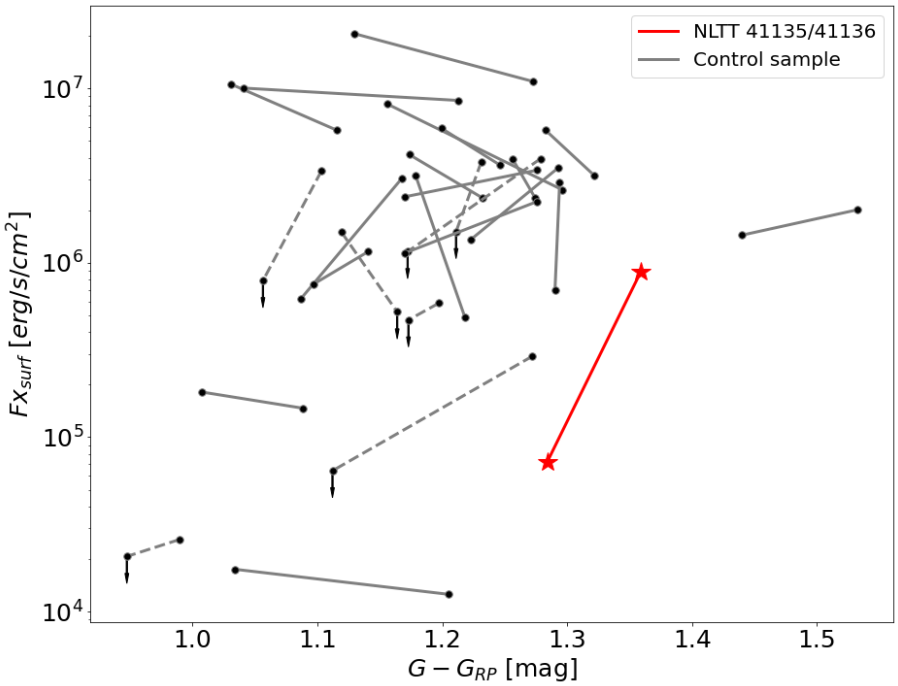

Figure 3.5: The X-ray surface flux as a function of the *Gaia* color of M dwarfs in the control sample and the NLTT 41135/41136 system. The two components of a binary are connected with a line: the gray solid line shows binaries where both components are detected, the gray dashed line shows systems where one component is undetected, and the red line connects NLTT 41135 and NLTT 41136.

3.4 Discussion

3.4.1 The activity difference distribution

It is well known that stars of similar mass, but different ages have X-ray emission levels that can differ by several orders of magnitude (see e.g. [Güd04] and references therein). When, on the other hand, we consider stars of similar mass and age, as in our control sample, their emission and activity levels should be more consistent. As we have shown, two stars of the same spectral type in a binary will have a certain degree of difference in their activity level, but typically within a factor of two in coronal brightness. This is much smaller than the range observed for differently-aged stars.

This is also shown in Fig. 3.5, where the distribution of all investigated stars is shown in the X-ray surface flux – *Gaia* color parameter space. There, individual stars are shown as black dots and those belonging to the same system are connected with a grey line. If both stars are detected, the connecting line is solid, otherwise, the line is dashed, which indicates that the slope of the connecting line is a minimum absolute value. The NLTT system is presented with red asterisks and a red connecting line; here we used the quiescent X-ray surface flux for the BD-hosting star.

The distribution of systems in Fig. 3.5 shows a spread of more than three orders of magnitude in the X-ray surface fluxes. The stars in our sample, thus, span nearly the full range of X-ray activity levels present in M dwarfs which was recently shown by [Car+23] on a volume-complete sample to range from $Fx_{\rm surf} < 10^4$ erg/s/cm^2 (corresponding to

the X-ray emission of solar coronal holes) to $Fx_{surf} > 10^7$ erg/s/cm^2 (corresponding to solar cores of active regions and flares). The X-ray activity level of coronally active stars is known to be linked to the stellar rotation rate, which evolves over time. Therefore, our stars likely represent a range of ages. In fact, within a given binary the X-ray surface fluxes of the two components (which can be assumed to be coeval) are similar to each other, and this leads to the low value of the average activity difference in our sample shown in Fig. 3.4. However, the activity levels of coeval stars are not equal to each other and there are several processes that can be considered as drivers of the activity difference distribution seen in Fig. 3.4 and 3.5. In the following, we discuss phenomena like saturated coronal emission, the fully convective boundary, and activity cycles.

3.4.1.1 Coronal saturation regime

According to various studies, the coronae of cool main-sequence stars can operate in the saturated or unsaturated regime of emission [Mag+20; Mag+22; Pal+81; Piz+03; Rei+22; Wri+11; Wri+18]. In the first regime, the X-ray emission reaches a maximum value and does not depend on the stellar rotation rate, while in the latter, the X-ray emission decreases with the increasing rotation period of the star.

To estimate the coronal emission state, we calculated the parameter $\log R_x = \log \frac{L_x}{L_{bol}}$ for each individual star in our sample. Here, we calculated the bolometric luminosity, similar to the stellar radius in Sec. 3.2.5, by using the L_{bol} values for main-sequence stars published by [PM13], and interpolating them over the absolute G magnitudes given in Table 3.2. The $\log R_x$ values of individual stars are given in Table 3.3.

We estimated the saturation limit for M dwarf stars to be $\log R_x = -3.26^{+0.38}_{-0.36}$, by employing the saturation values for different mass bins from Fig. 9b by [Mag+22], and estimating the average value for their full mass range. Taking the average lower saturation limit of $\log R_x = -3.62$, we find that 18 of the pairs in our control sample have at least one star in the saturated regime. These *high-activity* systems are also seen in Fig. 3.5 with X-ray surface fluxes above $Fx_{surf} \approx 10^6$erg/s/cm^2. Having the majority of the control systems in the high-activity regime is most probably due to the fact that we employ archival data, where the probability of detecting active stars is higher than for low-activity stars. Therefore, our control sample is biased toward brighter X-ray stars.

One might argue that the high-activity systems are more likely to have equal surface fluxes for both stars because they are saturated, which is often interpreted to mean that most of their corona is full with X-ray-emitting magnetic structures. Consequently, it is difficult (or impossible) to produce a coronal activity difference of one order of magnitude between two coeval saturated stars. However, the control sample also includes seven low-activity systems (where both M dwarfs have $Fx_{surf} \lesssim 10^6$erg/s/cm^2). Unsaturated stars are not expected to have a coronal filling factor near 100%, and thus the coronal activity difference between the two components of such binaries may take larger values than found in highly active, saturated systems. However, we measure for the low-activity stars $|\log(Fx_{surfA}/Fx_{surfB})| = 0.30$, lower than the average for all systems. Here, it has to be noted that some low-activity systems have one star undetected and the calculated mean activity difference is a lower limit.

3.4.1.2 Fully convective boundary

The fully convective boundary occurs in mid-M dwarfs (e.g. [CB97; CJJ70]) and is encompassed by the sample selection we made. It is assumed that, due to high opacity in later M dwarfs, efficient energy transport inside the star is possible only through convection and the star becomes fully convective.

While it was expected that the coronal properties might change at this boundary due to a switch in dynamo mode from an $\alpha\Omega$-dynamo to a different one (e.g. [CK06]), observations showed that there is no abrupt change in X-ray luminosity or other coronal activity indicators [Ste+13; WD16]. Rather, changes in coronal properties were found at the very low-mass end of the M dwarf sequence, where the low temperature of the photosphere may start to affect the formation of active regions [Ber+10; RS09; Ste+12; WCB14].

In our sample, we have a few pairs that straddle the fully convective boundary. If this boundary is set at the spectral type $\approx$ M4 with the *Gaia* color of $G - G_{\mathrm{RP}} \approx 1.24$, in eight systems the primary is partially convective while the secondary is fully convective. However, in these systems, the less-massive star has the spectral type M4 and not later. Therefore, we cannot with certainty say that it is a fully convective star, only that it is potentially fully convective. Therefore, any potential effect due to having fully convective stars in our sample might not be present in our sample.

3.4.1.3 Activity cycles

One aspect of magnetic activity we were not able to account for is the activity cycle of stars in the X-ray regime. It is well established that stars other than the Sun can have these kinds of cycles [Cof+20; DDG10; Fav+08; Hem+06; RSH07]; however, activity cycles in saturated stars and stars close to the fully convective boundary seem to be elusive not only in the coronal part of the stellar atmosphere but in the chromosphere as well [Fuh+23; Rob+13]. It is hypothesized that activity cycles in fully convective stars are absent because the efficiency of magnetic braking decreases (e.g. [CK06]). For saturated stars, activity cycles might be absent because their coronae are fully covered with magnetic X-ray emitting structures leaving no space for additional X-ray emitting regions. In fact, none of the stars with a detected activity cycle is saturated (Drake & Stelzer, in prep.). However, since in the control sample, we have stars that are both unsaturated and partly convective, the existence of X-ray activity cycles cannot be fully excluded, and their contribution to the observed activity difference remains unconstrained.

3.4.2 The coronal activity level difference between NLTT 41135 and NLTT 41136 and its physical interpretation

The spin evolution of a star with a close-in companion is driven by processes that can have opposite effects: magnetic braking and tidal interactions. While the wind-driven braking slows down the stellar rotation rate, tidal interactions with a close-in companion can induce spin-up via angular momentum transfer if the configuration of the system is such that the orbital rate of the companion is greater than the rotation rate of the star. As a consequence of the spin-up scenario, the star can experience a higher magnetic activity level than would be the case without tidal interactions. To test this hypothesis

when the companion is a substellar object, we analysed the subsystem NLTT 41135, a brown dwarf-M dwarf pair, together with their stellar companion NLTT 41136, which is expected to have the baseline activity level which is governed only by magnetic braking.

Since, in general, a difference in activity between coeval stars with the same spectral type should be expected, we introduced a control sample which showed that the average difference in activity between these stars is $|\log(Fx_{\mathrm{surfA}}/Fx_{\mathrm{surfB}})| = 0.34 \pm 0.22$. In comparison to that sample, the coronal activity level difference in the NLTT 41135/41136 system is $|\log(Fx_{\mathrm{surfA}}/Fx_{\mathrm{surfB}})| = 1.1 \pm 0.2$. This result makes the difference in the coronal activity level between the two stars of this system highly significant – it is at a $\approx 3.44\sigma$ level of the control sample. This value is, however, an upper limit since the control sample also consists of systems with one undetected component. If we consider only systems with both stars detected, the significance level of the activity difference in the NLTT 41135/41136 system rises to 3.7σ, where the mean activity difference of the detected binaries is $|\log(Fx_{\mathrm{surfA}}/Fx_{\mathrm{surfB}})| = 0.31 \pm 0.21$.

The possible sources of activity difference between the stellar components of binary systems in our control sample were discussed in Section 3.4.1. Considering their impact on the activity difference in the NLTT 41135/41136 system, the effect of the fully convective boundary should be negligible since both stars are, given their *Gaia* color, fully convective, as well as the effect of the coronal emission regime since both stars have unsaturated X-ray emission. The effects we cannot quantify are the possible impact of activity cycles and the stochastic, short-term X-ray variability. However, the control sample provides a good estimate of the combined effect of all aforementioned phenomena and confirms the high significance of tidal interactions occurring between the brown dwarf and its host.

Furthermore, we can also exclude that the brown dwarf itself contributes significantly to the observed X-ray photons. Only very young brown dwarfs at ages of a few million years have been found to be X-ray emitters [MS02; Neu+99; PF05], with flaring events providing their peak luminosity [Rut+00; Ste04]. Old brown dwarfs are found to be X-ray quiet with $\log L_{\mathrm{x}}[\mathrm{erg/s}] \lesssim 25$ [Ste+06]. Therefore, with the kinematic age of our target system being at least 1 Gyr [Irw+10], the quiescent X-ray emission from the brown dwarf corona can be considered insignificant.

We therefore physically interpret the activity difference as a consequence of star-brown dwarf interaction. Tidal interactions between a slowly rotating star and its quickly orbiting satellite are expected to lead to a transfer of angular momentum from the orbit of the satellite into the spin of the star [Zah77]. We do not have direct information about the rotational period of NLTT 41135 in order to compare it to the rotation of its stellar companion. However, we can estimate their expected rotational periods from activity-rotation relationships. We use the relationships from [Wri+18] for fully convective stars, respectively, to estimate the convective turnover times and then, from the activity indicator R_{x}, the stellar rotation period. We find an expected rotation period of ca. 36 days for NLTT 41135, and a much longer expected rotation period for NLTT 41136 of the order of 97 days. If NLTT 41135 had a similarly low activity level as its stellar companion, i.e. $\log R_{\mathrm{x}} \approx -4.9$, we would expect a rotation period of roughly 114 days.

Keeping in mind that these expected rotation periods have large uncertainties, we perform an order-of-magnitude estimate of the angular momentum transfer that we expect to have taken place to make NLTT 41135 rotate at a ca. 36-day period instead of a 114-day period. If we approximate the angular momentum of NLTT 41135 with that of a rotating solid sphere ($L_{\mathrm{ang}} = 2/5 M_* R_* \omega$, with $\omega = 2\pi/P_{\mathrm{rot}}$ being its rotational

frequency, and M_* and R_* being the stellar mass and radius, respectively), the difference in angular momentum between the 36-day and the 114-day rotational states amounts to about 2.5×10^{36} g cm/s. The present-day orbital motion of the brown dwarf has an angular momentum of $L_{\rm orb} = a_{\rm sem} M_{\rm BD} v_{\rm BD} \sim 1.7 \times 10^{50}$ g cm/s, with $M_{\rm BD}$ and $v_{\rm BD}$ being the mass and the orbital velocity of the brown dwarf, respectively, and $a_{\rm sem}$ being the orbital semi-major axis. The brown dwarf's orbital angular momentum is more than 10 orders of magnitude larger than the star's rotational angular momentum. Therefore, even a slight shrinking of the brown dwarf's orbit can easily supply enough angular momentum to spin up the central star to the observed levels. We, therefore, conclude that tidal interactions between low-mass stars and brown dwarfs is indeed a viable scenario for stellar spin-up.

3.4.3 The difference in observed energy ranges as a source of activity difference

One technical aspect that has to be considered in the discussion of the origin of activity differences in all our systems is the different energy ranges that are encompassed by the various instruments we use. As we discuss in Appendix 3.6.1 and show in Table 3.4, the eROSITA and *Chandra*/HRC instruments - with the energy bands of 0.2-2.3 and 0.08-10.0 keV, respectively - are collecting a similar amount of energy as if they were to observe within the canonical energy band of 0.2-2.0 keV for the given coronal emission and temperature[¶¶]. The differences in fluxes that arise from the difference in the observed energy bands are well within the coronal activity difference uncertainty given in Table 3.3. Also, we are interested in the flux ratio of two stars observed in the same energy band; therefore, the mismatch in energy bands should not affect the reliability of our results.

3.5 Summary and conclusion

To estimate the significance of tidal interactions between a star and its close-in companion, we analysed the X-ray observation of the system NLTT 41135/41136 taken by the *Chandra* X-ray Observatory. Here, the NLTT 41135 component consists of an M5V dwarf and a T6-T8 brown dwarf in close orbit, while their M4V dwarf companion, NLTT 41136, is the primary star of the system. Previous radial velocity and astrometric measurements have indicated that the whole system is kinematically old and belongs to the thick Galactic disk [Irw+10]. Our observations show that the quiescent X-ray surface flux of NLTT 41135 is more than an order of magnitude higher than that of NLTT 41136.

To put this flux difference in context, we calculated the X-ray surface fluxes of stars in 25 wide binary systems consisting of M dwarf stars similar in stellar parameters. We found the mean activity difference in these systems - the activity difference parameter being the absolute value of the logarithm of the surface flux ratio - to be $|\log(F\mathrm{x}_{\rm surfA}/F\mathrm{x}_{\rm surfB})| = 0.34 \pm 0.22$, while the same parameter for the NLTT 41135/41136 system has the value of $|\log(F\mathrm{x}_{\rm surfA}/F\mathrm{x}_{\rm surfB})| = 1.1 \pm 0.2$. This result makes the BD-hosting system a 3.44σ outlier.

[¶¶]The stellar coronae of cool stars emit the bulk of their magnetically induced high energy radiation in the 0.2-2.0 keV band (see e.g. [GGS97b]).

We found that in some of our reference systems, stars were in different coronal emission regimes, were likely on different sides of the boundary between partially and fully convective M dwarfs, and showed short-term stochastic variability. On the other hand, NLTT 41135 and NLTT 41136 are both fully convective, operate in the unsaturated emission regime, and have their quiescent activity level compared to one another. Therefore, the observed excess in the coronal activity of the brown dwarf-host NLTT 41135 is most likely induced by the spin-up process due to angular momentum transfer from the brown-dwarf orbit to the stellar spin via tidal interactions.

This is the first study that quantifies the impact of close-in brown dwarfs on the evolutionary path of main-sequence, low-mass stars. The estimated change in rotation period of $\approx$ 80 days and measured increase in the coronal activity level by one order of magnitude question the reliability of these parameters as proxies for the stellar age of main-sequence stars. This being said, tidal interactions might not be the only type of interaction occurring in these types of systems. Although tidal interactions - due to the mass ratio of $\approx$ 5:1 - most likely play a significant role between NLTT 41135 and its orbiting brown dwarf, as in a binary system consisting of a solar-type star and an M dwarf star, the existence of magnetic interactions between these two objects and their impact on NLTT 41135 remains an open question. Therefore, more studies of wide binary systems with and without close-in companions will improve our understanding of the impact the different types of interactions might have on the evolution of low-mass, main-sequence stars.

Acknowledgements

The authors thank the anonymous referee for their valuable comments. The authors thank Dusán Tubin for providing eROSITA-derived upper limits on the X-ray fluxes for several stars, Dr. Enza Magaudda for providing saturation limits for M dwarf stars in the saturation regime, and Dr. Matthias Mallonn for a fruitful discussion on the control sample for the presented analysis. NI and KP acknowledge support from the German Leibniz-Gemeinschaft under project number P67/2018. M.A.A. acknowledges support from a Fulbright U.S. Scholar grant co-funded by the Nouvelle-Aquitaine Regional Council and the Franco-American Fulbright Commission. M.A.A. also acknowledges support from a Chrétien International Research Grant from the American Astronomical Society. The scientific results reported in this article are based in part on observations made by the *Chandra* X-ray Observatory. This research has made use of data obtained from the 4XMM XMM-Newton serendipitous source catalogue compiled by the 10 institutes of the XMM-Newton Survey Science Centre selected by ESA. This work is based on data from eROSITA, the soft X-ray instrument aboard SRG, a joint Russian-German science mission supported by the Russian Space Agency (Roskosmos), in the interests of the Russian Academy of Sciences represented by its Space Research Institute (IKI), and the Deutsches Zentrum für Luft- und Raumfahrt (DLR). The SRG spacecraft was built by Lavochkin Association (NPOL) and its subcontractors, and is operated by NPOL with support from the Max Planck Institute for Extraterrestrial Physics (MPE). The development and construction of the eROSITA X-ray instrument was led by MPE, with contributions from the Dr. Karl Remeis Observatory Bamberg & ECAP (FAU Erlangen-Nürnberg), the University of Hamburg Observatory, the Leibniz Institute for Astrophysics Potsdam (AIP), and the

Table 3.4: Given are the input energy bands in which systems in our sample were observed, an assumed input flux F_{xi}, and the corresponding output flux F_{xo} in the canonical energy band for various coronal temperatures. The parameter $|\log(F_{xi}/F_{xo})|$ shows how much the activity difference parameter is affected due to the difference in energy bands (EB).

input EB [keV]	output EB [keV]	$\log_{10} T$ [K]	F_{xi} [erg/s/cm^2]	F_{xo} [erg/s/cm^2]	$\lvert\log(F_{xi}/F_{xo})\rvert$
0.08 - 10.0	0.2 - 2.0	6.0	10^{-14}	10^{-14}	0.0
		6.5		9.992×10^{-15}	0.00035
		7.0		9.453×10^{-15}	0.024
0.2 - 2.3	0.2 - 2.0	6.0	10^{-14}	10^{-14}	0.0
		6.5		9.995×10^{-15}	0.00022
		7.0		9.811×10^{-15}	0.008

Institute for Astronomy and Astrophysics of the University of Tübingen, with the support of DLR and the Max Planck Society. The Argelander Institute for Astronomy of the University of Bonn and the Ludwig Maximilians Universität München also participated in the science preparation for eROSITA. The eROSITA data shown here were processed using the eSASS software system developed by the German eROSITA consortium. This research has made use of the VizieR catalogue access tool, CDS, Strasbourg, France (DOI : 10.26093/cds/vizier). The original description of the VizieR service was published in 2000, A&AS 143, 23. This research made use of Astropy,[***] a community-developed core Python package for Astronomy [Ast+13; Ast+18]. This work has made use of data from the European Space Agency (ESA) mission *Gaia*[†††], processed by the *Gaia* Data Processing and Analysis Consortium (DPAC[‡‡‡]). Funding for the DPAC has been provided by national institutions, in particular the institutions participating in the *Gaia* Multilateral Agreement.

Data Availability

The eROSITA data used in this work will be part of an international data release and will be accessible via the eROSITA-DE Science Portal[§§§]. The *Chandra* and *XMM-Newton* data used in this work are publicly available at the *Chandra* Data Archive and the *XMM - Newton* Science Archive. The source ID of each observation used in this research is given in Appendix 3.6.2.

3.6 Appendix

3.6.1 Energy range flux comparison

The M dwarf binary systems considered here have been observed with various X-ray instrument set-ups and cover different energy ranges. From our control sample, eROSITA has observed 14 systems, nine systems were observed with *XMM-Newton's EPIC* camera, and eight systems with *Chandra*, out of which two were observed with HRC-I and HRC-S,

[***] http://www.astropy.org
[†††] https://www.cosmos.esa.int/gaia
[‡‡‡] https://www.cosmos.esa.int/web/gaia/dpac/consortium
[§§§] https://erosita.mpe.mpg.de/

and the rest with the ACIS instrument. NLTT 41135/41136 was observed with HRC-I. The eROSITA systems are observed in the 0.2-2.3 keV energy range; the HRC observations, both with the imager (I) and the spectrometer (S), are made in the 0.08-10.0 keV range, while the *XMM-Newton* systems have their flux estimated in the 0.2-2.0 keV range.

In Table 3.4, we show how the flux observed in one of the considered bands converts to the flux in the canonical 0.2-2.0 keV band. For this task, we used the online tool WEBPIMMS (v4.11a). As the parameter that shows the flux difference due to different energy bands, we used the absolute value of the logarithm of the flux ratio. This is a good representation of the impact the difference in the energy band will have on the activity difference parameter we use since it is also represented by the absolute value of the logarithm of the surface flux ratio. Although, we calculate the X-ray surface flux of stars, which aside from the observed flux, needs the knowledge of stellar radius and distance, not considering these values here is appropriate since we compare the flux of the same star in different energy bands.

3.6.2 Notes on individual systems

Here, we provide analysis details on systems that were observed with the XMM-Newton Space Observatory and the Chandra X-ray telescope. In general, the extraction region for sources observed with *XMM-Newton* has a radius of 15", while the radius of the background extraction region is 60". For *Chandra* sources, the extraction region has a radius of 1.5", while the background extraction region has a radius of 15". If the extraction radii differ from these values, we note it in Table 3.5 in column r_{source}.

We examined the X-ray light curve of each observation for flaring events and found one strong flare (peak count rate is $5-7\times$ the quiescent count rate) in the light curve of GJ 15 A. The X-ray flux given in Table 3.3 for this source is calculated excluding the time during which the flare occurred. All other sources observed with *XMM-Newton* and *Chandra* show occasional fluctuation, but no significant increase in count rate.

For stars where we could not determine the hardness ratio due to the detector properties or insufficient counts, we assumed the coronal temperature to be $\log_{10} T[\mathrm{K}] = 6.477$. The two bands used to estimate the hardness ratio are the soft band covering the range S = 0.2-0.7 keV, and the hard band covering the range H = 0.7-2.0 keV. The hardness ratio is estimated via HR = (H-S)/(H+S) (see [IPH22] for details).

Table 3.5: Notes on individual systems

component	obs ID	mission	camera	HR	$\log_{10} T$ [K]	r_{source}
Ross 868	500670201	XMM	pn	-0.171	6.593	12.0”
Ross 867	500670301 500670401			-0.204	6.582	
GJ 15 A	801400301	XMM	pn	-0.468	6.460	
GJ 15 B			MOS1 MOS2	-0.608	6.396	
TIC 355790951	406540301	XMM	pn	-0.438	6.501	
TIC 355790950			MOS2	/	6.477	
Gaia DR2 1608710752684301312	804270201	XMM	pn	-0.16	6.597	
Gaia DR2 1608710791338814208			MOS2	-0.289	6.552	
TIC 436632332	743070301	XMM	pn	-0.67	6.368	12.0”
TIC 436632331			MOS1 MOS2	-0.213	6.556	
TIC 293303829	211280101	XMM	MOS1 MOS2	/	6.477	
TIC 293303832			pn	/	6.477	
LTT 6326	550970101	XMM	pn	/	6.477	13.0”
LTT 6325			MOS1 MOS2	/	6.477	
G 202-66	605000501	XMM	pn	-0.345	6.533	12.0”
G 202-67			MOS2	/	6.477	
Gaia DR2 3074577322667614976	800400601	XMM	pn MOS1 MOS2	-0.167	6.594	
Gaia DR2 3074630580262065536			pn MOS2	-0.03	6.642	
Gaia DR2 4768120070358120064	744400301	XMM	pn	/	6.477	
Gaia DR2 4768120104717857792				/	6.477	
LP320-163	5767	Chandra	ACIS-I	/	6.477	1”
LP320-162				/	6.477	
LP920-61 A	13585	Chandra	ACIS-I	/	6.477	
LP920-61 B	13588			/	6.477	
SCR J0602-3952-A	3202	Chandra	ACIS-I	/	6.477	1.2”
SCR J0602-3952-B	3450			/	6.477	
Ross 868	1453	Chandra	ACIS-I	0.695	6.695	
Ross 867	3224 4361			0.587	6.641	
TIC 20446899	915	Chandra	ACIS-S	0.585	7.0	
Gaia DR2 3532611086293698560				/	6.477	
G236-1	6655	Chandra	HRC-I	/	6.7	1.2”
G236-2				/	6.7	
Gaia DR2 715928515183511040	16057	Chandra	ACIS-I	/	6.477	
TIC 16151129				/	6.477	
Ross 110 A	7607	Chandra	ACIS-I	/	6.477	
Ross 110 B				/	6.477	

4 Constraining stellar tidal quality factors from planet-induced stellar spin-up

Nikoleta Ilić, Katja Poppenhaeger, Anna Barbara de Andrade Queiroz, Cristina Chiappini

To be submitted to the peer-reviewed journal *Astronomische Nachrichten*

Abstract

The rotational evolution of tight star-planet systems is influenced by tidal interactions between the star and the planet, as was shown recently. The rate at which spins and orbits in such a system evolve depends on the stellar and planetary tidal dissipation efficiency. Here, we present a method to constrain the modified tidal quality factor Q'_* of a planet-hosting star, in the case where its rotational evolution has been altered by its planet through an angular momentum transfer from the planetary orbital motion into the rotation of the stellar convective zone. The altered rotation is estimated from an observed discrepancy of magnetic activity of the planet-hosting star and a coeval companion star, i.e. this method is applicable to star-planet systems with wide stellar companions. We give an example of the planet-hosting wide binary system HD189733AbB, and find that the planet host star's modified tidal quality factor is constrained to be $Q'_* = (1.19 \pm 1.14) \times 10^7$.

4.1 Introduction

The theory of tidal evolution of gravitationally bound systems dates back over two centuries [Dar79b; Hou97; LBB29] and has developed to a great extent since then [EKH98; GS66; Hub74; OL07; TW94]. It was applied when trying to explain the formation of the Solar System, as well as the various planet-moon configurations that it harbors [Fis67; GP68; Gre73; LP86]. The evolution of close stellar binary systems was only understood after considering tidal interactions between the companion stars [HTP02; Hut81; Zah77].

The consideration of tidal interactions between stars and planets began with the discovery of the first exoplanets [CSM00; MQ95a; RF96; Tri+98], and has since contributed to the understanding of the formation and evolution history of star-planet systems [BLM01; BM16; DJ18; OL04b; Pon09].

Generally, there are two types of tides that can occur in tidally interacting bodies: dynamical and equilibrium tides. Dynamical tides can take the form of inertial waves in convective layers or gravity waves in radiative layers. Inertial waves are excited if the tidal forcing frequency $\hat{\omega}$ is smaller than twice the spin frequency Ω of the star: $|\hat{\omega}| < 2|\Omega|$; their restorative force is the Coriolis force, while dissipation takes place due to the turbulent friction of convective motion [OL07]. Gravity waves whose frequency is close to the tidal forcing frequency are excited due to tidal interactions, their restorative force is the buoyancy force, while the dissipation takes place due to radiative dampening [Zah75]. It was found that dynamical tides only play an important role in the tidal

evolution of tight systems before or after the main-sequence phase of fast-rotating stars with outer convective or radiative zones [AMA21; Rao+18].

Equilibrium tides, on the other hand, are large-scale flows in the form of quasi-hydrostatic tidal bulges. They are formed in convective envelopes of low-mass stars or surface layers of planets under the influence of the tidal forcing induced by the orbiting body [Cha33; Dar79b; OV72; SH77; Zah77]. They occur in systems where the interacting bodies are not synchronous with each other's spin and orbital motion. This is typically due to their viscous interiors that give rise to a net tidal torque and facilitate the dissipation of energy. As a consequence, due to the secular transfer of angular momentum between the bodies, the spin and orbital parameters of the system can evolve.

The rate of tidal evolution depends, amongst others, on parameters that account for the efficiency of tidal dissipation in each interacting body. If we consider a star-planet system, these parameters are the tidal quality factor Q_* and Q_p of the star and of the planet, respectively. By definition, the tidal quality factor is the inverse of the phase lag angle between the tidal forcing potential and the tidal bulge [GS66]. Another representation of tidal dissipation efficiency is in combination with the potential Love number of the second order: $Q' \approx Q/k_2$ [OL07], which is the modified tidal quality factor. The Love number k_2 is a dimensionless measure of the interior density profile of the body, which is typically unknown. Therefore, constraining the values of Q'_* and Q'_p can quantify the rate of tidal evolution of star-planet systems, constrain their end configuration, and give insight into the internal structure of stars and planets.

In the past, the value of the stellar Q' was usually derived by applying tidal interaction models and reproducing observed distributions such as the distribution of orbital eccentricities of planets [Bon+17; JGB08], obliquity distribution in star-planet systems [Han12], distribution of extrasolar planets in circular orbits [Pen+12], the orbital separation distribution of planets [CJ18], the distribution of tidally evolved binary star systems [LBR96], and the remaining lifetime of Hot Jupiters [Pen+18], and was found to be in the range of $10^5 < Q'_* < 10^9$, where the lower value corresponds to higher dissipation efficiency and vice versa. Additionally, it was also found that the modified tidal quality factor might not be constant, but is rather a function of the tidal forcing frequency [JGB08; OL07; Pen+18]. Given the large range of possible stellar Q'-values derived from tidal interaction models, we introduce an analytical method to constrain the modified tidal quality factor of planet-hosting stars in wide stellar binary systems.

In section 2, we describe the method to constrain Q'_* from observed activity differences in wide planet-hosting binary systems. In section 3, we demonstrate the methodology by applying the steps on the wide binary system HD 189733AbB and calculating the modified tidal quality factor of the planet-hosting star. A comparison with literature values for planet-hosting stars is given in Section 4, where we also discuss issues regarding stellar spin-down, intrinsic activity variability, tidal evolution timescales, and uncertainties due to the employed activity-rotation relation. In section 5 we summarize the findings made in this study.

4.2 Methodology

It was shown that tidal interactions between a close-in planet and its host star can lead to a spin-up of the host star. Specifically, it was demonstrated that stars orbited by close-in

massive planets tend to have higher magnetic activity than their coeval, planet-free stellar companions, after accounting for the activity bias in planet detection [IPH22; PW14]. Since magnetic activity is driven by stellar rotation [Noy+84; Pal+81; Piz+03; Wri+11], this translates to an *over-rotation* of planet-hosting stars. The magnitude of the over-activity and over-rotation contains information about the strength of the tidal interaction between the planet and the host star. We outline a method here how a measurement of over-activity can be used to constrain the modified tidal quality factor of the host star.

As a short overview, we use the following steps, which are explained in more detail in the following subsections: When a planet-hosting star in a wide binary system has observationally been determined to be over-active, we assign the difference in the stellar X-ray luminosities - corrected by the spectral type (SpT) difference - to the tidal impact an orbiting planet may have on the host star (see [IPH22]). By applying the activity-rotation relation for unsaturated main-sequence stars with an outer convective layer [Wri+11], we estimate the corresponding change in the rotation rate of the host star. Further, using the change of the host's rotation rate, we estimate the angular momentum ΔL that was exchanged between the planetary orbit and the stellar spin, the change of the orbital semi-major axis Δa, and, lastly, the stellar modified tidal quality factor Q'_*.

4.2.1 X-ray luminosity change

In the most general case, binary stars have different spectral types. Therefore, firstly the activity difference due to the SpT difference has to be accounted for. [IPH22] introduced a method where they employ the volume-limited sample of F/G-, K-, and M-type field stars in the solar neighborhood [SL04a], observed with ROSAT, from which they assemble X-ray luminosity distribution function for each SpT (see Figure 3 in their study). The mean value of each distribution is shifted with respect to the other two, which is interpreted as the intrinsic difference in the activity level due to the SpT difference.

To account for the activity difference due to the SpT difference of the binary stars, [IPH22] compared the percentile positions of the stars, for which they employed the mean value and standard deviation of the respective luminosity distribution. If both stars have a similar state of their rotation and activity evolution, they should be found at similar percentiles of their respective distribution. However, if there is a significant difference in the percentile values, it is assumed to be due to the tidally induced spin-up and the subsequent X-ray luminosity increase of the planet host.

Similarly, here we assume the percentile value of the stellar companion as that of the planet-hosting star and use it to calculate the X-ray luminosity value if the orbiting planet has no tidal impact. If we assume that the A component is the planet host and has SpT Y, while the B component has SpT Z, the expected *no-tidal-impact* X-ray luminosity of the A component is:

$$L_{x(noTI)}(A) = f_Y^{-1}(f_Z(L_x(B))). \tag{4.1}$$

Here, f_Z is the X-ray luminosity distribution function for SpT Z and gives the percentile value for the given X-ray luminosity, while the f_Y^{-1}-function estimates the X-ray luminosity for the given percentile value in the X-ray luminosity distribution for SpT Y. For more details see Fig. 4.1.

However, one has to bear in mind that the field star sample obtained by [SL04a] and

used by [IPH22] to characterize the X-ray luminosity difference of coeval stars with different SpT consists of differently aged field stars found in various stages of their evolutionary paths. Although main-sequence stars are particularly stable, their rotation rates and activity levels decrease with age, which introduces a broadening of the observed X-ray luminosity distribution.

This implies that the coeval stars with different spectral types are expected to have an SpT-induced activity difference that is less pronounced than suggested by the field stars sample. A preliminary analysis of wide binary systems indeed shows that the activity difference due to SpT difference is lower (Dsouza et al. in prep.). Therefore, basing an estimate of the tidally-driven activity difference between a planet host and its coeval companion on stellar samples with mixed ages such as the solar neighborhood leads most likely to an underestimate. Further work on wide binary systems can help make the estimates we outline here more precise.

4.2.2 Rotation period change

Having estimated the expected X-ray luminosity of the planet-hosting star in the absence of the tidal influence of its planet, we can further estimate the (slower) rotation period the host would have in this case. For this task, we employ the activity-rotation relation:

$$\log R_x = \log C + \beta \log R_o. \tag{4.2}$$

Here, the activity indicator is the ratio of the stellar X-ray luminosity to the bolometric luminosity $R_\mathrm{X} = L_\mathrm{X}/L_\mathrm{bol}$, the Rossby number is the ratio of the stellar rotation period to the convective turnover time $R_\mathrm{o} = P_\mathrm{rot}/\tau$, C is the proportionality constant, and β is the power-law slope of the unsaturated regime. The slope value is adopted from the analysis by [Wri+11] who determined $\beta = -2.7 \pm 0.13$. They also estimated the convective turnover time as a function of the stellar mass M_* as follows:

$$\log \tau = 1.16 - 1.49 \log(M_*/M_\odot) - 0.54 \log^2(M_*/M_\odot). \tag{4.3}$$

This relationship is valid over the mass range between 0.09 - 1.36 $M_\odot$ and it engulfs main-sequence stars with a convective envelope.

Substituting $L_{\mathrm{x(noTI)}}(A)$ in Equation 4.2 and assuming that the bolometric luminosity L_bol and the convective turnover time τ of the planet host are unaffected by tidal interactions, the Rossby number $R_{\mathrm{o(noTI)}}$ and the rotation period $P_{\mathrm{rot(noTI)}}$ of the planet host in the case of no tidal impact of the planet can be estimated.

Here, it has to be considered that the observational stellar samples used to define the activity-rotation relation we employ, conatins significant scatter between the log Rx and log Ro relationship. We consider the scatter to be a source of uncertainty in the derivation of $R_{\mathrm{o(noTI)}}$, in addition to the measurement uncertainty of employed parameters. To quantify this uncertainty, we used the observed sample from [Wri+11] to calculate the standard deviation of stars in the unsaturated regime around the activity-rotation relation $d \log Ro = \log \frac{P_{rot}}{\tau} - \frac{(\log R_x - \log C)}{\beta}$. We computed a standard deviation of $\sigma = 0.166$ dex, which we add to the uncertainty budget of $\log R_{\mathrm{o(noTI)}}$. Since the uncertainty of $P_{\mathrm{rot(noTI)}}$ is asymmetric in linear space (see Table 4.2), we use the mean uncertainty and assume error propagation to calculate the uncertainties of subsequent *no-tidal-impact* parameters.

4.2.3 Angular momentum change

How an exchange of angular momentum between a planet's orbit and the stellar spin can influence the evolution of a star-planet system has been presented by [Pen+12; PZJ14]: a reduction in the semi-major axis of the planet leads to the increased angular momentum of the host star. We make the simplifying assumption that a shrinking planetary orbit due to tidal star-planet interactions just constitutes an angular momentum dump into the star, distributed over a certain amount of time. In reality, there may be subsequent changes to the stellar wind and magnetic braking due to this process, and we discuss the limitations arising from that in section 4.4.3.1.

Here we continue by estimating the expected change in angular momentum of the star from the estimated change in surface rotation derived in the previous step. Stars are known to have differential rotation, both at the surface and in radial depth. However, in a modeling context, one often resorts to a simplification, where the convective envelope and the radiative core of low-mass main sequence stars are approximated to rotate as solid bodies at different rates [All98; Bou08; Den+10; Irw+07]. To quantify the amount of angular momentum transferred from the planet's orbital motion to the stellar spin, we only consider the rotation of the convective envelope and assume that the coupling timescale and angular momentum transport between the envelope and the core are not influenced by tidal interactions.

The angular momentum of a spherical shell with a density profile $\rho(r)$ and the angular velocity ω_{surf} is:

$$L = 4\pi\omega_{surf} \int_{R_{cz}}^{R_*} r^4 \rho(r) dr, \tag{4.4}$$

where R_* is the radius of the star, while R_{cz} is the height of the convective zone base in units of the stellar radius. Here, we assume the density profile of the Sun [BP04]*, which, in the convective envelope, can be approximated by a second-order polynomial: $\rho(r) = a\,r^2 + b\,r + c$, where $a = 4.753 \times 10^{-15}\,\mathrm{kg/m^5}$, $b = -6.571 \times 10^{-6}\,\mathrm{kg/m^4}$, and $c = 2276\,\mathrm{kg/m^3}$.

The change in the angular momentum of the stellar convective envelope due to tidal interactions with an orbiting planet is:

$$\Delta L = 8\pi^2 \left(\frac{1}{P_{rot}} - \frac{1}{P_{rot(noTI)}} \right) \int_{R_{cz}}^{R_*} r^4 \rho(r) dr \tag{4.5}$$

4.2.4 Semi-major axis change

Having estimated the amount of the exchanged angular momentum, we can estimate the change of the semi-major axis due to tidal interactions:

$$\Delta a = \left(\frac{\Delta L}{M_p M_* \sqrt{\frac{G}{M_p + M_*}}} + \sqrt{a} \right)^2 - a. \tag{4.6}$$

*The density profile was adopted from the following source: http://www.sns.ias.edu/~jnb/SNdata/Export/BP2004/bp2004stdmodel.dat.

Here, M_p and M_* are the masses of the planet and the star, a is the observed semi-major axis of the planet's orbit, and G is the gravitational constant.

The above equation was derived by integrating Equation 2 given by [Pen+12; PZJ14] over the boundaries from $L \longrightarrow L + \Delta L$ for the stellar angular momentum and from $a+\Delta a \longrightarrow a$ for the orbital semi-major axis: the stellar rotation gained angular momentum, while the semi-major axis of the planetary orbit reduced due to the loss of angular momentum.

It is assumed that the angular momentum contribution from the planet's rotation is small and that the tides raised on the planet force it into synchronization with the orbital motion quite early in the system's evolution. Therefore, it is assumed that the angular momentum is only exchanged between the planetary orbit and the stellar spin. Also, by using the above equation, we assume that the planetary orbit is circular and aligned with the stellar equator. Therefore, the angular momentum loss only contributed to the reduction of the semi-major axis of the orbit, not the eccentricity or inclination.

4.2.5 The modified tidal quality factor Q'_*

Finally, to estimate the modified tidal quality factor Q'_*, we employ the equation for tidal evolution of the orbital semi-major axis given as Equation 1 by [Pen+12; PZJ14]. Here, we integrate over the time the planet migrates inward - $T_{\rm in} \longrightarrow T_{\rm sys}$ - and the semi-major axis change - $a + \Delta a \longrightarrow a$:

$$Q'_* = sign(\omega_{surf} - \omega_{orb}) \frac{117}{4} \Delta T R_*^5 M_p \sqrt{\frac{G}{M_*}} \left(a^{\frac{13}{2}} - (a + \Delta a)^{\frac{13}{2}} \right)^{-1}. \tag{4.7}$$

Here, $\omega_{\rm surf}$ and $\omega_{\rm orb}$ are the angular velocities of the stellar surface and the planet in its orbit, and $\Delta T = T_{\rm in} - T_{\rm sys}$, where $T_{\rm in}$ and $T_{\rm sys}$ are the time after formation when the planet started migrating inward and the age of the system, respectively. The factor $sign(\omega_{\rm surf} - \omega_{\rm orb})$ indicates the direction of angular momentum exchange: if the orbital angular velocity is higher than the angular velocity of the stellar surface, the angular momentum is transferred from the planet's orbit to the star. This is the case when the planet is found inside the system's co-rotation radius, the distance from the star where the planet's orbital rate and the stellar rotation rate are equal, i.e. the system is synchronized.

Depending on the initial conditions of the system, e.g. the initial stellar spin and the orbital distance of the planet after the protoplanetary disk has cleared, the outward or inward migration of the planet due to tidal interactions occurs. Typically, given that a newly formed star experiences a period of contraction and spin-up, the co-rotation radius is close to the star, while the planet is most likely located at a greater distance. Therefore, angular momentum is transferred from the stellar spin to the orbit, and the planet migrates outward.

After the stellar wind takes over the dominance over the stellar rotation evolution, the co-rotation radius gradually increases, crossing the planet's orbit and leading to the inward migration of the planet. The timescale of the described process is typically a few $\times 10^7$ yr [Bol+12], however, depends on the initial stellar spin and planet location, the efficiency of the stellar wind and tidal dissipation, as well as on the stellar and planetary mass. Hereafter, tidal interactions and magnetic braking dictate the evolution and stability of the star-planet system.

Table 4.1: Stellar and planetary parameters of the star-planet system HD 189733 Ab used and derived in this study.

Parameter	Value	Reference
M_* [$M_\odot$]	0.81 ± 0.03	[Add+19]
R_* [$R_\odot$]	0.78 ± 0.01	[Add+19]
$T_{\rm eff}$ [K]	5053^{+46}_{-45}	[Add+19]
log g	$4.563^{+0.021}_{-0.020}$	[Add+19]
[Fe/H]	$-0.003^{+0.031}_{-0.029}$	[Add+19]
A_v	$0.127^{+0.059}_{-0.058}$	[Add+19]
π [mas]	50.57 ± 0.02	[Gai+22]
G [mag]	7.4284 ± 0.0003	[Gai+22]
Age [Gyr]	6.97 ± 1.02	this work
$L_{\rm bol}$ [erg/s]	$(1.358 \pm 0.053) \times 10^{33}$	[Add+19]
L_x [erg/s]	$(1.296 \pm 0.016) \times 10^{28}$	[IPH22]
R_x	$(9.5 \pm 0.4) \times 10^{-6}$	this work
$P_{\rm rot}$ [day]	11.953 ± 0.009	[HW08]
τ [day]	19.8 ± 1.2	this work
R_o	0.605 ± 0.044	this work
M_p [$M_{\rm Jup}$]	$1.130^{+0.047}_{-0.045}$	[Add+19]
R_p [$R_{\rm Jup}$]	$1.142^{+0.036}_{-0.034}$	[Add+19]
$P_{\rm orb}$ [day]	$2.2185788^{+0.0000091}_{-0.0000076}$	[Add+19]
a [AU]	$0.03098^{+0.00043}_{-0.00039}$	[Add+19]
e	$0.024^{+0.026}_{-0.014}$	[Add+19]
i [°]	$85.27^{+0.24}_{-0.23}$	[Add+19]

As in the previous step, a circular orbit and synchronization between the planet's rotation and orbital motion are assumed.

4.3 Example: the planet-hosting wide binary system HD 189733

Here we present an application of the described method to the Hot Jupiter-hosting system HD 189733 AbB.

4.3.1 The system

The system HD 189733 AbB is composed of an early-K dwarf and a mid-M dwarf, that are separated by at least ≈ 220 AU, which makes it a wide stellar binary system [Bak+06; Mug19]. The primary star is orbited by a Hot-Jupiter-type planet with an orbital period of ≈ 2.2 days [Bou+05]. The stellar parameters of the host and the relevant planetary parameters are given in Table 4.1. The planet has a low-eccentricity orbit that is aligned with the stellar equator.

The system was observed in the X-ray regime by the Chandra X-ray Observatory and

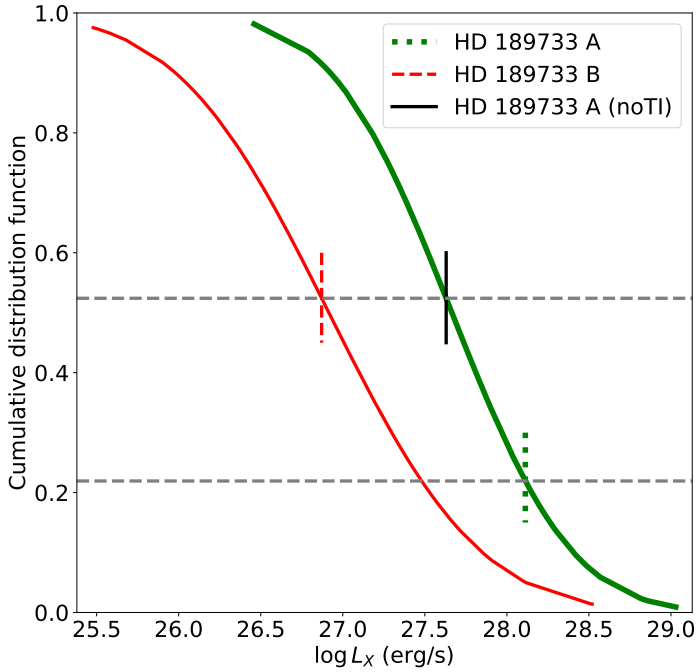

Figure 4.1: The X-ray luminosity cumulative distribution function of K-, and M-dwarfs in the solar neighborhood as thin red and thick green solid curves, respectively. The green dotted and red dashed lines show the position of HD 189733 A and B, respectively, while the black solid line indicates the position of HD 189733 A in the *no-tidal-impact* regime.

the XMM-Newton Space Telescope. Since the components have an angular separation of $\approx 11''$, only *Chandra* is able to resolve the two components. Here, we adopt the X-ray luminosity values estimated by [IPH22], who analysed the *Chandra* observations and provided the percentile values of the stars in their respective X-ray luminosity distributions (see Section 4.2.1 for more details). They found that HD 189733 A has an X-ray luminosity of $L_x(A) = 1.3 \times 10^{28}$ erg/s, corresponding to the 78^{th} percentile in the K-dwarf distribution, while HD 189733 B has an X-ray luminosity of $L_x(B) = 7.4 \times 10^{26}$ erg/s, corresponding to the 48^{th} percentile in the M-dwarf distribution.

Figure 4.1 shows the cumulative distribution functions of the X-ray luminosities for K- and M-dwarf stars in the solar neighborhood in the energy range 0.2-2.0 keV. The green dotted and red dashed lines show the position of HD 189733 A and B, respectively, while the black solid line indicates the position of HD 189733 A if the orbiting Hot Jupiter did not have any tidal impact on the star (see Section 4.3.3 for more details).

4.3.2 Age of the planet host

To estimate the value of the modified tidal quality factor Q'_* for the planet host, we need knowledge of the system's age. The time interval in which the planet has migrated inward and exchanged angular momentum with the star will constrain the efficiency

Table 4.2: Parameters of HD 189733 A observed and estimated in the cases when the orbiting planet has a tidal impact (TI) and when it does not (no TI). The uncertainty of $\log R_o$ for the noTI regime includes the contribution due to the stellar scatter around the activity-rotation relation.

parameters	TI	noTI
L_x [erg/s]	$(1.296 \pm 0.016) \times 10^{28}$	$(4.263 \pm 0.213) \times 10^{27}$
$\log R_x$	-5.020 ± 0.018	-5.503 ± 0.028
$\log R_o$	-0.218 ± 0.025	-0.039 ± 0.174
P_{rot} [day]	11.953 ± 0.009	$18.04^{+8.53}_{-5.79}$

of tidal dissipation within the system: the less time the system needed to evolve to the current state, the more efficient the tidal dissipation seems to be (see Eq. 4.7).

The age of HD 189733 A was estimated using stellar evolutionary models [Ghe+10; MSS15; Sou10; TWH08] and discussed in the context of the primary's and secondary's X-ray luminosity [PSW13; PW14; San+10]. Since tidal interactions with a Hot Jupiter-type planet has shown to be able to alter the stellar rotation rate and X-ray emission, i.e. making the host appear younger, we will not consider the ages estimated by using the primary's X-ray luminosity. The ages estimated with stellar evolutionary models range from 1-7 Gyr for HD 189733 A, with an uncertainty budget close to 100%.

To obtain a better constraint on the age of the planetary host, we used the isochrone-matching code `StarHorse`, a Bayesian tool for estimating stellar parameters, including age, based on photometric, spectroscopic and astrometric data [Que+18; San+16]. The code incorporates different priors for the main Galactic components and has been extensively validated against external methods such as asteroseismology [And+19; Que+20]. As input parameters for HD 189733 A, we apply the *Gaia* DR3 G magnitude and parallax, mass, radius, bolometric luminosity, effective temperature, surface gravity, metallicity, and V-band extinction given in Table 4.1. With this tool, we estimated the age of HD 189733 A to be 6.97 ± 1.02 Gyr, which indicates a system older than the Sun. The age of the host is now better constrained with an uncertainty of less than 15%.

4.3.3 Applying the analytical method

Having the observed X-ray luminosities of the HD 189733 stellar components, we can estimate the X-ray luminosity of the host if the orbiting planet did not have any tidal impact using Eq. 4.1. This corresponds to an X-ray luminosity of $L_{X(noTI)}(A) = (4.26 \pm 0.21) \times 10^{27}$ erg/s. Here, we assumed the luminosity uncertainty of 5%, corresponding to the X-ray luminosity uncertainty of the B component.

By applying Equation 4.2, and assuming that the bolometric luminosity L_{bol} and the convective turnover time τ are not affected by tidal interactions, the planet host would have a rotation period $P_{rot(noTI)} = 18.04^{+8.53}_{-5.79}$ days. Table 4.2 summarizes the activity and rotation parameters of the planet-hosting star in the regime of tidal impact (TI) and no tidal impact (noTI) from the planet. In addition, Figure 4.2 shows the stellar sample used by [Wri+11] and HD 189733 A. The difference in the position of the planet host in the two regimes shows the significance of tidal interactions in the evolution of star-planet systems.

The amount of angular momentum transferred from the planet's orbit to the stellar

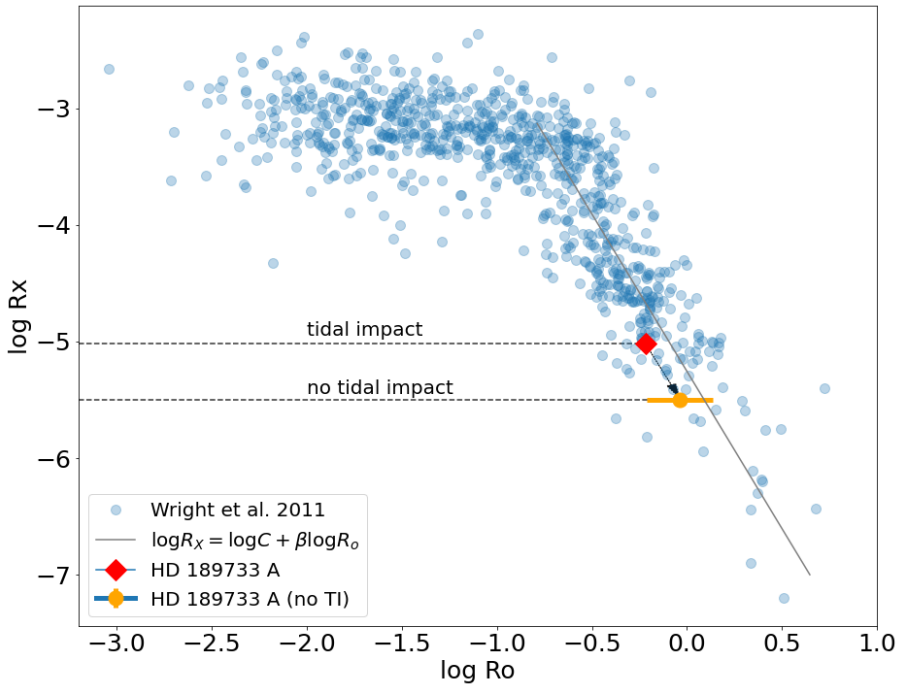

Figure 4.2: The stellar sample used by [Wri+11] and the activity-rotation relation fitted for the bulk of the unsaturated regime with the slope $\beta = 2.7$ (grey line). The planet host, as observed, is shown with the red diamond symbol, while the filled orange circle is the hypothetical *no-tidal-impact* position of HD 189733 A. The positional change of HD 189733 A due to tidal interactions is indicated by the black arrow.

Table 4.3: Parameters derived with our analytical method and used to deduce the tidal dissipation efficiency of HD 189733 A.

ΔL [kg m^2/s]	Δa [AU]	Q'_*
$(4.9 \pm 3.8) \times 10^{40}$	0.0020 ± 0.0016	$(1.19 \pm 1.14) \times 10^7$

convective envelope given by Equation 4.5, the change of the orbital semi-major axis given by Equation 4.6, and the stellar modified tidal quality factor Q'_* given by Equation 4.7 are summarized in Table 4.3. For Eq. 4.5, we estimated the height of the convective envelope base to be $R_{cz} = 0.677\,R_*$ using the K-dwarf stellar sample by [Wri+11]. The estimted modified tidal quality factor of HD 189733 A is $Q'_* = (1.19 \pm 1.14) \times 10^7$. The uncertainties are large, mainly driven by the scatter in the rotation-activity relationship. The derived order of magnitude of Q'_* indicates a moderately efficient tidal dissipation in the stellar interior.

4.4 Discussion

4.4.1 The derived Q'_* constraint in context

We have introduced a method to analytically, using X-ray observations of a planet-hosting wide binary system, constrain the modified tidal quality factor Q'_* of the host star which tidally interacts with its *close-in massive* planet. The main assumption is that if the planet

host appears to be more active than its stellar companion, the excess activity is due to the tidal spin-up or at least the slow-down of the process of magnetic braking due to the magnetized stellar wind. Our constraints, when used for a single star-planet system, are quite loose; however, with improvements to stellar rotation-activity relationships as well as with applications to larger samples of star-planet systems for stars of similar spectral types, one can expect to derive tighter constraints.

Until now, the usual approach in estimating the stellar Q'_*-value was to employ tidal evolution models and try to reproduce the distribution of observed star-planet parameters. The study of [JGB08] determined $Q'_* \approx 10^{5.5}$ by reproducing low-eccentricity values for exoplanets closer than $a = 0.2$ AU to their host. On the other hand, [Han12] estimated the stellar modified tidal quality factor of $Q'_* \approx 10^7 - 10^8$ by reproducing the orbital orientation of systems with $P_{\rm orb} < 3$ days. They also found indications that Q'_* depends on the thickness of the stellar convective envelope. Furthermore, [Bon+17] estimated $Q'_* \geq 10^6 - 10^7$ by comparing circularization timescales with stellar ages for planets within $a < 0.05$ AU, and [Pen+18] found that the observed rotation rate of planet hosts can be explained if tidal dissipation depends on the forcing frequency with $Q'_* \approx 10^5$ at $0.5\,\mathrm{day}^{-1}$ to $Q'_* \approx 10^7$ at $2\,\mathrm{day}^{-1}$ for $P_{\rm orb} < 3.5$ days.

The exoplanet HD 189733 Ab has an orbital period of $P_{\rm orb} = 2.2$ days and is separated from the host star by $a = 0.03$ AU. Its orbit is almost circular with $e = 0.024$ and aligned to host's equator with $i = 85.3°$. The modified tidal quality factor we estimated for the host HD 189733 A ranges from $Q'_* = 10^{5.7} - 10^{7.4}$ with a mean of $Q'_* = 10^{7.1}$. Here, we see that the tidal dissipation efficiency for a hot Jupiter-hosting star determined using our analytical method is within the estimates made by reproducing distributions of star-planet systems with tidal models. The tidal forcing frequency in the HD 189733 A star-planet system is $\hat{\omega} \approx 4.5\,\mathrm{day}^{-1}$, which shows that the Q'_*-value we estimated corresponds with the conclusion made by [Pen+18].

4.4.2 Applicability of the analytical method

Given the uncertainty budget of the modified tidal quality factor estimated with the introduced analytical method, its values span two orders of magnitude. The largest contributor to the uncertainty is the stellar scatter of the activity-rotation relation. Considering the study by [IPH22], the planet-hosting wide binary HD 189733 has the largest currently observed activity difference between two stellar components, i.e. already presenting a favourable case.

For the future, an analysis of a sample of planet-hosting wide binary systems with similar host and planetary orbit parameters should yield a well-constrained modified tidal quality factor for a specific star-planet configuration. Otherwise, analysing planet hosts with different spectral types could yield a dependence of the Q'_*-value with stellar parameters like the convective envelope depth, as was suggested by [Han12]. Also, estimating the forcing frequency $\hat{\omega}$ for each such star-planet system could contribute to a better understanding of the relationship between Q'_* and $\hat{\omega}$.

4.4.3 Caveats

4.4.3.1 The impact of magnetic braking

The way we treated the angular momentum exchange between planetary orbit and host star spin basically amounts to an angular momentum dump stretched over a certain time period, while assuming that all other spin-down relevant processes stay the same. However, stars with higher activity levels are expected to have more efficient magnetic braking due to their wind properties (e.g. [Mes68; MS87]). This indicates that the estimated amount of angular momentum exchanged between the star and the planet, derived from the X-ray luminosity difference between the stellar components, is actually a lower limit since the host star likely experiences a higher magnetic braking rate than its stellar companion.

Additional caution is needed when comparing stars with different internal structures, e.g. binary companions with an outer radiative and convective envelope, or partly and fully convective stars since the mechanisms contributing to their angular momentum loss might be different. We therefore consider our described method to be applicable to pairs of stars with a convective envelope and a radiative core.

4.4.3.2 Stellar activity variability

The stellar activity level can vary on different timescales. This will impact the observed activity difference between stellar components. The activity variability intrinsic to a star, not caused by external sources, can have various origins and has the form of stochastic variability on short timescales, or of activity cycles on longer timescales. Given the usual observation time of 30-100 ks in the X-ray domain, the stochastic variability of a star is to some degree accounted for when estimating the X-ray luminosity from one observation run. To also cover the activity variability due to an activity cycle, if the considered stars experience any at all, the binary system should be observed in different epochs, spanning over several years. This approach will cover the different activity regimes and will provide the average activity level of both stars. Comparing these activity levels will yield the tidal impact of an orbiting planet, with minimal contribution by the intrinsic activity variability of individual stars.

4.4.3.3 Tidal evolution timescales

The most general orbit is eccentric and inclined to the stellar equatorial plane. We have assumed that the timescales for orbital circularization and alignment are shorter than the stellar age. This might be applicable to the star-planet system HD 189733 A since the planet's orbit has a very small eccentricity and an almost aligned orbit. These characteristics however do not constrain the timescales or the amount of angular momentum that was lost to the stellar spin in the process of circularization or alignment. Therefore, the stellar angular momentum gain from the reduction of the orbital semi-major axis assumed in our methodology provides, strictly speaking, only a lower limit on the modified tidal quality factor Q'_*, meaning that the host star might be less efficient in tidal dissipation.

An issue related to the orbital timescales is the planet's spin-to-orbit synchronization time. Again, by neglecting the angular momentum that was exchanged between the planet's spin and the orbit, we are breaking the angular momentum conservation law.

However, the angular momentum of the planet is orders of magnitude smaller than that of the star and contributes to the overall angular momentum budget of the star-planet system only marginally. If the planet's spin and orbit are asynchronous and the orbit is eccentric, the synchronization process can contribute to the circularization of the orbit if the planet's spin rate is lower than the orbital rate [DLM04]. This alleviates the significance of an eccentric orbit and an asynchronous planet spin in the evolution of the stellar spin; however, the synchronization timescale for this scenario depends on the tidal dissipation efficiency of the planet [MPR10], which constrain is out of the scope of this paper.

4.5 Summary

To better understand the tidal evolution of star-planet systems, the knowledge of their tidal dissipation efficiencies in the form of the tidal quality factor Q_* for stars and Q_p for planets is needed. Here, we introduce an analytical method to estimate the stellar modified tidal quality factor $Q'_* \approx Q_*/k_2$, which is the ratio of the tidal quality factor and the second-order Love number, for planet-hosting stars that reside in wide stellar binary systems.

We demonstrate the analytical method on the planet-hosting wide binary system HD 189733. The planet-hosting star has a modified tidal quality factor of $Q'_* = (1.19 \pm 1.14) \times 10^7$, consistent with results for short orbital period systems. The uncertainty budget, stemming mostly from the stellar sample of the employed activity-rotation relation, suggests that a better constraint of the Q'_*-factor can be achieved on a sample of planet-hosting wide binary systems with similar star-planet configurations.

In general, we recommend considering binary systems where stellar components have a convective envelope and a radiative core, and, optimally, have the same SpT to minimize the impact of the different rates of magnetic braking between the two components. Further, assuming that stars have activity cycles, the best practice in estimating the average X-ray luminosities of stellar components is to use X-ray observations that span over several years, optimally covering different phases of the activity cycles. Lastly, this method should be applied to star-planet systems where the planet's orbit has low eccentricity and is aligned with the stellar equatorial plane, as well as where the stellar rotation period is at least double the orbital rotation period: $P_{rot} \geq 2P_{orb}$, to have no excitation of dynamical tides.

Acknowledgments

NI and KP acknowledge support from the German Leibniz-Gemeinschaft under project number P67/2018. This research made use of Astropy,[†] a community-developed core Python package for Astronomy [Ast+13; Ast+18]. This work has made use of data from the European Space Agency (ESA) mission *Gaia*[‡], processed by the *Gaia* Data Processing and Analysis Consortium (DPAC[§]). Funding for the DPAC has been provided by national institutions, in particular the institutions participating in the *Gaia* Multilateral Agreement.

[†] http://www.astropy.org
[‡] https://www.cosmos.esa.int/gaia
[§] https://www.cosmos.esa.int/web/gaia/dpac/consortium

5 Conclusions & Outlook

Wide stellar binary systems are powerful astrophysical tools. They allow us to distinguish the impact of tidal interactions on stars that host substellar companions by decoupling the tidal signature from the effect of the activity bias induced by planet detection methods. Our analysis of wide binary systems where one component has a planet or a brown dwarf in a tight* orbit showed that tidal interactions impact the evolution of the host star by increasing its rotation rate, and its coronal activity level observed in the X-ray regime. Firstly, we have seen, that close-in massive planets have a greater tidal impact on the host than less massive or further-out planets. Then, we have seen that a brown dwarf can impact an M dwarf so significantly that its rotation period can be decreased by ≈ 80 days and its surface X-ray flux increased by an order of magnitude when compared to its M-dwarf companion. Finally, using the X-ray luminosity difference between a host star and its wide binary stellar companion as a proxy for the tidal impact of an orbiting planet, we have developed an analytical method to estimate the modified tidal quality factor of the host star.

The study described in Chapter 2 is more of a qualitative nature, as we find correlations between various tidal interaction strength parameters and the coronal activity differences between stars in wide binary systems. The study described in Chapter 3 is a quantitative one, as we estimate the significance of the tidal impact on the host star. However, both studies show that given a sufficiently long time interval, a substellar object can make its host star appear younger than it actually is, rendering the typical stellar-age proxies as stellar rotation or X-ray activity as unreliable. This conclusion was anticipated before we introduced the activity difference between wide binary stars as tidal impact proxy, however, the studies described in the previous chapters are the first† to *undoubtedly* point to the significance of star-planet(brown dwarf) interactions.

5.1 Tidal and magnetic interactions

Above, I was consciously careful when I did not write *tidal* star-planet interactions. Tidal interactions are not the only ones postulated to occur between a star and a substellar companion. Magnetic interactions are expected to occur as well. However, for magnetic interactions to occur, both the star and the planet should have a magnetic field, and until the time of writing no exoplanetary magnetosphere was detected [Laz+19; Mur+15]. It is assumed that due to the tidal locking of exoplanets in tight star-planet systems, their rotation period is of the order of several days, which suggests that the planetary dynamo mechanism operating in close-in planets may not be as efficient as in e.g. Jupiter (in case of massive exoplanets) [Gri+04a]. If for a moment we disregard this assumption, and let a Hot Jupiter have a Jupiter-like magnetic field strength [Con+18], magnetic star-planet

*More precisely, a tight orbit is an orbit located inside the corotation radius of the star.

†The study by [PW14] used the X-ray activity in planet-hosting binaries to estimate the age of stars and point to their inequality in systems hosting close-in massive planets.

interactions in these kinds of systems are possible [Cau+19; Kav+19], and can shape star-planet systems alongside tidal interactions [Ahu+21; Ben+19].

However, the lack of a detected magnetosphere of an exoplanet only leaves space for speculation about long-term magnetic effects on the star. One of the most promising ways to detect magnetic fields in exoplanets is by observing the radio electron cyclotron maser emission [Hal+08]. It proved successful in detecting radio emission of magnetic fields of a previously unknown brown dwarf [Ved+20], and is expected to provide the first direct detection of an exoplanetary magnetosphere [Ash+22; Lyn+18; Tur+21]. Until this moment arrives, we can speculate. However, we don't have to speculate about the existence of magnetic fields around brown dwarfs since their auroral signature has been observed [Kao+16; PHK17]. Therefore, it is likely that the brown dwarf in the NLTT 41135/41136 system magnetically interacts with its host, and partly contributes to the measured activity difference between the stars.

The best way to estimate the effect of magnetic interactions on stellar evolution is to determine its impact on the stellar angular momentum. However, as long-term magnetic interactions do not contribute to angular momentum exchange between the orbital motion and stellar rotation, but only reduce the amount of angular momentum loss due to magnetic braking (see Section 1.3.2.1), a torque as in the case of tidal interactions cannot be defined. As a first approximation, magnetic interaction strength parameters as e.g. the magnetic energy flux released due to interactions [CSM00], or the Pointing flux at the base of the magnetic flux tube connecting the star and the substellar companion [Lan13], can be used. We can, then, compare the tidal and magnetic interaction strengths directly to the activity excess of the hosting star, and preferably do it on a sample of brown dwarf-hosting systems. The distribution of systems in the activity difference vs. interaction strength parameter space can reveal, or at least hint to the individual contribution of each interaction type. However, to make the magnetic and tidal impacts comparable, it would be best to use the tidal torque as defined by Equation 2.7, and to define an effective magnetic torque accounting for the angular momentum not lost due to magnetic interactions. This approach could provide empirical constraints on the impact of magnetic and tidal interaction on hosting stars, at least in wide stellar binary systems hosting brown dwarfs.

5.2 Activity difference in wide binary systems without close substellar companions

Another assumption that we considered, aside from assuming that magnetic interactions do not contribute significantly to stellar evolution due to tidal locking, is that coeval stars of the same spectral type *will* have the same X-ray activity level. The comparison sample analysis in Chapter 3 showed that the X-ray surface flux between coeval M dwarfs can vary by a factor of ≈ 2. Although that particular sample is fairly diverse (saturated vs unsaturated and fully convective vs. partly convective stars), it points to the fact that two coeval stars with the same spectral type will most likely differ in their activity levels. Even if the average activity level between them is very similar, having activity cycles in different phases will cause an activity difference in a particular observation epoch, which then can inappropriately be associated with tidal interactions.

On the other hand, using field stars from the solar neighborhood [SL04a] to correct

for the activity difference due to different spectral types might be the other extreme. Typically, field stars have different ages and therefore have more widely distributed activity levels. Using them to normalize the activity difference between coeval stars with different spectral types will provide a larger spectral-type activity correction and, therefore, a lower activity excess due to the tidal impact, thereby reducing the significance of tidal interactions.

The best way to mitigate these issues is to analyse a *comparison* sample (as in Chapter 3) for each spectral type individually (F/G-F/G, K-K, M-M), and each spectral type combination (F/G-K, F/G-M, K-M). Systems with stars of the same spectral type are already under analysis (Dsouza et al., in prep) and they already show that the activity difference between coeval stars is lower than between randomly chosen same-spectral type field stars[‡].

In that analysis, archival data and cataloged X-ray fluxes from the Chandra X-ray Telescope and the XMM-Newton Space Telescope are used. I expect that the Röntgen Survey with an Imaging Telescope Array (eROSITA) instrument onboard the Spectrum-Röntgen-Gamma spacecraft can contribute with many more detected wide binary systems, as its contribution to the comparison sample in Chapter 3 is more than $\approx$ 40%. The complete analysis will provide the baseline in activity difference between components in wide binary systems with every spectral type combination and will allow us to even better pinpoint the significance of interaction processes between stars and their close substellar companions.

5.3 Modified tidal quality factor Q_* across the Main Sequence

The analytical method introduced in Chapter 4 estimates the modified tidal quality factor of planet-hosting stars in wide binary systems. It is the first of its kind as no numerical modeling of tidal star-planet interactions has to be applied, therefore making it an accessible tool for probing parameters of the stellar interior. Although the activity difference used as an input parameter for this method still has to be refined in terms of the previous two discussions, the method is readily applicable to planet-hosting solar-like stars on the main sequence.

However, a drawback to this method is the large uncertainty budget of the modified tidal quality factor Q_*. The main contributor is the uncertainty in the Rossby number of the hypothetical *no-tidal-impact* star which stems from the stellar distribution of the employed activity-rotation relation. The broad distribution of stellar activity and rotation values in the unsaturated regime is most likely due to the sampling of stars with different ages and different spectral types. Refining the activity-rotation relation to the spectral type of the considered host star does not improve the uncertainty budget of Q_*.

A way to have a more precise modified tidal quality factor is to apply the analytical method to a sample of stars: we can constrain the Q-value of stars that cluster around a certain parameter like mass/spectral type and have similar planetary systems, and we can further expand by comparing multiple samples that span across the main sequence.

[‡]We do not expect this result to significantly impact the results shown in Chapter 2 as there we only have one wide binary system (GJ 15) with two M dwarfs. All other systems are a combination of two stars with different spectral types.

Firstly, if similar stars tend to have their (mean) modified tidal quality factors constrained to the same order of magnitude, it will imply that their mass or spectral type is an important determinant. This can further be interpreted as the effect of the convective envelope depth[§] and the convective turnover time, which has been suggested to affect the dissipation efficiency [Zah66b]. If the factor is more widely distributed, it implies that other properties play a significant role. After the behavior of one sample of stars is understood, comparing multiple samples to each other will reveal if the convective envelope plays a crucial role in tidal interactions between a star and its substellar companion.

5.4 Final remark

The focus of this doctoral dissertation was to provide clear observational evidence that substellar companions like planets and brown dwarfs can tidally affect their host stars. We know that tidal forces act between a star and its substellar companion, as the gravitational force necessary for tidal interactions is ubiquitous. Magnetic interactions between a star and its substellar companion are still in the realm of ambivalence, as no empirical studies determining their long-term effects were undertaken. However, we can assume that if the companion has a magnetosphere, it will have an effect on the host star. Furthermore, if the orbital and rotational motion of the companion are tidal locked, the tidal evolution of the system (inside the corotation radius of the star) will cause a tighter orbit and therefore a faster spin of the companion. This will potentially affect the formation of the companion's magnetosphere and cause magnetic interactions. Finally, an interaction effect not necessarily important for the host star, but for an orbiting planet is its atmospheric loss. The loss is caused by the interaction of the upper atmospheric layer of the planet with the stellar radiation and particles. Therefore, if a star is tidally spun-up, the planet will indirectly cause an increased (or at least a steady) loss of its atmosphere with time. Overall, tidal interactions between stars and substellar companions have many aspects, and all of them have to be considered if we want to understand the evolution of such systems.

[§]One of the steps of the method considers the convective envelope depth in the calculation of the convective angular momentum; therefore, it has to be tested if the step itself causes the correlation.

Acknowledgments

Almost 12 years ago, when I started my bachelor studies, my journey toward being a professional astrophysicist began. Along the way, I had small and significant accomplishments, as well as hurdles. The piece that you hold in your hands now (or look at on a screen) was the most difficult and the most rewarding part. I have learned so much about our Universe and I gained an understanding of its many facets (although I am far from understanding how our Universe works). However, I am most thankful for the awareness that the existence of all leaving beings here on planet Earth is extraordinary, given all the circumstances that have to add up so that life forms, evolves, and eventually wonders about its existence and the world around it. This thought always brings me joy and helps me gain perspective when things start to feel very stressful. Therefore, first and foremost I want to acknowledge that science helped me grow both professionally and personally.

It also brought many beautiful people into my life. Laura and Grace, thank you for cheering me up when my first project failed by bringing me beer, sweets, and emotional support. Ekaterina, thank you for being such a great office buddy, and for the enlightening discussions on star-planet interactions. Judy, you became such a dear friend to me, thank you for all the therapy sessions, especially this year. Eliana, I am happy that we will continue to be office buddies as you are such a joyful person. Thank you for reading the introduction to this thesis and your comments. Julian, thank you for introducing the Scotch Hour on Thursdays and creating the time and space for relaxed discussions. Desmond, thank you for being such a great student; I hope I was was a worthy mentor. Katja, thank you for being such a great supervisor and for teaching me how to be a scientist. I very much appreciate the opportunity you gave me by offering me the Ph.D. position in the first place, and I am even more thankful that you considered our talk almost two years ago seriously and created the opportunity for me to stay in Potsdam and in academia. That made the final few months of my student life much easier, and makes the upcoming several years a delight!

This whole journey would not have been possible without the support of my friends and family. Luka, without your wise insight that it does not make sense for me to study linguistics but that I should do something I love, I would not have decided to study astronomy. Iva, Sanja, Lara, my dear girlfriends, Berlin would have been utterly dull if I did not have you. Thank you for being a part of my life. Brate, Mamice, you were with me the whole journey, and you know how much I depended on having you by my side at the beginning and now at the end. Thank you for being here. Tata, I miss you. Finally, Damjan, my love, you know how much I appreciate having your support throughout the 10 years we are together. But in the last few months, when I had the most stressful time of my life (till now), you gave me all the love and support a partner can give. Thank you!

List of Publications

The Ph.D candidate has contributed to the following list of papers published in peer-review journals during her doctoral studies.

Publications

[Fos+22] **Exoplanet X-ray irradiation and evaporation rates with eROSITA**. *A&A* 661 (2022), A23. DOI: 10.1051/0004-6361/202141097. URL: https://doi.org/10.1051/0004-6361/202141097. Authors: Grace Foster, Katja Poppenhaeger, **Nikoleta Ilić**, and Axel Schwope.

[Ili+23] **The first evidence of tidally induced activity in a brown dwarf-M dwarf pair: a Chandra study of the NLTT 41135/41136 system**. 524:4 (Oct. 2023), 5954–5970. DOI: 10.1093/mnras/stad2277. arXiv: 2307.14056 [astro-ph.SR]. Authors: **Nikoleta Ilić**, Katja Poppenhaeger, Desmond Dsouza, Scott J. Wolk, Marcel A. Agüeros, and Beate Stelzer.

[IPH22] **Tidal star-planet interaction and its observed impact on stellar activity in planet-hosting wide binary systems**. 513:3 (July 2022), 4380–4404. DOI: 10.1093/mnras/stac861. arXiv: 2203.13637 [astro-ph.SR]. Authors: **Nikoleta Ilić**, Katja Poppenhaeger, and S. Marzieh Hosseini.

Bibliography

[AB22] **In the Trenches of the Solar-Stellar Connection. VI. Total EclipSS**. 263:2, 41 (Dec. 2022), 41. DOI: 10.3847/1538-4365/ac8cfc (see page 66). Authors: Thomas Ayres and Derek Buzasi.

[Add+19] **Minerva-Australis. I. Design, Commissioning, and First Photometric Results**. 131:1005 (Nov. 2019), 115003. DOI: 10.1088/1538-3873/ab03aa. arXiv: 1901.11231 [astro-ph.IM] (see page 93). Authors: Brett Addison et al..

[Ahu+21] **Magnetic and tidal migration of close-in planets. Influence of secular evolution on their population**. 650A126 (June 2021), A126. DOI: 10.1051/0004-6361/202040173. arXiv: 2104.01004 [astro-ph.EP] (see pages 21, 102). Authors: J. Ahuir, A. Strugarek, A. -S. Brun, and S. Mathis.

[Ake+13] **The NASA Exoplanet Archive: Data and Tools for Exoplanet Research**. 125:930 (Aug. 2013), 989. DOI: 10.1086/672273. arXiv: 1307.2944 [astro-ph.IM] (see page 44). Authors: R. L. Akeson et al..

[AL80a] **Outer atmospheres of cool stars. III. IUE spectra and transition region models for alf CEN A and B.** 235 (Jan. 1980), 76–84. DOI: 10.1086/157612 (see page 11). Authors: T. R. Ayres and J. L. Linsky.

[AL80b] **Outer atmospheres of cool stars. V. IUE observations of Capella: the rotation-activity connection.** 241 (Oct. 1980), 279–299. DOI: 10.1086/158341 (see page 12). Authors: T. R. Ayres and J. L. Linsky.

[Alb+12] **Obliquities of Hot Jupiter Host Stars: Evidence for Tidal Interactions and Primordial Misalignments**. 757:1, 18 (Sept. 2012), 18. DOI: 10.1088/0004-637X/757/1/18. arXiv: 1206.6105 [astro-ph.SR] (see pages 22, 41, 49). Authors: Simon Albrecht et al..

[Alf42] **Existence of Electromagnetic-Hydrodynamic Waves**. 150:3805 (Oct. 1942), 405–406. DOI: 10.1038/150405d0 (see page 10). Authors: H. Alfvén.

[Alf47] **Magneto hydrodynamic waves, and the heating of the solar corona**. 107 (Jan. 1947), 211. DOI: 10.1093/mnras/107.2.211 (see page 10). Authors: H. Alfvén.

[All98] **Modelling the angular momentum evolution of low-mass stars with core-envelope decoupling**. 333 (May 1998), 629–643 (see page 91). Authors: S. Allain.

[AMA21] **Dynamical tide in stellar radiative zones. General formalism and evolution for low-mass stars**. 651A3 (July 2021), A3. DOI: 10.1051/0004-6361/202040174. arXiv: 2104.05349 [astro-ph.SR] (see page 88). Authors: J. Ahuir, S. Mathis, and L. Amard.

[And+05] **The Ca II Infrared Triplet as a stellar activity diagnostic . I. Non-LTE photospheric profiles and definition of the R_{IRT} indicator**. 430 (Feb. 2005), 669–677. DOI: 10.1051/0004-6361:20041745 (see page 6). Authors: V. Andretta, I. Busà, M. T. Gomez, and L. Terranegra.

[And+19] **Photo-astrometric distances, extinctions, and astrophysical parameters for Gaia DR2 stars brighter than G = 18**. 628A94 (Aug. 2019), A94. DOI: 10.1051/0004-6361/201935765. arXiv: 1904.11302 [astro-ph.GA] (see page 95). Authors: F. Anders et al..

[Are+18] **Gaia Data Release 2 - Catalogue validation**. *A&A* 616 (2018), A17. DOI: 10.1051/0004-6361/201833234. URL: https://doi.org/10.1051/0004-6361/201833234 (see page 34). Authors: Arenou, F. et al..

[Ash+22] **Detecting Magnetospheric Radio Emission from Giant Exoplanets**. 939:1, 24 (Nov. 2022), 24. DOI: 10.3847/1538-4357/ac92f5 (see page 102). Authors: Reza Ashtari, Anthony Sciola, Jake D. Turner, and Kevin Stevenson.

[Ast+13] **Astropy: A community Python package for astronomy**. 558A33 (Oct. 2013), A33. DOI: 10.1051/0004-6361/201322068. arXiv: 1307.6212 [astro-ph.IM] (see pages 27, 52, 65, 83, 99). Authors: Astropy Collaboration et al..

[Ast+18] **The Astropy Project: Building an Open-science Project and Status of the v2.0 Core Package**. 156:3, 123 (Sept. 2018), 123. DOI: 10.3847/1538-3881/aabc4f. arXiv: 1801.02634 [astro-ph.IM] (see pages 27, 52, 65, 83, 99). Authors: Astropy Collaboration et al..

[Aud+00] **Extreme-Ultraviolet Flare Activity in Late-Type Stars**. 541:1 (Sept. 2000), 396–409. DOI: 10.1086/309426. arXiv: astro-ph/0005062 [astro-ph] (see page 26). Authors: Marc Audard, Manuel Güdel, Jeremy J. Drake, and Vinay L. Kashyap.

[Ayr04] **Positional Uncertainties and Detection Limits of ROSAT X-Ray Sources**. 608:2 (June 2004), 957–970. DOI: 10.1086/420688 (see page 27). Authors: Thomas R. Ayres.

[Ayr14] **The Ups and Downs of α Centauri**. 147:3, 59 (Mar. 2014), 59. DOI: 10.1088/0004-6256/147/3/59. arXiv: 1401.0847 [astro-ph.SR] (see page 62). Authors: Thomas R. Ayres.

[Bab61] **The Topology of the Sun's Magnetic Field and the 22-YEAR Cycle.** 133 (Mar. 1961), 572. DOI: 10.1086/147060 (see page 5). Authors: H. W. Babcock.

[Bai+18a] **Estimating Distance from Parallaxes. IV. Distances to 1.33 Billion Stars in Gaia Data Release 2**. *The Astronomical Journal* 156:2 (July 2018), 58. DOI: 10.3847/1538-3881/aacb21. URL: https://doi.org/10.3847/1538-3881/aacb21 (see pages 33, 34, 39). Authors: C. A. L. Bailer-Jones, J. Rybizki, M. Fouesneau, G. Mantelet, and R. Andrae.

[Bai+18b] **Estimating Distance from Parallaxes. IV. Distances to 1.33 Billion Stars in Gaia Data Release 2**. 156:2, 58 (Aug. 2018), 58. DOI: 10.3847/1538-3881/aacb21. arXiv: 1804.10121 [astro-ph.SR] (see pages 66, 67, 72). Authors: C. A. L. Bailer-Jones, J. Rybizki, M. Fouesneau, G. Mantelet, and R. Andrae.

[Bak+06] **A Stellar Companion in the HD 189733 System with a Known Transiting Extrasolar Planet**. 641:1 (Apr. 2006), L57–L60. DOI: 10.1086/503671. arXiv: astro-ph/0602136 [astro-ph] (see page 93). Authors: Gáspár Á. Bakos, András Pál, David W. Latham, Robert W. Noyes, and Robert P. Stefanik.

[Bak+11] **HAT-P-20b–HAT-P-23b: FOUR MASSIVE TRANSITING EXTRASOLAR PLANETS**. *The Astrophysical Journal* 742:2 (Nov. 2011), 116. DOI: 10.1088/0004-637x/742/2/116. URL: https://doi.org/10.1088/0004-637x/742/2/116 (see page 44). Authors: G. Á. Bakos et al..

[Bal+95] **Chromospheric Variations in Main-Sequence Stars. II.** 438 (Jan. 1995), 269. DOI: 10.1086/175072 (see page 62). Authors: S. L. Baliunas et al..

[Ben+19] **Evolution of star-planet systems under magnetic braking and tidal interaction**. 621A124 (Jan. 2019), A124. DOI: 10.1051/0004-6361/201833314. arXiv: 1811.06354 [astro-ph.SR] (see pages 22, 102). Authors: M. Benbakoura, V. Réville, A. S. Brun, C. Le Poncin-Lafitte, and S. Mathis.

[Ber+10] **Simultaneous Multi-Wavelength Observations of Magnetic Activity in Ultracool Dwarfs. III. X-ray, Radio, and Hα Activity Trends in M and L dwarfs**. 709:1 (Jan. 2010), 332–341. DOI: 10.1088/0004-637X/709/1/332. arXiv: 0909.4783 [astro-ph.SR] (see page 79). Authors: E. Berger et al..

[Ber05] **Starspots: A Key to the Stellar Dynamo**. *Living Reviews in Solar Physics* 2:1, 8 (Dec. 2005), 8. DOI: 10.12942/lrsp-2005-8 (see page 6). Authors: Svetlana V. Berdyugina.

[BFA97] **The angular momentum evolution of low-mass stars.** 326 (Oct. 1997), 1023–1043 (see page 2). Authors: J. Bouvier, M. Forestini, and S. Allain.

[Bie48] **Über die Ursache der chromosphärischen Turbulenz und des UV-Exzesses der Sonnenstrahlung**. 25 (Jan. 1948), 161 (see page 10). Authors: Ludwig Biermann.

[Bie51] **Kometenschweife und solare Korpuskularstrahlung**. 29 (Jan. 1951), 274 (see page 3). Authors: L. Biermann.

[Bie52] **Über den Schweif des Kometen Halley im Jahre 1910**. *Zeitschrift Naturforschung Teil A* 7:1 (Jan. 1952), 127–136. DOI: 10.1515/zna-1952-0122 (see page 3). Authors: L. Biermann.

[Bie57] **Solar corpuscular radiation and the interplanetary gas**. *The Observatory* 77 (June 1957), 109–110 (see page 3). Authors: L. Biermann.

[BLM01] **On the Tidal Inflation of Short-Period Extrasolar Planets**. 548:1 (Feb. 2001), 466–472. DOI: 10.1086/318667 (see pages 21, 87). Authors: Peter Bodenheimer, D. N. C. Lin, and R. A. Mardling.

[BM16] **Effect of the rotation and tidal dissipation history of stars on the evolution of close-in planets**. *Celestial Mechanics and Dynamical Astronomy* 126:1-3 (Nov. 2016), 275–296. DOI: 10.1007/s10569-016-9690-3. arXiv: 1603.06268 [astro-ph.EP] (see page 87). Authors: Emeline Bolmont and Stéphane Mathis.

[BM76] **Magnetic acceleration of winds from solar-type stars.** 210 (Dec. 1976), 498–507. DOI: 10.1086/154853 (see pages 22, 62). Authors: J. W. Belcher and K. B. MacGregor.

[Bol+12] **Effect of the stellar spin history on the tidal evolution of close-in planets**. 544A124 (Aug. 2012), A124. DOI: 10.1051/0004-6361/201219645. arXiv: 1207.2127 [astro-ph.EP] (see pages 22, 92). Authors: E. Bolmont, S. N. Raymond, J. Leconte, and S. P. Matt.

[Bon+17] **The GAPS Programme with HARPS-N at TNG . XIV. Investigating giant planet migration history via improved eccentricity and mass determination for 231 transiting planets**. 602A107 (June 2017), A107. DOI: 10.1051/0004-6361/201629882. arXiv: 1704.00373 [astro-ph.EP] (see pages 44, 88, 97). Authors: A. S. Bonomo et al..

[Bou+05] **ELODIE metallicity-biased search for transiting Hot Jupiters. II. A very hot Jupiter transiting the bright K star HD 189733**. 444:1 (Dec. 2005), L15–L19. DOI: 10.1051/0004-6361:200500201. arXiv: astro-ph/0510119 [astro-ph] (see page 93). Authors: F. Bouchy et al..

[Bou+18] **The 55 Cancri system reassessed**. 619A1 (Oct. 2018), A1. DOI: 10.1051/0004-6361/201833154. arXiv: 1807.04301 [astro-ph.EP] (see page 44). Authors: V. Bourrier et al..

[Bou08] **Lithium depletion and the rotational history of exoplanet host stars**. 489:3 (Oct. 2008), L53–L56. DOI: 10.1051/0004-6361:200810574. arXiv: 0808.3917 [astro-ph] (see page 91). Authors: J. Bouvier.

[BP04] **What Do We (Not) Know Theoretically about Solar Neutrino Fluxes?** 92:12, 121301 (Mar. 2004), 121301. DOI: 10.1103/PhysRevLett.92.121301. arXiv: astro-ph/0402114 [astro-ph] (see page 91). Authors: John N. Bahcall and M. H. Pinsonneault.

[Bro+11] **Are falling planets spinning up their host stars?** 415:1 (July 2011), 605–618. DOI: 10.1111/j.1365-2966.2011.18729.x. arXiv: 1103.3599 [astro-ph.EP] (see page 22). Authors: D. J. A. Brown, A. Collier Cameron, C. Hall, L. Hebb, and B. Smalley.

[Bro08] **Simulations of Dynamo Action in Fully Convective Stars**. 676:2 (Apr. 2008), 1262–1280. DOI: 10.1086/527432. arXiv: 0712.1603 [astro-ph] (see page 5). Authors: Matthew K. Browning.

[Bru+22] **The eROSITA Final Equatorial Depth Survey (eFEDS). X-ray catalogue**. 661A1 (May 2022), A1. DOI: 10.1051/0004-6361/202141266. arXiv: 2106.14517 [astro-ph.HE] (see page 70). Authors: H. Brunner et al..

[Bur49] **Soft X-radiation in the upper atmosphere**. *Phys. Rev* 76:165 (1949), 19–9 (see page 9). Authors: Thomas Robert Burnight.

[But+01] **Two New Planets from the Anglo-Australian Planet Search**. 555:1 (July 2001), 410–417. DOI: 10.1086/321467 (see page 54). Authors: R. Paul Butler, C. G. Tinney, Geoffrey W. Marcy, Hugh R. A. Jones, Alan J. Penny, and Kevin Apps.

[But+06] **Catalog of Nearby Exoplanets**. *The Astrophysical Journal* 646:1 (July 2006), 505–522. DOI: 10.1086/504701. URL: https://doi.org/10.1086/504701 (see page 44). Authors: R. P. Butler et al..

[But+97] **Three New "51 Pegasi-Type" Planets**. 474:2 (Jan. 1997), L115–L118. DOI: 10.1086/310444 (see page 44). Authors: R. Paul Butler, Geoffrey W. Marcy, Eric Williams, Heather Hauser, and Phil Shirts.

[Cam+15] **AN ANCIENT EXTRASOLAR SYSTEM WITH FIVE SUB-EARTH-SIZE PLANETS**. *The Astrophysical Journal* 799:2 (Jan. 2015), 170. DOI: 10.1088/0004-637x/799/2/170. URL: https://doi.org/10.1088/0004-637x/799/2/170 (see page 56). Authors: T. L. Campante et al..

[Car+23] **Complete X-ray census of Mdwarfs in the solar Neighborhood I. GJ 745 AB: Coronal-hole Stars in the 10 pc Sample**. *arXiv e-prints* arXiv:2305.14971 (May 2023), arXiv:2305.14971. DOI: 10.48550/arXiv.2305.14971. arXiv: 2305.14971 [astro-ph.SR] (see page 77). Authors: M. Caramazza et al..

[Cat+96] **Photometric and H alpha modulation on active stars**. In: *Stellar Surface Structure*. Ed. by Klaus G. Strassmeier and Jeffrey L. Linsky. Vol. 176. Jan. 1996, 403 (see page 12). Authors: S. Catalano, M. Rodono, A. Frasca, and C. Cutispoto.

[Cau+19] **Magnetic field strengths of hot Jupiters from signals of star-planet interactions**. *Nature Astronomy* 3 (July 2019), 1128–1134. DOI: 10.1038/s41550-019-0840-x. arXiv: 1907.09068 [astro-ph.EP] (see page 102). Authors: P. Wilson Cauley, Evgenya L. Shkolnik, Joe Llama, and Antonino F. Lanza.

[CB97] **Structure and evolution of low-mass stars**. 327 (Nov. 1997), 1039–1053. DOI: 10.48550/arXiv.astro-ph/9704118. arXiv: astro-ph/9704118 [astro-ph] (see pages 5, 79). Authors: Gilles Chabrier and Isabelle Baraffe.

[CDB17] **The Global Solar Dynamo**. 210:1-4 (Sept. 2017), 367–395. DOI: 10.1007/s11214-015-0230-3. arXiv: 1602.01754 [astro-ph.SR] (see page 6). Authors: R. H. Cameron, M. Dikpati, and A. Brandenburg.

[Cha33] **The equilibrium of distorted polytropes. II. the tidal problem**. 93 (Apr. 1933), 449. DOI: 10.1093/mnras/93.6.449 (see page 88). Authors: S. Chandrasekhar.

[Chi+17] **Measuring stellar granulation during planet transits**. 597A94 (Jan. 2017), A94. DOI: 10.1051/0004-6361/201528018. arXiv: 1609.08966 [astro-ph.EP] (see page 19). Authors: A. Chiavassa et al..

[Cho+16] **Mesa Isochrones and Stellar Tracks (MIST). I. Solar-scaled Models**. 823:2, 102 (June 2016), 102. DOI: 10.3847/0004-637X/823/2/102. arXiv: 1604.08592 [astro-ph.SR] (see page 2). Authors: Jieun Choi, Aaron Dotter, Charlie Conroy, Matteo Cantiello, Bill Paxton, and Benjamin D. Johnson.

[CJ18] **Hierarchical Bayesian calibration of tidal orbit decay rates among hot Jupiters**. 476:2 (May 2018), 2542–2555. DOI: 10.1093/mnras/sty292. arXiv: 1801.10561 [astro-ph.EP] (see page 88). Authors: Andrew Collier Cameron and Moira Jardine.

[CJJ70] **Homogeneous Models for Population I and Population II Compositions**. 5 (Mar. 1970), 12 (see page 79). Authors: H. Copeland, J. O. Jensen, and H. E. Jorgensen.

[CK06] **Large-scale $\alpha\hat{2}$-dynamo in low-mass stars and brown dwarfs**. 446:3 (Feb. 2006), 1027–1037. DOI: 10.1051/0004-6361:20042475. arXiv: astro-ph/0510075 [astro-ph] (see pages 5, 12, 79). Authors: G. Chabrier and M. Küker.

[Cof+20] **An X-ray activity cycle on the young solar-like star Eridani**. 636A49 (Apr. 2020), A49. DOI: 10.1051/0004-6361/201936479. arXiv: 2002.11009 [astro-ph.SR] (see page 79). Authors: M. Coffaro et al..

[Coh+09] **Interactions of the Magnetospheres of Stars and Close-In Giant Planets**. 704:2 (Oct. 2009), L85–L88. DOI: 10.1088/0004-637X/704/2/L85. arXiv: 0909.3093 [astro-ph.SR] (see page 15). Authors: O. Cohen et al..

[Coh+10] **The Impact of Hot Jupiters on the Spin-down of their Host Stars**. 723:1 (Nov. 2010), L64–L67. DOI: 10.1088/2041-8205/723/1/L64. arXiv: 1009.5955 [astro-ph.SR] (see pages 15, 50). Authors: O. Cohen, J. J. Drake, V. L. Kashyap, I. V. Sokolov, and T. I. Gombosi.

[Con+18] **A New Model of Jupiter's Magnetic Field From Juno's First Nine Orbits**. 45:6 (Mar. 2018), 2590–2596. DOI: 10.1002/2018GL077312 (see page 101). Authors: J. E. P. Connerney et al..

[CS15] **The crucial role of surface magnetic fields for the solar dynamo**. *Science* 347:6228 (Mar. 2015), 1333–1335. DOI: 10.1126/science.1261470. arXiv: 1503.08469 [astro-ph.SR] (see page 4). Authors: Robert Cameron and Manfred Schüssler.

[CSM00] **On Stellar Activity Enhancement Due to Interactions with Extrasolar Giant Planets**. 533:2 (Apr. 2000), L151–L154. DOI: 10.1086/312609 (see pages 18, 21, 41, 42, 62, 87, 102). Authors: Manfred Cuntz, Steven H. Saar, and Zdzislaw E. Musielak.

[Cur+11] **A fourth planet orbiting dromedae**. *A&A* 525 (2011), A78. DOI: 10.1051/0004-6361/201015693. URL: https://doi.org/10.1051/0004-6361/201015693 (see page 44). Authors: Curiel, S., Cantó, J., Georgiev, L., Chávez, C. E., and Poveda, A..

[Dam+15] **The GAPS programme with HARPS-N at TNG - V. A comprehensive analysis of the XO-2 stellar and planetary systems**. *A&A* 575 (2015), A111. DOI: 10.1051/0004-6361/201425332. URL: https://doi.org/10.1051/0004-6361/201425332 (see page 44). Authors: Damasso, M. et al..

[Dar79a] **A tidal theory of the evolution of satellites**. *The Observatory* 3 (July 1879), 79–84 (see page 16). Authors: G. H. Darwin.

[Dar79b] **A tidal theory of the evolution of satellites**. *The Observatory* 3 (July 1879), 79–84 (see pages 87, 88). Authors: G. H. Darwin.

[Dar79c] **On the Bodily Tides of Viscous and Semi-Elastic Spheroids, and on the Ocean Tides upon a Yielding Nucleus**. *Philosophical Transactions of the Royal Society of London Series I* 170 (Jan. 1879), 1–35 (see page 16). Authors: G. H. Darwin.

[Dav+15] **Asteroseismic inference on rotation, gyrochronology and planetary system dynamics of 16 Cygni**. 446:3 (Jan. 2015), 2959–2966. DOI: 10.1093/mnras/stu2331. arXiv: 1411.1359 [astro-ph.SR] (see page 44). Authors: G. R. Davies et al..

[Dav01] Authors: P. A. Davidson. **An Introduction to Magnetohydrodynamics**. 2001 (see page 4).

[DB07] **Properties of planets in binary systems. The role of binary separation**. 462:1 (Jan. 2007), 345–353. DOI: 10.1051/0004-6361:20066319. arXiv: astro-ph/0610623 [astro-ph] (see pages 24, 40, 71). Authors: S. Desidera and M. Barbieri.

[DDG10] **X-ray, FUV, and UV Observations of α Centauri B: Determination of Long-term Magnetic Activity Cycle and Rotation Period**. 722:1 (Oct. 2010), 343–357. DOI: 10.1088/0004-637X/722/1/343. arXiv: 1009.1652 [astro-ph.SR] (see pages 62, 79). Authors: L. E. DeWarf, K. M. Datin, and E. F. Guinan.

[DDR93] **On the Generation of the Largescale and Turbulent Magnetic Fields in the Solar Type Stars**. 145:2 (June 1993), 207–225. DOI: 10.1007/BF00690652 (see page 5). Authors: Bernard R. Durney, David S. De Young, and Ian W. Roxburgh.

[Den+10] **Angular Momentum Transport in Solar-type Stars: Testing the Timescale for Core-Envelope Coupling**. 716:2 (June 2010), 1269–1287. DOI: 10.1088/0004-637X/716/2/1269. arXiv: 0911.1121 [astro-ph.SR] (see page 91). Authors: Pavel A. Denissenkov, Marc Pinsonneault, Donald M. Terndrup, and Grant Newsham.

[Den+20] **The calibration of eROSITA on SRG**. In: *Society of Photo-Optical Instrumentation Engineers (SPIE) Conference Series*. Vol. 11444. Society of Photo-Optical Instrumentation Engineers (SPIE) Conference Series. Dec. 2020, 114444Q, 114444Q. DOI: 10.1117/12.2562330 (see page 70). Authors: Konrad Dennerl et al..

[Des+07] **Search for exoplanets with the radial-velocity technique: quantitative diagnostics of stellar activity***. *A&A* 473:3 (2007), 983–993. DOI: 10.1051/0004-6361:20078144. URL: https://doi.org/10.1051/0004-6361:20078144 (see page 48). Authors: Desort, M., Lagrange, A.-M., Galland, F., Udry, S., and Mayor, M..

[Día+18a] **The Test Case of HD 26965: Difficulties Disentangling Weak Doppler Signals from Stellar Activity**. 155:3, 126 (Mar. 2018), 126. DOI: 10.3847/1538-3881/aaa896. arXiv: 1801.03970 [astro-ph.EP] (see page 24). Authors: Matías R. Díaz et al..

[Día+18b] **The Test Case of HD 26965: Difficulties Disentangling Weak Doppler Signals from Stellar Activity**. *The Astronomical Journal* 155:3 (Feb. 2018), 126. DOI: 10.3847/1538-3881/aaa896. URL: https://doi.org/10.3847/1538-3881/aaa896 (see page 44). Authors: Matías R. Díaz et al..

[DJ18] **Origins of Hot Jupiters**. 56 (Sept. 2018), 175–221. DOI: 10.1146/annurev-astro-081817-051853. arXiv: 1801.06117 [astro-ph.EP] (see pages 49, 87). Authors: Rebekah I. Dawson and John Asher Johnson.

[DLM04] **Spin-Orbit Evolution of Short-Period Planets**. 610:1 (July 2004), 464–476. DOI: 10.1086/421510. arXiv: astro-ph/0408191 [astro-ph] (see pages 21, 99). Authors: Ian Dobbs-Dixon, D. N. C. Lin, and Rosemary A. Mardling.

[Dou+14] **The Factory and the Beehive. II. Activity and Rotation in Praesepe and the Hyades**. 795:2, 161 (Nov. 2014), 161. DOI: 10.1088/0004-637X/795/2/161. arXiv: 1409.7603 [astro-ph.SR] (see page 9). Authors: S. T. Douglas et al..

[DR89] **Coronal Activity–Rotation Relations for Lower–Main-Sequence Stars**. 344 (Sept. 1989), 907. DOI: 10.1086/167858 (see page 8). Authors: Andrea K. Dobson and Richard R. Radick.

[DSB06] **Magnetic Field Generation in Fully Convective Rotating Spheres**. 638:1 (Feb. 2006), 336–347. DOI: 10.1086/498634. arXiv: astro-ph/0410645 [astro-ph] (see page 5). Authors: Wolfgang Dobler, Michael Stix, and Axel Brandenburg.

[Dul85] **Radio emission from the sun and stars.** 23 (Jan. 1985), 169–224. DOI: 10.1146/annurev.aa.23.090185.001125 (see page 6). Authors: G. A. Dulk.

[DW17] **The Oblique Orbit of WASP-107b from K2 Photometry**. 153:5, 205 (May 2017), 205. DOI: 10.3847/1538-3881/aa65d1. arXiv: 1702.04734 [astro-ph.EP] (see page 41). Authors: Fei Dai and Joshua N. Winn.

[EC18] **The Chandra Source Catalog release 2.0**. *Astronomy and Geophysics* 59:2 (Apr. 2018), 2.17–2.18. DOI: 10.1093/astrogeo/aty079 (see page 69). Authors: Ian N. Evans and Francesca Civano.

[Edd76] **The Maunder Minimum**. *Science* 192:4245 (1976), 1189–1202. ISSN: 0036-8075. DOI: 10.1126/science.192.4245.1189. eprint: https://science.sciencemag.org/content/192/4245/1189.full.pdf. URL: https://science.sciencemag.org/content/192/4245/1189 (see page 50). Authors: John A. Eddy.

[EKH98] **The Equilibrium Tide Model for Tidal Friction**. 499:2 (May 1998), 853–870. DOI: 10.1086/305670. arXiv: astro-ph/9801246 [astro-ph] (see page 87). Authors: Peter P. Eggleton, Ludmila G. Kiseleva, and Piet Hut.

[ER18] **Imprints of white dwarf recoil in the separation distribution of Gaia wide binaries**. 480:4 (Nov. 2018), 4884–4902. DOI: 10.1093/mnras/sty2186. arXiv: 1807.06011 [astro-ph.SR] (see pages 68–70). Authors: Kareem El-Badry and Hans-Walter Rix.

[ES42] **Term Analysis of the Third Spectrum of Iron (Fe III).** 95 (May 1942), 532. DOI: 10.1086/144421 (see page 9). Authors: B. Edlén and P. Swings.

[Esp+17] **The GAPS Programme with HARPS-N at TNG. XIII. The orbital obliquity of three close-in massive planets hosted by dwarf K-type stars: WASP-43, HAT-P-20 and Qatar-2**. 601A53 (May 2017), A53. DOI: 10.1051/0004-6361/201629720. arXiv: 1702.03136 [astro-ph.EP] (see page 44). Authors: M. Esposito et al..

[Eva+16] **High-resolution Imaging of Transiting Extrasolar Planetary systems (HITEP) - I. Lucky imaging observations of 101 systems in the southern hemisphere**. *A&A* 589 (2016), A58. DOI: 10.1051/0004-6361/201527970. URL: https://doi.org/10.1051/0004-6361/201527970 (see page 39). Authors: Evans, D. F. et al..

[Fav+08] **The X-ray cycle in the solar-type star HD 81809. XMM-Newton observations and implications for the coronal structure**. 490:3 (Nov. 2008), 1121–1126. DOI: 10.1051/0004-6361:200809694. arXiv: 0806.2279 [astro-ph] (see pages 62, 79). Authors: F. Favata, G. Micela, S. Orlando, J. H. M. M. Schmitt, S. Sciortino, and J. Hall.

[Fed+11] **Mach Number Dependence of Turbulent Magnetic Field Amplification: Solenoidal versus Compressive Flows**. 107:11, 114504 (Sept. 2011), 114504. DOI: 10.1103/PhysRevLett.107.114504. arXiv: 1109.1760 [physics.flu-dyn] (see page 12). Authors: C. Federrath, G. Chabrier, J. Schober, R. Banerjee, R. S. Klessen, and D. R. G. Schleicher.

[Fer+15] **Interplay of Tidal Evolution and Stellar Wind Braking in the Rotation of Stars Hosting Massive Close-In Planets**. 807:1, 78 (July 2015), 78. DOI: 10.1088/0004-637X/807/1/78. arXiv: 1503.04369 [astro-ph.EP] (see page 22). Authors: S. Ferraz-Mello, M. Tadeu dos Santos, H. Folonier, Sz. Csizmadia, Jr. do Nascimento J. -D., and M. Pätzold.

[FF14] **A Simulation of Convective Dynamo in the Solar Convective Envelope: Maintenance of the Solar-like Differential Rotation and Emerging Flux**. 789:1, 35 (July 2014), 35. DOI: 10.1088/0004-637X/789/1/35. arXiv: 1405.3926 [astro-ph.SR] (see page 5). Authors: Yuhong Fan and Fang Fang.

[Fil+15] **Fundamental Parameters and Spectral Energy Distributions of Young and Field Age Objects with Masses Spanning the Stellar to Planetary Regime**. 810:2, 158 (Sept. 2015), 158. DOI: 10.1088/0004-637X/810/2/158. arXiv: 1508.01767 [astro-ph.SR] (see page 63). Authors: Joseph C. Filippazzo, Emily L. Rice, Jacqueline Faherty, Kelle L. Cruz, Mollie M. Van Gordon, and Dagny L. Looper.

[Fis+98] **Coronal Heating in Active Regions as a Function of Global Magnetic Variables**. 508:2 (Dec. 1998), 885–898. DOI: 10.1086/306435 (see page 10). Authors: George H. Fisher, Dana W. Longcope, Thomas R. Metcalf, and Alexei A. Pevtsov.

[Fis67] **Angular momenta of the planets**. 7:1-3 (Jan. 1967), 251–256. DOI: 10.1016/0019-1035(67)90069-3 (see page 87). Authors: Ferol F. Fish.

[FL88] **Magnetic Modulation of Solar Luminosity by Photospheric Activity**. 328 (May 1988), 347. DOI: 10.1086/166297 (see page 6). Authors: P. Foukal and J. Lean.

[Fon+19] **A high binary fraction for the most massive close-in giant planets and brown dwarf desert members**. 485:4 (June 2019), 4967–4996. DOI: 10.1093/mnras/stz671. arXiv: 1903.02332 [astro-ph.EP] (see page 40). Authors: C. Fontanive et al..

[Fos+21] **Exoplanet X-ray irradiation and evaporation rates with eROSITA**. *arXiv e-prints* arXiv:2106.14550 (June 2021), arXiv:2106.14550. arXiv: 2106.14550 [astro-ph.EP] (see pages 30, 35). Authors: G. Foster, K. Poppenhaeger, N. Ilic, and A. Schwope.

[Fos+22] **Exoplanet X-ray irradiation and evaporation rates with eROSITA**. 661A23 (May 2022), A23. DOI: 10.1051/0004-6361/202141097. arXiv: 2106.14550 [astro-ph.EP] (see pages 70, 71). Authors: G. Foster, K. Poppenhaeger, N. Ilic, and A. Schwope.

[Fre+20] **SRG/eROSITA in-flight background at L2**. In: *Society of Photo-Optical Instrumentation Engineers (SPIE) Conference Series*. Vol. 11444. Society of Photo-Optical Instrumentation Engineers (SPIE) Conference Series. Dec. 2020, 114441O, 114441O. DOI: 10.1117/12.2562709 (see page 70). Authors: Michael Freyberg et al..

[Fuh+23] **The CARMENES search for exoplanets around M dwarfs. Variability on long timescales as seen in chromospheric indicators**. 670A71 (Feb. 2023), A71. DOI: 10.1051/0004-6361/202244829. arXiv: 2212.03514 [astro-ph.SR] (see page 79). Authors: B. Fuhrmeister et al..

[FV05] **The Planet-Metallicity Correlation**. *The Astrophysical Journal* 622:2 (Apr. 2005), 1102–1117. DOI: 10.1086/428383. URL: https://doi.org/10.1086/428383 (see page 54). Authors: Debra A. Fischer and Jeff Valenti.

[Gai+16a] **The Gaia mission**. *A&A* 595 (2016), A1. DOI: 10.1051/0004-6361/201629272. URL: https://doi.org/10.1051/0004-6361/201629272 (see page 34). Authors: Gaia Collaboration et al..

[Gai+16b] **The Gaia mission**. 595A1 (Nov. 2016), A1. DOI: 10.1051/0004-6361/201629272. arXiv: 1609.04153 [astro-ph.IM] (see page 67). Authors: Gaia Collaboration et al..

[Gai+18a] **Gaia Data Release 2 - Summary of the contents and survey properties**. *A&A* 616 (2018), A1. DOI: 10.1051/0004-6361/201833051. URL: https://doi.org/10.1051/0004-6361/201833051 (see page 34). Authors: Gaia Collaboration et al..

[Gai+18b] **Gaia Data Release 2. Summary of the contents and survey properties**. 616A1 (Aug. 2018), A1. DOI: 10.1051/0004-6361/201833051. arXiv: 1804.09365 [astro-ph.GA] (see page 67). Authors: Gaia Collaboration et al..

[Gai+22] **Gaia Data Release 3: Summary of the content and survey properties**. *arXiv e-prints* arXiv:2208.00211 (July 2022), arXiv:2208.00211. DOI: 10.48550/arXiv.2208.00211. arXiv: 2208.00211 [astro-ph.GA] (see page 93). Authors: Gaia Collaboration et al..

[Gal+18] **Planetary tidal interactions and the rotational evolution of low-mass stars. The Pleiades' anomaly**. 619A80 (Nov. 2018), A80. DOI: 10.1051/0004-6361/201833576. arXiv: 1808.08728 [astro-ph.EP] (see page 22). Authors: F. Gallet, E. Bolmont, J. Bouvier, S. Mathis, and C. Charbonnel.

[GGS97a] **The X-Ray Sun in Time: A Study of the Long-Term Evolution of Coronae of Solar-Type Stars**. 483:2 (July 1997), 947–960. DOI: 10.1086/304264 (see pages 26, 30). Authors: Manuel Güdel, Edward F. Guinan, and Stephen L. Skinner.

[GGS97b] **The X-Ray Sun in Time: A Study of the Long-Term Evolution of Coronae of Solar-Type Stars**. 483:2 (July 1997), 947–960. DOI: 10.1086/304264 (see pages 69, 81). Authors: Manuel Güdel, Edward F. Guinan, and Stephen L. Skinner.

[Ghe+10] **Stellar Parameters and Metallicities of Stars Hosting Jovian and Neptunian Mass Planets: A Possible Dependence of Planetary Mass on Metallicity**. 720:2 (Sept. 2010), 1290–1302. DOI: 10.1088/0004-637X/720/2/1290. arXiv: 1007.2681 [astro-ph.SR] (see page 95). Authors: L. Ghezzi, K. Cunha, V. V. Smith, F. X. de Araújo, S. C. Schuler, and R. de la Reza.

[Gia+96] **The Coronae of Low-Mass Dwarf Stars**. 463 (June 1996), 707. DOI: 10.1086/177284 (see pages 11, 66). Authors: M. S. Giampapa, R. Rosner, V. Kashyap, T. A. Fleming, J. H. M. M. Schmitt, and J. A. Bookbinder.

[Gil+10] **The thermal emission of the young and massive planet CoRoT-2b at 4.5 and 8 *****. *A&A* 511 (2010), A3. DOI: 10.1051/0004-6361/200913507. URL: https://doi.org/10.1051/0004-6361/200913507 (see page 44). Authors: Gillon, M. et al..

[Gin+16] **A lucky imaging multiplicity study of exoplanet host stars – II**. *Monthly Notices of the Royal Astronomical Society* 457:2 (Feb. 2016), 2173–2191. ISSN: 0035-8711. DOI: 10.1093/mnras/stw049. eprint: https://academic.oup.com/mnras/article-pdf/457/2/2173/13770583/stw049.pdf. URL: https://doi.org/10.1093/mnras/stw049 (see page 55). Authors: C. Ginski et al..

[Gio+18] **ESASky: A science-driven discovery portal for space-based astronomy missions**. *Astronomy and Computing* 2497 (July 2018), 97. DOI: 10.1016/j.ascom.2018.05.002. arXiv: 1811.10459 [astro-ph.IM] (see page 69). Authors: F. Giordano et al..

[GP68] **The Dynamics of Planetary Rotations**. 6 (Jan. 1968), 287. DOI: 10.1146/annurev.aa.06.090168.001443 (see page 87). Authors: Peter Goldreich and Stanton J. Peale.

[Gre73] **Evolution of satellite resonances by tidal dissipation**. 78 (May 1973), 338. DOI: 10.1086/111423 (see page 87). Authors: Richard Greenberg.

[Gri+04a] **The effect of tidal locking on the magnetospheric and atmospheric evolution of "Hot Jupiters"**. 425 (Oct. 2004), 753–762. DOI: 10.1051/0004-6361:20035684 (see page 101). Authors: J. -M. Grießmeier et al..

[Gri+04b] **The effect of tidal locking on the magnetospheric and atmospheric evolution of "Hot Jupiters"**. *A&A* 425:2 (2004), 753–762. DOI: 10.1051/0004-6361:20035684. URL: https://doi.org/10.1051/0004-6361:20035684 (see page 51). Authors: Grießmeier, J.-M. et al..

[Gro39] **Zur Frage der Deutung der Linien im Spektrum der Sonnenkorona**. *Naturwissenschaften* 27:13 (Mar. 1939), 214–214. DOI: 10.1007/BF01488890 (see page 9). Authors: W. Grotrian.

[GS66] **Q in the Solar System**. 5:1 (Jan. 1966), 375–389. DOI: 10.1016/0019-1035(66)90051-0 (see pages 17, 87, 88). Authors: Peter Goldreich and Steven Soter.

[Güd04] **X-ray astronomy of stellar coronae**. 12:2-3 (Sept. 2004), 71–237. DOI: 10.1007/s00159-004-0023-2. arXiv: astro-ph/0406661 [astro-ph] (see page 77). Authors: Manuel Güdel.

[Gui+96] **Giant Planets at Small Orbital Distances**. 459 (Mar. 1996), L35. DOI: 10.1086/309935. arXiv: astro-ph/9511109 [astro-ph] (see page 14). Authors: T. Guillot, A. Burrows, W. B. Hubbard, J. I. Lunine, and D. Saumon.

[GWS95] **HR 5110 superflare: an interbinary flare identified?** 275:1 (July 1995), 129–142. DOI: 10.1093/mnras/275.1.129 (see page 12). Authors: V. G. Graffagnino, D. Wonnacott, and S. Schaeidt.

[Hal+08] **Confirmation of the Electron Cyclotron Maser Instability as the Dominant Source of Radio Emission from Very Low Mass Stars and Brown Dwarfs**. 684:1 (Sept. 2008), 644–653. DOI: 10.1086/590360. arXiv: 0805.4010 [astro-ph] (see page 102). Authors: G. Hallinan, A. Antonova, J. G. Doyle, S. Bourke, C. Lane, and A. Golden.

[Hal+19] **The Magnetic Polarity of Sun-Spots**. 49 (Apr. 1919), 153. DOI: 10.1086/142452 (see page 4). Authors: George E. Hale, Ferdinand Ellerman, S. B. Nicholson, and A. H. Joy.

[Hal08] **On the Probable Existence of a Magnetic Field in Sun-Spots**. 28 (Nov. 1908), 315. DOI: 10.1086/141602 (see pages 2, 4). Authors: George E. Hale.

[Han12] **Calibration of Equilibrium Tide Theory for Extrasolar Planet Systems. II**. 757:1, 6 (Sept. 2012), 6. DOI: 10.1088/0004-637X/757/1/6. arXiv: 1204.3903 [astro-ph.EP] (see pages 88, 97). Authors: Brad M. S. Hansen.

[Har10] **A Correlation Between Stellar Activity and the Surface Gravity of Hot Jupiters**. 717:2 (July 2010), L138–L142. DOI: 10.1088/2041-8205/717/2/L138. arXiv: 1004.4252 [astro-ph.EP] (see page 20). Authors: J. D. Hartman.

[Hat02] **Starspots and exoplanets**. *Astronomische Nachrichten* 323:3-4 (2002), 392–394. DOI: https://doi.org/10.1002/1521-3994(200208)323:3/4<392::AID-ASNA392>3.0.CO;2-M. eprint: https://onlinelibrary.wiley.com/doi/pdf/10.1002/1521-3994%28200208%29323%3A3/4%3C392%3A%3AAID-ASNA392%3E3.0.CO%3B2-M. URL: https://onlinelibrary.wiley.com/doi/abs/10.1002/1521-3994%28200208%29323%3A3/4%3C392%3A%3AAID-ASNA392%3E3.0.CO%3B2-M (see page 48). Authors: A.P. Hatzes.

[Hem+06] **Coronal activity cycles in 61 Cygni**. 460:1 (Dec. 2006), 261–267. DOI: 10.1051/0004-6361:20065459 (see page 79). Authors: A. Hempelmann, J. Robrade, J. H. M. M. Schmitt, F. Favata, S. L. Baliunas, and J. C. Hall.

[Her58] **Geomagnetic Dynamos**. *Philosophical Transactions of the Royal Society of London Series A* 250:986 (Aug. 1958), 543–583. DOI: 10.1098/rsta.1958.0007 (see page 4). Authors: A. Herzenberg.

[Her85] **Catalogue of Double Stars. By William Herschel, Esq. F. R. S.** *Philosophical Transactions of the Royal Society of London Series I* 75 (Jan. 1785), 40–126 (see page 12). Authors: William Herschel.

[HM05] **Rotational Evolution of Solar-like Stars in Clusters from Pre-Main Sequence to Main Sequence: Empirical Results**. 633:2 (Nov. 2005), 967–985. DOI: 10.1086/491577. arXiv: astro-ph/0508009 [astro-ph] (see page 2). Authors: William Herbst and Reinhard Mundt.

[Hou97] **On the Application of Harmonic Analysis to the Dynamical Theory of the Tides. Part I. On Laplace's "Oscillations of the First Species," and on the Dynamics of Ocean Currents**. *Philosophical Transactions of the Royal Society of London Series A* 189 (Jan. 1897), 201–257. DOI: 10.1098/rsta.1897.0009 (see page 87). Authors: S. S. Hough.

[How+14] **THE NASA-UC-UH ETA-EARTH PROGRAM. IV. A LOW-MASS PLANET ORBITING AN M DWARF 3.6 PC FROM EARTH**. *The Astrophysical Journal* 794:1 (Sept. 2014), 51. DOI: 10.1088/0004-637x/794/1/51. URL: https://doi.org/10.1088/0004-637x/794/1/51 (see page 44). Authors: Andrew W. Howard et al..

[How09] **Solar Interior Rotation and its Variation**. *Living Reviews in Solar Physics* 6:1, 1 (Dec. 2009), 1. DOI: 10.12942/lrsp-2009-1. arXiv: 0902.2406 [astro-ph.SR] (see page 4). Authors: Rachel Howe.

[HS19] **Hot Jupiters Are Destroyed by Tides While Their Host Stars Are on the Main Sequence**. 158:5, 190 (Nov. 2019), 190. DOI: 10.3847/1538-3881/ab3c56. arXiv: 1908.06998 [astro-ph.EP] (see page 22). Authors: Jacob H. Hamer and Kevin C. Schlaufman.

[HTP02] **Evolution of binary stars and the effect of tides on binary populations**. 329:4 (Feb. 2002), 897–928. DOI: 10.1046/j.1365-8711.2002.05038.x. arXiv: astro-ph/0201220 [astro-ph] (see page 87). Authors: Jarrod R. Hurley, Christopher A. Tout, and Onno R. Pols.

[Hub+08] **Magnetic field measurements of O stars with FORS 1 at the VLT**. 490:2 (Nov. 2008), 793–800. DOI: 10.1051/0004-6361:200810171. arXiv: 0808.2039 [astro-ph] (see page 2). Authors: S. Hubrig, M. Schöller, R. S. Schnerr, J. F. González, R. Ignace, and H. F. Henrichs.

[Hub74] **Tides in the Giant Planets**. 23:1 (Sept. 1974), 42–50. DOI: 10.1016/0019-1035(74)90102-X (see page 87). Authors: W. B. Hubbard.

[Hut81] **Tidal evolution in close binary systems.** 99 (June 1981), 126–140 (see pages 12, 21, 62, 87). Authors: P. Hut.

[HW07] **THE ROTATION PERIOD OF THE PLANET-HOSTING STAR HD 189733**. *The Astronomical Journal* 135:1 (Nov. 2007), 68–71. DOI: 10.1088/0004-6256/135/1/68. URL: https://doi.org/10.1088/0004-6256/135/1/68 (see page 44). Authors: Gregory W. Henry and Joshua N. Winn.

[HW08] **The Rotation Period of the Planet-Hosting Star HD 189733**. 135:1 (Jan. 2008), 68–71. DOI: 10.1088/0004-6256/135/1/68. arXiv: 0709.2142 [astro-ph] (see page 93). Authors: Gregory W. Henry and Joshua N. Winn.

[IKH04] **On the Star-Magnetosphere Interaction of Close-in Exoplanets**. 602:1 (Feb. 2004), L53–L56. DOI: 10.1086/382274 (see pages 14, 22). Authors: Wing-Huen Ip, Andreas Kopp, and Juei-Hwa Hu.

[Ili+19] **Flares in open clusters with K2 . I. M 45 (Pleiades), M 44 (Praesepe), and M 67**. 622A133 (Feb. 2019), A133. DOI: 10.1051/0004-6361/201834400. arXiv: 1812.06725 [astro-ph.SR] (see page 26). Authors: Ekaterina Ilin, Sarah J. Schmidt, James R. A. Davenport, and Klaus G. Strassmeier.

[IPH22] **Tidal star-planet interaction and its observed impact on stellar activity in planet-hosting wide binary systems**. 513:3 (July 2022), 4380–4404. DOI: 10.1093/mnras/stac861. arXiv: 2203.13637 [astro-ph.SR] (see pages 62, 65, 69, 70, 84, 89, 90, 93, 94, 97). Authors: N. Ilic, K. Poppenhaeger, and S. Marzieh Hosseini.

[Irw+07] **The Monitor project: rotation of low-mass stars in the open cluster NGC2516**. 377:2 (May 2007), 741–758. DOI: 10.1111/j.1365-2966.2007.11640.x. arXiv: astro-ph/0702518 [astro-ph] (see page 91). Authors: Jonathan Irwin et al..

[Irw+10] **NLTT 41135: A Field M Dwarf + Brown Dwarf Eclipsing Binary in a Triple System, Discovered by the MEarth Observatory**. 718:2 (Aug. 2010), 1353–1366. DOI: 10.1088/0004-637X/718/2/1353. arXiv: 1006.1793 [astro-ph.SR] (see pages 63, 66, 80, 81). Authors: Jonathan Irwin et al..

[JBG21a] **The active lives of stars: A complete description of the rotation and XUV evolution of F, G, K, and M dwarfs**. 649A96 (May 2021), A96. DOI: 10.1051/0004-6361/202038407. arXiv: 2009.07695 [astro-ph.SR] (see page 2). Authors: C. P. Johnstone, M. Bartel, and M. Güdel.

[JBG21b] **The active lives of stars: A complete description of the rotation and XUV evolution of F, G, K, and M dwarfs**. *A&A* 649 (2021), A96. DOI: 10.1051/0004-6361/202038407. URL: https://doi.org/10.1051/0004-6361/202038407 (see page 48). Authors: Johnstone, C. P., Bartel, M., and Güdel, M..

[JG15] **The coronal temperatures of low-mass main-sequence stars**. 578A129 (June 2015), A129. DOI: 10.1051/0004-6361/201425283. arXiv: 1505.00643 [astro-ph.SR] (see pages 63, 66, 67). Authors: C. P. Johnstone and M. Güdel.

[JGB08] **Tidal Evolution of Close-in Extrasolar Planets**. *The Astrophysical Journal* 678:2 (May 2008), 1396–1406. DOI: 10.1086/529187. URL: https://doi.org/10.1086/529187 (see pages 22, 88, 97). Authors: Brian Jackson, Richard Greenberg, and Rory Barnes.

[Joh+06] **An Eccentric Hot Jupiter Orbiting the Subgiant HD 185269**. *The Astrophysical Journal* 652:2 (Dec. 2006), 1724–1728. DOI: 10.1086/508255. URL: https://doi.org/10.1086/508255 (see page 55). Authors: John Asher Johnson et al..

[JSA03] **An Estimate of the Sun's ROSAT-PSPC X-Ray Luminosities Using SNOE-SXP Measurements**. 593:1 (Aug. 2003), 534–548. DOI: 10.1086/376405 (see page 62). Authors: Philip G. Judge, Stanley C. Solomon, and Thomas R. Ayres.

[JU99] **Coronal emission and dynamo saturation**. 346 (June 1999), 883–891 (see page 12). Authors: M. Jardine and Y. C. Unruh.

[Kah92] **Solar flares and coronal mass ejections.** 30 (Jan. 1992), 113–141. DOI: 10.1146/annurev.aa.30.090192.000553 (see page 6). Authors: S. W. Kahler.

[Kan+15] **ON THE STELLAR COMPANION TO THE EXOPLANET HOSTING STAR 30 ARIETIS B**. *The Astrophysical Journal* 815:1 (Dec. 2015), 32. DOI: 10.1088/0004-637x/815/1/32. URL: https://doi.org/10.1088%2F0004-637x%2F815%2F1%2F32 (see page 53). Authors: Stephen R. Kane et al..

[Kao+16] **Auroral Radio Emission from Late L and T Dwarfs: A New Constraint on Dynamo Theory in the Substellar Regime**. 818:1, 24 (Feb. 2016), 24. DOI: 10.3847/0004-637X/818/1/24. arXiv: 1511.03661 [astro-ph.SR] (see page 102). Authors: Melodie M. Kao et al..

[Kav+19] **MOVES - II. Tuning in to the radio environment of HD189733b**. 485:4 (June 2019), 4529–4538. DOI: 10.1093/mnras/stz655. arXiv: 1903.01809 [astro-ph.SR] (see pages 14, 102). Authors: R. D. Kavanagh et al..

[Kaw88] **Angular Momentum Loss in Low-Mass Stars**. 333 (Oct. 1988), 236. DOI: 10.1086/166740 (see page 3). Authors: Steven D. Kawaler.

[KB98] **Energy Distribution of Heating Processes in the Quiet Solar Corona**. 501:2 (July 1998), L213–L216. DOI: 10.1086/311474 (see page 10). Authors: Säm Krucker and Arnold O. Benz.

[KBN91a] **Determination of Confidence Limits for Experiments with Low Numbers of Counts**. 374 (June 1991), 344. DOI: 10.1086/170124 (see pages 27, 65). Authors: Ralph P. Kraft, David N. Burrows, and John A. Nousek.

[KBN91b] **Determination of Confidence Limits for Experiments with Low Numbers of Counts**. 374 (June 1991), 344. DOI: 10.1086/170124 (see page 71). Authors: Ralph P. Kraft, David N. Burrows, and John A. Nousek.

[KD96] **The Theoretical Calculation of the Rossby Number and the "Nonlocal" Convective Overturn Time for Pre-Main-Sequence and Early Post-Main-Sequence Stars**. 457 (Jan. 1996), 340. DOI: 10.1086/176733 (see page 6). Authors: Yong-Cheol Kim and Pierre Demarque.

[KDS08] **Extrasolar Giant Planets and X-Ray Activity**. 687:2 (Nov. 2008), 1339–1354. DOI: 10.1086/591922. arXiv: 0807.1308 [astro-ph] (see pages 19, 22, 62). Authors: Vinay L. Kashyap, Jeremy J. Drake, and Steven H. Saar.

[Kee14] 299–324. In: *Principles of Astrophysics: Using Gravity and Stellar Physics to Explore the Cosmos*. New York, NY: Springer New York, 2014. ISBN: 978-1-4614-9236-8. DOI: 10.1007/978-1-4614-9236-8_15. URL: https://doi.org/10.1007/978-1-4614-9236-8_15 (see page 1). Authors: Charles Keeton.

[Ker+16] **The red dwarf pair GJ65 AB: inflated, spinning twins of Proxima. Fundamental parameters from PIONIER, NACO, and UVES observations**. 593A127 (Oct. 2016), A127. DOI: 10.1051/0004-6361/201628631. arXiv: 1607.04351 [astro-ph.SR] (see page 67). Authors: P. Kervella, A. Mérand, C. Ledoux, B. -O. Demory, and J. -B. Le Bouquin.

[KHH06] **Continued Hyperactivity on the Secondary Star of AM Herculis**. 131:5 (May 2006), 2673–2680. DOI: 10.1086/503281 (see page 12). Authors: S. Kafka, R. K. Honeycutt, and S. B. Howell.

[Kim+19] **Exploring the Age-dependent Properties of M and L Dwarfs Using Gaia and SDSS**. 157:6, 231 (June 2019), 231. DOI: 10.3847/1538-3881/ab1753. arXiv: 1904.05911 [astro-ph.SR] (see page 35). Authors: Rocio Kiman, Sarah J. Schmidt, Ruth Angus, Kelle L. Cruz, Jacqueline K. Faherty, and Emily Rice.

[Knu+14] **FRIENDS OF HOT JUPITERS. I. A RADIAL VELOCITY SEARCH FOR MASSIVE, LONG-PERIOD COMPANIONS TO CLOSE-IN GAS GIANT PLANETS**. *The Astrophysical Journal* 785:2 (Apr. 2014), 126. DOI: 10.1088/0004-637x/785/2/126. URL: https://doi.org/10.1088/0004-637x/785/2/126 (see page 24). Authors: Heather A. Knutson et al..

[Koe91] **Disk Accretion onto Magnetic T Tauri Stars**. 370 (Mar. 1991), L39. DOI: 10.1086/185972 (see page 2). Authors: Arieh Koenigl.

[Kou+10] **The formation of very wide binaries during the star cluster dissolution phase**. 404:4 (June 2010), 1835–1848. DOI: 10.1111/j.1365-2966.2010.16399.x. arXiv: 1001.3969 [astro-ph.GA] (see page 35). Authors: M. B. N. Kouwenhoven, S. P. Goodwin, Richard J. Parker, M. B. Davies, D. Malmberg, and P. Kroupa.

[Kra67] **Studies of Stellar Rotation. V. The Dependence of Rotation on Age among Solar-Type Stars**. 150 (Nov. 1967), 551. DOI: 10.1086/149359 (see pages 6, 12, 22, 62). Authors: Robert P. Kraft.

[KTR73] **A Coronal Hole and Its Identification as the Source of a High Velocity Solar Wind Stream**. 29:2 (Apr. 1973), 505–525. DOI: 10.1007/BF00150828 (see page 11). Authors: A. S. Krieger, A. F. Timothy, and E. C. Roelof.

[KW90a] 48–55. In: *Stellar Structure and Evolution*. Berlin, Heidelberg: Springer Berlin Heidelberg, 1990. ISBN: 978-3-642-61523-8. DOI: 10.1007/978-3-642-61523-8_7. URL: https://doi.org/10.1007/978-3-642-61523-8_7 (see page 3). Authors: Rudolf Kippenhahn and Alfred Weigert.

[KW90b] 27–35. In: *Stellar Structure and Evolution*. Berlin, Heidelberg: Springer Berlin Heidelberg, 1990. ISBN: 978-3-642-61523-8. DOI: 10.1007/978-3-642-61523-8_5. URL: https://doi.org/10.1007/978-3-642-61523-8_5 (see page 3). Authors: Rudolf Kippenhahn and Alfred Weigert.

[L L18] Authors: L. Lindegren. **Re-normalising the astrometric chi-square in Gaia DR2**. Technical Note. GAIA-C3-TN-LU-LL-124. Aug. 2018. URL: http://www.rssd.esa.int/docfetch.php?id=3757412 (see page 34).

[Lac+99] **Age determinations of main-sequence stars: combining different methods**. 348 (Aug. 1999), 897–909 (see page 62). Authors: R. Lachaume, C. Dominik, T. Lanz, and H. J. Habing.

[Lan+09] **Magnetic activity in the photosphere of CoRoT-Exo-2a. Active longitudes and short-term spot cycle in a young Sun-like star**. 493:1 (Jan. 2009), 193–200. DOI: 10.1051/0004-6361:200810591. arXiv: 0811.0461 [astro-ph] (see page 44). Authors: A. F. Lanza et al..

[Lan08] **Hot Jupiters and stellar magnetic activity**. 487:3 (Sept. 2008), 1163–1170. DOI: 10.1051/0004-6361:200809753. arXiv: 0805.3010 [astro-ph] (see page 15). Authors: A. F. Lanza.

[Lan09] **Stellar coronal magnetic fields and star-planet interaction**. 505:1 (Oct. 2009), 339–350. DOI: 10.1051/0004-6361/200912367. arXiv: 0906.1738 [astro-ph.SR] (see page 15). Authors: A. F. Lanza.

[Lan10] **Hot Jupiters and the evolution of stellar angular momentum**. 512A77 (Mar. 2010), A77. DOI: 10.1051/0004-6361/200912789. arXiv: 0912.4585 [astro-ph.SR] (see page 15). Authors: A. F. Lanza.

[Lan13] **Star-planet magnetic interaction and evaporation of planetary atmospheres**. 557A31 (Sept. 2013), A31. DOI: 10.1051/0004-6361/201321790. arXiv: 1307.2341 [astro-ph.EP] (see page 102). Authors: A. F. Lanza.

[Lar69] **Numerical calculations of the dynamics of collapsing proto-star**. 145 (Jan. 1969), 271. DOI: 10.1093/mnras/145.3.271 (see page 2). Authors: Richard B. Larson.

[Laz+19] **Magnetic Fields of Extrasolar Planets: Planetary Interiors and Habitability**. 51:3, 135 (May 2019), 135. DOI: 10.48550/arXiv.1803.06487. arXiv: 1803.06487 [astro-ph.EP] (see page 101). Authors: Joseph Lazio et al..

[LBA97] **The End of the Main Sequence**. 482:1 (June 1997), 420–432. DOI: 10.1086/304125 (see page 1). Authors: Gregory Laughlin, Peter Bodenheimer, and Fred C. Adams.

[LBB29] Authors: Pierre Simon Laplace, Nathaniel Bowditch, and N. I. Bowditch. **Mécanique céleste**. 1829 (see page 87).

[LBR96] **Orbital migration of the planetary companion of 51 Pegasi to its present location**. 380:6575 (Apr. 1996), 606–607. DOI: 10.1038/380606a0 (see page 88). Authors: D. N. C. Lin, P. Bodenheimer, and D. C. Richardson.

[LDM10] **Using the Sun to estimate Earth-like planets detection capabilities - I. Impact of cold spots**. *A&A* 512 (2010), A38. DOI: 10.1051/0004-6361/200913071. URL: https://doi.org/10.1051/0004-6361/200913071 (see page 48). Authors: Lagrange, A.-M., Desort, M., and Meunier, N..

[Leg92] **Infrared Colors of Low-Mass Stars**. 82 (Sept. 1992), 351. DOI: 10.1086/191720 (see page 66). Authors: S. K. Leggett.

[Lei69] **A Magneto-Kinematic Model of the Solar Cycle**. 156 (Apr. 1969), 1. DOI: 10.1086/149943 (see page 5). Authors: Robert B. Leighton.

[Lin+18] **Gaia Data Release 2 - The astrometric solution**. *A&A* 616 (2018), A2. DOI: 10.1051/0004-6361/201832727. URL: https://doi.org/10.1051/0004-6361/201832727 (see page 34). Authors: Lindegren, L. et al..

[Lin+84] **Solar hard X-ray microflares**. 283 (Aug. 1984), 421–425. DOI: 10.1086/162321 (see page 10). Authors: R. P. Lin, R. A. Schwartz, S. R. Kane, R. M. Pelling, and K. C. Hurley.

[LL17] Authors: Henny J. G. L. M. Lamers and Emily M. Levesque. **Understanding Stellar Evolution**. 2017. DOI: 10.1088/978-0-7503-1278-3 (see page 1).

[LP86] **On the Tidal Interaction between Protoplanets and the Protoplanetary Disk. III. Orbital Migration of Protoplanets**. 309 (Oct. 1986), 846. DOI: 10.1086/164653 (see page 87). Authors: D. N. C. Lin and John Papaloizou.

[Lyn+18] **The detectability of radio emission from exoplanets**. 478:2 (Aug. 2018), 1763–1775. DOI: 10.1093/mnras/sty1138. arXiv: 1804.11006 [astro-ph.EP] (see page 102). Authors: C. R. Lynch, Tara Murphy, E. Lenc, and D. L. Kaplan.

[Ma+18] **The first super-Earth detection from the high cadence and high radial velocity precision Dharma Planet Survey**. 480:2 (Oct. 2018), 2411–2422. DOI: 10.1093/mnras/sty1933. arXiv: 1807.07098 [astro-ph.EP] (see page 24). Authors: Bo Ma et al..

[Mag+20] **Relation of X-ray activity and rotation in M dwarfs and predicted time-evolution of the X-ray luminosity**. 638A20 (June 2020), A20. DOI: 10.1051/0004-6361/201937408. arXiv: 2004.02904 [astro-ph.SR] (see pages 6, 8, 78). Authors: E. Magaudda, B. Stelzer, K. R. Covey, St. Raetz, S. P. Matt, and A. Scholz.

[Mag+22] **First eROSITA study of nearby M dwarfs and the rotation-activity relation in combination with TESS**. 661A29 (May 2022), A29. DOI: 10.1051/0004-6361/202141617. arXiv: 2106.14548 [astro-ph.SR] (see pages 66, 71, 78). Authors: E. Magaudda, B. Stelzer, St. Raetz, A. Klutsch, M. Salvato, and J. Wolf.

[Man+15] **How to Constrain Your M Dwarf: Measuring Effective Temperature, Bolometric Luminosity, Mass, and Radius**. 804:1, 64 (May 2015), 64. DOI: 10.1088/0004-637X/804/1/64. arXiv: 1501.01635 [astro-ph.SR] (see page 67). Authors: Andrew W. Mann, Gregory A. Feiden, Eric Gaidos, Tabetha Boyajian, and Kaspar von Braun.

[Max+13] **WASP-77 Ab: A Transiting Hot Jupiter Planet in a Wide Binary System**. 125:923 (Jan. 2013), 48. DOI: 10.1086/669231. arXiv: 1211.6033 [astro-ph.EP] (see pages 40, 44). Authors: P. F. L. Maxted et al..

[Maz+15] **Photometric Amplitude Distribution of Stellar Rotation of KOIs—Indication for Spin-Orbit Alignment of Cool Stars and High Obliquity for Hot Stars**. 801:1, 3 (Mar. 2015), 3. DOI: 10.1088/0004-637X/801/1/3. arXiv: 1501.01288 [astro-ph.EP] (see page 41). Authors: Tsevi Mazeh, Hagai B. Perets, Amy McQuillan, and Eyal S. Goldstein.

[MB00] **Planets Orbiting Other Suns**. 112:768 (Feb. 2000), 137–140. DOI: 10.1086/316516 (see page 12). Authors: Geoffrey W. Marcy and R. Paul Butler.

[MD16] **Follow-up spectroscopic observations of HD 107148 B: A new white dwarf companion of an exoplanet host star**. *Astronomische Nachrichten* 337:6 (June 2016), 627. DOI: 10.1002/asna.201512306. URL: https://doi.org/10.1002/asna.201512306 (see page 55). Authors: M. Mugrauer and B. Dincel.

[Mei+20] **The eROSITA camera array on the SRG satellite**. In: *Society of Photo-Optical Instrumentation Engineers (SPIE) Conference Series*. Vol. 11444. Society of Photo-Optical Instrumentation Engineers (SPIE) Conference Series. Dec. 2020, 114444O, 114444O. DOI: 10.1117/12.2560518 (see page 70). Authors: Norbert Meidinger et al..

[Men+18] **Radial Velocities from the N2K Project: Six New Cold Gas Giant Planets Orbiting HD 55696, HD 98736, HD 148164, HD 203473, and HD 211810**. *The Astronomical Journal* 156:5 (Oct. 2018), 213. DOI: 10.3847/1538-3881/aae1f5. URL: https://doi.org/10.3847/1538-3881/aae1f5 (see page 44). Authors: Kristo Ment, Debra A. Fischer, Gaspar Bakos, Andrew W. Howard, and Howard Isaacson.

[Mer+12] **eROSITA Science Book: Mapping the Structure of the Energetic Universe**. *arXiv e-prints* arXiv:1209.3114 (Sept. 2012), arXiv:1209.3114. DOI: 10.48550/arXiv.1209.3114. arXiv: 1209.3114 [astro-ph.HE] (see page 70). Authors: A. Merloni et al..

[Mes68] **Magnetic braking by a stellar wind-I**. 138 (Jan. 1968), 359. DOI: 10.1093/mnras/138.3.359 (see pages 3, 22, 62, 98). Authors: L. Mestel.

[MH08] **Improved Age Estimation for Solar-Type Dwarfs Using Activity-Rotation Diagnostics**. 687:2 (Nov. 2008), 1264–1293. DOI: 10.1086/591785. arXiv: 0807.1686 [astro-ph] (see pages 6, 9). Authors: Eric E. Mamajek and Lynne A. Hillenbrand.

[MI00] **A Radiation Hydrodynamic Model for Protostellar Collapse. II. The Second Collapse and the Birth of a Protostar**. 531:1 (Mar. 2000), 350–365. DOI: 10.1086/308439 (see page 2). Authors: Hirohiko Masunaga and Shu-ichiro Inutsuka.

[Mie05] **Large-Scale Dynamics of the Convection Zone and Tachocline**. *Living Reviews in Solar Physics* 2:1, 1 (Dec. 2005), 1. DOI: 10.12942/lrsp-2005-1 (see page 5). Authors: Mark S. Miesch.

[Mil+15] **A COMPREHENSIVE STATISTICAL ASSESSMENT OF STAR-PLANET INTERACTION**. *The Astrophysical Journal* 799:2 (Jan. 2015), 163. DOI: 10.1088/0004-637x/799/2/163. URL: https://doi.org/10.1088/0004-637x/799/2/163 (see pages 22, 39, 62). Authors: Brendan P. Miller, Elena Gallo, Jason T. Wright, and Elliott G. Pearson.

[MIM07] **Magnetic Fields and Rotations of Protostars**. 670:2 (Dec. 2007), 1198–1213. DOI: 10.1086/521779. arXiv: astro-ph/0702183 [astro-ph] (see page 3). Authors: Masahiro N. Machida, Shu-ichiro Inutsuka, and Tomoaki Matsumoto.

[MK04] **Control of star formation by supersonic turbulence**. *Reviews of Modern Physics* 76:1 (Jan. 2004), 125–194. DOI: 10.1103/RevModPhys.76.125. arXiv: astro-ph/0301093 [astro-ph] (see page 2). Authors: Mordecai-Mark Mac Low and Ralf S. Klessen.

[MMP00] **A systematic analysis of X-ray variability of dM stars**. 353 (Jan. 2000), 177–185 (see page 71). Authors: A. Marino, G. Micela, and G. Peres.

[MNM07] **The multiplicity of exoplanet host stars. Spectroscopic confirmation of the companions GJ 3021 B and HD 27442 B, one new planet host triple-star system, and global statistics**. 469:2 (July 2007), 755–770. DOI: 10.1051/0004-6361:20065883. arXiv: astro-ph/0703795 [astro-ph] (see page 54). Authors: M. Mugrauer, R. Neuhäuser, and T. Mazeh.

[MPR10] **Tidal Evolution of Close-in Planets**. 725:2 (Dec. 2010), 1995–2016. DOI: 10.1088/0004-637X/725/2/1995. arXiv: 1007.4785 [astro-ph.EP] (see page 99). Authors: Soko Matsumura, Stanton J. Peale, and Frederic A. Rasio.

[MQ95a] **A Jupiter-mass companion to a solar-type star**. 378:6555 (Nov. 1995), 355–359. DOI: 10.1038/378355a0 (see pages 12, 87). Authors: Michel Mayor and Didier Queloz.

[MQ95b] **A Jupiter-mass companion to a solar-type star**. 378:6555 (Nov. 1995), 355–359. DOI: 10.1038/378355a0 (see page 21). Authors: Michel Mayor and Didier Queloz.

[MS02] **X-ray emission near the substellar limit: The sigma Orionis and Taurus star forming regions**. 391 (Sept. 2002), 1025–1032. DOI: 10.1051/0004-6361:20020887. arXiv: astro-ph/0206329 [astro-ph] (see page 80). Authors: F. Mokler and B. Stelzer.

[MS87] **On magnetic braking of late-type stars**. 226 (May 1987), 57–66. DOI: 10.1093/mnras/226.1.57 (see page 98). Authors: L. Mestel and H. C. Spruit.

[MSS15] **Comparison of gyrochronological and isochronal age estimates for transiting exoplanet host stars**. 577A90 (May 2015), A90. DOI: 10.1051/0004-6361/201525774. arXiv: 1503.09111 [astro-ph.EP] (see pages 22, 62, 95). Authors: P. F. L. Maxted, A. M. Serenelli, and J. Southworth.

[Mug19] **Search for stellar companions of exoplanet host stars by exploring the second ESA-Gaia data release**. *Monthly Notices of the Royal Astronomical Society* 490:4 (Nov. 2019), 5088–5102. ISSN: 0035-8711. DOI: 10.1093/mnras/stz2673. eprint: https://academic.oup.com/mnras/article-pdf/490/4/5088/30656870/stz2673.pdf. URL: https://doi.org/10.1093/mnras/stz2673 (see pages 23, 53, 56, 63, 93). Authors: M Mugrauer.

[Muk93] **PIMMS and Viewing: proposal preparation tools**. *Legacy* 3 (May 1993), 21–31 (see page 30). Authors: K. Mukai.

[Mur+15] **Limits on low-frequency radio emission from southern exoplanets with the Murchison Widefield Array**. 446:3 (Jan. 2015), 2560–2565. DOI: 10.1093/mnras/stu2253. arXiv: 1410.6819 [astro-ph.EP] (see page 101). Authors: Tara Murphy et al..

[MW18] **Reanalysis of the Gaia Data Release 2 photometric sensitivity curves using HST/STIS spectrophotometry**. *A&A* 619 (2018), A180. DOI: 10.1051/0004-6361/201834051. URL: https://doi.org/10.1051/0004-6361/201834051 (see page 34). Authors: Maíz Apellániz, J. and Weiler, M..

[Nel+13] **Magnetic Wreaths and Cycles in Convective Dynamos**. 762:2, 73 (Jan. 2013), 73. DOI: 10.1088/0004-637X/762/2/73. arXiv: 1211.3129 [astro-ph.SR] (see page 5). Authors: Nicholas J. Nelson, Benjamin P. Brown, Allan Sacha Brun, Mark S. Miesch, and Juri Toomre.

[Neu+99] **Search for X-ray emission from bona-fide and candidate brown dwarfs**. 343 (Mar. 1999), 883–893. arXiv: astro-ph/9812436 [astro-ph] (see page 80). Authors: R. Neuhäuser et al..

[New+17] **The Hα Emission of Nearby M Dwarfs and its Relation to Stellar Rotation**. 834:1, 85 (Jan. 2017), 85. DOI: 10.3847/1538-4357/834/1/85. arXiv: 1611.03509 [astro-ph.SR] (see page 9). Authors: Elisabeth R. Newton, Jonathan Irwin, David Charbonneau, Perry Berlind, Michael L. Calkins, and Jessica Mink.

[New+19] **TESS Hunt for Young and Maturing Exoplanets (THYME): A Planet in the 45 Myr Tucana-Horologium Association**. 880:1, L17 (July 2019), L17. DOI: 10.3847/2041-8213/ab2988. arXiv: 1906.10703 [astro-ph.EP] (see page 23). Authors: Elisabeth R. Newton et al..

[Nic+16] **Temporal variability of the wind from the star τ Boötis**. 459:2 (June 2016), 1907–1915. DOI: 10.1093/mnras/stw731. arXiv: 1603.09242 [astro-ph.SR] (see page 14). Authors: B. A. Nicholson et al..

[Noy+84] **Rotation, convection, and magnetic activity in lower main-sequence stars.** 279 (Apr. 1984), 763–777. DOI: 10.1086/161945 (see pages 6, 7, 89). Authors: R. W. Noyes, L. W. Hartmann, S. L. Baliunas, D. K. Duncan, and A. H. Vaughan.

[NU90] **Chromospheric and Coronal Heating Mechanisms**. 54:3-4 (Dec. 1990), 377–445. DOI: 10.1007/BF00177801 (see page 10). Authors: U. Narain and P. Ulmschneider.

[Oba+17] **The Small-scale Structure of Photospheric Convection Retrieved by a Deconvolution Technique Applied to Hinode/SP Data**. 849:1, 7 (Nov. 2017), 7. DOI: 10.3847/1538-4357/aa8e44. arXiv: 1709.06933 [astro-ph.SR] (see page 4). Authors: T. Oba, T. L. Riethmüller, S. K. Solanki, Y. Iida, C. Quintero Noda, and T. Shimizu.

[OL04a] **Tidal Dissipation in Rotating Giant Planets**. 610:1 (July 2004), 477–509. DOI: 10.1086/421454. arXiv: astro-ph/0310218 [astro-ph] (see page 21). Authors: G. I. Ogilvie and D. N. C. Lin.

[OL04b] **Tidal Dissipation in Rotating Giant Planets**. 610:1 (July 2004), 477–509. DOI: 10.1086/421454. arXiv: astro-ph/0310218 [astro-ph] (see page 87). Authors: G. I. Ogilvie and D. N. C. Lin.

[OL07] **Tidal Dissipation in Rotating Solar-Type Stars**. 661:2 (June 2007), 1180–1191. DOI: 10.1086/515435. arXiv: astro-ph/0702492 [astro-ph] (see pages 18, 87, 88). Authors: G. I. Ogilvie and D. N. C. Lin.

[Orl+17] **Fifteen years in the high-energy life of the solar-type star HD 81809. XMM-Newton observations of a stellar activity cycle**. 605A19 (Sept. 2017), A19. DOI: 10.1051/0004-6361/201731301. arXiv: 1707.06437 [astro-ph.SR] (see page 62). Authors: S. Orlando et al..

[OV72] **Io's Triaxial Figure**. 17:1 (Aug. 1972), 209–215. DOI: 10.1016/0019-1035(72)90057-7 (see page 88). Authors: Brian O'Leary and Thomas C. Van Flandern.

[Pal+81] **Relations among stellar X-ray emission observed from Einstein, stellar rotation and bolometric luminosity.** 248 (Aug. 1981), 279–290. DOI: 10.1086/159152 (see pages 8, 22, 50, 78, 89). Authors: R. Pallavicini, L. Golub, R. Rosner, G. S. Vaiana, T. Ayres, and J. L. Linsky.

[Par09] **Solar Magnetism: The State of Our Knowledge and Ignorance**. 144:1-4 (Apr. 2009), 15–24. DOI: 10.1007/s11214-008-9445-x (see pages 5, 12). Authors: E. N. Parker.

[Par55a] **Hydromagnetic Dynamo Models.** 122 (Sept. 1955), 293. DOI: 10.1086/146087 (see page 4). Authors: Eugene N. Parker.

[Par55b] **The Formation of Sunspots from the Solar Toroidal Field.** 121 (Mar. 1955), 491. DOI: 10.1086/146010 (see page 5). Authors: Eugene N. Parker.

[Par58] **Dynamics of the Interplanetary Gas and Magnetic Fields.** 128 (Nov. 1958), 664. DOI: 10.1086/146579 (see page 3). Authors: E. N. Parker.

[Par60] **The Hydrodynamic Theory of Solar Corpuscular Radiation and Stellar Winds.** 132 (Nov. 1960), 821. DOI: 10.1086/146985 (see page 3). Authors: E. N. Parker.

[Par72] **Topological Dissipation and the Small-Scale Fields in Turbulent Gases**. 174 (June 1972), 499. DOI: 10.1086/151512 (see page 11). Authors: E. N. Parker.

[Par75] **The generation of magnetic fields in astrophysical bodies. X. Magnetic buoyancy and the solar dynamo.** 198 (May 1975), 205–209. DOI: 10.1086/153593 (see page 5). Authors: E. N. Parker.

[Par83] **The propagation of torsion along flux tubes subject to dynamical nonequilibrium**. *Geophysical and Astrophysical Fluid Dynamics* 24:4 (Jan. 1983), 245–272. DOI: 10.1080/03091928308209068 (see page 11). Authors: E. N. Parker.

[Pat+02] **Stellar Companions to Stars with Planets**. 581:1 (Dec. 2002), 654–665. DOI: 10.1086/342982. arXiv: astro-ph/0207538 [astro-ph] (see page 40). Authors: J. Patience et al..

[Pav+21] **The ART-XC telescope on board the SRG observatory**. 650A42 (June 2021), A42. DOI: 10.1051/0004-6361/202040265. arXiv: 2103.12479 [astro-ph.HE] (see page 70). Authors: M. Pavlinsky et al..

[Pay25] **Stellar Atmospheres; a Contribution to the Observational Study of High Temperature in the Reversing Layers of Stars.** PhD thesis. RADCLIFFE COLLEGE., Jan. 1925 (see page 2). Authors: Cecilia Helena Payne.

[PE04] **Isochrone ages for field dwarfs: method and application to the age-metallicity relation**. 351:2 (June 2004), 487–504. DOI: 10.1111/j.1365-2966.2004.07780.x. arXiv: astro-ph/0401418 [astro-ph] (see page 62). Authors: Frédéric Pont and Laurent Eyer.

[Pee+09] **Old, Rich, and Eccentric: Two Jovian Planets Orbiting Evolved Metal-Rich Stars1**. *Publications of the Astronomical Society of the Pacific* 121:880 (June 2009), 613–620. DOI: 10.1086/599862. URL: https://doi.org/10.1086/599862 (see page 54). Authors: Kathryn M. G. Peek et al..

[Pen+12] **CONSTRAINING TIDAL DISSIPATION IN STARS FROM THE DESTRUCTION RATES OF EXOPLANETS**. *The Astrophysical Journal* 751:2 (May 2012), 96. DOI: 10.1088/0004-637x/751/2/96. URL: https://doi.org/10.1088/0004-637x/751/2/96 (see pages 41–43, 88, 91, 92). Authors: Kaloyan Penev, Brian Jackson, Federico Spada, and Nicole Thom.

[Pen+16] **HATS-18b: An Extreme Short-period Massive Transiting Planet Spinning Up Its Star**. 152:5, 127 (Nov. 2016), 127. DOI: 10.3847/0004-6256/152/5/127. arXiv: 1606.00848 [astro-ph.EP] (see page 22). Authors: K. Penev et al..

[Pen+18] **Empirical Tidal Dissipation in Exoplanet Hosts From Tidal Spin-up**. 155:4, 165 (Apr. 2018), 165. DOI: 10.3847/1538-3881/aaaf71. arXiv: 1802.05269 [astro-ph.SR] (see pages 88, 97). Authors: Kaloyan Penev, L. G. Bouma, Joshua N. Winn, and Joel D. Hartman.

[Pen65] **Gravitational Collapse and Space-Time Singularities**. *Phys. Rev. Lett.* 14 (3 Jan. 1965), 57–59. DOI: 10.1103/PhysRevLett.14.57. URL: https://link.aps.org/doi/10.1103/PhysRevLett.14.57 (see page 2). Authors: Roger Penrose.

[Pev+03] **The Relationship Between X-Ray Radiance and Magnetic Flux**. 598:2 (Dec. 2003), 1387–1391. DOI: 10.1086/378944 (see page 10). Authors: Alexei A. Pevtsov et al..

[PF00] Authors: Eric Priest and Terry Forbes. **Magnetic Reconnection**. 2000 (see page 4).

[PF05] **The Evolution of X-Ray Emission in Young Stars**. 160:2 (Oct. 2005), 390–400. DOI: 10.1086/432094. arXiv: astro-ph/0506052 [astro-ph] (see page 80). Authors: Thomas Preibisch and Eric D. Feigelson.

[PHK17] **A Panchromatic View of Brown Dwarf Aurorae**. 846:1, 75 (Sept. 2017), 75. DOI: 10.3847/1538-4357/aa8596. arXiv: 1708.02942 [astro-ph.SR] (see page 102). Authors: J. Sebastian Pineda, Gregg Hallinan, and Melodie M. Kao.

[Pil+22] **X-ray variability of HD 189733 across eight years of XMM-Newton observations**. 660A75 (Apr. 2022), A75. DOI: 10.1051/0004-6361/202142232. arXiv: 2201.12149 [astro-ph.SR] (see page 62). Authors: I. Pillitteri, G. Micela, A. Maggio, S. Sciortino, and J. Lopez-Santiago.

[Pin+18] **The HADES RV Programme with HARPS-N at TNG - VIII. GJ15A: a multiple wide planetary system sculpted by binary interaction**. *A&A* 617 (2018), A104. DOI: 10.1051/0004-6361/201732535. URL: https://doi.org/10.1051/0004-6361/201732535 (see page 44). Authors: Pinamonti, M. et al..

[Piz+03] **The stellar activity-rotation relationship revisited: Dependence of saturated and non-saturated X-ray emission regimes on stellar mass for late-type dwarfs**. 397 (Jan. 2003), 147–157. DOI: 10.1051/0004-6361:20021560 (see pages 8, 22, 49, 50, 78, 89). Authors: N. Pizzolato, A. Maggio, G. Micela, S. Sciortino, and P. Ventura.

[Pla+20] **A planet within the debris disk around the pre-main-sequence star AU Microscopii**. 582:7813 (June 2020), 497–500. DOI: 10.1038/s41586-020-2400-z. arXiv: 2006.13248 [astro-ph.EP] (see page 23). Authors: Peter Plavchan et al..

[PM13] **Intrinsic Colors, Temperatures, and Bolometric Corrections of Pre-main-sequence Stars**. 208:1, 9 (Sept. 2013), 9. DOI: 10.1088/0067-0049/208/1/9. arXiv: 1307.2657 [astro-ph.SR] (see pages 35, 63, 67, 78). Authors: Mark J. Pecaut and Eric E. Mamajek.

[Pon09] **Empirical evidence for tidal evolution in transiting planetary systems**. 396:3 (July 2009), 1789–1796. DOI: 10.1111/j.1365-2966.2009.14868.x. arXiv: 0812.1463 [astro-ph] (see pages 18, 19, 22, 62, 87). Authors: Frédéric Pont.

[PR02] **Where Are the Massive Close-in Extrasolar Planets?** 568:2 (Apr. 2002), L117–L120. DOI: 10.1086/339794 (see page 22). Authors: M. Pätzold and H. Rauer.

[Pre+21a] **The eROSITA X-ray telescope on SRG**. 647A1 (Mar. 2021), A1. DOI: 10.1051/0004-6361/202039313. arXiv: 2010.03477 [astro-ph.HE] (see page 35). Authors: P. Predehl et al..

[Pre+21b] **The eROSITA X-ray telescope on SRG**. 647A1 (Mar. 2021), A1. DOI: 10.1051/0004-6361/202039313. arXiv: 2010.03477 [astro-ph.HE] (see page 70). Authors: P. Predehl et al..

[PRS10] **Coronal properties of planet-bearing stars**. 515A98 (June 2010), A98. DOI: 10.1051/0004-6361/201014245. arXiv: 1003.5802 [astro-ph.SR] (see pages 22, 23, 62). Authors: K. Poppenhaeger, J. Robrade, and J. H. M. M. Schmitt.

[PS11a] **A CORRELATION BETWEEN HOST STAR ACTIVITY AND PLANET MASS FOR CLOSE-IN EXTRASOLAR PLANETS?** *The Astrophysical Journal* 735:1 (June 2011), 59. DOI: 10.1088/0004-637x/735/1/59. URL: https://doi.org/10.1088/0004-637x/735/1/59 (see pages 22, 23). Authors: K. Poppenhaeger and J. H. M. M. Schmitt.

[PS11b] **A CORRELATION BETWEEN HOST STAR ACTIVITY AND PLANET MASS FOR CLOSE-IN EXTRASOLAR PLANETS?** *The Astrophysical Journal* 735:1 (June 2011), 59. DOI: 10.1088/0004-637x/735/1/59. URL: https://doi.org/10.1088/0004-637x/735/1/59 (see page 62). Authors: K. Poppenhaeger and J. H. M. M. Schmitt.

[PS11c] **A Correlation Between Host Star Activity and Planet Mass for Close-in Extrasolar Planets?** 735:1, 59 (July 2011), 59. DOI: 10.1088/0004-637X/735/1/59. arXiv: 1106.0189 [astro-ph.SR] (see page 20). Authors: K. Poppenhaeger and J. H. M. M. Schmitt.

[PSW13] **Transit Observations of the Hot Jupiter HD 189733b at X-Ray Wavelengths**. 773:1, 62 (Aug. 2013), 62. DOI: 10.1088/0004-637X/773/1/62. arXiv: 1306.2311 [astro-ph.SR] (see pages 51, 95). Authors: K. Poppenhaeger, J. H. M. M. Schmitt, and S. J. Wolk.

[PW14] **Indications for an influence of hot Jupiters on the rotation and activity of their host stars**. 565L1 (May 2014), L1. DOI: 10.1051/0004-6361/201423454. arXiv: 1404.1073 [astro-ph.SR] (see pages 23, 62, 89, 95, 101). Authors: K. Poppenhaeger and S. J. Wolk.

[PZJ14] **POET: A Model for Planetary Orbital Evolution Due to Tides on Evolving Stars**. 126:940 (June 2014), 553. DOI: 10.1086/677042. arXiv: 1405.1050 [astro-ph.EP] (see pages 91, 92). Authors: Kaloyan Penev, Michael Zhang, and Brian Jackson.

[Que+18] **StarHorse: a Bayesian tool for determining stellar masses, ages, distances, and extinctions for field stars**. 476:2 (May 2018), 2556–2583. DOI: 10.1093/mnras/sty330. arXiv: 1710.09970 [astro-ph.IM] (see page 95). Authors: A. B. A. Queiroz et al..

[Que+20] **From the bulge to the outer disc: StarHorse stellar parameters, distances, and extinctions for stars in APOGEE DR16 and other spectroscopic surveys**. 638A76 (June 2020), A76. DOI: 10.1051/0004-6361/201937364. arXiv: 1912.09778 [astro-ph.GA] (see page 95). Authors: A. B. A. Queiroz et al..

[Rag+10] **A SURVEY OF STELLAR FAMILIES: MULTIPLICITY OF SOLAR-TYPE STARS**. *The Astrophysical Journal Supplement Series* 190:1 (Aug. 2010), 1–42. DOI: 10.1088/0067-0049/190/1/1. URL: https://doi.org/10.1088/0067-0049/190/1/1 (see page 23). Authors: Deepak Raghavan et al..

[Rao+18] **Star-planet interactions. V. Dynamical and equilibrium tides in convective zones**. 618A18 (Oct. 2018), A18. DOI: 10.1051/0004-6361/201833107. arXiv: 1807.01474 [astro-ph.SR] (see pages 19, 88). Authors: Suvrat Rao et al..

[RCG17] **Evidence for photometric activity cycles in 3203 Kepler stars**. 603A52 (July 2017), A52. DOI: 10.1051/0004-6361/201730599. arXiv: 1705.03312 [astro-ph.SR] (see page 62). Authors: Timo Reinhold, Robert H. Cameron, and Laurent Gizon.

[Rei+22] **Magnetism, rotation, and nonthermal emission in cool stars. Average magnetic field measurements in 292 M dwarfs**. 662A41 (June 2022), A41. DOI: 10.1051/0004-6361/202243251. arXiv: 2204.00342 [astro-ph.SR] (see pages 6, 78). Authors: A. Reiners et al..

[RF96] **Dynamical instabilities and the formation of extrasolar planetary systems**. *Science* 274 (Nov. 1996), 954–956. DOI: 10.1126/science.274.5289.954 (see pages 21, 87). Authors: Frederic A. Rasio and Eric B. Ford.

[Rib06] **Masses and Radii of Low-Mass Stars: Theory Versus Observations**. 304:1-4 (Aug. 2006), 89–92. DOI: 10.1007/s10509-006-9081-4. arXiv: astro-ph/0511431 [astro-ph] (see page 68). Authors: I. Ribas.

[Rob+13] **Hα Activity of Old M Dwarfs: Stellar Cycles and Mean Activity Levels for 93 Low-mass Stars in the Solar Neighborhood**. 764:1, 3 (Feb. 2013), 3. DOI: 10.1088/0004-637X/764/1/3. arXiv: 1211.6091 [astro-ph.SR] (see page 79). Authors: Paul Robertson, Michael Endl, William D. Cochran, and Sarah E. Dodson-Robinson.

[Rob+15] **KNOW THE STAR, KNOW THE PLANET. III. DISCOVERY OF LATE-TYPE COMPANIONS TO TWO EXOPLANET HOST STARS**. *The Astronomical Journal* 149:4 (Mar. 2015), 118. DOI: 10.1088/0004-6256/149/4/118. URL: https://doi.org/10.1088%2F0004-6256%2F149%2F4%2F118 (see page 53). Authors: Lewis C. Roberts et al..

[Rob70] **Spatially Periodic Dynamos**. *Philosophical Transactions of the Royal Society of London Series A* 266:1179 (July 1970), 535–558. DOI: 10.1098/rsta.1970.0011 (see page 4). Authors: G. O. Roberts.

[RS05] **X-ray properties of active M dwarfs as observed by XMM-Newton**. 435:3 (June 2005), 1073–1085. DOI: 10.1051/0004-6361:20041941. arXiv: astro-ph/0504145 [astro-ph] (see pages 11, 66). Authors: J. Robrade and J. H. M. M. Schmitt.

[RS09] **X-ray emission from the M9 dwarf 1RXS J115928.5-524717. Quasi-quiescent coronal activity at the end of the main-sequence**. 496:1 (Mar. 2009), 229–233. DOI: 10.1051/0004-6361/200811224. arXiv: 0901.3027 [astro-ph.SR] (see page 79). Authors: J. Robrade and J. H. M. M. Schmitt.

[RSF12] **Coronal activity cycles in nearby G and K stars - XMM-Newton monitoring of 61 Cygni and tauri**. *A&A* 543 (2012), A84. DOI: 10.1051/0004-6361/201219046. URL: https://doi.org/10.1051/0004-6361/201219046 (see pages 51, 62). Authors: Robrade, J., Schmitt, J. H. M. M., and Favata, F..

[RSH07] **X-ray activity cycles in stellar coronae**. 78 (Jan. 2007), 311. DOI: 10.48550/arXiv.astro-ph/0702520. arXiv: astro-ph/0702520 [astro-ph] (see page 79). Authors: J. Robrade, J. H. M. M. Schmitt, and A. Hempelmann.

[Rut+00] **Chandra Detection of an X-Ray Flare from the Brown Dwarf LP 944-20**. 538:2 (Aug. 2000), L141–L144. DOI: 10.1086/312817. arXiv: astro-ph/0005559 [astro-ph] (see page 80). Authors: Robert E. Rutledge, Gibor Basri, Eduardo L. Martín, and Lars Bildsten.

[Sal+15] **High-energy irradiation and mass loss rates of hot Jupiters in the solar neighborhood**. *A&A* 576 (2015), A42. DOI: 10.1051/0004-6361/201425243. URL: https://doi.org/10.1051/0004-6361/201425243 (see page 44). Authors: Salz, M., Schneider, P. C., Czesla, S., and Schmitt, J. H. M. M..

[San+10] **A scenario of planet erosion by coronal radiation**. 511L8 (Feb. 2010), L8. DOI: 10.1051/0004-6361/200913670. arXiv: 1002.1875 [astro-ph.SR] (see page 95). Authors: J. Sanz-Forcada et al..

[San+16] **Spectro-photometric distances to stars: A general purpose Bayesian approach**. 585A42 (Jan. 2016), A42. DOI: 10.1051/0004-6361/201323177. arXiv: 1501.05500 [astro-ph.IM] (see page 95). Authors: Basílio X. Santiago et al..

[SC01] **A search for Ca II emission enhancement in stars resulting from nearby giant planets**. 325:1 (July 2001), 55–59. DOI: 10.1046/j.1365-8711.2001.04296.x (see pages 14, 18). Authors: S. H. Saar and M. Cuntz.

[SCG17] **Accurate Empirical Radii and Masses of Planets and Their Host Stars with Gaia Parallaxes**. *The Astronomical Journal* 153:3 (Mar. 2017), 136. DOI: 10.3847/1538-3881/aa5df3. URL: https://doi.org/10.3847/1538-3881/aa5df3 (see page 44). Authors: Keivan G. Stassun, Karen A. Collins, and B. Scott Gaudi.

[Sch+11] **The corona and companion of CoRoT-2a. Insights from X-rays and optical spectroscopy**. 532A3 (Aug. 2011), A3. DOI: 10.1051/0004-6361/201116961. arXiv: 1106.1522 [astro-ph.SR] (see pages 33, 34, 39, 40, 51, 53). Authors: S. Schröter, S. Czesla, U. Wolter, H. M. Müller, K. F. Huber, and J. H. M. M. Schmitt.

[Sch+85] **An Einstein Observatory X-ray survey of main-sequence stars with shallow convection zones.** 290 (Mar. 1985), 307–320. DOI: 10.1086/162986 (see page 7). Authors: J. H. M. M. Schmitt, L. Golub, Jr. Harnden F. R., C. W. Maxson, R. Rosner, and G. S. Vaiana.

[Sch+90] **Einstein Observatory Coronal Temperatures of Late-Type Stars**. 365 (Dec. 1990), 704. DOI: 10.1086/169525 (see pages 11, 30, 66, 71). Authors: J. H. M. M. Schmitt, A. Collura, S. Sciortino, G. S. Vaiana, Jr. Harnden F. R., and R. Rosner.

[Sch+98] **Helioseismic Studies of Differential Rotation in the Solar Envelope by the Solar Oscillations Investigation Using the Michelson Doppler Imager**. 505:1 (Sept. 1998), 390–417. DOI: 10.1086/306146 (see page 4). Authors: J. Schou et al..

[Sch10] **POSSIBLE CONSTRAINTS ON EXOPLANET MAGNETIC FIELD STRENGTHS FROM PLANET-STAR INTERACTION**. *The Astrophysical Journal* 722:2 (Sept. 2010), 1547–1555. DOI: 10.1088/0004-637x/722/2/1547. URL: https://doi.org/10.1088/0004-637x/722/2/1547 (see page 62). Authors: Caleb A. Scharf.

[Sch48] **On Noise Arising from the Solar Granulation.** 107 (Jan. 1948), 1. DOI: 10.1086/144983 (see page 10). Authors: Martin Schwarzschild.

[Sch49] **Sonnen-und Saturn-Beobachtungen im Jahre 1848, von Herrn Hofrath Schwabe in Dessau**. *Astronomische Nachrichten* 28 (Apr. 1849), 302 (see page 4). Authors: M. Schwabe.

[Sch97] **Coronae on solar-like stars.** 318 (Feb. 1997), 215–230 (see pages 7, 66). Authors: J. H. M. M. Schmitt.

[SD97] **Activity-Related Radial Velocity Variation in Cool Stars**. 485:1 (Aug. 1997), 319–327. DOI: 10.1086/304392 (see pages 20, 48). Authors: Steven H. Saar and Robert A. Donahue.

[SH77] **Are striations on PHOBOS evidence for tidal stress**. 268 (Aug. 1977), 421. DOI: 10.1038/268421a0 (see page 88). Authors: S. Soter and A. Harris.

[Shk+05] **Hot Jupiters and Hot Spots: The Short- and Long-Term Chromospheric Activity on Stars with Giant Planets**. *The Astrophysical Journal* 622:2 (Apr. 2005), 1075–1090. DOI: 10.1086/428037. URL: https://doi.org/10.1086/428037 (see pages 21, 22). Authors: E. Shkolnik, G. A. H. Walker, D. A. Bohlender, P.-G. Gu, and M. Kurster.

[Shk+08] **The On/Off Nature of Star-Planet Interactions**. 676:1 (Mar. 2008), 628–638. DOI: 10.1086/527351. arXiv: 0712.0004 [astro-ph] (see pages 14, 22). Authors: Evgenya Shkolnik, David A. Bohlender, Gordon A. H. Walker, and Andrew Collier Cameron.

[Sku72] **Time Scales for Ca II Emission Decay, Rotational Braking, and Lithium Depletion**. 171 (Feb. 1972), 565. DOI: 10.1086/151310 (see pages 3, 6, 62). Authors: A. Skumanich.

[SL04a] **NEXXUS: A comprehensive ROSAT survey of coronal X-ray emission among nearby solar-like stars**. 417 (Apr. 2004), 651–665. DOI: 10.1051/0004-6361:20030495. arXiv: astro-ph/0308510 [astro-ph] (see pages 7, 89, 102). Authors: J. H. M. M. Schmitt and C. Liefke.

[SL04b] **NEXXUS: A comprehensive ROSAT survey of coronal X-ray emission among nearby solar-like stars***. *A&A* 417:2 (2004), 651–665. DOI: 10.1051/0004-6361:20030495. URL: https://doi.org/10.1051/0004-6361:20030495 (see page 35). Authors: Schmitt, J. H. M. M. and Liefke, C..

[Sod+93] **Rotation and Chromospheric Emission among F, G, and K Dwarfs of the Pleiades**. 85 (Apr. 1993), 315. DOI: 10.1086/191767 (see page 6). Authors: David R. Soderblom, John R. Stauffer, J. D. Hudon, and Burton F. Jones.

[Sou10] **Homogeneous studies of transiting extrasolar planets - III. Additional planets and stellar models**. 408:3 (Nov. 2010), 1689–1713. DOI: 10.1111/j.1365-2966.2010.17231.x. arXiv: 1006.4443 [astro-ph.EP] (see page 95). Authors: John Southworth.

[Spö79] **Beobachtung der Sonnenflecken etc.** *Astronomische Nachrichten* 96:2 (Oct. 1879), 23. DOI: 10.1002/asna.18790960205 (see page 4). Authors: F. W. Gustav Spörer.

[Sta+19] **The Revised TESS Input Catalog and Candidate Target List**. *The Astronomical Journal* 158:4 (Sept. 2019), 138. DOI: 10.3847/1538-3881/ab3467. URL: https://doi.org/10.3847/1538-3881/ab3467 (see pages 40, 44). Authors: Keivan G. Stassun et al..

[Ste+06] **X-ray emission of brown dwarfs: towards constraining the dependence on age, luminosity, and temperature**. 448:1 (Mar. 2006), 293–304. DOI: 10.1051/0004-6361:20053677. arXiv: astro-ph/0511168 [astro-ph] (see page 80). Authors: B. Stelzer, G. Micela, E. Flaccomio, R. Neuhäuser, and R. Jayawardhana.

[Ste+12] **The ultracool dwarf DENIS-P J104814.7-395606. Chromospheres and coronae at the low-mass end of the main-sequence**. 537A94 (Jan. 2012), A94. DOI: 10.1051/0004-6361/201118097. arXiv: 1111.6880 [astro-ph.SR] (see page 79). Authors: B. Stelzer et al..

[Ste+13] **The UV and X-ray activity of the M dwarfs within 10 pc of the Sun**. 431:3 (May 2013), 2063–2079. DOI: 10.1093/mnras/stt225. arXiv: 1302.1061 [astro-ph.SR] (see pages 6, 71, 79). Authors: B. Stelzer, A. Marino, G. Micela, J. López-Santiago, and C. Liefke.

[Ste+22] **A first eROSITA view of ultracool dwarfs**. 661A44 (May 2022), A44. DOI: 10.1051/0004-6361/202141232. arXiv: 2106.14547 [astro-ph.SR] (see page 71). Authors: B. Stelzer, A. Klutsch, M. Coffaro, E. Magaudda, and M. Salvato.

[Ste04] **Quiescent X-Ray Emission from an Evolved Brown Dwarf?** 615:2 (Nov. 2004), L153–L156. DOI: 10.1086/426121. arXiv: astro-ph/0409617 [astro-ph] (see page 80). Authors: B. Stelzer.

[Ste94] **Applicability of the Rossby number in activity-rotation relations for dwarfs and giants.** 292 (Dec. 1994), 191–207 (see page 6). Authors: K. Stepien.

[Sti03] **On the time scale of energy transport in the sun**. 212:1 (Jan. 2003), 3–6. DOI: 10.1023/A:1022952621810 (see page 1). Authors: Michael Stix.

[Str+01] **The European Photon Imaging Camera on XMM-Newton: The pn-CCD camera**. 365 (Jan. 2001), L18–L26. DOI: 10.1051/0004-6361:20000066 (see page 24). Authors: L. Strüder et al..

[Str+14] **On the Diversity of Magnetic Interactions in Close-in Star-Planet Systems**. 795:1, 86 (Nov. 2014), 86. DOI: 10.1088/0004-637X/795/1/86. arXiv: 1409.5268 [astro-ph.EP] (see page 50). Authors: A. Strugarek, A. S. Brun, S. P. Matt, and V. Réville.

[Str+15] **Magnetic Games between a Planet and Its Host Star: The Key Role of Topology**. 815:2, 111 (Dec. 2015), 111. DOI: 10.1088/0004-637X/815/2/111. arXiv: 1511.02837 [astro-ph.EP] (see page 14). Authors: A. Strugarek, A. S. Brun, S. P. Matt, and V. Réville.

[Str+17] **The Fate of Close-in Planets: Tidal or Magnetic Migration?** *The Astrophysical Journal* 847:2 (Sept. 2017), L16. DOI: 10.3847/2041-8213/aa8d70. URL: https://doi.org/10.3847/2041-8213/aa8d70 (see page 22). Authors: A. Strugarek et al..

[Str+19] **Chasing Star-Planet Magnetic Interactions: The Case of Kepler-78**. 881:2, 136 (Aug. 2019), 136. DOI: 10.3847/1538-4357/ab2ed5. arXiv: 1907.01020 [astro-ph.EP] (see page 14). Authors: A. Strugarek, A. S. Brun, J. -F. Donati, C. Moutou, and V. Réville.

[Sun+21] **SRG X-ray orbital observatory. Its telescopes and first scientific results**. 656A132 (Dec. 2021), A132. DOI: 10.1051/0004-6361/202141179. arXiv: 2104.13267 [astro-ph.HE] (see page 70). Authors: R. Sunyaev et al..

[SZ92] **The solar tachocline.** 265 (Nov. 1992), 106–114 (see page 5). Authors: E. A. Spiegel and J. -P. Zahn.

[Tak+07] **Structure and Evolution of Nearby Stars with Planets. II. Physical Properties of ~1000 Cool Stars from the SPOCS Catalog**. *The Astrophysical Journal Supplement Series* 168:2 (Feb. 2007), 297–318. DOI: 10.1086/509763. URL: https://doi.org/10.1086/509763 (see page 49). Authors: Genya Takeda, Eric B. Ford, Alison Sills, Frederic A. Rasio, Debra A. Fischer, and Jeff A. Valenti.

[Ter+98] **On the Tidal Interaction of a Solar-Type Star with an Orbiting Companion: Excitation of g-Mode Oscillation and Orbital Evolution**. 502:2 (Aug. 1998), 788–801. DOI: 10.1086/305927. arXiv: astro-ph/9801280 [astro-ph] (see page 62). Authors: C. Terquem, J. C. B. Papaloizou, R. P. Nelson, and D. N. C. Lin.

[Tok+00] **The Triple System HR 7272**. *Astronomy Letters* 26 (Feb. 2000), 116–121. DOI: 10.1134/1.20374 (see pages 40, 55). Authors: A. A. Tokovinin, R. F. Griffin, Yu. Yu. Balega, E. A. Pluzhnik, and S. Udry.

[Tor13] **Fundamental properties of lower main-sequence stars**. *Astronomische Nachrichten* 334:1-2 (Feb. 2013), 4. DOI: 10.1002/asna.201211743. arXiv: 1209.1279 [astro-ph.SR] (see page 68). Authors: G. Torres.

[Tri+98] **Orbital Evolution and Migration of Giant Planets: Modeling Extrasolar Planets**. 500:1 (June 1998), 428–439. DOI: 10.1086/305711. arXiv: astro-ph/9801292 [astro-ph] (see page 87). Authors: D. E. Trilling, W. Benz, T. Guillot, J. I. Lunine, W. B. Hubbard, and A. Burrows.

[Tsu+91] **The Soft X-ray Telescope for the SOLAR-A mission**. 136:1 (Nov. 1991), 37–67. DOI: 10.1007/BF00151694 (see page 11). Authors: S. Tsuneta et al..

[Tur+01] **The European Photon Imaging Camera on XMM-Newton: The MOS cameras**. 365 (Jan. 2001), L27–L35. DOI: 10.1051/0004-6361:20000087. arXiv: astro-ph/0011498 [astro-ph] (see page 24). Authors: M. J. L. Turner et al..

[Tur+21] **The search for radio emission from the exoplanetary systems 55 Cancri, υ Andromedae, and τ Boötis using LOFAR beam-formed observations**. 645A59 (Jan. 2021), A59. DOI: 10.1051/0004-6361/201937201. arXiv: 2012.07926 [astro-ph.EP] (see page 102). Authors: Jake D. Turner et al..

[TW94] **Evolution of the Earth-Moon System**. 108 (Nov. 1994), 1943. DOI: 10.1086/117209 (see page 87). Authors: Jihad Touma and Jack Wisdom.

[TWH08] **Improved Parameters for Extrasolar Transiting Planets**. 677:2 (Apr. 2008), 1324–1342. DOI: 10.1086/529429. arXiv: 0801.1841 [astro-ph] (see page 95). Authors: Guillermo Torres, Joshua N. Winn, and Matthew J. Holman.

[Udr+00] **The CORALIE survey for southern extra-solar planets. II. The short-period planetary companions to <ASTROBJ>HD 75289</ASTROBJ> and <ASTROBJ>HD 130322</ASTROBJ>**. 356 (Apr. 2000), 590–598 (see pages 44, 49). Authors: S. Udry et al..

[Ulr10] **Solar Meridional Circulation from Doppler Shifts of the Fe I Line at 5250 Å as Measured by the 150-foot Solar Tower Telescope at the Mt. Wilson Observatory**. 725:1 (Dec. 2010), 658–669. DOI: 10.1088/0004-637X/725/1/658. arXiv: 1010.0487 [astro-ph.SR] (see page 4). Authors: Roger K. Ulrich.

[Vah95] **Magnetic interaction in binary stars.** 300 (Aug. 1995), 158 (see page 12). Authors: M. N. Vahia.

[Vai+81] **Results from an extensive Einstein stellar survey.** 245 (Apr. 1981), 163–182. DOI: 10.1086/158797 (see page 7). Authors: G. S. Vaiana et al..

[Val+15] **Uncertainties in asteroseismic grid-based estimates of stellar ages. SCEPtER: Stellar CharactEristics Pisa Estimation gRid**. 575A12 (Mar. 2015), A12. DOI: 10.1051/0004-6361/201424686. arXiv: 1412.5895 [astro-ph.SR] (see page 62). Authors: G. Valle, M. Dell'Omodarme, P. G. Prada Moroni, and S. Degl'Innocenti.

[van+11] **Heating of the Solar Chromosphere and Corona by Alfvén Wave Turbulence**. 736:1, 3 (July 2011), 3. DOI: 10.1088/0004-637X/736/1/3. arXiv: 1105.0402 [astro-ph.SR] (see page 10). Authors: A. A. van Ballegooijen, M. Asgari-Targhi, S. R. Cranmer, and E. E. DeLuca.

[Van+15] **CHARACTERIZING K2 PLANET DISCOVERIES: A SUPER-EARTH TRANSITING THE BRIGHT K DWARF HIP 116454**. *The Astrophysical Journal* 800:1 (Feb. 2015), 59. DOI: 10.1088/0004-637x/800/1/59. URL: https://doi.org/10.1088/0004-637x/800/1/59 (see page 56). Authors: Andrew Vanderburg et al..

[van47] **Zodiacal Light in the Solar Corona.** 105 (May 1947), 471. DOI: 10.1086/144921 (see page 3). Authors: H. C. van de Hulst.

[Ved+20] **Direct Radio Discovery of a Cold Brown Dwarf**. 903:2, L33 (Nov. 2020), L33. DOI: 10.3847/2041-8213/abc256. arXiv: 2010.01915 [astro-ph.EP] (see page 102). Authors: H. K. Vedantham et al..

[Vil84] **The nature of magnetic activity in lower main sequence stars.** 133 (Apr. 1984), 117–126 (see page 12). Authors: O. Vilhu.

[Vis09] **The Saturation Limit of the Magnetorotational Instability**. 696:1 (May 2009), 1021–1028. DOI: 10.1088/0004-637X/696/1/1021. arXiv: 0902.0942 [astro-ph.HE] (see page 12). Authors: Ethan T. Vishniac.

[VR78] **Recent advances in coronal physics.** 16 (Jan. 1978), 393–428. DOI: 10.1146/annurev.aa.16.090178.002141 (see page 6). Authors: G. S. Vaiana and R. Rosner.

[Wal+11] **White-light Flares on Cool Stars in the Kepler Quarter 1 Data**. 141:2, 50 (Feb. 2011), 50. DOI: 10.1088/0004-6256/141/2/50. arXiv: 1008.0853 [astro-ph.SR] (see page 26). Authors: Lucianne M. Walkowicz et al..

[Wal82] **On the Coronae of rapidly rotating stars. III. an improved coronal rotation-activity relation in late type dwarfs.** 253 (Feb. 1982), 745–751. DOI: 10.1086/159675 (see page 8). Authors: F. M. Walter.

[WCB14] **Trends in Ultracool Dwarf Magnetism. I. X-Ray Suppression and Radio Enhancement**. 785:1, 9 (Apr. 2014), 9. DOI: 10.1088/0004-637X/785/1/9. arXiv: 1310.6757 [astro-ph.SR] (see page 79). Authors: P. K. G. Williams, B. A. Cook, and E. Berger.

[WD16] **Solar-type dynamo behaviour in fully convective stars without a tachocline**. 535:7613 (July 2016), 526–528. DOI: 10.1038/nature18638. arXiv: 1607.07870 [astro-ph.SR] (see pages 5, 79). Authors: Nicholas J. Wright and Jeremy J. Drake.

[WD67a] **The Angular Momentum of the Solar Wind**. 148 (Apr. 1967), 217–227. DOI: 10.1086/149138 (see page 3). Authors: Edmund J. Weber and Jr. Davis Leverett.

[WD67b] **The Angular Momentum of the Solar Wind**. 148 (Apr. 1967), 217–227. DOI: 10.1086/149138 (see pages 22, 62). Authors: Edmund J. Weber and Jr. Davis Leverett.

[Web+20] **The XMM-Newton serendipitous survey. IX. The fourth XMM-Newton serendipitous source catalogue**. 641A136 (Sept. 2020), A136. DOI: 10.1051/0004-6361/201937353. arXiv: 2007.02899 [astro-ph.HE] (see page 69). Authors: N. A. Webb et al..

[Web+23] **Understanding Active Region Emergence and Origins on the Sun and Other Cool Stars**. *arXiv e-prints* arXiv:2306.06536 (June 2023), arXiv:2306.06536. DOI: 10.48550/arXiv.2306.06536. arXiv: 2306.06536 [astro-ph.SR] (see page 5). Authors: Maria A. Weber, Hannah Schunker, Laurène Jouve, and Emre Işık.

[Wes+04] **Spectroscopic Properties of Cool Stars in the Sloan Digital Sky Survey: An Analysis of Magnetic Activity and a Search for Subdwarfs**. 128:1 (July 2004), 426–436. DOI: 10.1086/421364. arXiv: astro-ph/0403486 [astro-ph] (see page 63). Authors: Andrew A. West et al..

[WG01] **Observational Constraints on the Formation and Evolution of Binary Stars**. 556:1 (July 2001), 265–295. DOI: 10.1086/321542. arXiv: astro-ph/0103098 [astro-ph] (see page 35). Authors: R. J. White and A. M. Ghez.

[Win+10] **Hot Stars with Hot Jupiters Have High Obliquities**. 718:2 (Aug. 2010), L145–L149. DOI: 10.1088/2041-8205/718/2/L145. arXiv: 1006.4161 [astro-ph.EP] (see pages 22, 41, 49). Authors: Joshua N. Winn, Daniel Fabrycky, Simon Albrecht, and John Asher Johnson.

[WN77] **Mass and energy flow in the solar chromosphere and corona.** 15 (Jan. 1977), 363–387. DOI: 10.1146/annurev.aa.15.090177.002051 (see page 30). Authors: G. L. Withbroe and R. W. Noyes.

[Wri+09] **TEN NEW AND UPDATED MULTIPLANET SYSTEMS AND A SURVEY OF EXOPLANETARY SYSTEMS**. *The Astrophysical Journal* 693:2 (Mar. 2009), 1084–1099. DOI: 10.1088/0004-637x/693/2/1084. URL: https://doi.org/10.1088/0004-637x/693/2/1084 (see page 44). Authors: J. T. Wright, S. Upadhyay, G. W. Marcy, D. A. Fischer, Eric B. Ford, and John Asher Johnson.

[Wri+11] **The Stellar-activity-Rotation Relationship and the Evolution of Stellar Dynamos**. 743:1, 48 (Dec. 2011), 48. DOI: 10.1088/0004-637X/743/1/48. arXiv: 1109.4634 [astro-ph.SR] (see pages 6, 8, 9, 12, 22, 50, 78, 89, 90, 95, 96). Authors: Nicholas J. Wright, Jeremy J. Drake, Eric E. Mamajek, and Gregory W. Henry.

[Wri+18] **The stellar rotation-activity relationship in fully convective M dwarfs**. 479:2 (Sept. 2018), 2351–2360. DOI: 10.1093/mnras/sty1670. arXiv: 1807.03304 [astro-ph.SR] (see pages 5, 6, 8, 78, 80). Authors: Nicholas J. Wright, Elisabeth R. Newton, Peter K. G. Williams, Jeremy J. Drake, and Rakesh K. Yadav.

[WS98] **The age of the most nearby star**. 332 (Apr. 1998), 215–223. arXiv: astro-ph/9706149 [astro-ph] (see page 62). Authors: A. Weiss and H. Schlattl.

[WW94] **A New Evolutionary Model for Am-Herculis Binaries**. 266 (Jan. 1994), L1. DOI: 10.1093/mnras/266.1.L1 (see page 12). Authors: D. T. Wickramasinghe and K. Wu.

[Yad+15] **Explaining the Coexistence of Large-scale and Small-scale Magnetic Fields in Fully Convective Stars**. 813:2, L31 (Nov. 2015), L31. DOI: 10.1088/2041-8205/813/2/L31. arXiv: 1510.05541 [astro-ph.SR] (see page 5). Authors: Rakesh K. Yadav et al..

[Yak+09] **Close binary and other variable stars in the solar-age Galactic open cluster M 67**. 503:1 (Aug. 2009), 165–176. DOI: 10.1051/0004-6361/200911918. arXiv: 0906.4908 [astro-ph.SR] (see page 62). Authors: K. Yakut et al..

[Zah08] **Tidal dissipation in binary systems**. In: *EAS Publications Series*. Ed. by M. -J. Goupil and J. -P. Zahn. Vol. 29. EAS Publications Series. Jan. 2008, 67–90. DOI: 10.1051/eas:0829002. arXiv: 0807.4870 [astro-ph] (see page 16). Authors: J. -P. Zahn.

[Zah66a] **Les marées dans une étoile double serrée**. *Annales d'Astrophysique* 29 (Feb. 1966), 313 (see page 17). Authors: J. P. Zahn.

[Zah66b] **Les marées dans une étoile double serrée (suite)**. *Annales d'Astrophysique* 29 (Feb. 1966), 489 (see pages 17, 104). Authors: J. P. Zahn.

[Zah75] **The dynamical tide in close binaries.** 41 (July 1975), 329–344 (see pages 18, 87). Authors: J. -P. Zahn.

[Zah77] **Tidal friction in close binary systems.** 57 (May 1977), 383–394 (see pages 12, 16, 17, 21, 41, 62, 80, 87, 88). Authors: J. -P. Zahn.